

Spectral evolution of GRBs: new insights into their physics

Thesis submitted for the degree of
“Doctor Philosophiæ”

CANDIDATE

Giancarlo Ghirlanda

SUPERVISORS

Prof. Annalisa Celotti
Prof. Gabriele Ghisellini
Dr. Marco Tavani

October 2002

Dedicated to the memory of my mother

Contents

Acknowledgments	7
Introduction	1
1 GRBs: observations and theories	7
1.1 Introduction	7
1.2 Observational evidences	7
1.2.1 The distance scale	7
1.2.2 Temporal properties	9
1.2.3 The Afterglow	10
1.2.4 Hosts and Cosmology	15
1.3 The Standard Model	16
1.3.1 The fireball: internal/external shock model	17
1.4 Progenitor	18
2 Spectral properties of GRBs	23
2.1 Introduction	23
2.2 Definitions	24
2.3 Pre-CGRO era	26
2.4 The characterization of the GRB spectrum by BATSE	27
2.4.1 Time integrated burst spectrum	28
2.4.2 The spectral evolution	31
2.5 Spectral evolution models	44
2.5.1 The geometric model	44
3 Emission processes acting in GRBs	47
3.1 Introduction	47
3.2 Synchrotron Model	48
3.2.1 Optically thin synchrotron emission	48
3.2.2 Synchrotron self absorption	50

3.2.3	Synchrotron Cooling	50
3.2.4	The synchrotron shock model	51
3.2.5	Non homogeneous spatial distribution in fast cooling regime	53
3.2.6	Jitter Radiation	54
3.2.7	Small Pitch Angle Distribution	57
3.3	Comptonization Model	58
3.3.1	Inverse Compton Process	59
3.3.2	Comptonization	61
3.3.3	Compton scattering by flash heated circumstellar clouds	64
3.3.4	Compton Attenuation Model	66
3.3.5	Saturated Compton Cooling	68
3.3.6	Quasi-Thermal Comptonization	70
3.3.7	Photosphere	72
3.3.8	Compton Drag	73
4	BATSE and the spectral data analysis	75
4.1	From the Vela satellites to CGRO	75
4.1.1	The Compton Gamma Ray Observatory	76
4.2	The Burst and Transient Source Experiment	77
4.2.1	Technical characteristics	78
4.2.2	The trigger method	78
4.3	Data Products	80
4.3.1	Burst Data	80
4.3.2	Burst Data Files	81
4.4	GRB960924 - A case study	82
4.4.1	SD and LAD data analysis	88
5	Time resolved spectral analysis of bright GRBs	97
5.1	Introduction	97
5.2	Data selection and analysis	98
5.2.1	Data Selection	98
5.2.2	The bursts sample	99
5.2.3	Spectral analysis	99
5.2.4	Spectral Models	101
5.3	Results	105
5.3.1	Time integrated pulse spectrum	106
5.3.2	Time resolved spectra	109
5.3.3	The Synchrotron limit violation	117

5.4	Conclusions	120
6	Extremely hard GRB spectra prune down the forest of emission models	127
6.1	Introduction	127
6.1.1	Spectral slopes and emission models	129
6.2	Data Analysis	131
6.3	Results	132
6.3.1	GRB 980306	133
6.3.2	GRB 911118	134
6.3.3	Tests of the significance of the spectral results	137
6.4	Other hard bursts	139
6.5	Black body spectra	142
6.6	Discussion	146
6.6.1	Synchrotron emission	147
6.6.2	Compton attenuation	150
6.6.3	Quasi-thermal Comptonization	150
6.6.4	Photospheric emission	151
6.6.5	Compton drag	151
6.7	The possible thermal character of the initial phase	152
6.7.1	Photospheric emission	152
6.7.2	Compton drag	158
6.8	Conclusions	160
7	Spectral evolution morphologies	173
7.1	Introduction	173
7.2	The standard spectral evolution analysis	174
7.3	A different approach	176
7.3.1	Evolutionary Morphologies	177
7.4	Correlations and trends	178
7.4.1	The envelope	181
7.4.2	Peculiar evolutions	182
7.4.3	The hard to soft evolution in mixed morphologies	183
7.5	Conclusions	184
	Conclusions	1
	Bibliography	5

I would like to thank my supervisor, Annalisa Celotti, for her guiding and supporting me during these three years of PhD research. I am particularly grateful to Annalisa and Gabriele Ghisellini because they showed me how to approach in a positive, critical and open-minded way any scientific possibilities that one might encounter during the research process.

Many thanks also to Dr. David Band for his careful reading of this thesis and for his constructive comments on it.

I am also grateful to all my friends and colleagues and particularly to Roberta and Stefano who supported me in the final rush.

Introduction

Since their discovery in the late sixties, Gamma-ray Bursts (GRBs) have been one of the greatest puzzles of science. They are intense bursts of gamma ray photons with energy in the range 0.1-1 MeV lasting few tens of seconds, with heterogeneous spectral and temporal features. The progress in the knowledge of their observational characteristics and, consequently, of their theoretical interpretation, has always been strictly connected with the technological advances in the detectors and satellites design for the specific observation and study of these transient and extremely energetic events.

GRBs were discovered by the VELA satellites monitoring the respect of the nuclear test ban treaty (Klebesadel et al. [84]). Their existence was confirmed by the observations of the soviet Konus satellites (Mazets et al. [103]) and subsequently by other missions. The low positional accuracy of these first experiments did not allow for their distance determination and opened the first great debate about their energetics. In fact, if GRBs were placed at cosmological distances, their observed fluences, implied a huge ($E \leq 10^{54}$ erg) isotropic energy.

The distance problem was partially solved by the discovery of their isotropic distribution (Meegan et al [108]) by the Burst And Transient Source Experiment (BATSE) on board the Compton Gamma Ray Observatory (CGRO), launched in spring 1991. This detector, which accumulated a large homogeneous collection of GRBs (more than 3000) during its nine year activity, provided the first solid hint about their cosmological origin combining the evidence of an isotropic space distribution with a deficiency of faint GRBs with respect to a homogeneous distribution of sources in Euclidean space. BATSE also supplied additional informations on GRBs: their spectra were confirmed to have a non-thermal character (see chap.3 for details) typically represented by a single or multiple power law (Band et al. [4]) with a break in the energy range 200 - 300 keV. The light curves show single smooth peaks or complicated multi-peaked structures, the burst durations range from 1 ms to about 1000 sec, with a bimodal distribution separated at ~ 2 sec (Kouveliotou et al. [86]), and an anticorrelation between the spectral hardness and duration, with the short bursts being harder than long ones (e.g. Fishman & Meegan [38]).

The cosmological origin of GRBs was definitely confirmed in 1997 by the observation of their counterparts by the Italian - Dutch satellite Beppo-SAX. The first X-ray afterglow discovery (GRB 970228 - Costa et al. [17]) was followed by an increasing num-

ber of afterglow observations (at a rate of about 10 yr^{-1}) at other wavelengths (e.g. van Paradijs et al. [124], Frail et al. [43]) which allowed the determination of the redshift and the study of the host galaxies (Kulkarni et al. [87]). The first redshift measurement, from the absorption line in the optical transient of GRB 970508, resulted in $z=0.835$ (Frail et al. [43]) and the actual redshift distribution for 20 GRBs (Djorgovsky et al. [30]) has a mean value $\langle z \rangle = 1.27$ and extends to $z_{max} = 4.5$, for GRB 000131 (Andersen et al. [2]).

The host galaxies seemed to be faint galaxies with intense on-going star formation (Djorgovsky et al. [30], Totani et al. [155]): this evidence supports the massive star progenitor scenario (Woosley [162], Paczynski [121], Vietri et al. [157]) in which the burst is expected to explode in the same region where its progenitor was formed, and has important cosmological implications for the study of the star formation rate (e.g. Lamb [89]).

The afterglow observations also provided some evidence of the possible anisotropic structure of GRBs, with an opening angle of about $\sim 5^\circ$ (Israel et al. [73], Sari et al. [142], Frail et al. [44]), while the possible detections of iron lines in a few X-ray afterglows (Piro et al. [127]) have been interpreted to constrain environment densities and bursts energetic (Ghisellini et al. [58]).

The discovery and analysis of 17 X-Ray Flashes (XRF) detected by the Wide Field Camera (on board SAX) in the 2-26 keV energy range, with duration between 10 and 200 sec and quite isotropic sky distribution, have been recently reported by Heise et al. ([69]). The comparison of their temporal and spectral properties with classical GRBs seems to favor the idea that XRF could be the low energy (X-ray) extension of the GRB population (Kippen et al. [81]).

A possible theoretical interpretation of these observational evidences has been proposed through the “standard” fireball scenario. According to this model the inner engine of GRBs releases a large amount of energy ($\sim 10^{52}$ erg) in a small volume ($\sim 10^7$ cm) then producing a relativistic outflow which expands in the surrounding medium, i.e. the fireball. The energy and matter density is initially so high that these components thermalize and when the fireball becomes transparent it should release its internal energy in form of thermal photons. The typical non thermal character of GRB spectra, instead, motivated the formulation of an efficient mechanism for the extraction of the internal energy and then for its conversion into non thermal radiation. The simplest model of energy transport in the relativistic flow is in the form of kinetic energy of particles. A proposed variant is based on the possibility that a fraction of energy is transported by Poynting flux (Spruit et al. [151]). Among the possible mechanisms for the conversion of this energy into radiation, the most successful was the internal/external shock model. The internal shocks (Rees & Meszaros [133]), which are produced by the collision of fireballs with different Γ , accelerate the electrons responsible of the synchrotron emission. The external shock (Meszaros & Rees [112]) is determined by the deceleration of the fireballs by the ISM and produces the Afterglow emission.

Some observational confirms of this model have been found: the scintillation of the radio afterglow of GRB 970508 (Goodman et al. [62], Frail et al. [43]) and its optical spectrum, proved the small size of the emission region representing a “direct” measure of the relativistic expansion. Another important observational fact was the narrow range of peak energies of the bursts spectra, typically clustered around 300 keV which is predicted by synchrotron emission under particular assumptions. Finally the observations of the breaks in the afterglow light curves, if interpreted as due to the expansion of the jet (Sari et al. [144], Kulkarni et al. [87]), would require a beamed (anisotropic) fireball model (Rhoads [134], Sari et al. [144]).

Currently the most widely accepted scenarios for the progenitor of GRBs are the collapsar or single star model (Woosley [162], Paczynski [121], Fryer et al. [45]) or the merger of NS and/or BH in binary systems (Paczynski [119], Goodman [61], Meszaros & Rees [112]).

This thesis presents the time resolved spectral analysis of a sample of bright long bursts observed by BATSE and discusses the main findings in the light of the proposed emission models.

GRB spectra are characterized by several properties and by different evolution morphologies on small timescales (briefly reviewed in chapt.2). Extensive analysis of burst samples, with high spectral and temporal resolution (e.g. Preece et al. [130]) has led to the definition of these spectral properties. No unique spectral shape seems to describe all spectra which span a rather wide range of slopes at low and high energies. Moreover, no clear trends in the spectral evolution emerged from previous spectral analysis due to the large variety of evolutionary morphologies.

Within this observational picture we analyzed the time resolved spectra of bright bursts, on the smallest timescale available, in order to determine if there is a preferential function, among those typically assumed to represent the spectrum, which better fits the time resolved or time integrated spectra and in order to investigate the differences between the spectrum integrated on the duration of single pulses or time resolved within the same pulses.

The analysis of 25 bursts, with high temporal and spectral resolution BATSE data, is presented in chapter 5. The procedure adopted for the data reduction and their analysis is presented in chapter 4.

The most accepted scenario for the GRB prompt emission is synchrotron radiation of relativistic electrons in a strong magnetic field (Katz [77], Tavani [154]). This model predicts, in its simplest formulation, a limiting slope for the spectrum at low energies ($F(E) \propto E^{1/3}$) which agrees with different spectral evidences. Nonetheless, a considerable number of bursts (15%) was found to be harder than this limit.

An important test for the optically thin synchrotron model, which we performed for the first time on the time resolved spectra of bright bursts, is the direct fit of its spectral shape to the observed spectra. The results are reported in chapter 5 and compared to the spectral parameters obtained fitting other (canonical) spectral functions. The violation of the synchrotron limit in these spectra is discussed.

Possible alternative scenarios for the GRB prompt emission, based on synchrotron theory (Lloyd & Petrosian [99], Medvedev [107]) or on Comptonization (Brainerd [12], Liang [97], Ghisellini & Celotti [55]), have been proposed to justify the violation of this limit and the totality of the observed spectral properties, and they are summarized in chapter 3.

Although these models allow for the existence of spectra harder than $E^{1/3}$, they predict other limiting slopes which can be compared with the observations. In this sense we searched for the hardest spectra observed by BATSE which can constrain these alternative models. 5 bursts with low energy spectral slopes harder than E^0 are analyzed in chapter 6. Their hardness is verified with different tests in order to derive robust constraints which are compared and discussed within the above emission models.

The particularly hard low energy spectrum of some of these bursts ($F(E) \propto E^2$) results to be even consistent with a thermal black body spectrum. This was tested systematically on all the spectra of the bursts reported in chapter 6 and found to reasonably fit the initial phases of these GRBs. The interpretation of these results, within the context of the photospheric or Compton drag model, is detailed in chapter 6.

The other aspect which emerged from the time resolved analysis of this sample of bright bursts is the presence of different spectral evolution morphologies. The variability of the low and high energy spectrum of GRBs on small timescales (Ford et al. [42]) and the complexity of the spectral evolution have been reported by different authors (Crider et al. [23], Preece et al. [129]) through the study of the temporal evolution of the peak of the spectrum.

A different approach which describes the spectral evolution in terms of the complete set of parameters, obtained fitting the observed spectra, is proposed in chapter 7. The correlations of the spectral parameters with the flux are explored and the spectral evolution morphologies, revealed by this analysis, are discussed.

The Conclusions summarize the main implications of these results on the physics of GRBs, and outlines the opportunities of studying their spectral properties with unprecedented spectral coverage and time resolution, offered by the forthcoming missions (AGILE, GLAST, SWIFT).

Most of the content of this thesis (chapter 5 and 6) is part of published and submitted papers:

Ghirlanda G., Celotti A., Ghisellini G.

Time resolved spectral analysis of bright Gamma Ray Bursts
2002, *Astronomy & Astrophysics*, Vol. 393, 409.

Ghirlanda G., Celotti A., Ghisellini G.

Extremely hard GRB spectra prune down the forest of emission models
2002 to appear in *A&A* 406, 879.

and proceedings:

Ghirlanda G., Celotti A. and Ghisellini G.

Spectral analysis of Bright GRBs

2001 astro-ph/0112514

Proceedings of "Gamma-Ray Burst and Afterglow Astronomy 2001"

Woods Hole (MA) 5-9 November 2001

Tavani M, Band D., Ghirlanda G.

Time resolved GRB spectroscopy

"5th Huntsville Symposium"

Huntsville, Alabama, USA, 18-22 October, 1999.

Editors: R. Marc Kippen, Robert S. Mallozzi, Gerald J. Fishman.

AIP Conference Series, Vol. 526, 185

Chapter 1

GRBs: observations and theories

1.1 Introduction

This chapter describes the main characteristics of GRBs and of the theoretical models proposed for their interpretation. Exhaustive reviews on these subjects can be found in Piran ([126]), Meszaros ([114]) and Djorgovski [31].

In sec.1.2 are summarized the most important findings about gamma ray bursts obtained in more than 30 years of study: from the distance scale problem (sec.1.2.1), through the afterglow discovery (sec.1.2.3), to the most recent host galaxies analysis and their implications for cosmology (sec.1.2.4). Sec.1.3 outlines the standard model of GRBs and the internal/external shock scenario (sec.1.3.1). The possible progenitors, and their relation to the burst properties, are sketched in sec.1.4.

The spectral properties of GRBs, being the specific subject of this thesis, are presented in more details in chapt.2, whereas the emission models proposed for the burst γ -ray prompt phase, are detailed in chapt.3.

1.2 Observational evidences

1.2.1 The distance scale

Soon after their discovery, GRBs were interpreted as the transient emission of Galactic neutron stars. Unfortunately, this picture could not justify the isotropic sky distribution of a large sample of bursts observed by BATSE which opened the debate about the bursts origin. In fig.1.1 (*left panel*) is reported the angular distribution for 1637 GRBs in the 4B BATSE catalog¹, complete until 1996 (Paciesas et al. [118]): this distribution has a dipole moment $\langle \cos\theta \rangle = -0.025 \pm 0.014$ and a quadrupole moment $\langle \sin^2\theta - 1/3 \rangle = -0.001 \pm 0.007$ which deviates 1.1σ and 0.4σ from the corresponding moments

¹<http://coss.gsfc.nasa.gov/batse/4Bcatalog/index.html>

of an isotropic angular distribution, opportunely corrected for non uniform sky coverage (Paciesas et al. [118]).

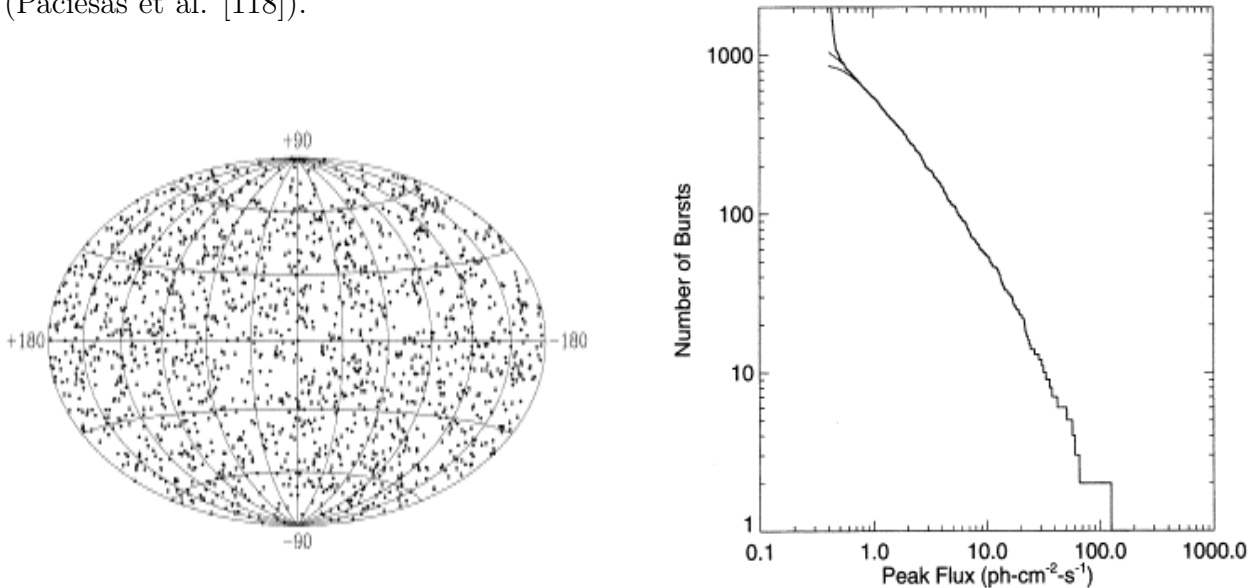


Figure 1.1: *Left*: distribution of the bursts of the 4B catalog with revised galactic coordinates. *Right*: peak flux distribution for bursts exceeding the 256 ms threshold. From Paciesas et al. [118].

A recent search for the untriggered bursts within the BATSE database (Kommers et al. [85]) has revealed a sample of 873 GRBs under the detection thresholds: these events, extending the sample of triggers, confirm the isotropic angular distribution of GRBs (with dipole and quadrupole moment -0.0029 ± 0.0195 and -0.0015 ± 0.0101 , respectively).

The isotropic distribution of the bursts detected by BATSE might be consistent only with a population of sources which are distributed in an extended galactic halo or at cosmological distances.

The necessity of fixing the typical distance of GRBs was closely related to their energy reservoir which, in fact, is very different if they originate within the galaxy or at cosmological distances. An important BATSE result which, combined with the above distribution favored the cosmological distance scale (Paczynski [120]), is the peak flux distribution: in fig.1.1 (*right panel*) is reported the cumulative distribution of the flux (photon $\text{cm}^{-2} \text{sec}^{-1}$), at the peak of the light curve, accumulated on 256 ms timescale for the bursts of the 4B catalog. It shows a departure from the $-3/2$ slope predicted for an homogeneous distribution of sources in Euclidean space. The homogeneity test $\langle V/V_{max} \rangle \sim 0.32$ has a substantial deviation from the value (i.e. 0.5) predicted for the same homogeneous population of sources distributed in Euclidean space, and this, combined with the deviation of the LogN–LogS at low fluxes, favours the cosmological nature of GRBs. The final and conclusive evidence that GRBs originate at cosmological distances was the first redshift measurement of GRB 970508 (Frail et al. [43]) at $z=0.835$. This was followed by an increasing number of bursts with associated redshift and the

actual z distribution (excluding the case of GRB980425 associated with the the relative close by supernova 1998bw at $z \sim 0.008$, Galama et al. [48]) extends from 0.4 to 4.5.

1.2.2 Temporal properties

The light curves of GRBs reveal a wide range of temporal characteristics: they last from few seconds to kiloseconds and present extremely different intensities and morphologies.

The duration distribution, defined with the T_{90} parameter² and reported in fig.1.2, shows a bimodality with a separation at about 2 sec (Kouveliotou et al. [86]). This is considered a signature of the possible existence of two different populations of bursts: long GRBs, lasting more than 2 sec (with a typical duration around 10 sec), and short bursts (about a third of the total) with $T_{90\%} \leq 2$ sec (Mitrofanov et al. [115]). This bimodality was confirmed also by the associated spectral shape, since short bursts, on average, appear harder than long ones. Moreover, these duration separation has been suggested to reflect a possible different origin for long and short bursts, i.e. the single star core collapse or the binary merger (Fryer et al. [45]), although this theoretical prediction still need a confirm.

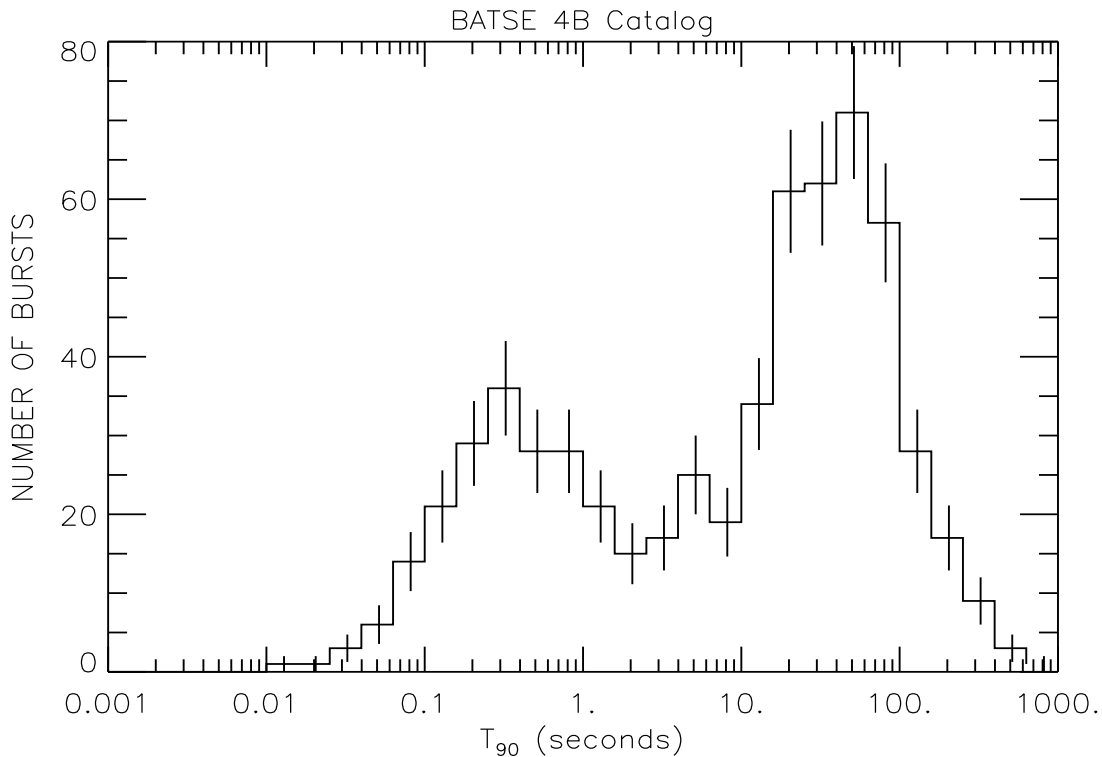


Figure 1.2: Duration distribution (T_{90}) for the bursts of the 4B catalog (Paciesas et al. [118]).

The GRB light curves have different morphologies and cannot be easily classified

² $T_{90\%}$ is the time interval containing the 90% of the burst fluence

according to a simple scheme (Fishman & Meegan [38]) although there are evidences that the burst pulses might be represented by a stretched exponential function (Norris et al. [117]) $N(t) \propto \exp(-[(t - t_{max})/\sigma_{r,d}]^\nu)$, where t_{max} represents the time of the pulse peak, $\sigma_{r,d}$ is the rise or decay constant and ν is a measure of the peakedness of the function. This expression has been fitted to samples of pulses and Norris et al. ([117]) have found that the decay phase is mostly represented by a pure exponential ($\nu = 1$) or a gaussian tail ($\nu = 2$). These results have been confirmed by Li & Fenimore ([93]) through direct fitting of this function to single spikes in highly variable light curves. Their analysis also showed that the rise phase is typically faster than the decay, confirming the FRED (Fast Rise Exponential Decay) temporal morphology.

The light curve of GRBs is also erratic and the flux can vary significantly on very small timescales. This burst variability is typically of 1 – 4 ms with a minimum of 0.2 ms (Schaefer & Walker [148]) and represent a constraint for the burst models (Walker et al. [159]). In multi-peaked bursts the variability timescale is invariant from the beginning to the end of the burst (Ramirez-Ruiz & Fenimore [132]). The short and invariant timescale of the burst emission would favor the internal shock scenario because it associates the observed variability to the distribution of the Lorentz factors of the colliding shells. In the external shock model, instead, the decrease of Γ , due to the interaction with the ISM, would produce a stretching of the variability timescale in late pulses.

Recently, Fenimore & Ramirez–Ruiz ([37]) have shown that the variability measure, for a sample of bursts, is significantly anti-correlated with their absolute luminosity: smooth bursts are intrinsically less luminous. This relation, if confirmed, could be used to determine the GRBs redshift, only from their temporal properties.

1.2.3 The Afterglow

The Afterglow of the burst is its emission in the X-ray, optical, IR and Radio band. GRB 970228 is the first γ -ray burst for which an optical counterpart was found (Costa et al. [17], Frontera et al. [46]) thanks to the fast and precise determination of its position in the WFC. The optical transient, a 21st magnitude source in a position consistent with the γ ray detection (van Paradijs et al. [124]), was embedded in an extended object (Groot et al. [64]), i.e. the host galaxy. Subsequent HST observations showed the typical power law decay in flux of the Optical Transient (OT) and determined its redshift $z=0.695$ (Djorgovski et al. [31]).

The light curve of the optical afterglow of GRB 970228, 2 weeks after the burst, shows a deviation from a pure power law (fig.1.3): this was speculated to be a possible signature of the presence of a SN type Ic whose flux, as possibly shown in fig.1.3 (Galama et al. [49]) becomes important when the afterglow is dim enough. Observations of GRB afterglows span a broad range of frequencies, roughly from ~ 1 GHz to 10^9 GHz, and timescales from hours (or even minutes) to a few years after the burst. Their broad band light curves, as shown for example in fig.1.4, convey useful informations on the afterglow and also on the nature of the progenitor. As shown in the examples reported in fig.1.4

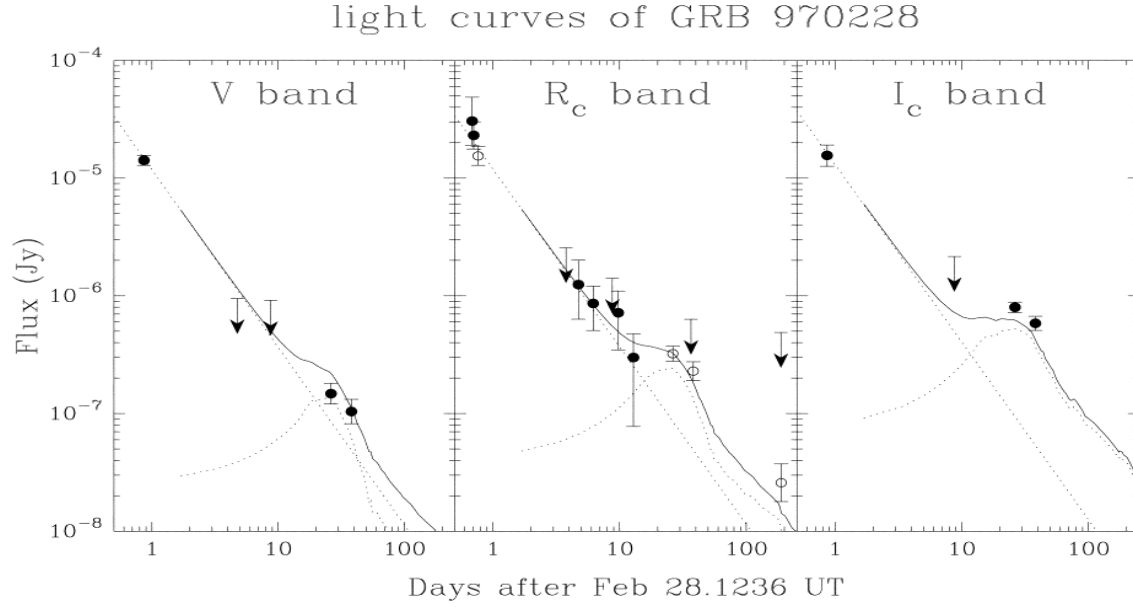


Figure 1.3: Light curves of GRB 970228. Dotted curves indicate power-law decays with index -1.51 and the redshifted SN 1998bw light curve. From Galama et al. [49]

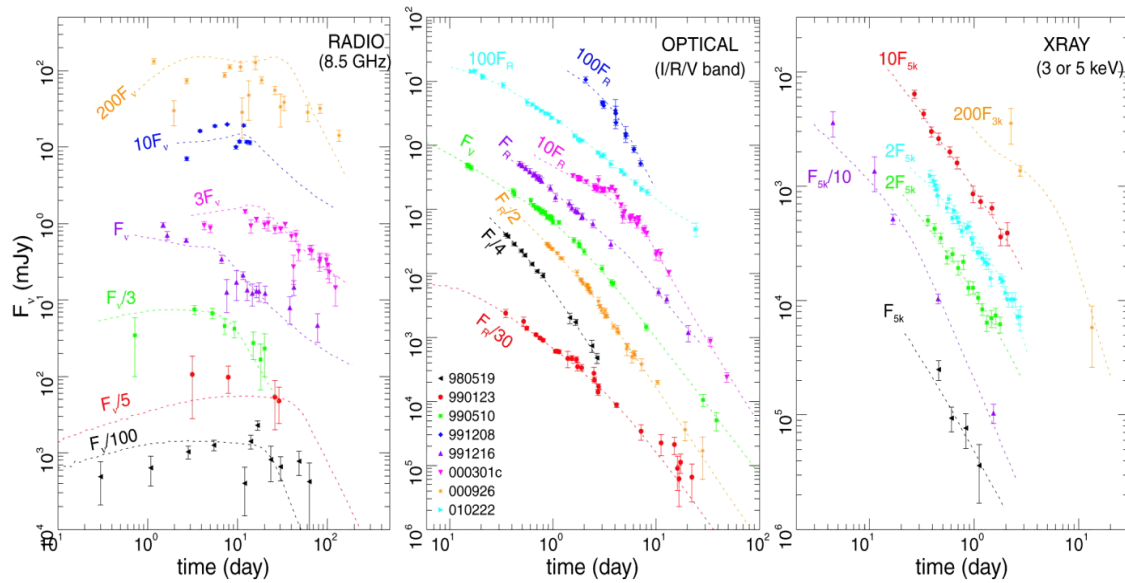


Figure 1.4: Radio, optical, and X-ray emission and model light curves for the GRB afterglows 980519, 990123, 990510, 991208, 991216, 000301c, 000926, and 010222. Optical data have been corrected for Galactic dust extinction. Fluxes have been multiplied by the indicated factors, for graphical purposes. From Panaitescu & Kumar [122]

(from Panaitescu & Kumar [122]), the afterglow light curve is often modeled by a single or a multiple power law which has its natural explanation in the context of the external shock model as due to the deceleration (Γ decrease) of the expanding shell by the ISM.

From these data, Panaitescu & Kumar ([122]), propose that the kinetic energies involved in the afterglow phase (i.e. still available after the GRB) are clustered around a mean value of 3×10^{50} erg.

Another consequence of a possible analysis of these data is that they could imply jet apertures of $\sim 2^\circ$. For all the eight afterglows reported in fig.1.4, the total energy in the shock-accelerated electrons, according to the standard external shock model, is close to the equipartition value and the slope of the power-law electron energy distribution varies between 1.4 and 2.8. The implied densities of the medium are $\sim 0.1 - 50 \text{ cm}^{-3}$ with the exception of GRB 990123 which, according to the analysis of Panaitescu & Kumar ([122]), indicates a density of 10^{-2} cm^{-3} . Such low densities could find a possible explanation in the super bubble model (Scalo & Weeler [146]) although observational evidence is still required to support this theory.

Interestingly, the deviations and complications of the simple power law shape observed in several broad band afterglows, and partly determined by observational limitations, represent useful tools for the determination of some physical properties of the afterglow environment:

- interstellar scintillation, which affects the radio observation, has been used to resolve the afterglow size (Frail et al. [43]) in the case of GRB 970508;

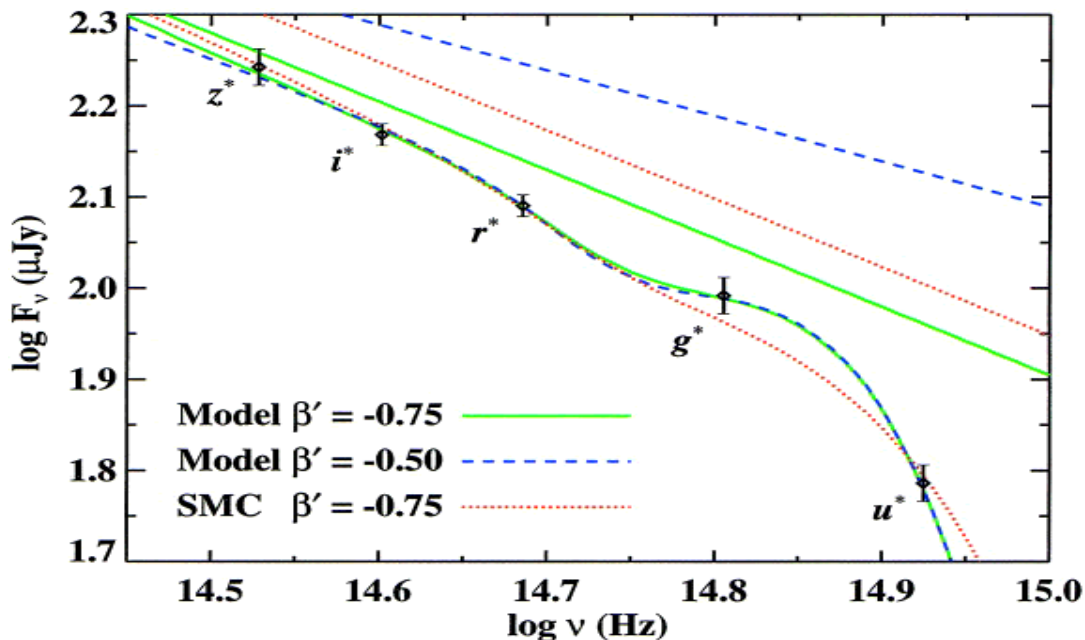


Figure 1.5: Multi-band observations of GRB 010222. The solid and dotted curves through the data points correspond to the extinction model fit for $z = 1.477$ and a source spectrum with slope of $\nu^{-0.75}$ (green solid curve) and $\nu^{-0.5}$ (blue dashed curve). From Lee et al. [92].

- extinction in the optical and NIR (corresponding to the UV rest frame), which alters the observed optical light curve, provides informations on the GRB environment: Lee et al. [92] report the multicolor observations of GRB 010222 (fig.1.5), corrected for reddening and for the afterglow temporal decay, and suggests that they can be reasonably fitted by a power law $F \propto \nu^{-0.90 \pm 0.03}$ with the exception of the UV (fig.1.5, u^* measure) which mostly suffers from the dust extinction of the star forming region in which the burst exploded.
- the inverse Compton scattering, which can dominate the electron cooling and produce an excess in the X-ray band, can provide an estimate of the density of the medium: Harrison et al. [68] report the broad band light curve of GRB 000926, and, though the model is quite complex, if compared to the low number of data points at high energies, they suggest that the X-ray data are consistent with the presence of an IC component (fig.1.6).

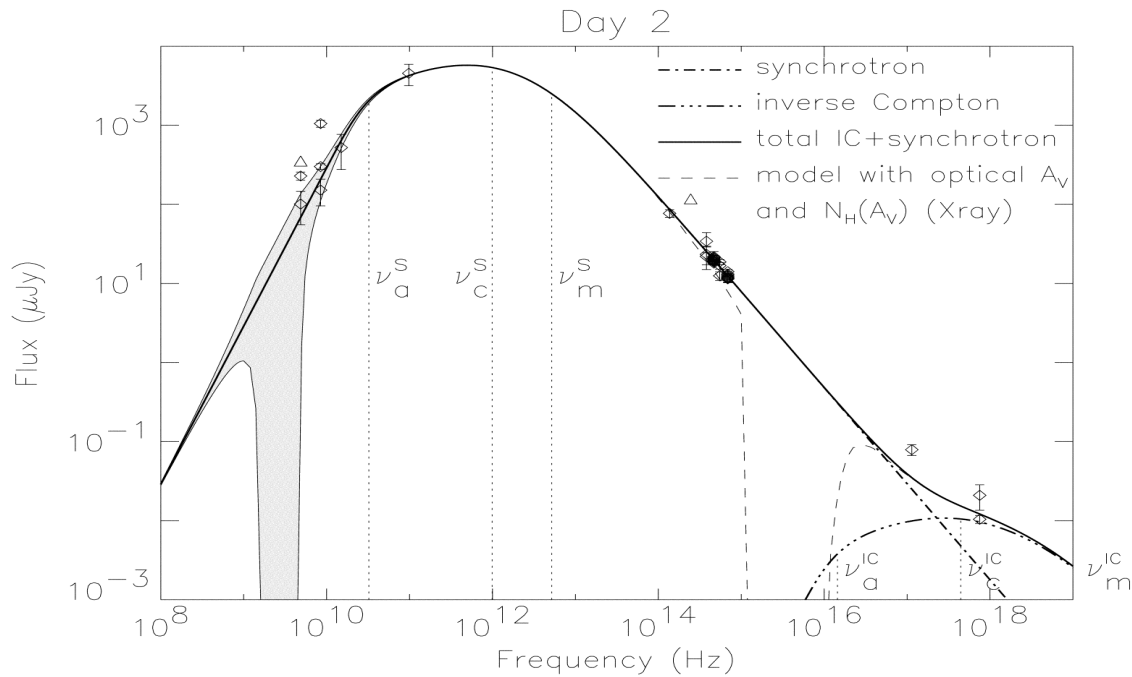


Figure 1.6: Broad-band spectrum of the afterglow of GRB 000926, two days after the jet break. The data, corrected for host extinction, are shown by diamonds, with their 1σ errors, the solid line is the best-fit model without host extinction, and the dashed line shows model plus extinction. The locations of the synchrotron spectral breaks, associated with self-absorption, cooling, and the maximum electron energy, respectively, are indicated. The IC component (*dot-dashed line*) in the right hand corner contributes the X-ray excess of the early afterglow. Form Harrison et al. [68]

Detecting the IC emission in the X-ray band directly implies a lower limit on the density (Sari & Esin [145]) which, in this case, results $n = 30 \text{ cm}^{-3}$. This value is higher than the average ISM density in a typical galaxy and is consistent with a diffuse interstellar cloud, as those commonly found in star-forming regions. Combining the density with the host column density N_H derived from optical observations and assuming typical dust-to-gas ratios, Sari & Esin ([145]) derive a 2 pc size for the cloud. These results have been suggested as additional possible evidence of the association of GRBs with SF region.

- the presence of a host galaxy (sec.1.2.4) which may obscure the afterglow at late times, can provide better estimates of the star formation rate: late-time observations of GRB 980703 by Berger & Kulkarni [7], for example, revealed a steady radio component, with a flux density $F(1.43\text{GHz}) = 68.0 \pm 6.6 \text{ Jy}$ and spectral and temporal signatures typical of star forming regions. This led to the interpretation that this host galaxy is a Ultra Luminous Infra Red Galaxy, undergoing a starburst, likely concentrated within its inner 3 kpc.

These are just few examples indicating how the observations of GRBs in different bands and the analysis of their environments can provide important constraints on their physical parameters.

Another feature of the afterglow radiation is its polarization: synchrotron emission, in fact, should reach a level of 60% of polarization for ordered magnetic fields, which might be observed as 10%-20% if the emission occurs within a collimated outflow. This percentage of polarization is lowered in the case of GRBs due to the averaging of the polarimetric measure on unresolved sources (de-polarization effect). Hjoth et al. [70] report an upper limit for the R band polarization of 2.3% in the case of GRB 990123. Another measure comes from GRB 990510 (Covino et al. [19]) with a polarization of 1.7 ± 0.2 . Such low level of polarization has been suggested to be possibly produced by a magnetic field which is highly tangled, because generated by some instability (Gruzinov & Waxman [66]), or due to the aberration effects of the ring shape of the emitting region (Ghisellini & Lazzati [53]).

The discovery and analysis of emission lines in the GRB X-ray afterglow (Piro et al. [127]) provide constrains on the line-emitting material (Ghisellini et al [59]). These lines are usually identified as iron K_α emission features with an estimated energy $\sim 10^{49} \text{ erg}$, which implies a γ -ray energy, responsible for the ionization of the medium and of the consequent line emission, of 10^{51} erg . This value represents a lower limit for the burst energy derived independently from the beaming or collimation argument (Ghisellini et al [59]).

1.2.4 Hosts and Cosmology

The galaxies which host GRBs provide insights on the burst source:

- they allow to study the environment in which the GRB occurs and in which its progenitor evolved;
- they can be used to measure (or confirm) the redshift of the GRB, especially when too late afterglow detections do not allow a spectroscopic absorption line identification or when the OT is not detected;
- the displacement of the OT with respect to the center of the host provides useful information about the GRB progenitor and its association with star forming regions.

The observations in the visible (UV rest frame) are particularly difficult, due to the large intrinsic and galactic extinction. The absolute magnitudes, determined from the R band, assuming a power law spectrum with index -1 and no extinction correction (Djorgovski et al. [30]), show that the hosts of GRBs are sub luminous relative to present day luminous galaxies with possible implications for GRB–star formation association.

The sample of host galaxies, complete to GRB 010222, indicates a median apparent magnitude $R \sim 24.8$, with a possible upper limit $R \sim 29$. Down to $R \sim 25$ the magnitude distribution is consistent with deep field galaxy counts (Smail et al. [150]).

The analysis of the star formation rate (through the [O II] 3727 doublets and UV continuum at 2800 Å or the Ly α 1216 Å line - which are all susceptible to the extinction within the host galaxy) indicates that it ranges from a few tenths to a few $M_{\odot} \text{ yr}^{-1}$ which is typical for the normal field galaxies, at comparable redshifts.

The host galaxy morphologies seem to favor the late and irregular type, as shown by the analysis of 20 hosts by Bloom et al [10] in which it is found that the most close-to-center GRBs have blue compact and irregular hosts, which are indicative of intense star formation. Some examples of hosts are reported in fig.1.7 with the positional circle of the associated GRBs.

The GRB offset, with respect to its host center, shows that bursts (at least the long GRBs for which the hosts have been observed) are within some Kpc from the galaxy center: this could favor the massive star progenitor with respect to the binary system because, in the latter case, the system would be characterized by a large proper velocity and, consequently, the burst should occur far from the formation region.

Finally, GRBs represent a very powerful tool for cosmological studies. In fact, if long bursts are produced by the collapse of massive stars, one expects to find them out to $z \sim 15 - 20$ (Lamb [88]). Therefore GRBs could give information about the star formation history of the universe and on the first generation of stars. Moreover, the absorption–line systems and the Ly α forest visible in the spectra of GRB afterglows can be used to trace the evolution of the metallicity in the universe and to probe its large scale structure.

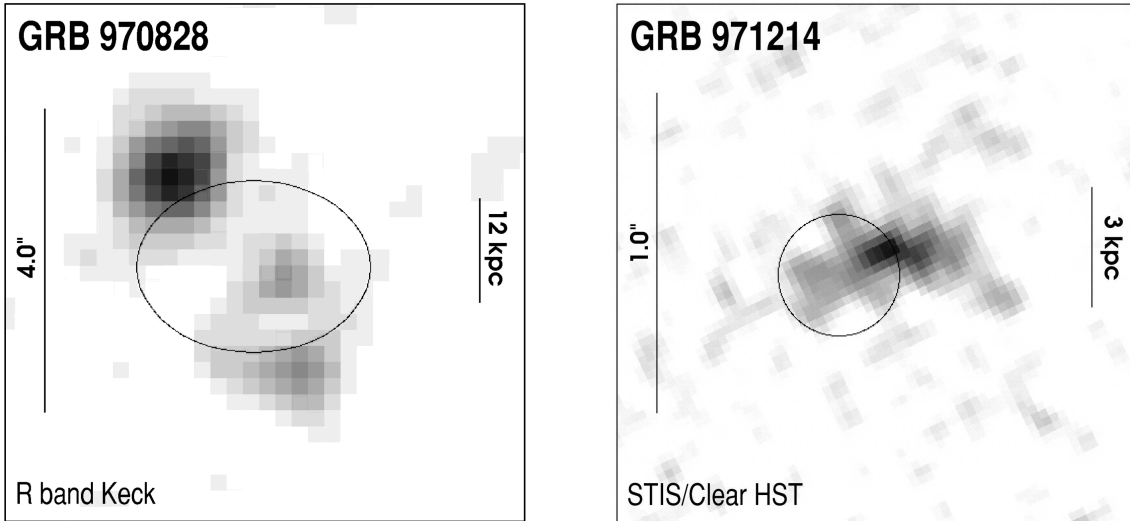


Figure 1.7: Some examples of host galaxies and related GRB error box, from Bloom et al. [10].

Nonetheless, measurements of the Ly α break in the afterglow spectra can constrain the reionization epoch.

1.3 The Standard Model

The observed GRB fluxes, at cosmological distances, imply a release of energy $\leq 10^{54}$ erg (assuming isotropic emission). The observed variability timescale $\delta t \sim 1$ ms indicates typical size of the emitting region $r_{min} \sim c\delta t \sim 10^7$ cm. The confinement of such a huge amount of energy, mostly in photons, in a small volume is called a *fireball*. within this volume a lot of pairs would be produced due to the high optical depth:

$$\tau_{\gamma\gamma} = \frac{f_p \sigma_T F D^2}{r_{min}^2 m_e c^2} = 10^{13} f_p F_{(-7)} D_{3000Mpc}^2 \delta t_{1ms}^{-2} \quad (1.1)$$

where f_p represents the fraction of photon couples which satisfy the condition for e^\pm production (i.e. $\sqrt{E_1 E_2} > m_e c^2$) and F and D are the fluence (in erg/cm 2) and the distance expressed with fiducial values. This opacity is extremely high for a burst with a 10^{-7} erg/cm 2 fluence at 10^3 Mpc with a variability timescale of 1 ms such that no high energy photon would escape from this thick fireball. This apparent paradox, i.e. the impossibility of releasing γ -ray photons which are indeed observed in the GRB, is known as the *compactness problem* (Goodman et al. [61], Paczynski et al. [119]) and was solved considering that the fireball expands relativistically with Lorentz factor $\Gamma = 1/\sqrt{1 - v^2/c^2}$. In this case the photons, observed with energy $h\nu$, have a lower energy in the source rest frame, i.e. $h\nu/\Gamma$, and, consequently, the fraction of photons which can produce pairs is reduced at least by a factor Γ^2 (if their spectral energy distribution is

a powerlaw with slope -1). Similarly, the radius of the emission is $r_{min} \leq \Gamma^2 c\delta t \Gamma^2$. Allowing for these relativistic effects, the resulting optical depth is

$$\tau_{\gamma\gamma} = \frac{f_p \sigma_T F D^2}{\Gamma^{2\alpha+4} r_{min}^2 m_e c^2} = 10^{13} f_p F_{(-7)} D_{3000Mpc}^2 \delta t_{1ms}^{-2} \quad (1.2)$$

and the Lorentz factor required to make the fireball optically thin to pair production ($\tau_{\gamma\gamma} \sim 1$) results $\Gamma \geq 100$.

The expansion with a large Lorentz factor is limited by the baryon loading of the fireball (Shemi & Piran [149]) : if the baryon content is large, most of the fireball internal energy will be transferred to the baryons which, will gain only newtonian velocities. The baryon loading is typically parametrized as $\eta = E_0/M_0 c^2$ where E_0 and M_0 are the fireball initial energy and mass.

If the fireball is intially dominated by its internal energy (a possible alternative is the a fireball driven by magnetic energy, e.g. Spruit [151]), its evolution is radiation dominated and, assuming adiabatic expansion, the bulk Lorentz factor Γ increases with r while the comoving temperature T scales as r^{-1} . Obviously, Γ cannot exceed $\Gamma_0 = E_0/M_0 c^2 = \eta$ and this acceleration phase is then followed by a coasting phase with constant bulk Lorenz factor.

The intial expansion of the thick fireball determines the thermalization of its components (radiation and matter). When the fireball has expanded enough and becomes transparent (i.e. $\tau \leq 1$) it should release the bulk of its radiation in form of thermal photons with a black body spectrum. Nonetheless, the observational evidence that GRB spectra are non thermal (see chapt.2) required the formulation of an efficient mechanism for the extraction of the internal energy and for its subsequent transformation in non-thermal radiation. This is realized in the Internal/External shock scenario.

1.3.1 The fireball: internal/external shock model

In the coasting phase the possible difference of the Γ of different shells (or of different regions within the continuously ejected wind), can determine their collision which produces the *internal shocks* (Rees & Meszaros [133]). Very approximately, if shells are emitted with differences in their Lorentz factors $\Delta\Gamma \sim \Gamma$ then the typical radius of the internal shock formation is:

$$r_{IS} \sim ct_{var} \Gamma^2 \sim 3 \times 10^{14} t_{var} \Gamma_2^2 \text{ cm} \quad (1.3)$$

where t_{var} is the variability timescale (of the order of milliseconds).

The internal shock, then, converts the kinetic energy of the fireball into random energy of the particles which are accelerated by successive shock crossings. These particles are responsible for the emission of synchrotron radiation due to the presence (or formation) of an intense magnetic field. This process, together with its alternatives, for the production of the γ -ray emission of bursts are described in some details in chapt.3.

The internal shock is followed by the interaction of the ejecta with the interstellar medium which decelerates the shells and produces the *external shock* (Meszaros & Rees [110]) This, in a similar way, transfers its energy to the electrons which subsequently radiate through synchrotron, producing the afterglow emission (Sari et al. [142]). The condition for the formation of the external shock is that the swept up material is M_0/Γ and the radius at which it happens is:

$$r_{ES} \sim 10^{17} E_{53}^{1/3} n_0^{-1/3} \Gamma_2^{-2/3} \text{ cm} \quad (1.4)$$

where n_0 is the external medium density.

The external shock luminosity is $\propto t^{-1+g}$ with the Lorentz factor $\Gamma \propto t^{-g/(1+2g)}$ ($g=3$ or $3/2$ for the radiative or the adiabatic case, respectively). As the synchrotron characteristic frequency is $\nu_m \propto \Gamma B' \gamma_e^2$, both B' and γ_e^2 are proportional to Γ and the peak of the emission moves to longer wavelengths. Meszaros & Rees [112] calculate that the afterglow flux and frequency dependence, as long as the expansion is relativistic, are:

$$F_\nu \propto t^{-3\beta/2} \quad , \quad \nu_m \propto t^{-3/2} \quad (1.5)$$

under the adiabatic assumption.

1.4 Progenitor

The greatest unknown in GRB science is what is the progenitor of the burst. There is no direct observable which can unveil the nature of the central engine but only an incomplete set of observational evidences about the GRB prompt and afterglow phase which should be used to infer the identity of the progenitor.

Any progenitor model should deliver few 10^{51} erg in relativistic collimated (≤ 0.1 radiant) ejecta in form of a continuous wind or of discrete shells with highly variable Lorentz factor. The variety of light curves (single/multi-peaked) and durations (short/long GRBs) could reflect a variable progenitor or a variety of progenitors and the study of the host galaxies and of the burst environments suggests a possible association between GRBs and star forming regions.

At present there are two main classes of proposed progenitors of GRBs: the *collapsar model* where a single massive star core–collapses to form a Black Hole (BH) surrounded by a torus, i.e. the (Woosley [162], Paczynski [121]), or the double compact object merger in which a binary Neutron Star (NS) or a NS-BH system undergoes a merger and forms a BH surrounded by an accreting torus (Goodman [61]). Both models produce, as a final result, a fast spinning BH surrounded by a very dense neutron rich torus and their energetic content is quite similar. The main phases associated with these models are: the progenitor evolution until the formation of the disk-BH system and the energy extraction to form the pair-radiation fireball which then produces the burst

The available sources of energy, a part from gravitational radiation, are in the form of neutrinos, accretion of the torus material onto the black hole, and rotation of both the torus and BH.

The mechanisms for the extraction of the energy are:

1. energy extraction from the torus (Woosley [162]):

- one energy source is the binding energy of the torus which by viscous dissipation produces an intense neutrino flux and by annihilation an e^+e^- fireball. This mechanism can extract up to 10^{50-51} erg, which is consistent with recent estimates by e.g. Frail [44], Ghisellini [58];
- an alternative method is the dissipation of magnetic fields generated by the differential rotation of the torus (e.g. Katz J. [78]). In this case the energy is

$$E_d \leq 8 \times 10^{53} \epsilon_m q \frac{M_d}{M_\odot} \quad (1.6)$$

where $\epsilon_m \leq 0.3$ is the efficiency and q the BH rotational parameter. The torus mass M_d/M_\odot ranges from 0.01 to 1, for the double or single star scenario (Paczynski [121]);

2. energy extraction from the BH e.g. through the Blandford–Znajek (BZ) mechanism (Blandford & Znajek [9]). In this case the energy extracted is comparable to the previous value (Meszaros & Rees [111]):

$$E_{BH} \leq 5 \times 10^{53} \epsilon_m \frac{M_{BH}}{M_\odot} \quad (1.7)$$

where ϵ_m and M_{BH} are the efficiency and BH mass, respectively. The BZ mechanism can produce bursts with similar energy content whereas the extraction of the torus binding energy or of the BH rotational energy can power bursts with different energy content (Meszaros [114]).

Collapsar

A collapsar (Woosley [162]) is a massive ($M > 40M_\odot$) rotating star whose core collapses to form a black hole, while the infalling outer layers, due to the high angular momentum, form a centrifugally supported disk. The faster accretion along the rotational axis of the BH creates a depletion funnel, while the disk accretes at a rate of $0.1 M_\odot \text{sec}^{-1}$. For the first 10 - 20 sec the accretion of matter onto the BH produces (e.g. assuming the first energy extraction mechanism) a huge neutrino flow ($\sim 5 \times 10^{53}$ erg) which annihilate to form pairs. These pairs are conveyed within the funnel producing the outflowing jet of high Lorentz factor ($\Gamma \geq 200$) that escapes from the central engine along the polar axis and powers the GRB prompt and afterglow phase.

Two essential ingredients for the collapsar model are a sufficiently massive core to form a BH and a sufficient rotation rate at the time of collapse to allow the formation of the disk. Simulations of the collapsar model (MacFadyen & Woosley [101]) suggest that large angular momentum and a core mass $M_{He} \geq 10M_{\odot}$ are required. Moreover, the propagation of the relativistic jet through the hydrogen envelope of typical massive stars is of the order of 100 sec. This requires that the star has already lost (through wind-mass loss or due to the gravitational stripping of a companion) most of its H envelope, which, otherwise, could prevent the jet to penetrate it on timescales comparable to the GRB duration (Haeger et al. [67]).

The collapsar scenario has different possible realizations which are characterized by the mass of the collapsing He core:

- Type I: $10 \leq M_{He} \leq 15 M_{\odot}$. The black hole forms directly from the core-collapse.
- Type II: $15 \leq M_{He} \leq 40 M_{\odot}$. The black hole formation is delayed by a time which is necessary to the initially ejected envelope to fall back.
- Type III: $M_{He} \geq 137 M_{\odot}$. These values correspond to the Pop. III stars (primordial generation, Haeger & Woosley [67]), which (also without rotation) form a $100 M_{\odot}$ BH. Their accretion rate is about $10 M_{\odot} \text{ sec}^{-1}$, and the corresponding burst timescale would be 20 sec, in the comoving frame. The spectrum and duration of the resulting burst should be diluted for the redshift of these primordial stars so that, if at least some GRBs have these progenitors, they should be more likely detected as long X-ray bursts.

One key feature of the collapsar model is the formation of an accretion torus around the BH which is the primary energy source for the GRB. This can be prevented by the magnetic field and the mass loss during the core collapse which have been considered in recent simulations. The first, due to the differential rotation of the stratified star (Spruit [151]), can be more effective in the transport of the angular momentum than the hydrodynamic mechanisms and then produce (Haeger & Woosley [67]) a disk which is hardly supported by the centrifugal forces. The second effect undermines the disk formation because the mass loss rate carries away also angular momentum: a possibility to avoid this problem is considering low metallicity stars which are supposed to have lower mass loss rates.

Supranova

This model is a variant of the collapsar and was first proposed by Vietri & Stella [156]: it considers the implosion of a massive neutron star that has lost sufficient angular momentum (by gravitational radiation or magnetic torques) to collapse and form a BH. About $0.1 M_{\odot}$ is left behind for the formation of the disk and the GRB powering (Vietri & Stella [156]). One immediate consequence of this model is the production of an environment surrounding the star rich in heavy elements which can be responsible of the

X-ray emission by illumination from the central object (Piro et al. [127]). Moreover, this model solves the problem of the heavy baryon loading (which could prevent the relativistic motion of the ejecta) because the SN explosion, which led to the formation of the NS, has swept most of the surrounding matter far from the center. This in turn requires that the NS to BH collapse occurred days/years before the GRB. But in this case the range of masses which can produce a SNe and such a delayed explosion is largely reduced (McLaughlin et al.[104]). Another problem could be the fact that the time necessary for the jet to drill the distant ejected envelope, might be longer than the GRB duration.

Double compact merger

The standard evolution of a binary system composed by two massive stars can lead to the formation of a compact object system which eventually merge producing the GRB. The merging system can be composed either by two NS or by a NS and a BH. Apart from the details of the evolution and of the merger (e.g. Fryer & Woosley [45]), the double NS form a single object which is not supported against collapse by nuclear or degeneracy pressure and a BH is formed with a surrounding $0.03\text{-}0.3 M_{\odot}$ disk whereas in the NS-BH the neutron star is disrupted by the BH to form an accretion disk of $0.1\text{-}1 M_{\odot}$. The NS-BH evolution ($t \sim 10^9$ yr) leads to a final escape velocity of the compact system (due to the successive kicks determined by the explosions of the primary components during their evolution) of $100\text{-}1000 \text{ km sec}^{-1}$ which would likely place the GRB outside the star forming region (Fryer & Woosley [45]).

Chapter 2

Spectral properties of GRBs

2.1 Introduction

The energy distribution of the photons emitted by Gamma Ray Bursts (i.e. their spectrum) is an observable directly associated with the burst prompt emission and represents the best tool for investigating the physics of the burst and its progenitor nature. The amount of energy released in the burst, the fraction which is converted into radiation in the Internal/External shock scenario, the dynamical and radiative timescales, mechanism producing the observed flux (chapt.3) and the interaction of the burst with its environment can be studied through the analysis of the temporal and spectral properties of GRB light curves and spectra.

Since their discovery, different instruments have been collecting an increasing amount of bursts with better temporal and spectral resolution (see chapt.4 - for an historical overview) and, consequently, the knowledge about GRBs properties has increased. Moreover, the refinement of the spectral analysis methodology has led to a more accurate definition of the spectral evolution of the burst. For this reason a description of the spectral properties of GRBs can be roughly subdivided into the pre-BATSE era (sec.2.2), when the spectral analysis of the first gamma ray bursts detectors posed the basis of the spectral characterization of bursts, and the BATSE era (sec.2.4), characterized by the study of large, statistically significant, samples of burst spectra, with improved resolution.

The aim of this chapter is to give a global review of the spectral properties of GRBs as a brief but specific introduction to the subject of this thesis. The typical shape of the spectrum and its temporal evolution are described in sec.2.4.1 and 2.4.2, respectively. A possible basic model, recently proposed, for the interpretation of these results is outlined in sec.2.5.

2.2 Definitions

The spectral properties of any GRB are strictly related to its typical timescales: the GRB has a global duration which can be quantified by the time interval containing the 90% of its fluence in [erg/cm²] (defined as the time integral of the energy flux), and a short timescale, of few milliseconds, corresponding to the variability of its light curve. Other significant timescales can be identified e.g.: the duration of the pulses for multi-peaked bursts, the time in which the flux rises, reaching a maximum, and then decreases (rise/decay timescale).

For every timescale a corresponding category of spectra (e.g duration-integrated, pulse-integrated, etc.) can be obtained integrating the spectral signal, separated in different energy channels, over the selected time interval.

The spectrum

If $C(E, t)$ is the count spectrum accumulated by the instrument during the burst event per unit time and per unit energy, i.e. in [counts/cm² sec keV], its time integral defined the type of spectrum:

- *time integrated spectrum*, or time average spectrum, which is integrated for the duration (e.g. $T_{90\%}$) of the burst:

$$\overline{C(E)} = \int_{T_{90\%}} dt C(E, t) \quad (2.1)$$

This spectrum, being integrated for some seconds (at least for the population of long bursts with $T_{90\%} \geq 2$ sec) has typically a good S/N and can be used to characterize the average spectral properties of GRBs and compare them among different bursts.

- *time resolved spectrum* which, despite its name, is integrated in time over a typical sub-second timescale (usually longer than the variability timescale t_v):

$$C(E) = \int_{t_v} dt C(E, t) \quad (2.2)$$

The sequence of many time resolved spectra, covering the duration of the burst, describes the GRB spectral evolution. Integration over small timescales is limited by the S/N ratio of the time resolved spectrum. For this reason only particularly bright bursts, like those analyzed in chapt.5 (Ghirlanda et al.[51]), can be analyzed in terms of time resolved spectra on very short timescales (e.g. 128 ms, in the case of BATSE data). Integration over the rise/decay phase of the flux in the light curve defines, correspondingly, the *rise/decay phase spectrum*.

When dealing with the spectral properties of GRBs different notations can be found to indicate the spectrum and its representations: we denote the count spectrum in

[count/cm² sec keV], the photon spectrum, which is $C(E)$ deconvolved by the detector response matrix (see. chapt.4), is indicated as $N(E)$ and has units of [photons/cm² sec keV]. The energy spectrum and the usual νF_ν spectra are indicated as $F(E)$ and $EF(E)$ and are expressed in [keV/cm² sec keV] and [keV (keV/cm² sec keV)].

A typical GRB spectrum is composed of two power laws connecting in correspondence of a spectral break: the low energy power law is conventionally represented as E^α and high energy power law as E^β , for the photon spectrum. The spectral indices α and β in the rest of these thesis indicate these two components and a negative value of these parameters indicate a photon spectrum which decreases with increasing energy.

Hardness

The characterization of the hardness of a burst can be associated with its spectral parameters ($E_{peak,\alpha,\beta}$), obtained fitting the observed spectrum with a model function or with its count rate:

- *peak energy*, E_{peak} which represents the energy corresponding to the peak of the νF_ν spectrum. This is a spectral parameter obtained from the fit of the observed spectra and indicates where most of the power is emitted. For GRBs it is often chosen to indicate the hardness of the spectrum. In terms of peak energy a spectrum is defined hard (soft) if its E_{peak} is high or low: $E_{peak} \sim 100$ keV describes a softer spectrum than $E_{peak} \sim 1$ MeV.
- *spectral indices*, α or β , which characterize the slope of the corresponding power laws. A burst spectrum is typically described at low energies by a power law with photon spectral index $\alpha \sim -1$. A larger value (e.g. $\alpha = -0.5$) characterizes a harder spectrum which in a log log representation is flatter than the previous case. The same definitions and nomenclature apply to the high energy spectral component described by β whose typical value is -2.5.
- *hardness ratio*, HR , defined as the ratio between the count rate (background-subtracted) in a high energy channel and the count rate in a low energy channel. It is directly obtained from the instrumental count and the resulting spectral hardness depends on the response of the instrument. A high (low) hardness ratio characterizes a hard (soft) spectrum.

These definitions of the spectral hardness of a burst have been largely adopted by different authors to describe the spectral evolution of GRBs, also for the simplicity to associate to a *single* parameter a measure of the hardness. Other possibilities can be considered, as suggested in chapt.7, which make use of the complete set of spectral parameters, e.g. $E_{peak,\alpha}$ and β , to characterize the spectral hardness and its evolution over the complete energy band of the instrument.

2.3 Pre–CGRO era

Since the beginning, it was evident (e.g. Cline & Desai [15]) that the spectrum of gamma ray bursts has a non-thermal shape well represented by a single power law or by a power law with an exponential cutoff (Klebesadel [84]). This experimental evidence opened the debate about the leading radiative process responsible for the GRB emission.

The spectral analysis of 6 bright bursts detected by the IMP-6 satellite (Cline et al. 1973) in the range 0.1-2 MeV showed that they could be reasonably well fitted by an exponential function $N(E) \propto E^0 \exp(-E/E_c)$ with the e-folding energy $E_c \sim 150$ keV.

The IMP maximum time resolution was 2.5 sec so that particularly long bright bursts could be described by a sequence of some time resolved spectra. Although this was the first attempt to characterize the time resolved spectrum and its evolution, no evidence for a temporal variation of the spectral shape was found, probably due to the limited time and spectral resolution of these data. In fact, this analysis could not exclude the presence of an high energy spectral component, whose existence was later confirmed by Cline & Desai ([16]) through the study of 11 bursts detected by the IMP-7 satellite: some of these spectra, extending above 400 keV, had a typical power law shape $N(E) \propto E^{-2.5}$ at high energies.

The presence of an high energy spectral component was also confirmed by a larger sample of bursts (79) collected by the Solar Maximum Mission (SMM) in the energy range (0.3-9) MeV. The 66% of these bursts showed significant emission above 1 MeV and 25% even above 5 MeV (Matz et al [102]). These results supported the idea of representing GRB spectra with multiple components and, preferentially, with power laws at low and high energies, i.e. below and above a characteristic energy of some hundred keV.

The first study of the average and of the time resolved spectrum of GRBs revealed the different information conveyed by these two types of observables: Golenetskii et al. ([60]) analyzed the spectra of 150 bursts detected by the KONUS experiment, on board the VENERA 13 and 14 satellites, and found that the time integrated spectrum could be well represented by a power law $N(E) \propto E^{-1}$, at low energies, and an high energy exponential cutoff. The time resolved spectra (with a maximum resolution of 0.5 sec), fitted with the same spectral function, showed that the characteristic energy kT decreased with time and it was correlated with the intensity I . Golenetskii et al. ([60]) reported $I \propto kT^\gamma$ with $\gamma = [-1.5, -1]$, and showed some evidences of candidates spectral lines, possibly evolving with time. The presence of line candidates in the γ -ray spectrum of GRBs was seemingly excluded by intense statistical analysis of the BATSE catalog by different authors (e.g. Band et al. [5], [6]).

The intensity–energy correlation $I - kT$ was also verified, with a better time resolution (0.25 sec), with the hardness ratio (HR) instead of the spectral parameter kT (Golenetskii et al. [60]). It should be stressed, anyway, that the HR (see sec.2.2 for a definition) is obtained from the count rate and is not deconvolved by the detector response matrix as in the case of the fitted spectrum. Moreover, HR should be considered a “rough”

hardness estimate because it implicitly assumes that the spectrum is represented by a power law over a fixed energy band, without considering the curved and fast evolving GRB spectra.

Additional indications that burst spectrum can evolve in time according to some recurrent morphologies were given by the analysis of 10 bursts observed by the Hard X Ray Burst Spectrometer and Gamma Ray Spectrometer (Norris et al. [116]). They reported a hard-to-soft spectral evolution common to these burst: the hardness ratio and the peak energy decrease with time, since the beginning of the burst. Although the time resolution was only of 0.5-1 sec this evidence of an hard-to-soft spectral evolution apparently undermined the previous findings of an intensity-energy correlation. Still this morphology could have been determined by the low temporal resolution of these data (see chapt.7 for a discussion).

Nowdays, the increased time resolution of spectral data which allows to have a larger number of time resolved spectra per burst, confirmed that both these evolutionary morphologies characterize different GRBs.

The search for hardness-intensity correlation in GRBs was also performed by Kargatis et al. ([75]) with a sample of 16 bursts observed by SIGNE, a gamma ray detector with 0.5 sec resolution. They found both the hardness-intensity correlation of Golenetskii et al. ([60]) and the hard to soft evolution of Norris et al. ([116]), and, for the first time, gave a scheme of spectral evolution classification according to the following classes:

- *Hard-to-Soft* spectral evolution with the hardness indicator decreasing independently of the increase and decrease of the flux in the light curve;
- *Soft-to-Hard* spectral evolution which is the opposite of the one described before;
- *Tracking* morphology in which the hardness parameter reproduces the increase and decrease of the flux light curve.

As will be discussed in chapt.7, these morphologies can be present in different phases of the burst emission and in many cases the classification can be strongly biased by the time resolution of the spectral analysis.

2.4 The characterization of the GRB spectrum by BATSE

The Burst And Transient Source Experiment (BATSE) provided a fundamental contribution to the understanding of the GRB spectral properties because, accumulating a large sample of bursts with high spectral and temporal resolution (see chapt.4), allowed the comparison of the average spectral properties among different classes of bursts and the study of their spectral evolution.

The next sections describe the time integrated and time resolved spectrum of GRBs observed by BATSE. In particular, the average spectral characteristics of bursts are presented in sec.2.4.1, the time evolution of the spectrum and its low and high energy spectral shape are discussed in sec.2.4.2.

2.4.1 Time integrated burst spectrum

The burst spectrum, integrated over its duration as defined in sec.2.2, presents some basic features:

- it has a non thermal character which is evident from its low and high energy power law shape connected by a wide smooth curvature (Band et al. [4]);
- it can be fitted by an analytical spectral model, the BAND function (Band et al. [4]), which in most cases characterizes the peak of the νF_ν spectrum through its spectral parameters, giving a direct measure of the hardness of the burst;
- large samples of bursts present spectral parameter distributions (sec.2.4.2) indicating a prevailing spectral shape described by $N(E) \propto E^{-1}$, $N(E) \propto E^{-2}$ connecting at $E_{peak} \sim 300$ keV;
- there is no evident connection between the spectral properties and other burst properties (e.g. duration, position, intensity), as far as the time integrated spectrum can reveal;
- in few cases, data from the other CGRO instruments are available, the average spectrum extends above the typical 2MeV energy upper threshold of BATSE showing its non-thermal character also at high energies.

The analysis of a sample of 54 bright bursts by Band et al. ([4]) confirmed the non thermal character of the time integrated spectrum, which is well fitted by an empirical analytical form (defined in chap.5) composed by two power laws, at low and high energies, characterized by their spectral indices α and β , smoothly connected by an exponential cutoff with e-folding energy E_0 . This spectral model (BAND, hereafter) has been extensively adopted to represent the burst spectra and, within the limits of its spectral parameters (α , β , E_{peak}), also accounts for the previously adopted spectral representation (e.g. single powerlaw with exponential cutoff, exponential function).

The search for correlations among the best fit parameters α , β (Band et al.[4]), only showed that they cluster in the ranges $-1.5 \leq \alpha \leq 0$ and $-2.5 \leq \beta \leq -2$. Two examples of time integrated spectra and the relative GRB light curve are reported in fig.2.1 where the spectrum and the best fit BAND model are represented (*bottom panels*). Notice that they are both well fitted by the BAND model although the spectral parameters are different and in particular the peak energy is slightly different.

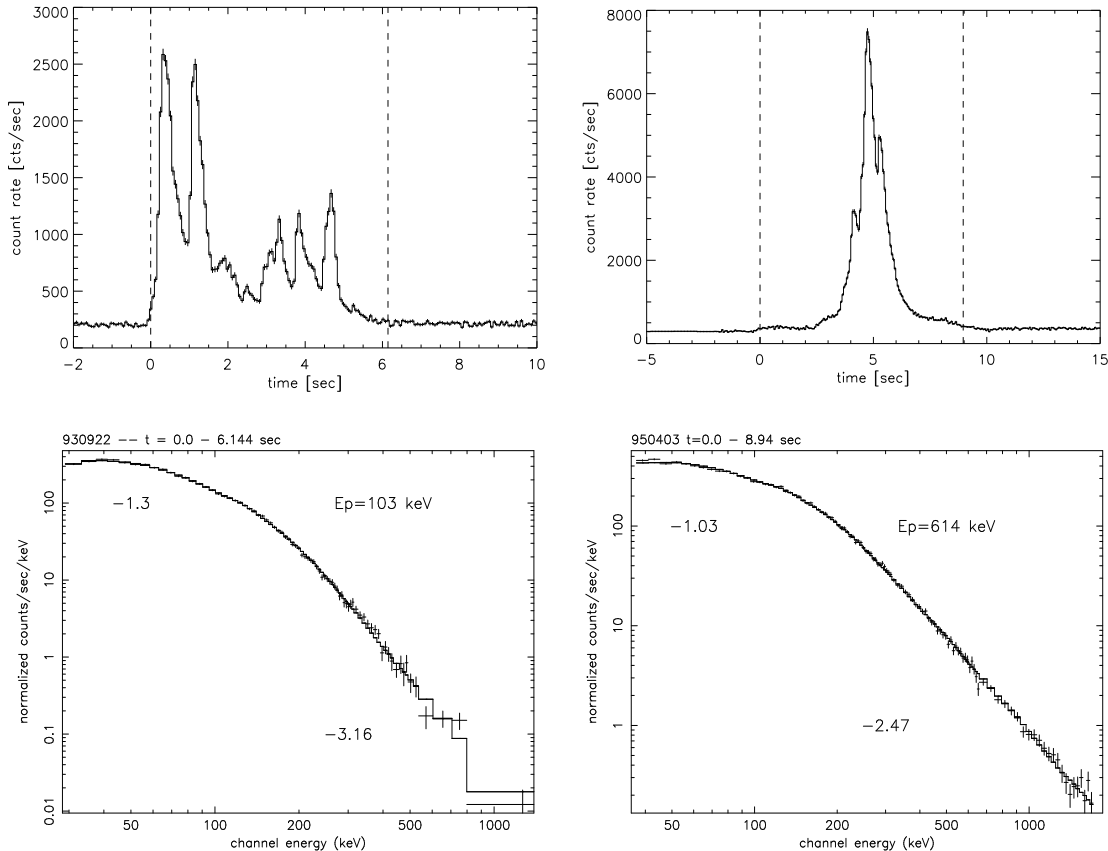


Figure 2.1: Examples of time integrated spectra. Left column: GRB 930922. Top panel: light curve with 64ms time resolution and integrated from 25 to 300 keV. Bottom panel: spectrum with best fit model (BAND) and relative parameters. E_p is the peak energy of the νF_ν spectrum, namely $E_{peak} = (\alpha + 2)E_0$. Right column: GRB 950403. The dotted vertical lines mark the time interval of accumulation of the spectrum.

In some cases extremely soft spectra at high energies (i.e. well represented by exponential cutoff components) were found although the low statistics of the high energy spectrum does not allow to definitely classify these spectra as a soft subclass.

The low energy spectral slope instead could be better studied because of the higher S/N ratio at low energies: Preece et al.([128]) analyzed a sample of 86 bright bursts considering also the hard X-ray data and then extending the low energy spectral threshold to 5 keV. Fitting the BAND model to the time integrated spectra they found a wide distribution of the α parameter, confirming the spectral diversity of the low energy spectrum among different bursts. They also report some extremely hard bursts, at low energies, with $\alpha > -2/3$ which call for an explanation within the proposed emission models. In fact, as it will be discussed in chapt.3, most of the radiative mechanisms, which have been thought to produce the spectrum of GRBs, make strong predictions on the slope of the low energy spectral shape. Until now, no exhaustive comparison of these

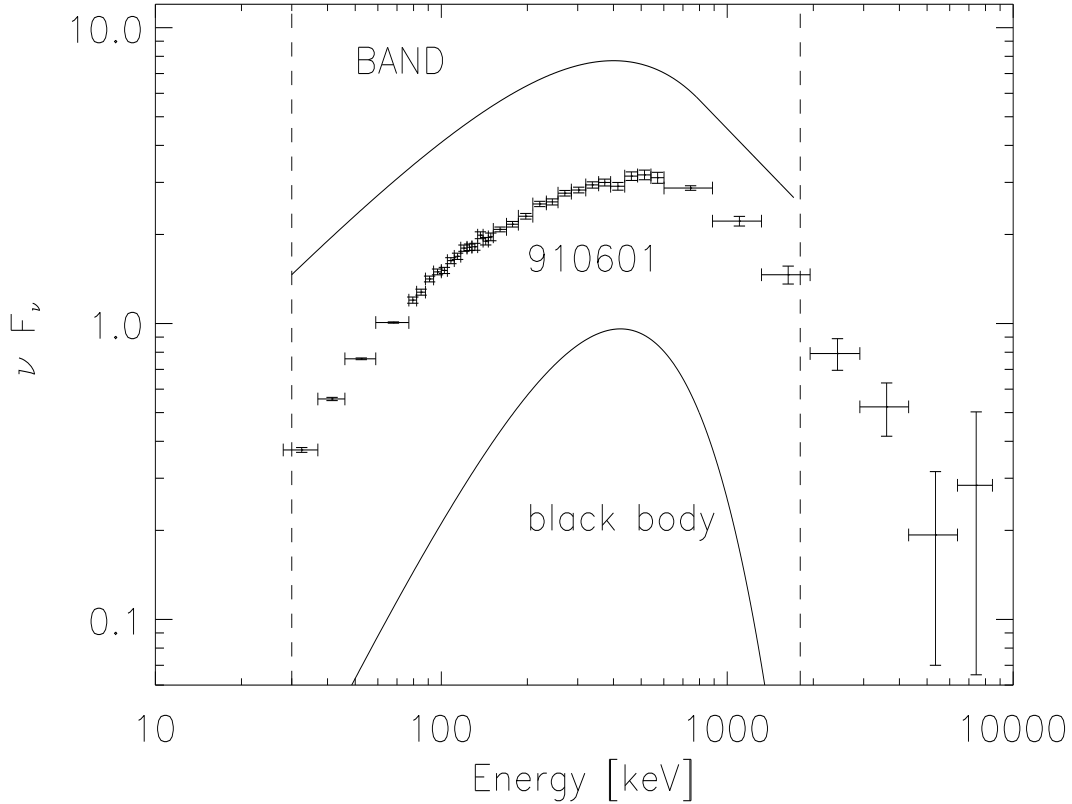


Figure 2.2: νF_ν spectrum of GRB910601. The BAND model with $\alpha = -1$, $\beta = -3$ and $E_{break} = 400$ keV is reported for comparison as representative of the non thermal spectral functions together with the black body spectrum with $kT=150$ keV. The *dashed* vertical lines represent the limits of the BATSE energy range. The data points are from Schaefer et al.([147]).

predictions with all the most significant experimental evidences has been attempted: we will consider this task in chapt.6 in the light of new results on some extremely hard low energy GRB spectra, discussing the proposed emission models.

Preece et al.([128]) report an anticorrelation between the low energy spectral hardness (indicated by the value of α) and the peak energy E_{peak} : bursts with hard low energy power law spectra ($\alpha > -1$) tend to have smaller E_{peak} . In most cases the spectrum at very low energies (below 30 keV) is consistent with the extrapolation of the fitted function in the gamma ray band although some exceptions, showing a low energy X ray excess, exist.

Although the BAND model is not based on any physical assumption, it gives a direct measure of the peak energy E_{peak} which is often used to characterize the hardness of the spectrum. Its distribution, as reported by Band et al. ([4]) for the time integrated spectrum, is log-normal and centered around $\sim 150 - 200$ keV and narrow. This last

feature is extremely interesting if compared to the wide spread of the temporal properties of GRBs: some possible explanations of this peculiar narrow peak energy distribution are reviewed in sec.3.4.2.

The time integrated GRB spectrum has also been studied extending the BATSE energy range to some MeV with data from the other instruments on board the CGRO (Schaefer et al. [147]). They report 4 broad band (10keV - 100 MeV) spectra which are well represented by the BAND model. In fig.2.2 is reported, as an example, the case of GRB 910601 adapted from Schaefer et al ([147]). It is evident the power law shape of the spectrum, at low and high energies, and also its curvature, peaking at 300 keV. For comparison in fig.2.2 are also reported the BAND spectral model and the a black body spectrum (*solid lines*), with arbitrary parameters, as representative of the non-thermal and thermal spectral forms, respectively. It is evident that the broad band spectrum is better represented by a non-thermal model with a smooth curvature. Nonetheless, it might not be excluded that the spectrum, considered over a narrow band, can show, in some particular cases as those presented in chapt.6, a thermal character which indeed is hidden by the time integration of different spectral contributions over time. For this reason the best characterization of the spectrum is through its time resolved properties and their temporal evolution.

2.4.2 The spectral evolution

Considering the fast variability of bursts (e.g. Walker [159], Fenimore & Ramirez-Ruiz [37]), also the spectrum, as shown in this section, should be expected to vary on small timescales.

The study of the spectral evolution of a GRB is based on the temporal analysis of the hardness of the burst spectrum, once a definition of a spectral hardness indicator has been given (sec.2.2).

In principle the requirement of studying the variation of the spectrum on the smallest integration timescale (set by the instrument temporal resolution), is limited by the low statistics of γ photons, particularly at high energies. For this reason the experimental choices for the analysis of the spectral evolution have been subject to different refinements also in connection with the advances of the spectral accumulation techniques.

The mass of data collected by BATSE allowed to fix some major observational evidences about the spectral evolution:

- the time resolved spectrum has a non-thermal character;
- it can be well represented by the BAND function although there are some other spectral forms (e.g. COMP, SSM, BPLW model, discussed in chap.5) which can adequately fit the spectrum.
- the evolution of the spectrum described with the hardness ratio or with a best fit

spectral parameter, like the peak energy, can be classified according to the relation between the hardness evolution and the flux time history;

- there is a correlation between the burst hardness and its intensity (represented by different parameters);
- the low energy spectral slope of a considerable fraction of spectra violates the limit predicted by the standard optically thin synchrotron model ($\alpha = -2/3$);
- the high energy spectral component highlights the possible existence of super-soft or super-hard bursts which could likely represent sub populations of the burst phenomenon.

In the following sections these findings are presented in more details.

Spectral evolution morphologies

The first comprehensive study of the spectral evolution of a sample of bright bursts observed by BATSE (Ford et al. [42]) showed that in many cases the hardness indicator, e.g. the peak energy E_{peak} , rises and decays during the burst reproducing its light curve. The higher time and spectral resolution of BATSE data confirmed the existence of the hard-to-soft and tracking morphologies and added to the classification scheme some new evidences:

1. *tracking*: the peak energy and the burst intensity are correlated. The peak energy can reach its maximum value before or after the peak of the light curve, and this time delay is typically less than 1 second;
2. *hard-to-soft*: the peak energy decreases during pulses. In this class Ford et al. ([42]) included also those cases in which the peak energy maximum anticipates the light curve maximum by more than 1 sec.
3. *hard-to-soft inter pulse*: the tracking evolution dominates the peaks, while, during the quiet phases (inter-pulse), the evolution is hard-to-soft.
4. *envelope*: there is a general softening of the burst shown by the lower hardness of the late pulses with respect to the early ones.

This classification is based on the dominant morphologies but some exceptions exist, and different evolutionary types can characterize different phases of the burst.

In fig.2.3 are reported some examples from Ford et al. ([42]). In the case of GRB 910807 (top left panel) the peak energy follows the light curve (tracking) in the second peak but softens during the first peak: this is an example of coexistence of the two morphologies. Notice also that the second peak, although it is dimmer than the first, has the same hardness indicating the absence of the hard-to-soft envelope, which is

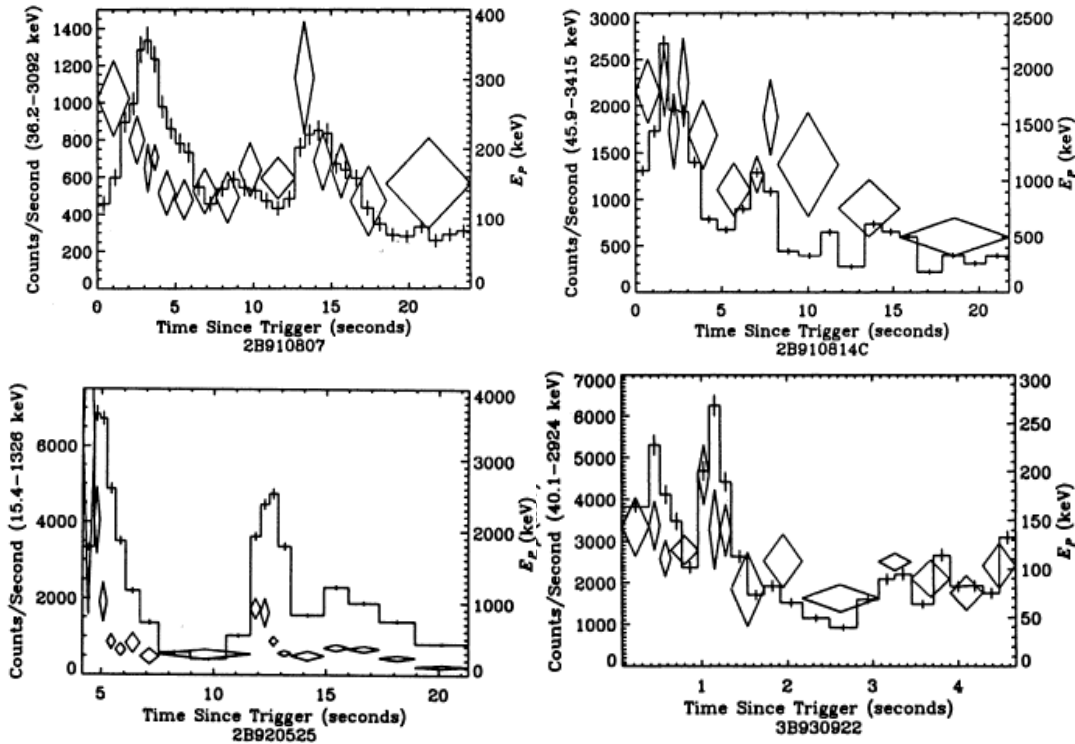


Figure 2.3: Examples of evolutionary morphologies from Ford et al. [42]. The light curve is reported (*histogram*) and the peak energy of the $\nu F\nu$ spectrum (*diamonds*) as a function of time.

instead present in GRB 920525 (bottom left panel). The simple hard-to-soft spectral evolution is shown by GRB 910814 (top right panel) in which E_{peak} decreases with time. GRB 930922 shows a hard to soft evolution during the second peak.

The evidence of the hard-to-soft envelope is shown also by the distribution of the peak energy of late spikes compared to that of early spikes: Ford et al. ([42]) found that for multi peaked bursts the late emission is systematically softer than in the first seconds of the burst. A possible quantification of this morphology, through the time resolved spectral analysis of the sample of bright bursts presented in this thesis, is actually under consideration and the first results will be detailed in chapt.7.

Spectral-temporal correlations

The quantitative description of the spectral evolution has been performed considering the possible correlations between the hardness parameter and the intensity of the burst (Kargatis et al. [76]) or the hardness and the fluence (Liang & Kargatis [94]). Ryde & Svensson ([137]) pointed out that these correlations can be used to derive an analytical function which can easily reproduce the observed light curves.

It should be stressed, anyway, that these analytical descriptions (Liang & Kargatis [94], Ryde & Svensson [137]) of the spectral evolution only apply to the decay phase of well defined long pulses, and then do not describe the spectral evolution before the burst peak, i.e. the initial phase of the emission. This is motivated by the fact that the rise phase is typically fast and characterized by a low S/N so that the number of time resolved spectra and their statistical quality is often less than in the decay phase.

The hardness (described by the peak energy E_{peak} of the νF_ν spectrum) was characterized by an exponential function of the fluence by Liang & Kargatis ([94]). They found, in a sample of 37 pulses, that the Hardness Fluence Correlation (HFC) could be described as:

$$E_{peak}(t) = E_{peak,0} e^{-\Phi(t)/\Phi_0} \quad (2.3)$$

where Φ represents the fluence and the constants, $E_{peak,0}$ and Φ_0 are the hardness and fluence corresponding to the peak of the light curve, respectively. A similar empirical relation was found by Crider et al. ([23]) from a sample of 41 pulses, although they used the energy fluence instead of the photon fluence, which was linear rather than the exponential. Liang & Kargatis ([94]) proposed that the decay constant Φ_0 is mostly invariant among different pulses of the same burst: this was interpreted as the signature of a recursive event generating the burst rather than of a single catastrophic event. This conclusion was discussed by Crider et al. ([23]), extending the sample of pulses and questioning the possibility that this parameter be constant only by coincidence.

The other empirical relation describing the decay phase of a pulse is the Hardness Intensity Correlation (HIC) which, from the spectral analysis of a sample of 28 pulses, resulted to be:

$$E_{peak}(t) = E_{peak,0} \left[\frac{N(t)}{N_0} \right]^\delta \quad (2.4)$$

where δ is the correlation index and $N(t)$ is the photon flux (Kargatis et al. [76]). They interpreted this correlation as the signature of the saturated comptonization model (Liang [96]). As discussed in Ryde & Svensson [137] this model could account different spectral evidences, although some of its predictions are quite extreme (see chapt.6).

The combination of the HIC and HFC leads to the dependence of photon flux $N(t)$ and peak energy $E_{peak}(t)$ from time (Ryde & Svensson [137]):

$$N(t) = \frac{N_0}{(1 + t/\tau)} \quad (2.5)$$

$$E_{peak} = \frac{E_{peak,0}}{(1 + t/\tau)^\delta} \quad (2.6)$$

where τ and δ are free parameters.

These correlations (HIC and HFC) are strongly dependent on the parameters used to represent the hardness and the intensity, as recently pointed out by Borgonovo & Ryde ([11]). In fact, the integration of the spectrum over the detector bandpass to derive

the intensity, can be influenced by the superposition of different spectral tails (at low energies, for instance) which are the residuals of the spectral evolution of previous pulses.

On the other hand Borgonovo & Ryde ([11]) propose to use the value of the νF_ν spectrum corresponding to the peak energy E_{peak} to indicate the intensity. They study a sample of 82 pulses, within 66 BATSE bursts, and find that in 57% of these the HIC is described by a power law:

$$\phi \propto E_{peak}^\eta \quad (2.7)$$

where ϕ is the intensity measure and the value of η , for single peaked bursts, is centered around 2 but with a wide dispersion. The same parameter seems to remain constant within multi-peaked bursts and this is an indication of a possible “memory” of the process (see below). In fig.2.4 and 2.5 are reported some examples of the HIC from Ryde & Petrosian ([138]). In fig.2.4 this relation is characterized by an index $\eta \sim 2$ whereas fig.2.5 reports a case of departure from this general value. The example reported in fig.2.5b and d are examples of the hard-to-soft evolution while fig.2.5c is an example of tracking morphology.

These findings have important implications for the emission model of GRBs: in fact if the internal shock model is based on the collision of different shells with different physical and geometrical parameters, it is unlikely that the same conditions are reproduced at every shock front but it is likely that the same stochastic distribution of physical parameters could be realized in different bursts. This implies that the expected dispersion in the HIC index could be seen in different bursts. On the other hand the internal shock model should explain the fact that in some multi-peaked bursts the correlation index is quite constant. This could be more easily explained by the single shell model in which the activation of different regions could give rise to the observed pulses with more or less the same HIC law. Furthermore, Borgonovo & Ryde ([11]) report a new evolutionary feature: a track-jump corresponding to a transition to successive pulses in multi-peaked bursts. This new evidence could be the result of the superposition of indistinguishable pulses.

The importance of the quantitative analysis of the HIC is that it could reveal the possible existence of a kind of “memory” among pulses: in fact if the peaks are the superposition of different emission episodes it could happen (in the case of “memory”) that the second emission episode is influenced by the environmental modification induced by the previous emission episode, and this small scale relation among subsequent spikes can be reflected in some evolutionary morphology, like, for example, the presence of an hard to soft envelope. This is just a tentative idea which has not been investigated yet but which should have some testable predictions in the field of the spectral evolution analysis.

Low energy spectral component

The low energy component of GRB spectra is typically described by the portion of the spectrum below the peak energy and, in particular, by the spectral index α of the fitted

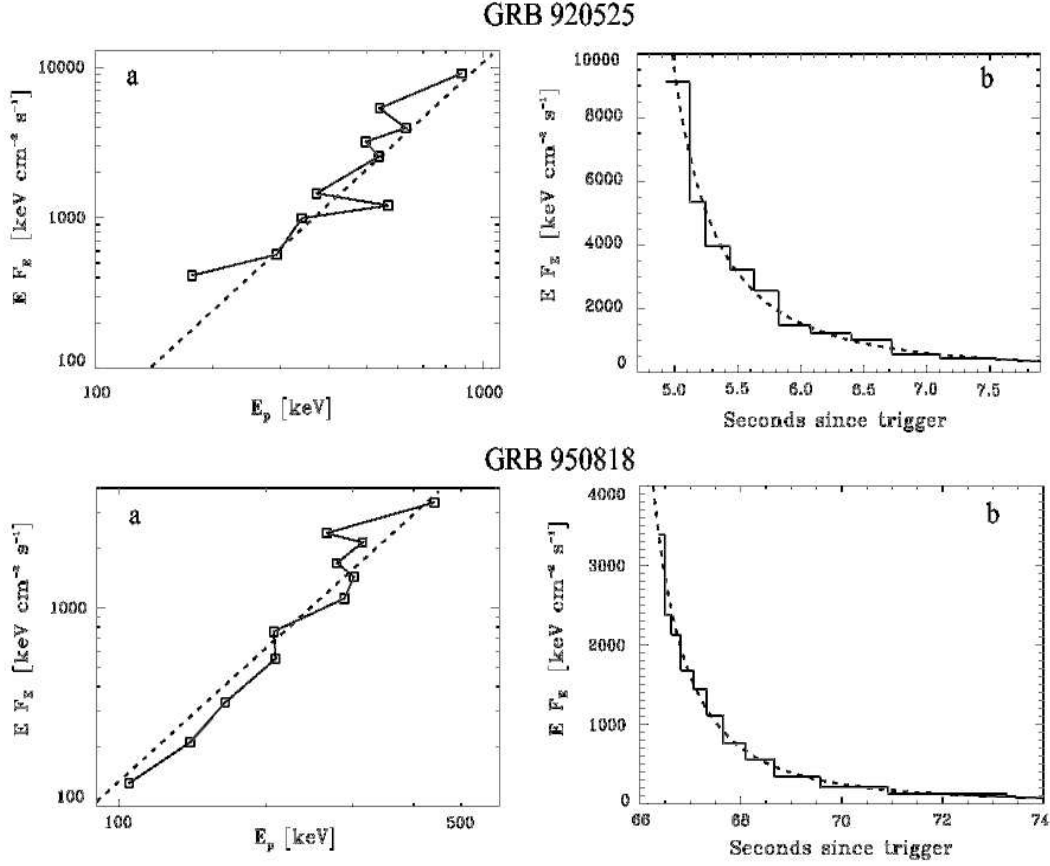


Figure 2.4: Examples of Hardness Intensity Correlation from Ryde & Petrosian (2002). Right panels (b) report the observed time evolution of the intensity (*solid histogram*) which is obtained assuming the HIC and the HFC relations (*dashed curves*). Panels (a) represent the HIC in log-log scale and the *dashed line* is the relation of eq. 1.8 with $\eta \sim 2$

power law. The distribution of this spectral parameter from the fits to the time resolved spectra of a large sample of bursts (from Preece et al. [130]) is reported in fig.2.6.

They found, from 5500 time resolved spectra, that α has a quite normal distribution with central value $\alpha = -1$. It is interesting to notice, also for the discussion of chap.5 and chap.6, that they have a quite large spread in the values of the low energy spectral index which extends far above the optically thin synchrotron model limit of $-2/3$ (see chapt.3). They suggest that this spread in the α distribution could be produced by the spectral evolution of the bursts.

It should be noticed that in this distribution (as in the others presented in the next sections from Preece et al. [130]) the possible dependence from the spectral model adopted to fit the spectra is not considered. In fact, they choose, as best model, the one fitting the time integrated spectrum: the fast spectral evolution of some bursts could determine an average spectrum with particular features (e.g. a smooth curvature

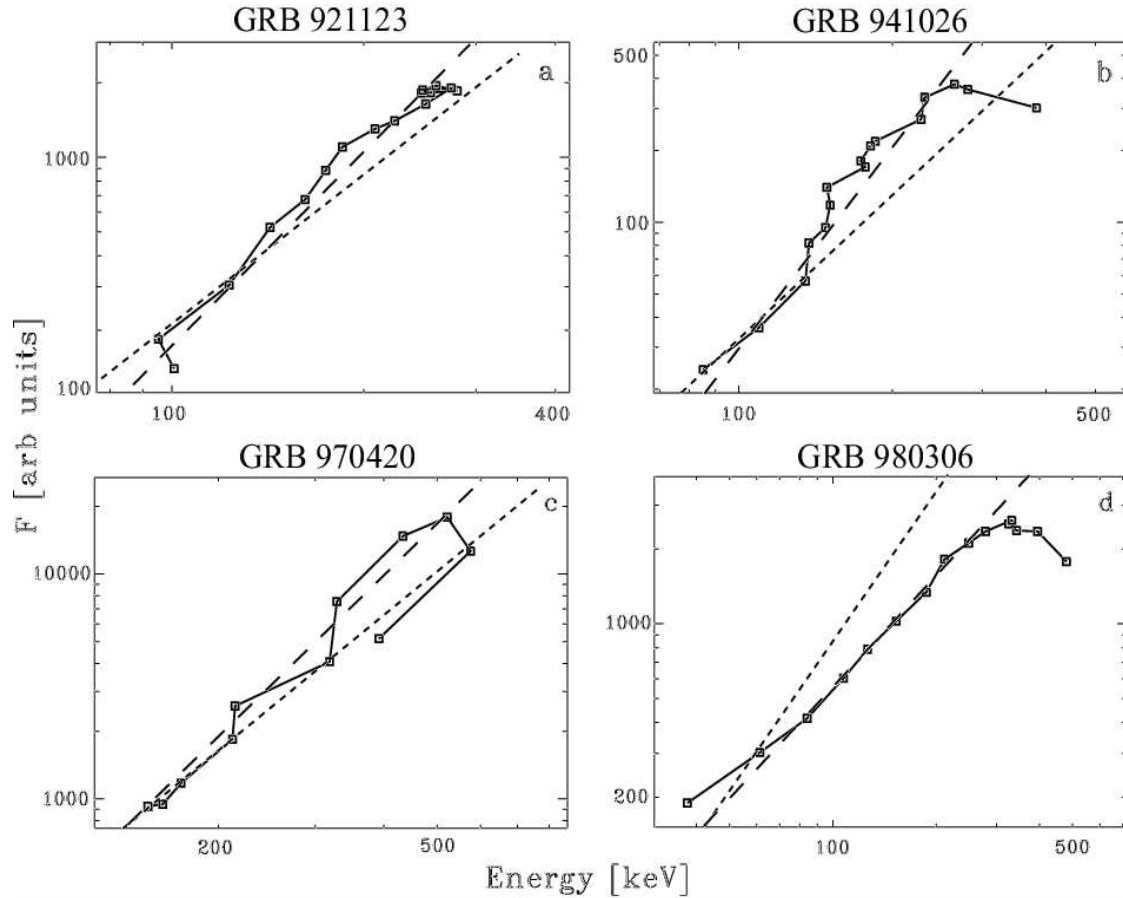


Figure 2.5: Examples of Hardness Intensity Correlation from Ryde & Petrosian (2002). Same as fig.2.4. The *long-dashed* lines are the fits to the observed HIC.

or an high energy power law tail) which result only from the superposition of many time resolved spectra but which are not necessarily present in the same time resolved spectra. This, coupled with the fact that the time resolved spectra, due to the lower S/N if compared to the time integrated, can be reasonably well fitted by different spectral models, should caution in interpreting the distribution of these spectral parameters.

In addition to this, in Preece spectral catalog, the spectral parameters of the time resolved spectra which result in unacceptable fits are set to the value obtained from the time resolved spectrum: this could lead to a biased interpretation of the spectral evolution because the time resolved spectrum can be different from the time integrated as shown in chap.5.

The temporal evolution of the low energy photon spectrum as represented by $\alpha(t)$ was considered an experimental evidence against those theoretical models, like the simplest synchrotron model (e.g. Katz 1994), which predict a fixed value for this spectral component. Crider et al. ([23]) found that the value of α , describing the low energy power law component of the time resolved spectra, evolves with time rather than remaining fixed

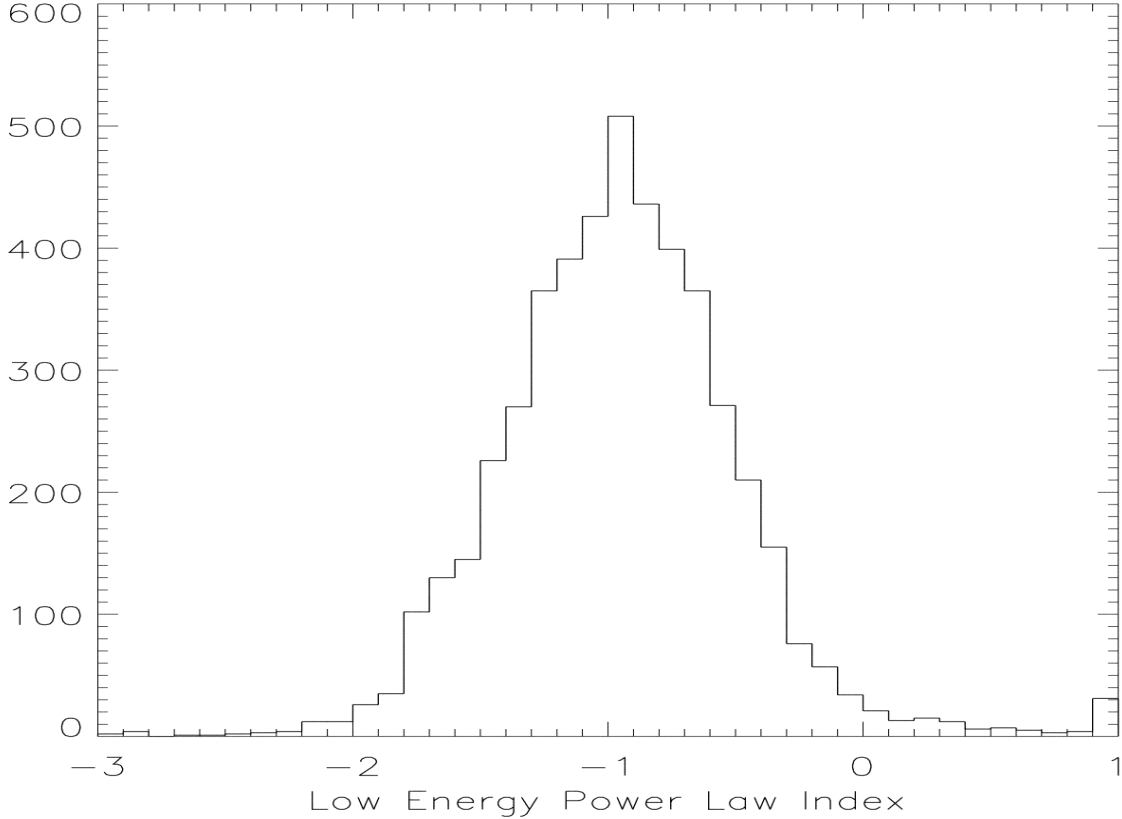


Figure 2.6: Low energy spectral index α distribution. From Preece et al. [130].

at the value of the time integrated spectrum in 58% of cases of their sample. They also observe a positive correlation between α and E_{peak} in a sample of 18 hard to soft and 12 tracking bursts at a high level of confidence (99.7% and 98% respectively). In the tracking cases, there is evidence that the value of α can be higher (harder spectrum) in the early burst phase. This could be another evidence of the existence of an evolutionary envelope, not only as represented by the break energy (Ford et al. [42]), but also by the low and high energy spectral components.

Some examples of the α evolution are reported in fig.2.7. GRB 911031 has an hard to soft spectral evolution described by its peak energy (*diamonds*) and the same behaviour characterizes the evolution of α (*crosses*). GRB 920525 is an example of tracking evolution which reproduces the flux change. GRB 931126 displays a mixed evolution, i.e. hard to soft and tracking on the first and second pulse, respectively.

High energy spectral component

The high energy spectral component can be characterized by a power law $\propto E^\beta$ with spectral index β , if the spectrum is represented by the BAND model. The distribution of

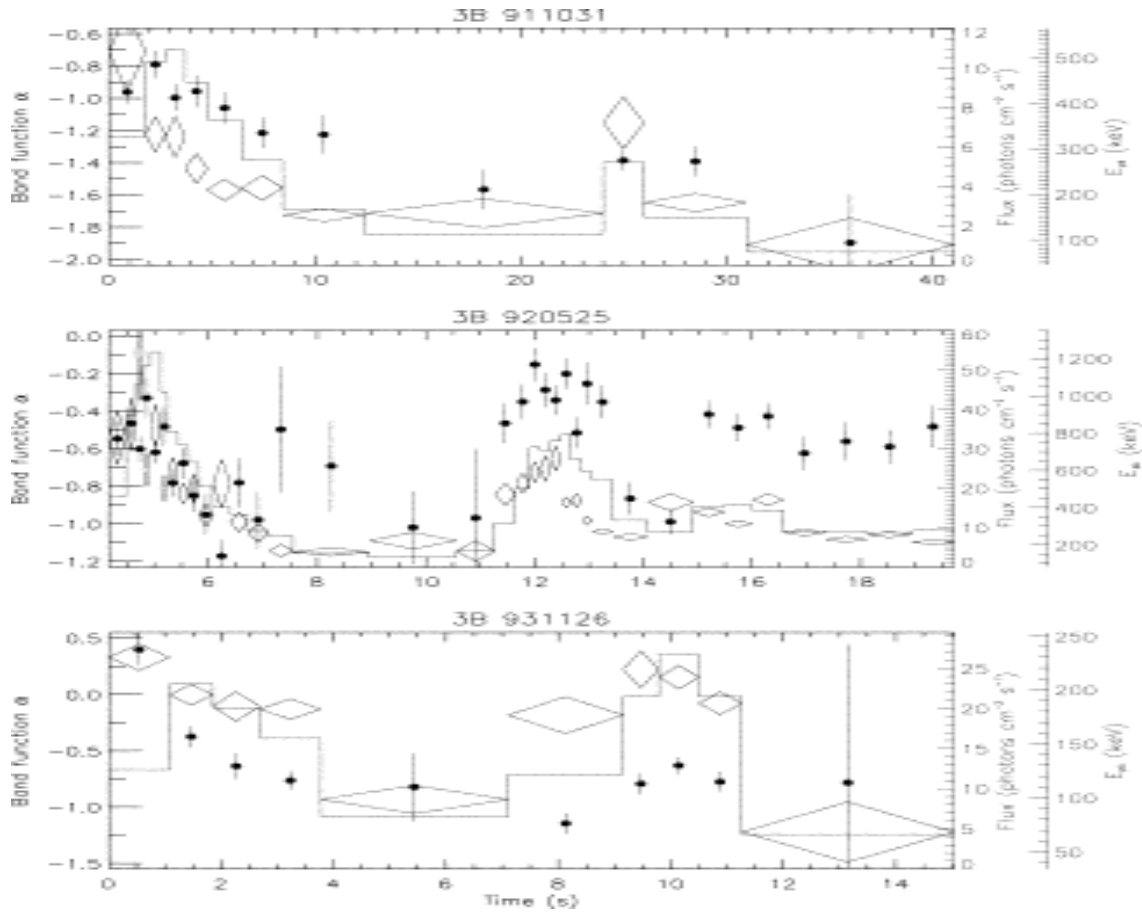


Figure 2.7: Examples of the evolution of the low energy spectral index α as reported by Crider et al. [21]. The peak energy E_{peak} (diamonds) and α (crosses) evolution are reported on the burst photon light curves.

β , as reported by Preece et al. ([130]), is centered around -2.25 although it has a broad dispersion as shown in fig.2.8.

A detailed analysis of the high energy spectral component in a sample of 126 bursts has been performed by Preece et al. ([129]). They fitted the BAND model to the time resolved spectra and applied statistical tests to verify the significance of their findings:

- β evolves with time rather than being constant in the 34% of their sample and the distribution of the average value of β is centered around -2.12;
- the excursion of this spectral parameter around its average value within most bursts is typically 0.4 which is small if compared with the typical variation of α and E_{peak} ;
- β evolves with time mainly (50 cases) with an hard to soft morphology and only 5 cases present a soft to hard β evolution.

The authors conclude that the evolution of the high energy spectral component is independent from the evolution of the other parts of the spectrum and it is small if

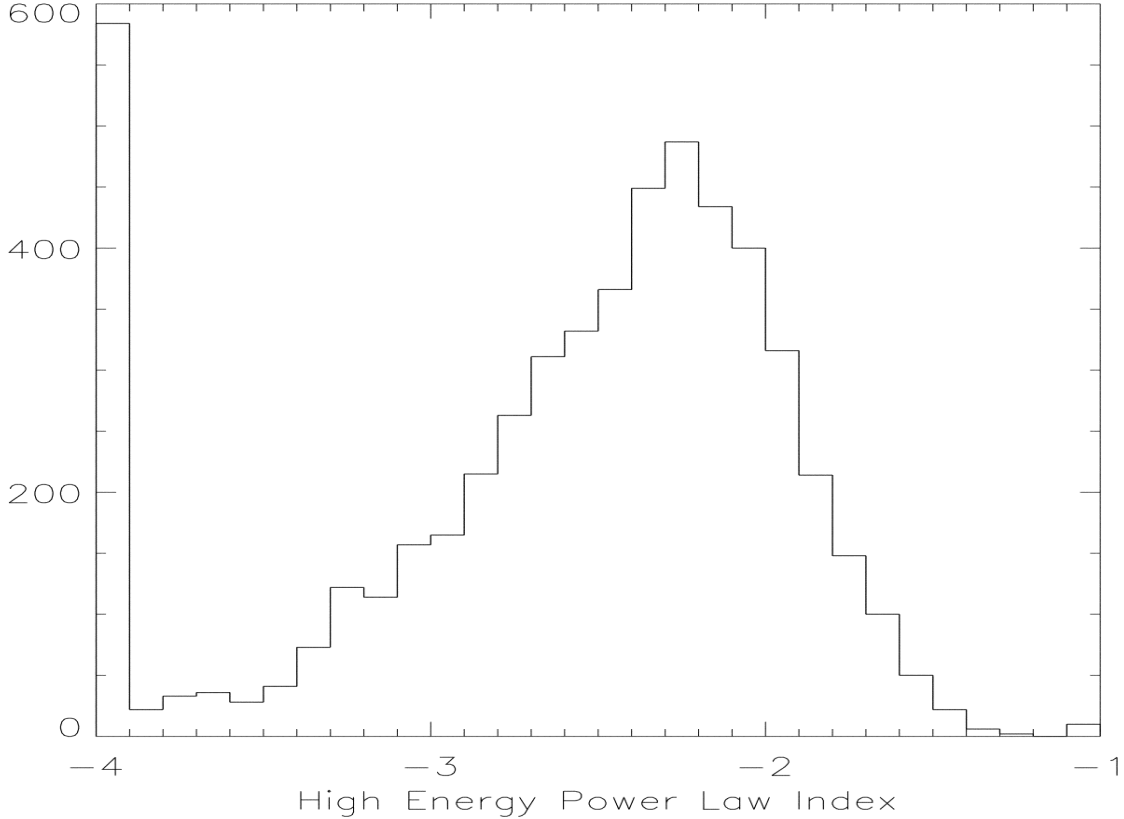


Figure 2.8: High energy spectral index β distribution. From Preece et al. [130].

compared to the typical spectral evolution experienced by α and E_{peak} : only in 15 cases there is a correlation between β and the peak energy and among these there could be also some peculiar evolutions like those discussed in chapt.7, in which there is a clear correlation between α and E_{peak} and both are anticorrelated with β .

The high energy spectral slope is better constrained for those bursts which have been observed by COMPTEL, simultaneously to BATSE: Halnon et al. (2000) showed that the distribution of β has an average lower value, i.e. -2.43, than that obtained only with the BATSE data, but also that the fraction of bursts with undetermined β is considerably smaller because of the presence of the high energy channels of COMPTEL, which better constraints the fits. These results should anyway be considered with cautions due to the possible selection effects in the detectability of GRBs by COMPTEL.

Peak Energy

The peak energy of the νF_ν spectrum has a narrow distribution with full width at half maximum less than a decade in energy (fig.2.9) and a maximum between 200 and 300 keV (Preece et al. 2000).

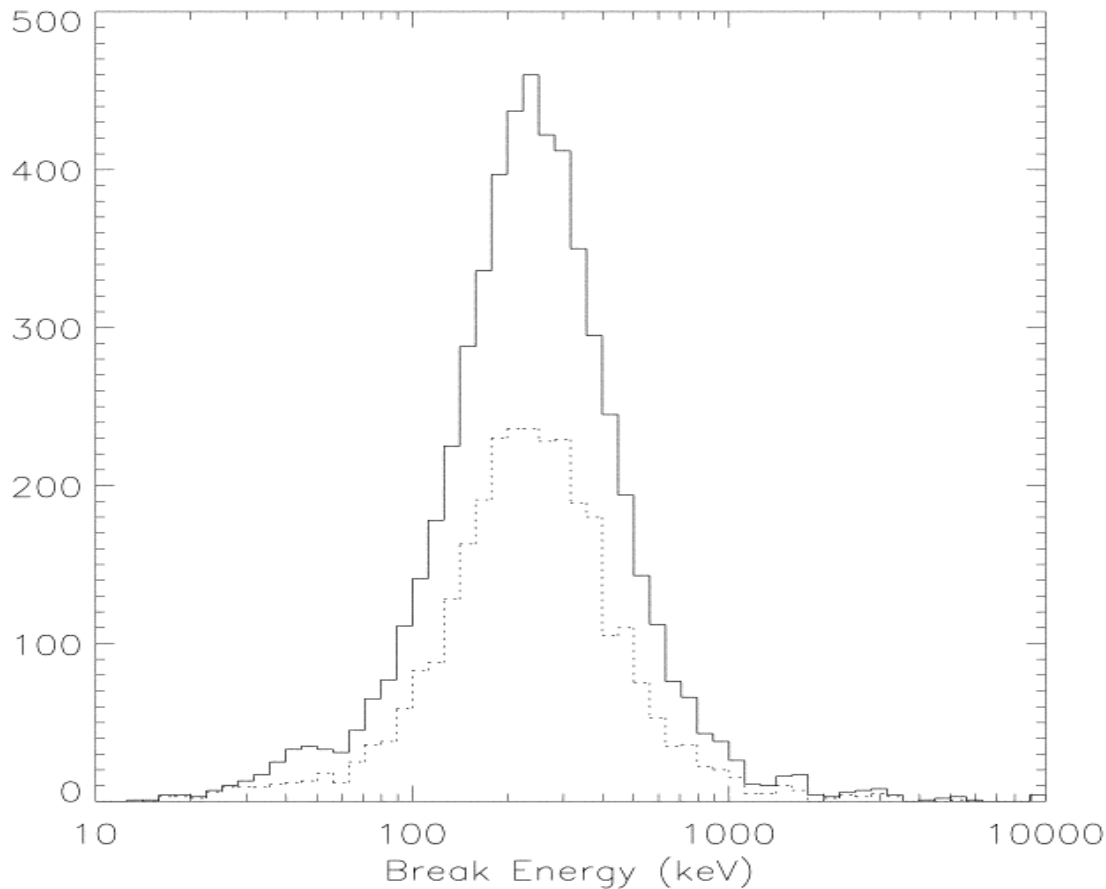


Figure 2.9: Peak energy distribution E_{peak} from Preece et al. [130] spectral catalog. The *dotted histogram* represents the E_{peak} distribution obtained from the spectra fitted with models different from the BAND function.

This parameter has been often assumed as the prime spectral hardness indicator for GRB spectral studies because it represents the energy at which most of the power is emitted. The correlation of E_{peak} with the intensity of the burst has already been discussed in the previous sections.

A recently discovered positive correlation between the peak energy and the burst variability, by Lloyd & Ramirez–Ruiz ([99]), has led to the possible correlation of the hardness (E_{peak}) with the intrinsic (isotropic) luminosity: $E_{peak} \propto L^\gamma$ with $0.5 < \gamma < 1.5$. The spectral model responsible for the GRB emission should explain also this result. Lloyd & Ramirez–Ruiz assume, as hardness indicator, the peak energy E_{peak} corresponding to the maximum of the light curve and, although this might not be necessarily the hardest spectrum, like in the case of an hard-to-soft spectral evolution, their findings seem statistically robust.

One interesting property of the peak energy, which is evident from fig.2.9, is its narrow distribution. If E_{peak} is determined by the radiative processes in the source frame, its distribution should be broad, within the framework of the proposed models, because

it results from the combination of differently distributed parameters, like the magnetic field B or the energy of the emitting electrons γ_e . Moreover, the variability of the bulk Lorentz factor Γ contributes in shaping the observed E_{peak} distribution.

Any viable emission model for the GRB prompt phase should reproduce the peak energy distribution as reported in fig.2.9 with: a) central value $E_{peak} \sim 300$ keV and b) a narrow scatter around this value.

A narrow peak energy distribution, as reported in fig.2.9, could be determined by different effects:

- a process, in the rest frame of the burst, which modifies all γ -ray spectra in the same way, producing a typical energy;
- the peak energy is independent from physical parameters such as the magnetic field B or the electron energy γ_e , but only depends on the bulk Lorentz factor Γ ;
- the peak energy depends on different physical parameters of the emitting source (B, γ_e , etc.) but the distribution of the bulk Lorentz factor Γ is so narrow that compensates for the broad distributions of the other parameters.

The problem of the narrow E_{peak} distribution has been recently discussed by Zhang & Meszaros ([158]). They review the possible prompt emission models aiming at reproducing the most evident spectral and temporal characteristics of GRBs: in particular many subclasses of the fireball scenario can give, due to the large spread in their physical parameter ranges, a typical peak energy in the range of some hundred keV, but they can be constrained by the narrowness of its distribution.

Without going into the details of the various scenarios described by Zhang & Meszaros ([158]), we can briefly summarize their fundamental results. In a typical fireball they consider that the total luminosity is the combination of a component, possibly associated with a Poynting flux (L_p) and another determined by the kinetic energy (L_k). Their ratio $\sigma = L_k/L_p$ characterizes the matter dominated regime ($\sigma > 1$) or the radiation dominated phase ($\sigma < 1$). Another parameter is R_{GRB} defined as the distance where the fireball or shell becomes transparent and/or the radiation is produced. Different combinations of these parameters characterize the possible variants of the standard model.

1. $r_{ph} \leq R_{GRB} \leq r_{dec}$. This is the classical internal model in which the bulk of the burst emission happens between the photospheric radius r_{ph} and the deceleration radius r_{dec} . The conversion of the fireball energy into radiation depends on the value of σ :
 - $\sigma < 1$ strong internal shocks develop and this corresponds to the classical internal shock model. Depending on the radiation process which dominates the emission (synchrotron or inverse Compton) the peak energy value ~ 300

keV is easily reproduced for typical fireball parameters (see also Ghisellini et al. 2000), while the narrow distribution of E_{peak} is better explained if synchrotron dominates.

- $\sigma > 1$ strong shocks cannot develop and the main internal energy conversion mechanism is magnetic reconnection. In this case synchrotron emission can reproduce the observed peak energy distribution under some ad-hoc assumptions on the magnetic field turbulence length scale. A more plausible possibility is to assume that the photons produced are extremely energetic and generate a large number of pairs which in turn regulate the maximum energy acquired by the electrons (Zhang & Meszaros [158]).
2. $R_{GRB} = r_{dec}$. This is the external model and also in this case the prevailing energy conversion mechanism depends on the value of σ :
- $\sigma < 1$ this is the familiar external shock model successfully applied to the afterglow of GRBs. It is based on the synchrotron emission by electrons which are accelerated by the shock to an equipartition regime; the peak energy results dependent on Γ^4 and, if a value of ~ 300 keV can be obtained, the distribution can be broad also for a narrow distribution of the bulk Lorentz factor.
 - $\sigma > 1$ the energy conversion is given by the interaction between the relativistic plasma and an external magnetic barrier. The resulting peak energy is high, if considered as due to simple synchrotron emission, and even larger in the context of synchrotron self Compton emission.

3. $R_{GRB} = r_{ph}$ this is the photospheric model. The emission comes from the photosphere when it becomes optically thin. In this case the peak of the spectrum is

$$E_{peak} = \begin{cases} 11 L_{52}^{-5/12} (1 + \sigma)^{5/12} t_{v,m,-3}^{1/6} \Gamma_2^{8/3} \text{ keV} & ; \quad \eta < \eta_1 \\ 370 L_{52}^{-1/12} (1 + \sigma)^{1/12} t_{v,m,-3}^{-1/6} \Gamma_3 \text{ keV} & ; \quad \eta_1 < \eta < \eta_2 \\ 2.7 L_{52}^{1/4} (1 + \sigma)^{-1/4} t_{v,m,-3}^{-1/2} \text{ MeV} & ; \quad \eta > \eta_2 \end{cases} \quad (2.8)$$

where $\eta = L/\dot{M}c^2$ represents the fireball dimensionless entropy and $t_{v,m,-3}$ is the variability timescale in units of 1 ms. For $\eta_1 < \eta < \eta_2$ the fireball becomes thin in the coasting (accelerating) regime. In this case the coasting regime seems to better justify the observed value and distribution width of the peak energy because of its quite linear dependence from Γ .

The freedom in the choice of the fireball parameters and the associated uncertainties validate most of these models in reproducing the observed average value of 300 keV for the peak energy. The width of the peak energy distribution, instead, can constrain some models although detailed formulation and numerical simulations are needed to determine the exact dependence of E_{peak} from the fireball parameters in the context of these models.

2.5 Spectral evolution models

This section presents an idea, recently proposed, for the interpretation of the the spectral evolution of GRBs. This theory, although in this simple formulation cannot reproduce the variety of the spectral evolution morphologies observed, considers an important effect which contributes in shaping the burst spectrum and its evolution.

2.5.1 The geometric model

This model has been proposed by Ryde & Petrosian ([138]) to interpret and reproduce the observed typical pulse shape and hardness intensity correlation (HIC). It is based on the assumption that the geometry of the emitting shell, i.e. its curvature and the relativistic boosting, might be responsible for the observed HIC during the pulse decay phase and for the pulse shape.

The basic idea is that the pulse and the spectrum evolution have an intrinsic shape which is determined by the unspecified physical details of the emission process. The observed temporal and spectral characteristics (i.e. the pulse shape and the HIC) are determined by the relativistic effects associated the GRB outflow.

In the standard model, the fireball emission originates from the shock produced by the collision of relativistic shells with different Lorentz factors. The electrons are supposed to be accelerated and to cool during the flux rise phase, while they only cool during the decay. Under some assumptions the spectral decay phase of the pulse and the entire temporal pulse shape may be modeled only by the geometric (curvature) and relativistic effects of the expanding shell.

There are three fundamental timescales in this model:

- the *cooling timescale*, determined assuming that the main emission processes are synchrotron and Inverse Compton, is $\tau_{cool} = 6 \times 10^{-5} (\Gamma_{rel} - 1)^{-1} R_{15}^2 \Gamma_2 L_{53}^{-1}$ sec (where Γ_{rel} is the relative Lorentz factor of one shell with respect to the other);
- the *angular timescale* $\tau_{ang} = 1.7 R_{15} \Gamma_2^{-2}$ sec determined by the assumption that the emitting surface is a sphere expanding with a Lorentz factor Γ ;
- the *dynamical timescale* determined by the shell crossing time: in the case the shell is not growing in width this is $\tau_{dyn} = 1.6 \times 10^{-4} \beta_{sh}'^{-1} \Gamma_2^{-1} \Delta_{0,9}$ sec (where $\beta_{sh}'^{-1}$ is the shock velocity and $\Delta_{0,9}$ is the shell width - equal to the initial width - in units of 10^9 cm); or in the case the shell is expanding, with its inner surface moving outward with Γ_s , it results $\tau_{dyn} = 1 \beta_{sh}'^{-1} R_{15} \Gamma_2^{-2} (\Gamma / \Gamma_s)$ sec.

The cooling timescale is the shorter and there is no way to arrange the fireball parameters to make it comparable to the other two timescales. The relative value of the dynamical and angular timescales $R = \tau_{ang} / \tau_{dyn}$ parameterizes the model:

- if $R \gg 1$, the geometric effect is dominant and determines the spectral evolution (with the simplifying assumption that the spectrum emitted from different parts of the shell is equal, e.g. with the same E_{peak} , α and β) which is described by $E_{peak}(t) = 2\Gamma E'_{peak}/(1 + t/\tau_{ang})$. In this case we notice that this result can account for the spectral decay of the pulse, i.e. after the peak, or for the spectral evolution of those pulses showing an hard to soft trend since the beginning, but yet do not predict the rise phase spectral evolution. The dynamical time, for $R \gg 1$, is small compared to the angular timescale, and the pulse shape can be represented by a δ function. The intensity profile is: $F_{bol}(t) = F_0/(1 + t/\tau_{ang})^2$. From these two relations the experimental HIC correlation is easily reproduced with $F_{bol} \propto E^\eta$ with $\eta = 2$ (Borgonovo & Ryde 2001);
- if $R \ll 1$, the dynamical timescale dominates: both the pulse shape and the spectrum observed are intrinsic and little modified by the angular effect.
- if $R \leq 1$, i.e. the dynamical timescale is finite and the δ function approximation is no more valid. The spectral evolution and light curve are produced by the combination of the intrinsic and angular effect. In this case the spectrum and the light curve pulse shape are complicated due to the superposition of different spectra and pulses, each one differently modified by the geometric effect. The temporal and spectral behaviour is still a power law but with index η different from the observed value 2. In this case they show that the HIC is $E_{peak}^{\eta_{int}}$, i.e. the intrinsic HIC correlation (with $\eta_{int} \neq 2$), eventually smoothed (for different values of R), by the curvature effect.

An interesting consequence of this model is that the intrinsic pulse shape and the intrinsic spectrum are slightly modified for $R \gg 1$: in particular the observed spectrum, as being the superposition of different single emission episode spectra, should be broader than the intrinsic one and its low energy spectral slope could be softer. This supports the idea that the spectra, as they are emitted by the process acting in the GRB prompt phase could have a different character (e.g. quasi thermal) from the one observed (i.e. non-thermal with soft low energy component), in agreement with the findings of chapt.6.

As noted by the authors these results are obtained under some simplifying assumption which they plan to relax in a future work. We stress that the assumption of a fixed low and high energy seed spectral shape should be relaxed, considering the variety of the spectral pattern and correlations between different parts of the spectrum.

A possible problem of this model is the cooling timescale which is of the order of 10^{-5} sec. The pulse shape is then determined by the superposition of many independent cooling episodes. On the other hand, as discussed in chapt.6, a small cooling timescale of the emitting electrons would contribute a $E^{-2/3}$ spectral component in any spectrum which is integrated on a timescale longer than τ_{cool} . This spectral component can not be eliminated by the superposition of many spectra but it is not observed in typical GRB spectra.

In general a more detailed description of the spectral evolution of GRBs possibly extending on a wider energy range and for a larger sample of bursts (not only those which have a clear decay pulse shape – like in the selection of the works dealing with the E_{peak} evolution) could give good results for the interpretation, and a more complete model which describes the rise and decay phase of the bursts, their spectral evolution and the variety of these morphologies is needed.

Chapter 3

Emission processes acting in GRBs

3.1 Introduction

This chapter is a brief review of the most common emission models proposed for the prompt emission of GRBs.

The emission mechanism acting in GRBs should reproduce the most common observed spectral characteristics which have been described in chapt.2:

- the typical GRB spectrum, which is a featureless non-thermal continuum, is commonly composed by two power laws connected smoothly by an exponential curvature: the low and high energy spectral components are $EF(E) \propto E^{\alpha=1}$ and $EF(E) \propto E^{\beta=-0.5}$, and the spectrum peaks at $\sim 300keV$.
- the spectral evolution represents how the spectrum changes with time according to the possible morphologies described in chapt.2.

Beside these general features there is a considerable number of bursts showing hard low or high energy spectra, extremely soft high energy components or particular evolutionary morphologies which complicate the simplest observational picture drawn above. Any spectral model aiming at explaining the origin of the GRB prompt emission should reproduce the typical characteristics as well as their exceptions.

The most popular emission model of GRBs (sec.3.2) is synchrotron radiation from relativistic electrons in an intense magnetic field (Rees & Meszaros [133], Katz [77], Tavani [154]). Alternative scenarios have been proposed such as Comptonization of low energy photons by particles with a thermal (sec.3.3.5) or quasi-thermal (sec.3.3.6) energy distribution (Liang [96], Ghisellini & Celotti [55]). Possible variants of the basic synchrotron emission process have also been considered, such as synchrotron emission from anisotropic small pitch angle particle distributions (Lloyd & Petrosian [98] - sec.3.2.7), jitter radiation (Medvedev [107] - sec.3.2.6) or emission from a two phase stratified medium (Granot et al. [63] - 3.2.5). In the context of Compton emission some alternatives have

been suggested such as the Comptonization of photospheric photons (Meszaros & Rees [113] - sec.3.3.7) or Compton drag (Lazzati et al. [91] - sec.3.3.8).

The following sections describe the basic predictions of these models for the spectral shape of GRB spectra, with particular emphasis on the low energy spectral component which can be directly compared with the results of the spectral analysis (chapt.6).

3.2 Synchrotron Model

Since the first studies of GRB spectra it was proposed that their non-thermal multiple power law spectra could be produced by synchrotron emission of relativistic electrons in an intense magnetic field. This radiation process found a natural placement within the standard internal shock scenario (Rees & Meszaros [133]) in which a shock formation, by the collision of shells with different Γ s, is a viable mechanism for the conversion of the shells kinetic energy into radiation. The acceleration of particles at the shock front and the formation of intense magnetic fields suggest synchrotron as a possible emission process. Also the afterglow emission is produced through synchrotron by particles accelerated at the external shock.

Synchrotron emission can explain the observed typical spectral peak of the prompt burst $E_{peak} \sim 300$ keV (under equipartition assumption, see Ghisellini et al. 2000) and the spectrum and time evolution of the afterglow. Nonetheless, there are several evidences which are not easily reproduced within this model which will be presented and discussed in chapt.5 and chapt.6.

The basic model of optically thin emission by accelerated particles (sec.3.2.1), which can be complicated considering cooling (sec.3.2.3) or self absorption (sec.3.2.2), has specialized leading to different alternatives (sec.3.2.5, 3.2.6 and 3.2.7).

3.2.1 Optically thin synchrotron emission

In the standard theory of synchrotron radiation it is supposed that the emitting plasma is optically thin in order to have a considerable photon flux like it is observed in GRBs. Within the internal shock model, electrons are accelerated at the shock front. If they assume a power law energy distribution with index p ,

$$dN(\gamma) = N_0 \gamma^{-p} d\gamma \quad (3.1)$$

for $\gamma > \gamma_m$, the total number of particles and associated energy is:

$$N_{tot} = \int_{\gamma_m}^{+\infty} N(\gamma) d\gamma; \quad E_{tot} = \int_{\gamma_m}^{+\infty} N_0 \gamma^{-p+1} d\gamma \quad (3.2)$$

The synchrotron energy spectrum, expressed in erg/cm² sec keV, produced by this electron energy distribution is (Jackson [74]):

$$F_\nu \propto \begin{cases} \nu^{-s} & \text{with } s = (p-1)/2 \text{ if } p > 1/3 \\ \nu^{1/3} & \text{if } p < 1/3. \end{cases} \quad (3.3)$$

Considering an energy index $p \sim 2$, which is predicted by Fermi second order acceleration processes, the second integral, i.e. the total energy, diverges unless a break energy γ_0 is introduced and the electron energy distribution is re-defined as:

$$dN(\gamma) \propto \begin{cases} \gamma^{-p_1} d\gamma & \text{for } \gamma \leq \gamma_0 \\ \gamma^{-p_2} d\gamma & \text{for } \gamma > \gamma_0 \end{cases} \quad (3.4)$$

The values of p_1 and p_2 should be lower than 1 and greater than 2, respectively, in order that the total number and energy of the accelerated particles be finite.

The synchrotron spectrum produced in a uniform magnetic field for $p_1 > 1/3$ is:

$$F_\nu \propto \begin{cases} \nu^{-s_1} & \text{with } s_1 < 0 & \text{for } \nu \leq \nu(\gamma_0) \\ \nu^{-s_2} & \text{with } s_2 > 1/2 & \text{for } \nu > \nu(\gamma_0) \end{cases} \quad (3.5)$$

Katz ([77]) pointed out that the typical assumption of a (single or double) power law particle distribution function does not apply in the case of relativistic collisionless shocks which, preferentially, build up a thermal energy distribution of shocked particles:

$$N(\gamma) \propto \gamma^2 \exp(-3\gamma/\gamma_0) \quad (3.6)$$

which can be eventually modified by an high energy power law component (Tavani [154]).

This distribution, in the limit of low energies ($\gamma \ll \gamma_0$) is $\propto \gamma^2$ and, consequently, $p_1 = -2$. Recalling that for $p < 1/3$ the synchrotron spectrum, at low energies, is dominated by the most energetic electrons (i.e. those with minimum energy, γ_m), the thermal energy distribution ($N(\gamma) \propto \gamma^2$ for $\gamma \ll \gamma_0$) produces a low energy spectrum:

$$F_\nu \propto \nu^{1/3} \quad \text{for } \nu \leq \nu(\gamma_m) \quad (3.7)$$

where $\nu(\gamma_m) = 3eB \sin\theta \gamma_m^2 / 4\pi m_e c$ is the synchrotron characteristic frequency corresponding to electrons with $\gamma = \gamma_m$.

In the more realistic case of a thermal distribution (eq.3.6) modified by a high energy power law with index p , the spectrum results:

$$F_\nu \propto \begin{cases} \nu^{1/3} & \text{for } \nu < \nu(\gamma_0) \\ \nu^{-\frac{p-1}{2}} & \text{for } \nu \geq \nu(\gamma_0) \end{cases} \quad (3.8)$$

From the basic theory of optically thin synchrotron emission, where the emitted spectrum is represented by eq.3.8, the low energy component has a fixed slope $\propto \nu^{1/3}$. This is a strong prediction of this model which can be verified by the observations. In fact, also considering the superposition of different spectra, the low energy $\nu^{1/3}$ component remains a distinctive feature of this model.

3.2.2 Synchrotron self absorption

The basic synchrotron spectrum can be modified at low energies (i.e. in the $\propto \nu^{1/3}$ part) by self absorption. For a non-thermal electron energy distribution with index p , the self-absorbed spectral component, below the absorption frequency ν_t , is:

$$F_\nu \propto \begin{cases} \nu^2 & \text{if } p < 1/3 \\ \nu^{5/2} & \text{if } p > 1/3 \end{cases} \quad (3.9)$$

and the absorption frequency is:

$$\nu_t = \left[\frac{3^{(p-1)/2} \pi^{3/2}}{4} A(p) \frac{e \tau_T}{\sigma_T B} \right]^{\frac{2}{p+4}} \nu_B \quad (3.10)$$

where $A(p)$ is a combination of the Gamma functions, and $\nu_B = e B / 2\pi m_e c$ is the Larmor frequency.

Synchrotron self absorption can produce, below ν_t , a spectrum with a maximum slope $F_\nu \propto \nu^{2.5}$, and this relaxes the limit of the optically thin synchrotron spectrum (1/3) described in sec.3.2.1.

3.2.3 Synchrotron Cooling

The standard synchrotron spectrum (thin and thick) can be further modified if the cooling of the electrons is considered. We first define the cooling timescale and frequency for a single electron and then consider the cooling spectrum for a power law electron energy distribution.

Single Electron

The synchrotron power emitted by a single relativistic electron with energy $\gamma m_e c^2$ in the comoving frame is:

$$P_{synch}(\gamma) = \frac{4}{3} \sigma_T c \gamma^2 \frac{B^2}{8\pi}$$

The timescale in which this electron radiates its energy is the cooling timescale and can be defined as $t_{cool} = \gamma / \dot{\gamma}$

$$t_{cool} = \frac{\gamma m_e c^2}{\frac{4}{3} \sigma_T c \gamma^2 \frac{B^2}{8\pi}} = \frac{6\pi m_e c}{\sigma_T \gamma B^2} \quad (3.11)$$

The corresponding cooling frequency, in the comoving reference frame, can be obtained substituting the expression for γ^2 in the synchrotron characteristic frequency $\nu \propto \gamma^2 (eB/2\pi m_e c)$ and results:

$$\nu_{cool} \propto \left[\frac{m_e c}{\sigma_T B^2 t_{cool}} \right]^2 \cdot \nu_B \quad (3.12)$$

The cooling timescale is typically small: Ghisellini et al. (2000) calculate it in the standard synchrotron shock scenario (i.e. under equipartition) and considering the bulk Lorentz factor, the possible redshift of the source and the relative motion of the colliding shells. They determine that for typical parameters $t_{cool} \sim 10^{-7} sec$ which is much shorter than the dynamical timescale and results in an efficient energy dissipation.

Power law population of electrons

The cooling spectrum produced by a population of electrons is mainly due to those electrons $\gamma > \gamma_{cool}$. The cooling timescale should be compared with the dynamical timescale which in the case of the internal shock scenario is defined as the shell light-crossing time $\tau_{dyn} \sim \Delta R/c$, where ΔR represents the shell width. The two possible regimes are (Sari et al. [142]):

- *fast cooling*: if $\gamma_{cool} < \gamma_m$, i.e. the lower limit of the electron energy distribution, then *all* the electrons cool rapidly and the observed spectrum will be produced by a cooling electron distribution. The energy spectrum is:

$$F_\nu \propto \begin{cases} \nu^{1/3} & \text{for } \nu < \nu_{cool} \\ \nu^{-1/2} & \text{for } \nu_{cool} < \nu < \nu_{max} \\ \nu^{-p/2} & \text{for } \nu > \nu_{max} \end{cases} \quad (3.13)$$

where $\nu_{max} = \nu(\gamma_m)$ is the characteristic frequency corresponding to γ_m ;

- *slow cooling*:, if $\gamma_{cool} > \gamma_m$ there is a limited number of electrons, namely only those with $\gamma_e \geq \gamma_{cool}$, which can cool. In this regime the spectrum is (Sari et al. [142]):

$$F_\nu \propto \begin{cases} \nu^{1/3} & \text{for } \nu < \nu_{cool} \\ \nu^{-(p-1)/2} & \text{for } \nu_{cool} < \nu < \nu_{max} \\ \nu^{-p/2} & \text{for } \nu > \nu_{max} \end{cases} \quad (3.14)$$

The highly variable light curve of GRBs and the requirement of high radiative efficiency suggest that in the prompt emission fast cooling dominates (Sari et al. [141]); in the afterglow phase, instead, the slow cooling regime becomes progressively important.

The synchrotron spectrum produced by a shocked electron population which takes into account the effect of self absorption and fast cooling is reported in fig 3.1, from Sari et al. ([142]).

3.2.4 The synchrotron shock model

An application of the synchrotron theory to GRB prompt emission is the synchrotron shock model (SSM) by Tavani ([154]). This model is based on optically thin synchrotron emission from relativistic particles (either electrons and/or electron-positron pairs). The

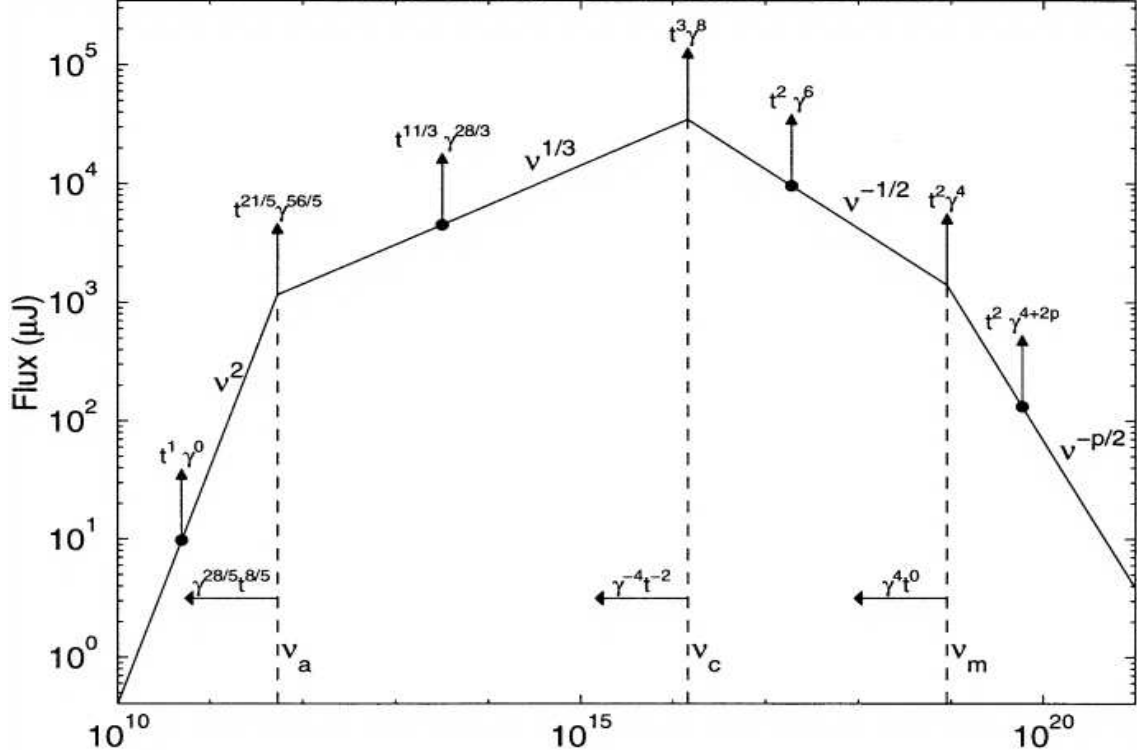


Figure 3.1: Synchrotron self absorbed spectrum with the cooling effect. From Sari et al. ([142]).

electron energy distribution $N(\gamma)$, which is a relativistic Maxwellian before the shock occurs, is modeled by the shock passage which adds a high energy power law component with index δ :

$$N(\gamma) \propto \begin{cases} \frac{\gamma^2}{\gamma_*^3} \exp\left(-\frac{\gamma}{\gamma_*}\right) & \text{for } \frac{\gamma}{\gamma_*} \leq 1 \\ \gamma^{-\delta} & \text{for } 1 \leq \frac{\gamma}{\gamma_*} \leq \frac{\gamma_{max}}{\gamma_*} \end{cases} \quad (3.15)$$

where $\gamma_* = k_B T^*/m_e c^2$ is the pre-shock equilibrium electron energy, $\gamma^{-\delta}$ is the supra-thermal component and γ_{max} is the maximum electron energy.

The synchrotron shock model spectrum, which will be tested in chapt.5 by the spectral analysis of a sample of bright bursts, has a substantial continuous curvature and is composed by two power laws:

$$F_\nu \propto \begin{cases} \nu^{1/3} & \text{for } \nu \leq \nu_{break} \\ \nu^{-\frac{\delta-1}{2}} & \text{for } \nu \geq \nu_{break} \end{cases} \quad (3.16)$$

This spectrum, in a νF_ν representation, peaks at a characteristic energy ν_{peak} , related to the pre-shock thermal energy: $\nu_{peak} \sim 2.5\nu_*$ and $\nu_* = (m_e c^2 \gamma_*)/h$. This spectral model can account for the high energy spectral variety of GRB observed spectra but has a fixed $(-2/3)$ slope at low energies.

3.2.5 Non homogeneous spatial distribution in fast cooling regime

Granot et al. [63] proposed a model of synchrotron emission by a population of shocked electrons with a non uniform spatial distribution in fast cooling regime:

- *fast cooling* is required by short variability timescales of the light curve of GRBs which, in turn, implies high radiative efficiency (Sari et al [141]).
- *inhomogeneous spatial distribution* is a natural configuration of the shocked electrons behind the shock front. In fact, it is very likely that the electrons which had no time to cool substantially (i.e. the lately accelerated electrons) are distributed in a narrow region just behind the shock front; on the other hand those electrons, which had been accelerated first, and had enough time to cool, are distributed further away from the shock front.

Allowing also for self absorption, this two-phase gas of shocked electrons introduces a third spectral break ν_{ac} which separates the spectral emission of the old (cooled) electrons from the part absorbed by recently accelerated, but yet not-much-cooled, electrons.

According to the relative position of the self absorption frequency ν_t with respect to ν_{cool} , which, in turn, is $< \nu_m$ due to the fast cooling assumption, the following cases can be distinguished:

1. $\nu_{sa} < \nu_{cool} < \nu_m$: the shock accelerates fresh electrons which do not have enough time to cool and are located in a thin shell just behind it, while the electrons accelerated earlier have cooled and are concentrated in a much larger layer. For $\nu < \nu_{sa}$ these two layers will absorb in different ways: old electrons, being colder are more efficient in absorbing the synchrotron photons, and contribute a ν^2 spectral component for $\nu < \nu_{ac}$; on the other hand the still hot electrons (concentrated in a thin layer right behind the shock) absorb photons less efficiently, producing a new $\nu^{11/8}$ power law component for $\nu_{ac} < \nu < \nu_{sa}$. The resulting spectrum is:

$$F_\nu \propto \begin{cases} \nu^2 & \text{for } \nu < \nu_{ac} \\ \nu^{11/8} & \text{for } \nu_{ac} < \nu < \nu_{sa} \\ \nu^{1/3} & \text{for } \nu_{sa} < \nu < \nu_{cool} \\ \nu^{-1/2} & \text{for } \nu_{cool} < \nu < \nu_m \\ \nu^{-p/2} & \text{for } \nu > \nu_m \end{cases} \quad (3.17)$$

2. $\nu_{cool} < \nu_{sa} < \nu_m$: the cooling frequency becomes unimportant for the computation of the spectrum and the non uniform spatial distribution suppresses the $\nu^{1/3}$ component. The resulting spectrum is:

$$F_\nu \propto \begin{cases} \nu^2 & \text{for } \nu < \nu_{ac} \\ \nu^{11/8} & \text{for } \nu_{ac} < \nu < \nu_{sa} \\ \nu^{-1/2} & \text{for } \nu_{sa} < \nu < \nu_m \\ \nu^{-p/2} & \text{for } \nu > \nu_m \end{cases} \quad (3.18)$$

3. $\nu_{cool} < \nu_m < \nu_{sa}$: the spectrum is inverted at low energies:

$$F_\nu \propto \begin{cases} \nu^2 & \text{for } \nu < \nu_m \\ \nu^{5/2} & \text{for } \nu_m < \nu < \nu_{sa} \\ \nu^{-p/2} & \text{for } \nu > \nu_{sa} \end{cases} \quad (3.19)$$

The exact value of these frequencies depends on the hydro-dynamical conditions assumed for the shells and are reported by Granot et al. [63].

It should be noticed that this “stratified” spectral model modifies the low energy synchrotron spectrum introducing a $\nu^{11/8}$ component. Moreover, within this model the observed spectrum of the prompt phase of GRBs should be characterized by four spectral breaks (eq.3.17).

3.2.6 Jitter Radiation

The standard theory of synchrotron radiation assumes a uniform magnetic field. Medvedev [106] developed the theory of synchrotron emission considering a magnetic field with very small inhomogeneity length scale. In this model the emitted spectral shape depends on the length scale λ_B of the magnetic field random variations and on the Larmor radius of the electrons $\rho_e = \gamma \frac{m_e c^2}{e B_\perp}$ (where B_\perp is the field component perpendicular to the electron velocity).

If the length scale $\lambda_B \gg \rho_e$ the standard synchrotron theory applies, whereas if $\lambda_B < \rho_e$ the emission is “jitter” radiation because the electron is forced to oscillate along a mean direction due to the small scale inhomogeneities. A parameter which accounts for the two situations is the deflection-to-beaming ratio $\delta = \alpha/\Delta\theta$, where α is the deflection angle, i.e. the angle formed between the electron initial direction of motion and the direction along which it is deviated due to the magnetic field action and $\Delta\theta$ is the beaming angle, depending on the electron energy γ . The deflection angle can be calculated considering that only the perpendicular component of the Lorentz force is responsible for the deviation of the electron from its original trajectory and that it acts on the perpendicular component of the electron momentum p_\perp . The ratio of $p = \gamma m_e c$ to p_\perp represents the deflection angle α . p_\perp can be obtained combining the momentum $p_\perp = F_L \cdot t$, with $F_L \propto e B_\perp$ and $t = \lambda_B/c$, i.e. the crossing time of the magnetic field inhomogeneity. The deflection angle results:

$$\alpha \sim \frac{p_\perp}{p} = \frac{e B_\perp \lambda_B}{\gamma m_e c^2} \quad (3.20)$$

The beaming angle is the inverse of the electron Lorentz factor γ ,

$$\Delta\theta \sim \frac{1}{\gamma} \quad (3.21)$$

and the deflection-to-beaming ratio results

$$\delta = \frac{\alpha}{\Delta\theta} = \frac{e B_\perp \lambda_B}{m_e c^2} \quad (3.22)$$

or, expressed with the wave number $k_B = 1/\lambda_B$,

$$\delta = \frac{\gamma}{k_B \rho_e} \quad (3.23)$$

Notice that δ (eq.3.22) is independent from the electron energy but only depends on the magnetic intensity and inhomogeneity length scale.

If the deflection angle α is small with respect to the beaming angle $\Delta\theta$ (i.e. $\delta \ll 1$), the electron, due to the non homogeneous magnetic field, will “jitter” around the average magnetic field direction.

Jitter Frequency

For small inhomogeneities of length scale λ_B , the corresponding crossing time is $t \sim \lambda_B/c$ and, in the comoving frame, $\tau = \lambda'_B/c$ with $\lambda'_B = \lambda_B/\gamma$. The characteristic jitter frequency is the inverse of the crossing time:

$$\nu'_j = \frac{1}{2\pi\tau} = \frac{\gamma k_B c}{2\pi} \quad (3.24)$$

and, transforming back to the observer frame:

$$\nu_j \propto \gamma^2 k_B c \quad (3.25)$$

ν_j represents the characteristic frequency of an electron with Lorentz factor γ radiating in a magnetic field with length scale $\lambda_B = 1/k_B$.

Magnetic Field Structure

In the jitter model a possible mechanism for the creation of a small scale magnetic field (Medvedev [105]) is through two-stream instabilities. The basic idea is that if the particle velocity distribution is anisotropic, any little oscillation of the magnetic field in one direction is amplified by the streaming of the electrons in the perpendicular plane in two separated regions. In this way the magnetic field amplitude is enhanced.

The magnetic field is formed by this two stream flow across the shock front: the in-flowing un-shocked particles meet the out-flowing (scattered) particles and a magnetic field in the plane perpendicular to the shock front velocity is formed.

It is very likely that a more general configuration at the shock front involves a double-component magnetic field: a large scale magnetic field B_{LS} and a small scale magnetic field B_{SS} , the latter being responsible for the jitter emission.

Jitter Spectrum

The Jitter spectrum produced by a population of electrons with a power law energy distribution is a broken power law with the spectral break corresponding to the jitter

frequency (in the comoving frame):

$$\nu_{j,break} = 6 \times 10^9 \gamma_m^2 \Gamma_{rel} \bar{\gamma}_e^{-1/2} n_{10}^{1/2} \text{ Hz} \quad (3.26)$$

where Γ_{rel} is the relative Lorentz factor of two colliding shells, n_{10} is the electron density in unit of 10 cm^{-3} , $\bar{\gamma}_e$ is the initial thermal Lorentz factor of the streaming electrons. The spectrum is:

$$F_\nu \propto \begin{cases} \nu^1 & \text{for } \nu < \nu_j \\ \nu^{-(p-1)/2} & \text{for } \nu > \nu_j \end{cases} \quad (3.27)$$

This spectrum depends on two additional (with respect to the standard theory) parameters: the deflection-to-beaming ratio δ and the peakedness of the magnetic field distribution μ which describes the most recurrent lengthscale of the magnetic field inhomogeneity. Numerical simulations show that the spectrum is quite insensitive to a variation of μ but is highly dependent on δ variations. This dependence is responsible for the shifting of the peak of the jitter spectrum toward lower frequencies as δ increases. Around the peak, in a small frequency range and for high δ , the spectrum can be as steep as $\nu^{3/2}$, but in general the limit for pure jitter radiation of the low energy component is ν^1 (Medvedev [106]).

Jitter + Synchrotron Spectrum

In presence of a large scale magnetic field (B_{LS}) and a small scale magnetic field (B_{SS}) synchrotron and Jitter emissions superimpose. This is the general model proposed by Medvedev ([106]) for the GRBs emission. $\bar{B}_{LS} = \langle B_{LS}^2 \rangle^{1/2}$ is the average value of the large scale magnetic field, responsible for the synchrotron emission with characteristic frequency ν_{cm} , and $\bar{B}_{SS} = \langle B_{SS}^2 \rangle^{1/2}$ is the small scale magnetic field, which produces the Jitter component with associated ν_{jm} . The relative importance of these two processes is represented by the ratio of their characteristic frequencies:

$$\frac{\nu_{cm}}{\nu_{jm}} = \frac{3 \bar{B}_{LS}}{2 \bar{B}_{SS}} \delta$$

The typical spectrum is reported in fig.3.2: it is characterized by a narrow bump at the Jitter frequency due to the intrinsic shallowness of this spectrum around the break frequency, and a second bump, at lower energies, due to the synchrotron curvature.

In conclusion, the Jitter + Synchrotron (J+S) composite spectrum (*solid line* in fig.3.2) can be described as the superposition of two components: the synchrotron spectrum, which is well described by a smoothly broken power law (e.g. the BAND model with the low energy powerlaw spectral index fixed at $-2/3$), and the Jitter component which is modeled by a sharply broken power law with low energy spectral slope $F_\nu \propto \nu^1$ and a high energy tail, with the typical slope of the synchrotron spectrum $F_\nu \propto \nu^{-(p+1)/2}$. The position of the Jitter peak does not depend on the magnetic field strength, like in the case of pure synchrotron, but only on the electron density. If measured directly this could be an important diagnostic for the emission site.

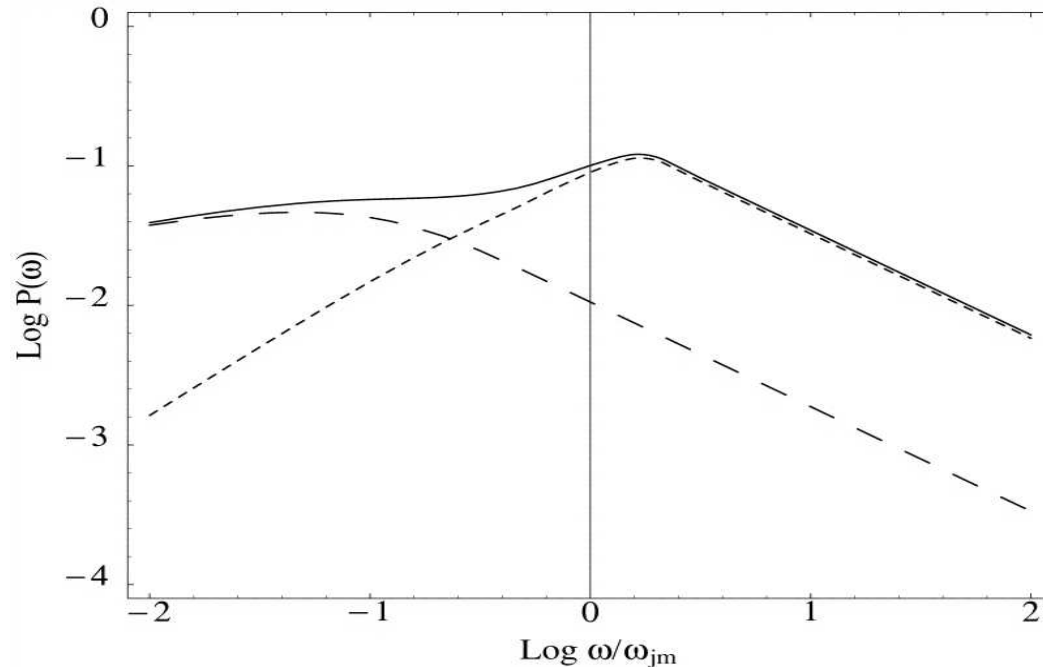


Figure 3.2: Synchrotron (*long dashed line*) + jitter (*short dashed line*) spectrum. ω/ω_{jm} represents the angular frequency in units of the jitter characteristic frequency. From Medvedev [106]

The J+S model also predicts the presence of line-like features in the spectrum: these are not real lines because they are broad and the spectrum, after the line peak, is like a power law instead of having a fast decreasing curvature, but in general they are caused by the prevailing of the Jitter spectral bump. The parameter range (δ and $\overline{B}_{LS}/\overline{B}_{SS}$) necessary to produce these features in the BATSE energy range, is anyway very narrow and this could justify the fact that they have not been found in the BATSE burst spectra.

3.2.7 Small Pitch Angle Distribution

Synchrotron emission depends on the relative velocity of the emitting electrons with respect to the magnetic field lines. This defines the pitch angles of the electrons Ψ which are typically assumed to have an isotropic distribution. A variant of the standard synchrotron theory which relaxes another basic assumption, is the emission by an electron population with *anisotropic pitch angle distribution*. This has been proposed by Lloyd & Petrosian ([100]).

A distribution of electrons with a mean pitch angle $\Psi \ll 1$ can be realized in GRB shock sites, because of the typically high densities and low intensity magnetic fields. In fact, in this situation, the Alfvén velocity of the plasma turbulence would be high and comparable with the speed of the particles: the particles would be accelerated quickly within few plasma instabilities patches and their pitch angle distribution could

not be isotropized. If $\Psi\gamma_m \sim 1$ (where γ_m is the energy dominating the electron energy distribution) the spectrum is:

$$F_\nu \propto \begin{cases} \nu^1 & \text{for } \nu \ll \nu_s \\ \nu^{1/3} & \text{for } \nu_s < \nu < \nu_m \\ \nu^{-(p-1)/2} & \text{for } \nu \gg \nu_m \end{cases} \quad (3.28)$$

where

$$\nu_s = \frac{2}{3} \frac{eB}{m_e c} \frac{1}{\gamma_m \Psi^2}$$

The natural evolution of such a spectrum is intimately related to the energy losses of the electron population.

In the limit $\Psi \ll \gamma_m^{-1}$ the $\nu^{1/3}$ slope is suppressed and the spectrum is:

$$F_\nu \propto \begin{cases} \nu^1 & \text{for } \nu \ll \nu_s \\ \nu^{-(p-1)/2} & \text{for } \nu_s \gg \nu_m \end{cases} \quad (3.29)$$

with

$$\nu_s = \frac{4}{3} \frac{eB}{m_e c} \gamma_m$$

The disappearance of the portion of the spectrum between ν_s and ν_m is due to the dependence of these frequencies on the gamma factor: if the electrons are cooling, their energy distribution moves self-similarly at lower energies and, consequently, also γ_m decreases:

$$\begin{aligned} \nu_s &\propto \frac{1}{\gamma_m \Psi^2} \\ \nu_m &\propto \gamma_m^2 \Psi \end{aligned}$$

and if both Ψ and γ_m decreases then ν_m decreases while ν_s increases and the $\nu^{1/3}$ slope, between these frequencies, is suppressed.

3.3 Comptonization Model

A possible alternative to the models based on synchrotron emission is given by the Compton theory, which can be successfully applied to explain some features of gamma ray burst spectra.

A dense population of relativistic electrons in a weak magnetic field could Compton scatter self emitted soft photons and produce the observed radiation (sec.3.3.3 and 3.3.5). A variant (sec.3.3.6) considers the emission by mildly relativistic quasi-thermal electrons. Also the bulk motion of the ejected shells can be responsible for the observed spectrum (sec.3.3.8).

3.3.1 Inverse Compton Process

The interaction of an electron with a photon is regulated (in terms of the scattering process) by their relative energies; the following situations can occur:

1. *low energy electron*

- (a) $E_{phot} \ll \gamma_e$ (in the electron reference frame) the electron scatters the photon leaving its energy unchanged (*Thomson scattering*). The process is regulated by the Thomson cross section σ_T .
- (b) $E_{phot} \sim \gamma_e$ (in the electron reference frame) the photon has enough energy to boost the electron (*Direct Compton scattering*). In this case the electron cross section decreases with energy and is regulated by the Klein–Nishina cross section σ_{KN} . The initial photon energy x_0 becomes:

$$x = \frac{x_0}{1 + x_0 \cos(\Psi)} \quad (3.30)$$

with $x = h\nu/mc^2$, and where Ψ is the angle of incidence of the photon with respect to the electron.

2. *high energy electron*

In this case γ_e can exceed E_{phot} so that a fraction of the electron energy is transferred to the photon, which is boosted by a factor γ_e^2 (*Inverse Compton*). The photon energy E , after the scattering, depends on the incidence and scattering angles (θ_{in} , θ_{sc}) and on the initial photon energy E_0 :

$$E = E_0 \frac{1 - \beta \cdot \cos\theta_{in}}{1 - \beta \cdot \cos\theta_{sc}} \quad (3.31)$$

where all the quantities are measured in the observer rest frame.

The maximum energy transfer from the electron to the photon is obtained for $\theta_{in} = \pi$ and $\theta_{sc} = 0$.

$$E = E_0 \frac{1 + \beta}{1 - \beta \cos\theta_{sc}} \quad (3.32)$$

$$E \cong 4\gamma^2 E_0 \quad (3.33)$$

In the opposite case, i.e. the electron and photon moving in the same direction, the photon energy is reduced by a factor $4\gamma^2$. An important consequence is the beaming of the Comptonized radiation which results concentrated within a small cone of semi-aperture $1/\gamma_e$

Inverse Compton from a Single Electron

Inverse Compton scattering only changes the photon energy and leaves the photon number unchanged. Consider a single relativistic electron in a region pervaded by radiation with average energy density U_{rad} and average photon energy $\langle \nu \rangle = \nu_0$. The difference between the electron initial and final energies represents the fraction of energy acquired by the photons. The average electron energy loss (for isotropic radiation field) is:

$$\left\langle \frac{d\nu}{dt} \right\rangle = \frac{4}{3} \sigma_T c U_{rad} \gamma^2 \beta^2 \quad (3.34)$$

The single electron spectrum is composed by a low energy power law $F_\nu \propto \nu^1$ and an high energy exponential cutoff (similar to the synchrotron spectrum) $\propto \exp(-\nu/\nu_0)$. The characteristic energy of this spectrum is:

$$\langle \nu_c \rangle = \frac{4}{3} \gamma^2 \nu_0 \quad (3.35)$$

In fig 3.3 is reported the Compton spectrum emitted by a single electron in a monochromatic radiation field.

Inverse Compton from a population of electrons

For an electron population with a power law energy distribution $N(\gamma) = N_0 \gamma^{-p}$ in a monochromatic and isotropic radiation field, the emissivity due to the Inverse Compton process is:

$$j(\nu_c) = \frac{1}{4\pi} \frac{(4/3)^{\frac{p-1}{2}}}{2} \frac{\sigma_T c N_0 U_{rad}}{\nu_0} \left(\frac{\nu_c}{\nu_0} \right)^{-\frac{(p-1)}{2}}$$

This can be expressed through the source parameters:

- R/c = photon escape time from the region of size R ;
- $\tau_c = \sigma_T N_0 R$ fraction of scattered photons;
- U_r/ϵ_0 = photon number density;
- ϵ_c/ϵ_0 gain per scattering

$$j(\epsilon_c) = \frac{1}{4\pi} \frac{(4/3)^{\frac{p-1}{2}}}{2} \frac{\tau_c}{R/c} \frac{U_r}{\epsilon_0} \left(\frac{\epsilon_c}{\epsilon_0} \right)^{-\frac{(p-1)}{2}} \quad (3.36)$$

this result can be generalized to the case of non-monochromatic radiation field (i.e. extending from $\nu_{0,min}$ to $\nu_{0,max}$):

$$j(\epsilon_c) = \frac{1}{4\pi} \frac{(4/3)^{\frac{p-1}{2}}}{2} \frac{\tau_c}{R/c} \epsilon_c^{-\frac{(p-1)}{2}} \int_{\epsilon_{min}}^{\epsilon_{max}} \frac{U(\epsilon)}{\epsilon} \epsilon^{-\frac{(p-1)}{2}} d\epsilon \quad (3.37)$$

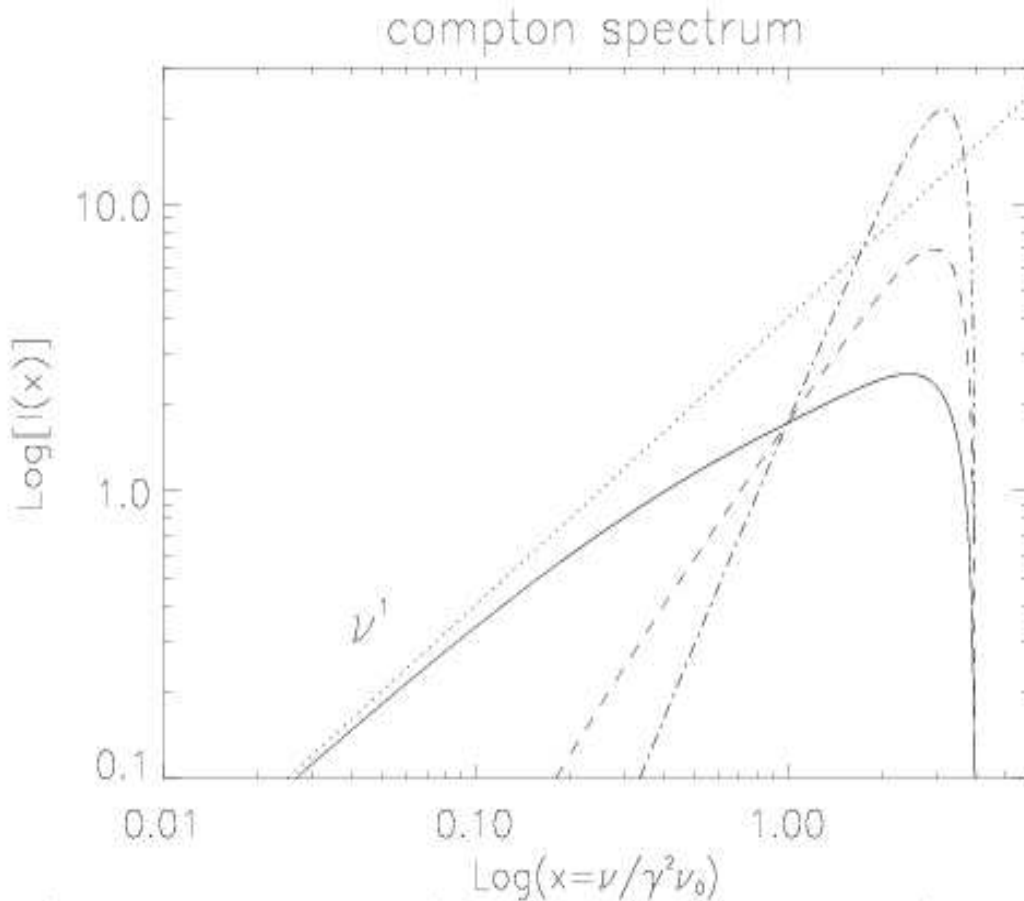


Figure 3.3: Compton spectrum emitted by a single electron in a monochromatic radiation field. *Solid line*: photon spectrum; *dashed line*: energy spectrum; *dot-dashed line*: νF_ν spectrum. Also reported (*dotted line*) the ν^1 slope for comparison.

3.3.2 Comptonization

Comptonization is the multiple Compton scattering of “seed” photons in a region pervaded by electrons. In the simplest case the electron energy distribution is supposed to be thermal. This process is regulated by the *Comptonization parameter* which is the product of the average *number of scatterings* done by photons (which, in turn, depends on the optical depth of the source), and the *mean gain of energy per scattering*. The Comptonization parameter describes the efficiency of Comptonization.

- Gain per scattering

It can be calculated statistically and depends on the optical depth of the source:

- if $\tau_T < 1$ the average number of scatterings is τ_T
- if $\tau_T > 1$ the average number of scatterings is τ_T^2 .

- Average energy gain

This factor depends on the energy distribution of the scattering particles. According to the typical energies of the electrons (relativistic or non-relativistic) there are two possible cases:

- *relativistic thermal electrons*: The energy distribution is a relativistic maxwellian:

$$N(\gamma) \propto \gamma^2 \exp(-\gamma/\theta) \quad (3.38)$$

where $\theta = kT/m_e c^2$. The average energy gain of a photon per Compton scattering is $(4/3)\gamma^2$. The ratio of the photon energy to the electron rest mass energy is $x = h\nu/m_e c^2$, and the average energy gain results

$$\langle x_f \rangle = \frac{4}{3} x_i \langle \gamma^2 \rangle = 16\theta^2 x_i \quad (3.39)$$

where x_i is the initial photon energy and the calculation has been made integrating the first and second order momentum of the electron energy distribution.

- *non relativistic thermal electrons*: the distribution function is:

$$N(\gamma) \propto \gamma \exp(-\gamma/\theta)$$

and in this case the gain is balanced by the energy loss due to direct Compton scattering: the electron, in fact, can also gain energy due to the scattering of a photon whose energy, in the rest frame of the electron, is lower than the electron rest mass energy $m_e c^2$. In the non relativistic case the photon energy gain is proportional to the electron energy θ :

$$\frac{\Delta x}{x} = \frac{x_f - x_i}{x_i} = \alpha\theta - x \quad (3.40)$$

The first term is due to Compton scattering by the electron and the second term is the energy loss of the photon due to direct Compton scattering. The exact calculation of the α parameter gives

$$\frac{\Delta x}{x} = 4\theta - x \quad (3.41)$$

These cases can be expressed in a general formula for the average gain per scattering:

$$\frac{\Delta x}{x} = 16\theta^2 + 4\theta - x \quad (3.42)$$

which characterizes the following situations:

- $\theta = kT/m_e c^2 > 1$ inverse Compton prevails and the average gain per scattering is $\propto 16\theta^2$
- $\theta < 1$, both the direct and inverse Compton are present and compete to determine the final energy gain $\propto 4\theta - x$ (which can also be negative).
- $\theta \ll 1$, only direct Compton is present and the photons loose energy because of electron scattering, $\propto -x$.

Thermal Comptonization: the spectrum

The Comptonization parameter can be expressed in a synthetic form as:

$$Y = \max(\tau_T, \tau_T^2) \cdot (16\theta^2 + 4\theta - x) \quad (3.43)$$

where $\max(\tau_T, \tau_T^2)$ represents the average number of scatterings expressed in terms of the optical depth, and $(16\theta^2 + 4\theta - x)$ is the average energy gain per scattering.

If $Y > 1$ Comptonization shapes the emergent spectrum: the primary effect is the boosting of the seed photon energy E_{peak} at higher values. Also the luminosity is modified according to the value of Y .

- $\tau_T < 1$:
 - if $Y > 1$, i.e efficient Comptonization. The resulting spectrum is boosted in energy by a factor $A = 16\theta^2$ and little reduced in intensity, by a factor τ_T , at each scattering. In this case the spectrum is the convolution of multiple scattered spectra and its shape is $F_\nu \propto \nu^{-\alpha}$, with $\alpha \leq 1$. This situation could be realized in a plasma with very energetic electrons that compensate for the low τ_T .
 - if $Y < 1$, the spectrum is little modified in amplitude and energy, and can be represented by a power law $F_\nu \propto \nu^{-\alpha}$, with $\alpha \geq 1$.
- $\tau_T \geq 1$: *unsaturated Comptonization*.

This case requires the solution of the Kompaneets equation but, in general, the spectrum can be described as a power law $F_\nu \propto \nu^{\alpha(Y)}$ at low energies. There are two regimes:

- $Y \gg 1$, Comptonization is efficient although does not reach saturation. The low energy spectrum is a power law with spectral index:

$$\alpha = \frac{3}{2} + \sqrt{\frac{9}{4} + \frac{4}{Y}} \quad (3.44)$$

followed by a Wien peak $\propto \nu^3 \exp(-\nu)$, at higher energies. In the limit $Y \rightarrow \infty$ the spectrum corresponds to saturated Comptonization with only the Wien peak.

- $Y \ll 1$, the solution of the Kompaneets equation leads to a power law spectral index

$$\alpha = \frac{3}{2} - \sqrt{\frac{9}{4} + \frac{4}{Y}}$$

which is a softer power law ending up with an exponential cut;

- $\tau_T \gg 1$:

- $Y \ll 1$ the spectrum is a blackbody, i.e. $F_\nu \propto \nu^2$ at low energies and modified by a bremsstrahlung spectrum $F_\nu \propto \nu^0$ at high energies.
- $Y \gg 1$, *saturated Comptonization*: it is characterized by the equilibrium between electrons and photons. The resulting spectrum is the Wien form:

$$I_\nu \propto \nu^3 \exp(-\nu) \quad (3.45)$$

which peaks at the equilibrium energy $h\nu_{eq} \sim 3kT$.

- $Y > 1$, *quasi-saturated Comptonization*: not all the soft photons are up-scattered but a fraction remains at low energies constituting a low energy power law $F_\nu \propto \nu^0$ which connects to the high energy Wien peak.

In the following sections the most popular emission models based on Compton mechanism for the GRB prompt radiation are briefly presented .

3.3.3 Compton scattering by flash heated circumstellar clouds

This model, proposed by Dermer et al. [26], combines synchrotron and inverse Compton emission to reproduce the observed GRB spectrum: the synchrotron emission from the internal shock, interacting with the burst environment, determines the observed spectral properties.

The association of GRBs with star formation regions, also substantiated by observations, places the burst in a dense environment constituted by cold molecular clouds, with relative low proper motion (e.g. η Carinae), located at a distance $> 10^{16}$ cm from the center of the star. The typical density and size are $n_c = 1.5 \cdot 10^9 \tau_T / r_{15}$ cm² and $r \sim 10^{15} r_{15}$ cm, respectively. The synchrotron photons produced by the internal shock are responsible, propagating into these clouds, of their ionization and heating.

In its simplest formulation (Dermer et al. [26]) this model considers that the internal shock produces a synchrotron photon flux $\Phi(\nu)$ which can be modeled as:

$$\Phi(\nu) = (4\pi d^2)^{-1} \frac{L}{m_e c^2 \nu_0^2 \chi} \left[\frac{1}{(\nu/\nu_0)^{2/3} + (\nu/\nu_0)^\alpha} \right] \quad (3.46)$$

where ν_0 is the peak energy of the νF_ν spectrum, d is the burst distance, α is the photon spectrum powerlaw index at energies $\nu \geq \nu_0$ and χ is a function of α .

This photon front has a thickness which is small if compared with the cloud width¹ and impinging on the cold cloud, ionizes its elements, from H to Fe, on a timescale $t \sim 10^{-5}$ sec (for typical luminosities and other bursts parameters - Dermer et al. [26])²

¹The front thickness is related to the duration of the burst by $c \cdot \Delta t$ (with $\Delta t \sim 10$ sec) and, for a cloud with a radius $r \sim 10^{15} r_{15}$ cm, it is $\sim 10^4$ smaller than the cloud width.

²In principle the transfer of momentum from the photons to the electrons would have also a dynamical effect on the cloud which should start moving outward, but at the beginning, this can be neglected if one considers the prevailing electrostatic coupling of the electrons with the ions and protons.

The most important effect of the photon flux on the cloud is the Compton up-scattering of the initially cold electrons of the cloud to energies comparable to those of the photons.

Most of the electrons will be up-scattered to keV or MeV energies (corresponding to the photon energies) by the first radiation front³. The successive photons, produced in the internal shock, encounter a hot cloud of electrons which will likely boost these photons to higher energies, reducing the number of soft photons: this is supposed to be the mechanism responsible for the production of arbitrarily hard low energy spectra observed in some GRBs. One possible complication of this mechanism is the pair production: the second or third radiation front, in fact, also find the back-scattered photons and this interaction is an efficient source of pairs⁴. These pairs, anyway, enhance the effect of Compton scattering of the successive photons, making the spectrum even harder. Notice that in this model the cloud optical depth is $\tau_T \sim 1 - 2$.

The typical spectrum, simulated absorbing a synchrotron spectrum through a hot (flash heated) electron scattering medium⁵, with temperatures 100 and 300 keV, is reported in fig 3.4.

From fig.3.4 is evident that the Comptonization of the spectrum by the hot electrons causes a depletion of soft photons making the observed spectrum (histogram in fig.3.4) harder at low energies than the incident photon spectrum (dashed line of fig.3.4). The high energy part of the spectrum is not changed by Comptonization but only by pair production (not included in the simulations), which steepens this spectral component. Notice also that the low energy power law slope is harder for hot and thick absorbers (i.e. $kT_e = 300$ keV and $\tau_T = 2$, *dotted histogram*).

The spectral characteristics predicted by this model are:

- the presence of a second break in the gamma ray spectrum determined by the scattering of soft photons to higher energies in addition to the intrinsic break energy of the GRB;
- spectra with particularly hard X-ray power laws should also have soft MeV components due to the effect of $\gamma\gamma$ photon absorption which is more efficient in this range.

³The successive radiation fronts, produced by internal shocks up-scatter a progressively lower fraction of the cloud electrons due to a lower number of low energy electrons combined with a decrease of the Klein–Nishina cross section with energy.

⁴The main condition for efficient pair production is the compactness of the cloud. For typical GRB luminosities $L_\gamma > 10^{50}$ erg sec⁻¹ and for a cloud located at $d_{16} > 1$ cm and a proper radius of $r_{15} \sim 1$ cm, the cloud is effectively thick for pair production (Dermer et al [27]).

⁵the electron are supposed to have a thermal distribution although the theory would assume a non thermal distribution (but the result should be similar).

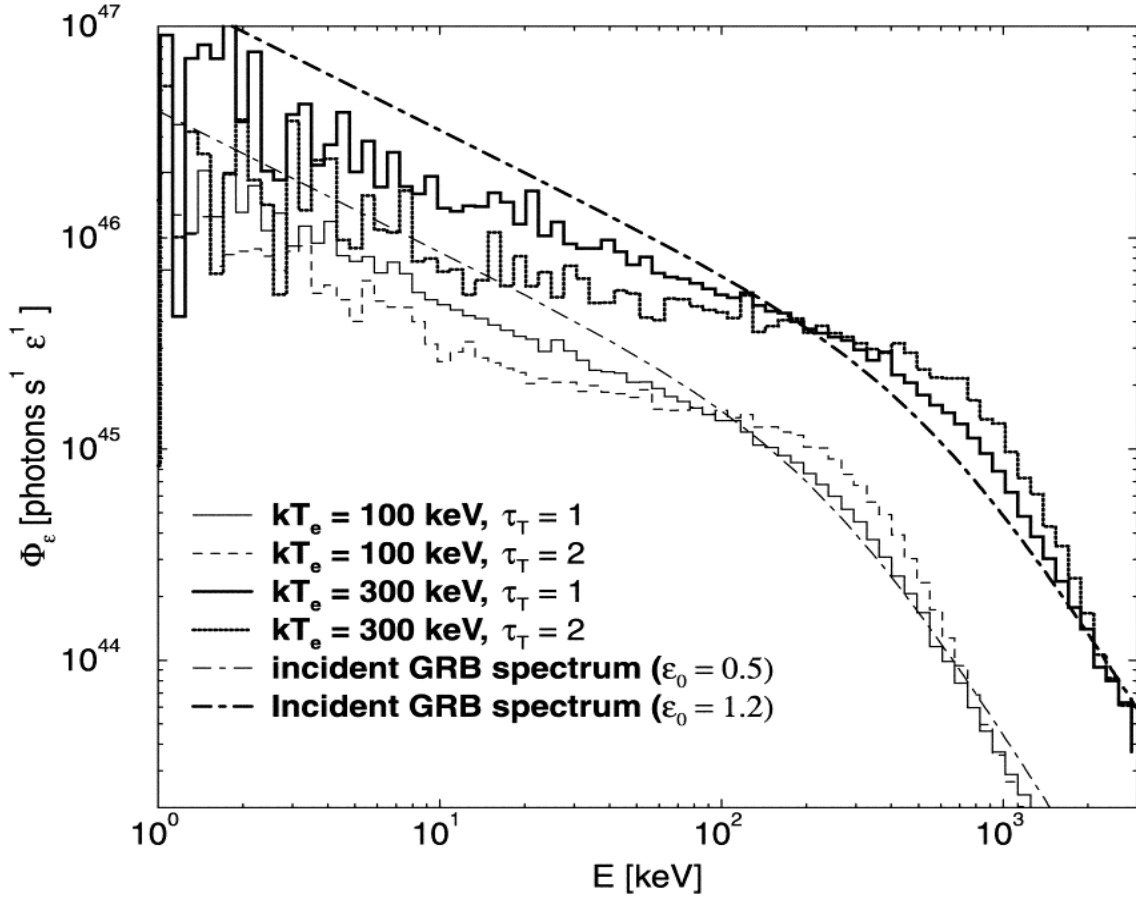


Figure 3.4: Comptonized GRB spectra by flash heated circumburst clouds; from Dermer & Boettcher [27]. The *dot-dashed* lines represent the incident spectrum, supposed to be the optically thin synchrotron emission with high energy spectral index $\beta = -2.2$, low energy slope $-2/3$ and two different peak energies $E_{peak} = 0.5m_e c^2$ and $1.2m_e c^2$, for the thin and thick line, respectively. The Comptonized spectra for different electron energies and opacities are represented by the histograms.

3.3.4 Compton Attenuation Model

This is not properly an emission process but it was proposed (Brainerd [12]) to reproduce the observed low energy spectral shape and the peak energy value and narrow distribution observed in GRBs (see sec.2.4.2). It consists in the attenuation of the burst spectrum by the interstellar medium, which is optically thick to Compton scattering. In particular the energy dependence of the Klein–Nishina cross section σ_{KN} is thought to be responsible for shaping the burst observed spectrum.

Assuming that the source of photons produces a simple power law unabsorbed spectrum, e.g. $F(\nu) \propto \nu^{-\delta}$, the attenuation can be modeled as:

$$F_\nu(obs) = F_\nu \exp \left[- \left(\tau_T(t) \frac{\sigma_{KN}}{\sigma_T} + \tau_T(t) \frac{\sigma_{ph}}{\sigma_T} \right) \right] \quad (3.47)$$

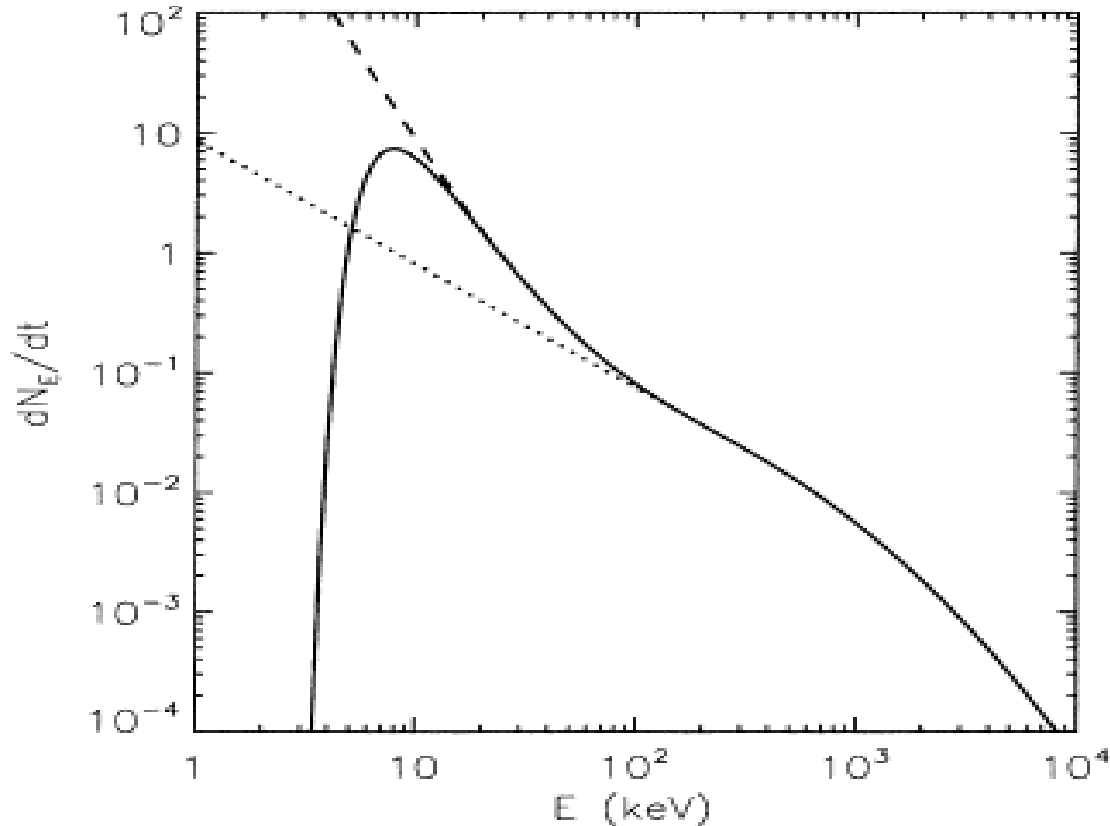


Figure 3.5: Compton attenuated spectrum (from Brainerd et al. 1998 ApJ 501, 325 fig.1 p.327). The incident non-absorbed power law spectrum (evident only in the high energy part of the solid line) has a spectral index $\delta = -3$, the redshift is $z=0$. The solid line represents the observed spectrum and the dotted line the incident spectrum absorbed only by the Compton process.

where σ_{ph} is the photoelectric absorption cross section. Notice that the optical depth $\tau_T(t)$ is modified by the same radiation which is absorbed.

The rapid decrease of the photoelectric absorption above 20–30 keV ensures that the spectrum observed in the BATSE band should be produced by Compton scattering, whereas, if a broad band (X-ray to γ -ray) spectrum would be available, both effects should become evident.

The spectrum resulting from the absorption of a power law spectrum by a cold medium, reported in fig.3.5, is composed by the same power law at high energies and by a harder low energy power law (dotted line in fig.3.5) due to the absorption of the soft photons. The 50–500 keV break produced by the Klein–Nishina cross section is independent of the matter bulk Lorentz factor and only depends on the optical depth, redshift and source spectrum.

The soft X-ray excess should be detectable with a broad band (e.g. BATSE and SAX–WFC) spectrum, unless the burst is at high redshift so that the the energy at which the

photoelectric effect prevails over the Compton attenuation lies below the lower end of the observing energy range (e.g. for $z > 2$ this energy is < 77 keV).

The main requirements of the Compton attenuation model is that the absorbing material is far enough from the source so that the photon density is low and the $\gamma - \gamma$ pair production has a low efficiency. A low pair production can be achieved if the ISM absorbing medium lies at a distance greater than 0.04 pc.

Notice that this model relates the observed spectral properties of GRBs to their environment. A possible consequence, which has not been investigated, is the possibility to reproduce the observed hard to soft spectral evolution by the modification of the opacity of the absorbing material by the same radiation. In fact, a small cloud can be optically thinned by the burst radiation, also over a single subpulse evolution, and, as a consequence, the hard-to-soft spectral evolution would be determined by optical thinning of the cloud itself.

3.3.5 Saturated Compton Cooling

This model was first proposed by Liang ([94]) to interpret the observed exponential decay of the peak energy, of the νF_ν spectrum, with photon fluence (defined as $\Phi = \int F_N dt$). It assumes that the observed emission results from Comptonization in saturated regime, i.e. equal average particles and photons energy.

The energy flux F_E (erg/cm² sec) corresponding to a shell with bulk Lorentz factor Γ and luminosity L' (in the comoving frame) for a burst at a distance d is:

$$F_E = \frac{L'\Gamma^2}{4\pi d^2} \quad (3.48)$$

If N' is the number density of the emitting particles, the average comoving energy loss $d\langle E' \rangle / dt'$ is related to the luminosity:

$$N' \frac{d\langle E' \rangle}{dt'} = -L' \quad (3.49)$$

If these particles loose their energy through multiple Compton scattering in saturated regime (i.e. $\langle E' \rangle \simeq \langle h\nu' \rangle$) the above equations can be combined,

$$N' \frac{d\langle E' \rangle}{dt'} = -\frac{4\pi d^2 F_E}{\Gamma^2} \quad (3.50)$$

and, with the saturation condition expressed in the comoving frame (i.e. $\langle E' \rangle = \langle h\nu \rangle / \Gamma$),

$$\frac{d(\ln[\langle h\nu \rangle])}{dt} = -\frac{8\pi d^2 F_N}{N'} \quad (3.51)$$

where the relation $F_E = \langle h\nu \rangle F_N$ has been used. Integration over time gives the experimental relation found by Liang et al. ([94]):

$$\langle \nu \rangle \propto \exp(-\Phi / \Phi_0) \quad (3.52)$$

with

$$\Phi_0 = \frac{N'}{8\pi d^2}$$

The saturated Comptonization model can justify the observed exponential decay of E_{peak} as a function of time and also the extremely hard low energy early time spectra observed in some GRBs.

From this model it is possible to derive (Liang [97]) some constraints on the radius of the shells and on the bulk Lorentz factor Γ . From the definition of optical depth ($\tau_T = n'\sigma_T R$ where n' is the particle comoving number density) follows that:

$$N' = \tau_T \frac{4\pi R^2}{\sigma_T} \quad (3.53)$$

where R is the comoving shell size. From the expression of Φ_0

$$\frac{d}{R} = 10^{12} \left(\frac{\tau_T}{\Phi_0} \right)^{1/2}$$

The variability argument (Fenimore et al. [35]) prescribes that the maximum light path difference from different points of the detectable source is $\Delta R \leq c\Delta t$. Δt is assumed to be ~ 1 sec as if each pulse, in the GRB light curve, would be produced by a single energization and cooling episode with no re-acceleration⁶. In this picture the maximum light path difference from a spherical shell of radius R at a distance d from the observer, subtending an angle $\theta = 1/\Gamma$, is $\Delta R = R(1 - \cos\theta) \sim R/2\Gamma^2$. This sets an upper limit on the size of the shell

$$R \leq \Gamma^2 \times 6 \cdot 10^{10} \text{ cm} \quad (3.54)$$

and on the distance to the source

$$d \leq \Gamma^2 6 \times 10^{22} \left(\frac{\tau_T}{\Phi_0} \right)^{1/2} \quad (3.55)$$

Considering a typical distance of 1 Gpc, a lower limit on the shell bulk Lorentz factor is

$$\Gamma \geq 224 d_{Gpc}^{1/2} \left(\frac{\tau_T}{\Phi_0} \right)^{-1/4} \quad (3.56)$$

This lower limit on Γ implies that, for an observed peak energy of the order of some hundred keV, the comoving peak energy is of few keV and, due to the saturated Comptonization regime, the particle distribution is thermal with, eventually, only a small non thermal tail.

An example of a Comptonized spectrum simulated with different optical depth is reported in fig.6.5.

⁶Re-acceleration would produce, in the late pulses, an increase of the pulse width due to the shell expansion and this was not observed in multi-peaked bursts.

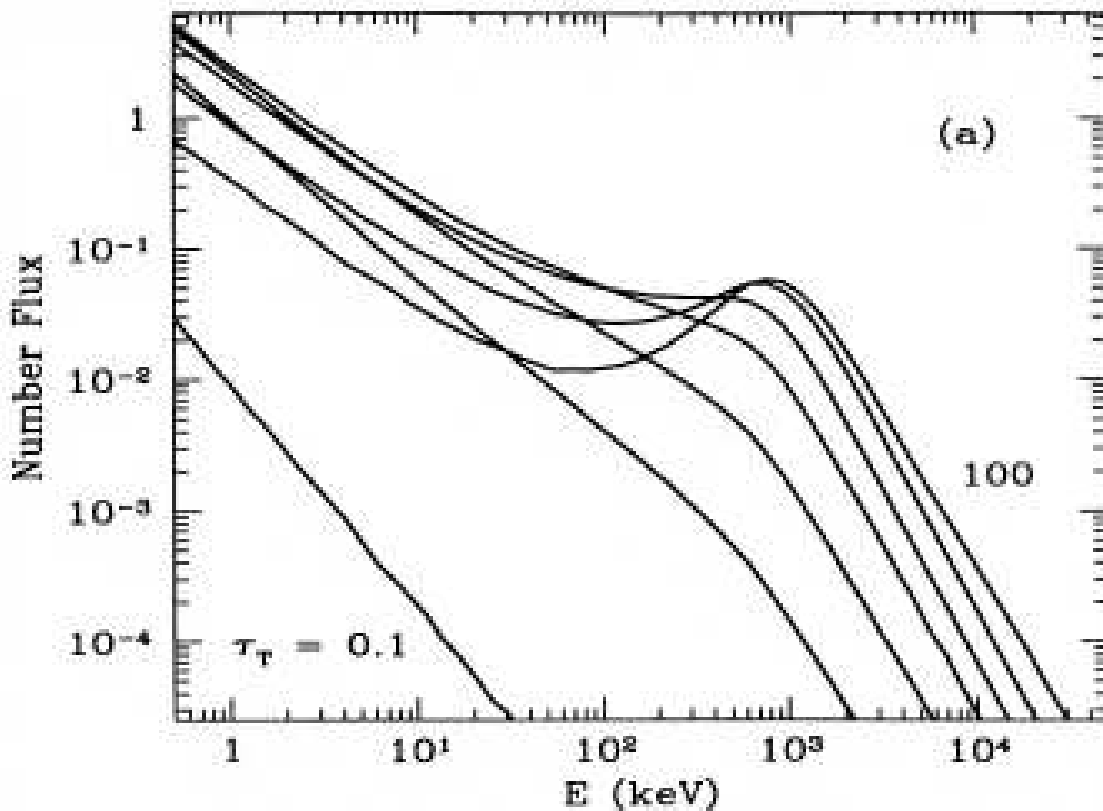


Figure 3.6: Comptonization of a soft synchrotron spectrum from a gas of electrons in a sphere of radius 10^8 cm with a power law energy distribution of index $p=2.5$ between $\gamma_{min} < \gamma < 1000$ in a uniform magnetic field of 1 G. The optical depth is $\tau_T = 0.1, 1.2, 4, 8, 25, 100$. From Liang et al. [96]

3.3.6 Quasi-Thermal Comptonization

This model, proposed by Ghisellini & Celotti ([55]), is based on saturated Comptonization, but it is formulated starting from the basic assumption of equipartition: this is a typical assumption of the shock status which is supposed to share its internal energy among the various components of the plasma, i.e. the electrons, the protons and the magnetic field. This assumption imposes some demanding constraints if applied in the context of the standard synchrotron model (Ghisellini et al. [57]), but it is instead consistent with Comptonization by non relativistic electrons with a quasi-thermal energy distribution. The difference, with respect to the standard Comptonization model, is the assumption of the equipartition values for the magnetic field B and particle energies.

One problem related to the application of the synchrotron model is that it requires that the acceleration timescale of the electrons (the heating time) be much smaller than the cooling time, otherwise the final random energy of the particle would be controlled

by its cooling rate and not by the equipartition condition. The quasi-thermal Comptonization model relaxes this condition though it conserves the equipartition of the shock internal energy between particles and magnetic field.

Assume that 2 shells with a comoving width and separation ΔR cross each other (due to the difference of their Lorentz factors) and produce the shock. The shell-shell interaction timescale is of the order of $\Delta R/c$. The maximum energy that can be transferred to the electrons is $m_p c^2 n_p/n_e$ (in the comoving frame). The total heating rate, in a shell crossing timescale, is:

$$\dot{E}_{heat} = \frac{m_p c^3 n_p}{\Delta R} \quad (3.57)$$

The cooling rate, due to synchrotron and Compton, can be expressed as

$$U_r \dot{E}_{cool} = P_{syn} + P_{comp}$$

where U_r is the radiation density, and then

$$\dot{E}_{cool} = \frac{4}{3} n_e \sigma_T c U_r \gamma^2 \beta^2 \left(1 + \frac{U_B}{U_r}\right) \quad (3.58)$$

and U_B is the magnetic field energy density. The balance between heating and cooling gives

$$\gamma^2 \beta^2 \sim \frac{3m_p c^3 n_p}{4n_e \sigma_T c U_r \left(1 + \frac{U_B}{U_r}\right)} = \frac{3\pi R^2 m_p c^3 n_p}{\Delta R n_e \sigma_T L \left(1 + \frac{U_B}{U_r}\right)} \quad (3.59)$$

and introducing the compactness parameter

$$l = \frac{L \sigma_T \Delta R}{R m_e c^3 R}$$

it becomes

$$\gamma^2 \beta^2 \sim \frac{n_p m_p}{n_e m_e} \frac{1}{1 + U_B/U_r} \frac{3\pi}{l} \quad (3.60)$$

Thus the particles, for typical compactness, will be moderately relativistic, at most, and their distribution will be quasi-thermal (they won't have time to thermalize) but will be still characterized by a peculiar energy. The main consequences of this result is that the synchrotron emission (self-absorbed) is concentrated at low energies and it provides the seed photons on which multiple Compton scattering can act. The typical spectrum is composed by a low $F(\nu) \propto \nu^0$ portion while the small optical depth prevent the formation of an evident Wien peak at higher energies.

In this model a key role can be played by the pairs: in fact the temperature can be regulated by the pair production which, if efficiently working, can increase the optical depth on one hand and decrease the temperature on the other, thus maintaining the electron characteristic temperature sub-relativistic.

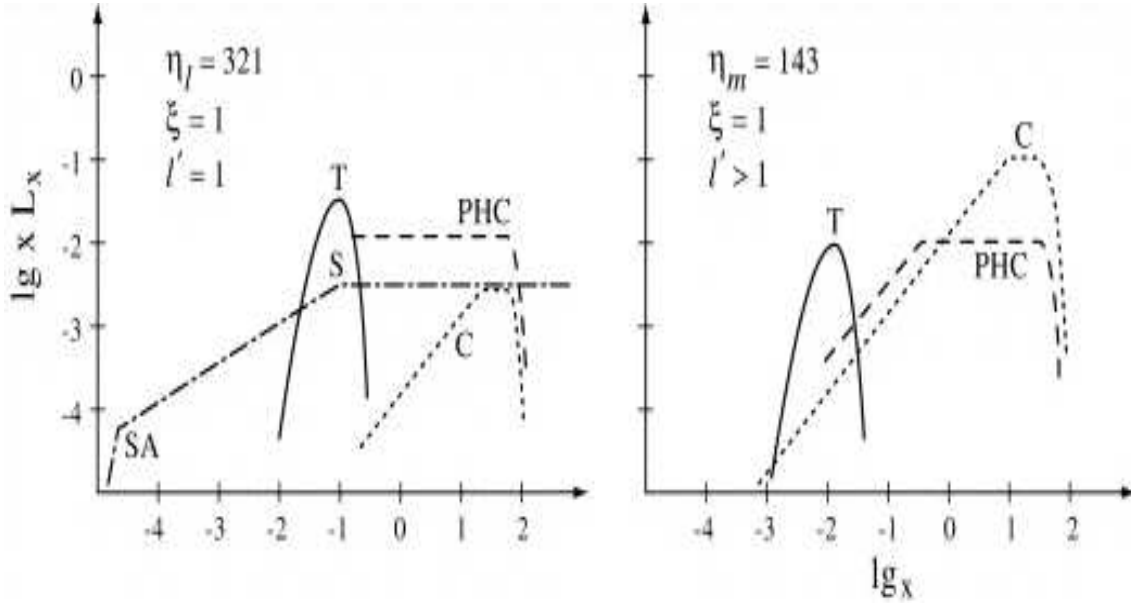


Figure 3.7: Two example spectra arising from the photosphere model in arbitrary units (from Meszaros & Rees [113]). The *solid line* represents the thermal photosphere, *dashed line* is the comptonization of this thermal component, *dotted line* is the Compton contribution and *dot-dashed line* is the synchrotron self absorption.

3.3.7 Photosphere

Comptonization needs a seed photon source, at low energies, to produce the observed spectrum. Meszaros & Rees ([113]), propose that an important component of the observed GRB spectrum might be the Comptonized thermal emission of the photosphere.

The fireball evolution depends on its baryon loading, parametrized with $\eta = L/\dot{M}c^2$, and on the radius at which the photosphere becomes transparent. If the fireball becomes optically thin below the saturation radius (i.e $\eta > \eta_*$ - in the acceleration phase), then its spectrum would be characterized by a thermal peak corresponding to the black body spectrum of the photosphere (solid line in fig.3.7); if the region is also highly compact there will be a second component due to the Comptonization of these thermal photons (dashed line in fig.3.7). If the thick/thin transition occurs in the coasting phase ($\eta < \eta_*$) and for small compactness of the region, the photosphere black body component is at the low end of the BATSE energy window, contributing to the low energy hard spectrum with its Rayleigh-Jeans part, whereas the Comptonization of its photons contributes with a component which can be as hard as $F_\nu \propto \nu^0$ and then becomes $\propto \nu^{-1}$. In this case, without considering the superposition of different spectra or the possibility to integrate the spectral component from different regions of the photosphere, the low energy spectral component (thermal photosphere) has a limiting slope $\propto \nu^2$, but at higher energies the spectral slope predicted by the model is between 0 and -1. Two cases in arbitrary units showing the different spectral contribution are presented in fig.3.7.

The thermal emission from the fireball was a natural prediction of the standard model although its absence in most of the observed GRB spectra led to the formulation of the internal shock model as a plausible source of non-thermal photons. Recently Daigne & Mochovitch (2002) have explored the possible appearance of a thermal spectrum in the initial burst phases (a precursor) from a theoretical point of view in the context of the fireball scenario. We will show and discuss in chapt.6 the observational evidences that we have found from the data analysis which show the presence of photospheric spectrum dominating the first seconds of the emission of some bursts.

3.3.8 Compton Drag

Another mechanism which can produce the observed γ ray spectral features and avoid the problem of accelerating particles and producing intense magnetic fields, is Compton Drag (Lazzati et al. [90]). This model is more than a simple emission process in the sense that it relates the burst to its source and to its environment. It is based on the Inverse Compton up-scattering of soft photons due to the bulk expansion (with Lorentz factor $\Gamma \gg 1$) of the relativistic plasma ejected by the central engine. Lazzati et al. [90] postulate the source of soft (seed) photons to be a supernova.

In the simplest formulation the supernova explosion should always precede the burst of some hours in order to produce a dense radiation field which can then be dragged by the ejecta. A plausible variant which allows the burst to be simultaneous to the SNe is the scenario in which the relativistic ejecta flow in a quasi-clean funnel, which is full of photons, created by a bow shock following the core collapse event. In this case the thermal blackbody spectrum of the supernova is boosted in temperature to produce a spectrum peaked at an energy of the order of $E_{peak} \propto \Gamma^2 T_{SN}$ ⁷. The resulting spectral shape should be a black body. The real spectrum can be reproduced relaxing the basic assumption of a perfectly homogeneous wind and an isothermal radiation field.

Ghisellini et al. ([56]) calculated the spectrum produced by the propagation of the ejecta (the fireball) with Lorentz factor $\Gamma(r)$ in a funnel whose walls emit a multi-temperature blackbody spectrum, constituting the seed photon spectrum which is dragged by the fireball, with a temperature profile $\propto r^{-b}$. They consider the most realistic case including the effect of the gradient in temperature between the internal and external parts of the funnel, the deceleration of the fireball (i.e Γ decreases with the distance from the source) due to the efficient drag of the photons, the interaction of the boosted photons with the ambient radiation which produces pairs (i.e. an extra opacity factor) and, finally the thick/thin transition which can occur far from the funnel where the photon density can be very low and the Compton drag less efficient. All these effect can,

⁷The energy is more precisely expressed as

$$E \sim \frac{1}{2} \Gamma_2^2 T_5 \frac{1}{(1+z)}$$

where $\Gamma_2 = \Gamma/10^2$ and $T_5 = T/10^5$ K.

in principle, reproduce a spectrum which is very similar to the observed one. Its main features are:

- a high energy tail produced by the Compton drag of the innermost photons, i.e. those filling the volume space between the radius at which the fireball acceleration ends r_0 and the distance r_d corresponding to its deceleration due to the efficient Compton drag. Its analytical approximation (neglecting the photon–photon opacity) is

$$E(x) \propto x^{-(3-3b)/b} \quad (3.61)$$

where $x = h\nu/m_e c^2$ and for $b=0.5$ it results $E(x) \propto x^{-3}$ (in $\text{erg/cm}^2 \text{ sec keV}$);

- a harder power law component produced by the drag of photons distributed between r_d and the top of the funnel r_* (above which the seed photons retain the temperature of the SN surface)

$$E(x) \propto x^{-3\frac{(1-b)}{(6-7b)}} \quad (3.62)$$

which, for $b=0.5$, is $\propto x^{-3/5}$.

- a third component produced by the Compton drag of the isothermal photon field (i.e. a blackbody with the same temperature of the top of the funnel) which fills the volume between r_* and r_T (i.e. the distance at which the fireball becomes optically thin)

$$E(x) \propto x^{-1/2} \quad (3.63)$$

- finally, the hardest part of the spectrum (at low energies) which is produced by the Compton drag (with a low efficiency at distances $r > r_T$) of the ambient photons by the fireball with a final low and constant Lorentz factor:

$$E(x) \propto x^2$$

It should be mentioned that the Compton drag model supports the formation of internal shocks because after the first fireball has expanded and decelerates significantly because of the dragging of the soft ambient photons, the subsequent ejecta can collide with it and produce internal shocks. Then an extra radiation source is plausible to become effective after the first seconds since the explosion and could also be an explanation for the hard to soft spectral evolution: the first second spectrum ($\propto \nu^2$) is due to Compton Drag and is hard at low energies, whereas at later times the spectrum produced by the internal shock through synchrotron or Comptonization is responsible for the softer ($\propto \nu^{1/3}$ or $\propto \nu^0$) component.

Chapter 4

BATSE and the spectral data analysis

The spectral and temporal analysis of GRBs developed, since their discovery, in connection with the advances in the detector design. The improved spectral and temporal resolution of BATSE have led to the characterization of the spectral properties of bursts and of their spectral evolution.

In the following sections the BATSE instrument and its spectral data are described. In particular, the detailed analysis of a burst is reported as an example of the procedure adopted in the spectral study of the GRBs discussed in the following chapters.

4.1 From the Vela satellites to CGRO

The first Gamma Ray Burst was recorded by the *Vela 4A* and *4B* satellites on July 2, 1967. The Vela missions detected 16 gamma ray flashes in the energy range 150–750 keV from June 1969 to July 1972; and recorded 73 bursts until April 1979.

These instruments were flown by the Advanced Research Projects of the U.S. Department of Defense and the U.S. Atomic Energy Commission to monitor the respect of the Nuclear Test Ban Treaty, but they gave important results in astrophysics.

The *Vela 5A*, *5B* and *Vela 6A*, *6B* [84]) were equipped with an All Sky X-ray scintillation Monitor sensible in the 3 – 12 keV range and a set of 6 gamma ray detectors of CsI operating in the range 150–750 keV. The Gamma Ray detectors had an on board triggering system based on continuous monitoring of the count rate for the detection of any statistically significant increase of the γ ray signal above the background.

These instruments were not equipped with an active anti-coincidence shielding system (like most gamma ray detectors) which can distinguish between a high energy photon and a cosmic ray trigger. They recorded 16 events which were robustly classified as GRBs due to their non solar origin and simultaneous detection by different detectors.

Another satellite which detected GRBs was the Solar Maximum Mission (SMM) launched in 1980 for the study of the solar cycle. Its payload included a Gamma Ray Spectrometer (GRS) designed for the investigation of the solar spectrum in the energy range 0.3–9.0 MeV with a time resolution of ~ 16 sec, and an Hard X-Ray Burst Spectrometer (HXRBS) with a geometrical area of ~ 69 cm² sensible to photons of energy 30–500 keV. The GRS detected 75 bursts until 1989 and the HXRBS only 15 due to night time Earth pointing.

Two dedicated gamma ray burst detectors were flown in 1980–1983: KONUS 11 and 12. These quasi omni-directional gamma ray burst monitors collected spectra in the range 30 keV to 2 MeV with maximum time resolution of 0.02 sec. These instruments detected 141 GRBs in 3 years of activity.

From 1978 to 1992 the Pioneer Venus Orbit (PVO), dedicated to the study of Venus and its atmosphere, was equipped with gamma ray detectors sensitive in the energy range 100–2000 keV. PVO revealed 225 GRBs with a uniform spatial distribution.

4.1.1 The Compton Gamma Ray Observatory

The Compton Gamma Ray Observatory (CGRO) was the second NASA’s “great observatory” mission after the Hubble Space Telescope and was launched in 1991. It was de-orbited in June 2000 due to the failure of one of its gyroscopes. This satellite was equipped with 4 main instruments and represented, during its 9 years activity, a unique high energy flying laboratory for the study of galactic and extra galactic diffuse and localized emission in the soft-to-hard gamma ray band from 10 keV to 30 GeV. Its main scientific objectives were the study of solar flares and gamma ray bursts, the analysis of the temporal properties of gamma ray pulsars, the study of nova and supernova explosions and accreting black holes and the interactions of cosmic rays with the interstellar medium.

The instruments composing the CGRO were: the Energetic Gamma Ray Experiment Telescope (EGRET), the Imaging Compton Telescope (COMPTEL), the Oriented Scintillation Spectrometer Experiment (OSSE) and the Burst and Transient Source Experiment (BATSE) which will be described in more details in the following sections.

1. EGRET was a combination of a spark chamber and a calorimeter for the reconstruction of the photons arrival directions and for their energy measurement. Its operating energy range was from 20 MeV to 30 GeV with a position dependent field of view. This instrument performed an all-sky survey of the diffuse and discrete gamma ray emission: 5 new gamma ray pulsars were discovered in our galaxy, the blazars class of object received a great impulse due to the analysis of their spectrum in the 30 MeV – 30 GeV range and they were also found to vary on timescales of days. EGRET also measured the high energy photons of 5 gamma ray burst (with a maximum energy of 18 GeV for GRB940217, also observed by

COMPTEL, Winkler et al. [161]) and the diffuse gamma emission of our galaxy which is produced by the interaction of cosmic rays with the ISM.

2. COMPTEL was composed by 7 liquid-filled scintillators and a crystal NaI(Tl) system. The system provided reconstructed images and spectra of sources in the range 0.8–30 MeV. The main findings of COMPTEL are the line map of ^{26}Al , tracing the sites of recent star nucleosynthesis, the observation of 31 GRBs and 32 steady sources, the insight into the acceleration mechanism operating in solar flares through the observation of fast variability on small timescales, the ^{57}Co emission from SN 1987A .
3. OSSE was an orientable scintillator for observations of sources in the 0.05–10 MeV energy range. This instrument detected the annihilation radiation of positron and electrons in the ISM within our galaxy, collected the spectra of some blazars and Seyfert galaxies with spectral breaks in the range 100–200 keV and revealed the hard X-ray continuum in SN 1993J.

4.2 The Burst and Transient Source Experiment

The Burst And Transient Source Experiment (BATSE) was designed for the detection, location, spectral and temporal analysis of Gamma Ray Bursts. During the 9 year of activity of the CGRO (21/04/1991 - 4/06/2000) its main results were:

- isotropic angular distribution of gamma ray bursts;
- non-uniform flux distribution of GRBs;
- statistical diversity of Gamma Ray Bursts temporal and spectral properties;
- bursting of pulsar GRO J1744-28
- X-ray transient in Scorpius (GRO J1655-40) and correlation between X-ray properties and radio jets;
- discovery of new X-ray pulsars and long term light curves.
- discovery of gamma-ray flashes produced by atmospheric thunderstorms.

Among the other results, BATSE produced a huge catalog of gamma ray bursts with more than 2700 events (updated at 26 May 2000).

4.2.1 Technical characteristics

BATSE was an all-sky viewing instrument composed by eight modules arranged on the corners of the CGRO. Each module (fig.4.1) contained 2 scintillation detectors: the Large Area Detector (LAD) optimized for sensitivity and directional response, and the Spectroscopic Detector (SD) optimized for broad band energy coverage and high resolution spectral analysis.

The LAD consisted of a thin (1.27 cm of thickness) circular ($\emptyset=50.8$ cm of diameter) layer of scintillation material (NaI) which converts the incident photon flux in optical light, afterwards collimated onto three photomultipliers and processed through a PHA analyzer. The system was provided with a front anticoincidence plastic layer, to reduce the charged particle background, and with an inside lead coated collector, to prevent contamination from back and side scattering ¹. The sensitive area of the LAD is 2025 cm² and it has a good sensitivity from 30 keV to 1.9 MeV; the location error is on average of 2 degrees with a systematic error (to be added in quadrature) of 1.6 deg, and the fluence sensitivity is 3×10^8 erg/cm² for a 1 sec burst. The energy resolution of the LAD was 27% at 88 keV and 20% at 511 keV and it remained quite stable in orbit [71]. Due to their large effective area, the LAD data are suited for time resolved spectral analysis of bright and dim bursts and for variability studies.

The Spectroscopic Detector (SD) provided high energy resolution spectra (due to its large thickness=7.62 cm) for the brightest bursts (small collecting area, 127 cm²). It consisted of a circular ($\emptyset = 12.7$ cm) uncollimated NaI(Tl) scintillation detector viewed by a single PMT, placed in a passive lead/tin shield coated housing. The crystal has a front beryllium window to provide high sensitivity down to 10 keV, for quite normal incident photons. The SD nominal energy range was between 10 keV and 100 MeV, depending on the operational ground control settings. The data products of the SD are suited for spectral evolution studies of bright bursts with an unprecedented energy resolution ² and for line search and variability studies.

4.2.2 The trigger method

High resolution GRB data were accumulated only in response to a burst trigger. In the usual configuration the count rates in at least 2 detectors integrated from 50 to 300 keV were required to increase, above a running background average, by an amount that is specified in terms of the standard deviation of the expected background counts (σ) in each detector. The count rates were tested, independently, on three integration time intervals: 64 ms, 256 ms and 1024 ms. The background was estimated over a fixed time interval (actually set at 17.4 sec) and, if the discriminator rates in channels 2 and 3 ($\sim 50 - 300$ keV) were 5.5σ above the averaged background count rate, a trigger signal was produced. There was an additional condition for the burst to pass the trigger control

¹<http://coss.gsfc.nasa.gov/coss/batse/4Bcatalog/4b_{basic}.html>

²Goddard Space Flight Center - guest investigator manual

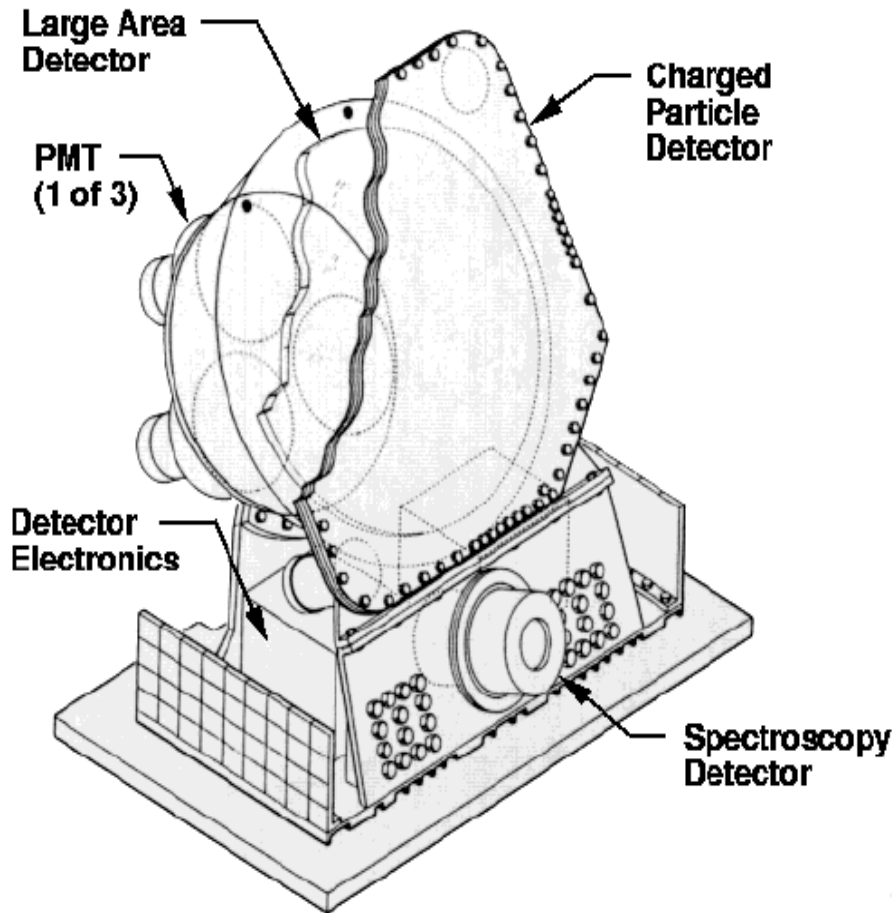


Figure 4.1: One of the eight modules composing BATSE. The LAD and SD detectors are indicated.

sequence: the detector with the highest signal should have a charged particle count rate less than a fraction of the neutral rate, in order to discard any event caused by charged particle showers interacting with the crystal.

When the on-board trigger criteria were satisfied, the Central Electronic Unit (CEU) started data storage with high temporal and spectral resolution for the “accumulation period”, which typically lasted from 180 to 573 seconds. Following the accumulation period there was a read-out interval of the burst memory which was transmitted to the ground, lasting from 28 minutes to 90 minutes.

The monitored count rates, the energy thresholds and detector combinations, which define the trigger criterion, were programmable so that the available burst catalogs have not uniform detection conditions. The number of triggers present in the final BATSE burst catalog is more than 2700 but this number can be increased if the non triggered bursts are included (Kommers et al. [85]): the scanning of the continuous data accumu-

lated by the instruments revealed 873 non-triggered GRBs which increase of 48% the BATSE sample, and 50 low energy bursts (25–50 keV) (possibly the equivalent of the population of X Ray Flashes recently discovered in the SAX data (Kippen et al. [82]).

4.3 Data Products

The BATSE daily data products were stored and transmitted every orbit to the Marshall Space Flight Center (MSFC). These data are grouped in 3 classes:

- *Burst Data*: contains the data relative to any trigger generated by a Gamma Ray Burst, solar flare or any other transient event satisfying the trigger condition.
- *Scheduled Data*: pulsar observations. It was performed if no trigger occurred during the observation, because the burst accumulation mode has the highest priority.
- *Background Data*: consist of continuously collected discriminator rates and medium resolution spectra of the background.

4.3.1 Burst Data

These data are used for temporal and spectral analysis of GRBs:

- **DISCSC** *Discriminator Science Data* - count rates, on 64 ms timescale, binned in 4 broad energy channels, summed from the LADs that were triggered by the GRB. These data cover the entire burst duration with a maximum time delay, with respect to the trigger time, of 64 ms. The energy ranges are approximately: ch1=25–50 keV, ch2=50–110 keV, ch3=110–320 keV and ch4>320 keV.
- **PREB** - *Pre-Burst data* - the eight LADs store continuously their data (4 energy channels, with 64 ms resolution) in a cyclic ring buffer. When a burst trigger occurs the buffer is read out and the data stored as PREB starting 2.048 s before the burst.
- **DISCLB** - *Discriminator Data* - these are collected to compensate the possible data gaps in DISCSC or DISCLA These data have 2.048 s time resolution for 16.384 s before the burst trigger, and 1.024 s time resolution for 49.154 s after the trigger time.
- **TTE** - *Time Tagged Events* - are obtained assigning to each photon event (for a total of 32768) the time of detection, the energy channel and the detector number. Combining this information the light curve in counts/sec with a time resolution of 2 ms in the usual 4 energy bands can be obtained. These data can be used to perform temporal and time resolved spectral analysis with a very high time

resolution but are limited to short bursts, due to the maximum number of events they can detect. In fact, one fourth of the total memory capacity is filled with the signal from all the eight LADs, for a variable time prior the burst trigger, and in the remaining three fourth are stored the counts, during the trigger, until the buffer is full.

- **STTE** - *Spectroscopy Time Tagged Event* - these are equivalent to the TTE data, but refer to the Spectroscopic Detectors (SDs) and have a higher spectral resolution (256 channels). They have a maximum memory capacity of 16384 counts and a limited time resolution of 128ms. These data can be used jointly with SHERB to accumulate the spectra on a portion of the burst (typically the rise phase) with a user-defined time integration scheme.
- **TTS** - *Time To Spill* - These data are used to set the times for the accumulation of a certain number of events from a LAD discriminator. Their temporal resolution is variable, also within the same data set, and they have 4 broad energy channels.
- **MER** - *Medium Energy Resolution* - 4096 spectra from the LADs (summed over the triggered detectors), accumulated in 16 energy channels with a time resolution of 16 ms, for the first 2048 spectra, and 64 ms for the remaining ones.
- **HERB** - *High Energy Resolution Burst* - burst data from the LADs, on 128 energy channels, with an accumulation time that is rate dependent (so that brighter bursts have higher time resolution than faint ones). The maximum time resolution is 64 ms. The data are gathered from the four most illuminated detectors.
- **SHERB** - *Spectroscopic High Energy Resolution Burst* - The same of HERB but these are collected from the SDs and consists of 256 channels energy spectra with maximum time resolution of 128 ms for a maximum of 192 spectra.

These data are first quickly analyzed by the BATSE mission team, and then stored in *Individual Burst Data Base* (IBDB). For the temporal and spectral analysis they are converted into FITS format.

4.3.2 Burst Data Files

The data files used for the spectral evolution analysis of GRBs can be downloaded from the Goddard Space Flight Center (GSFC) ftp site³ ; each trigger directory contains all the relevant data and calibration files for spectral and temporal analysis.

The burst location algorithm sometimes did not produce the best location at first run: there are cases for which the position determination has been refined during extensive data processing and the correct position for all the bursts are now available. The use of a precise position measure is required by the data reduction procedure because of the

³<ftp://coss.c.gsfc.nasa.gov/compton/data/batse/trigger>

dependence of the detector response matrix on the angle of incidence of the photons with respect to the detector normal [125],[128],[3].

The triggered events are classified according to the event type: Gamma Ray Bursts, Solar Flare, Soft Gamma Ray Repeater (SGR), Terrestrial Gamma Flash (TGF). Most of the files within each directory are in Flexible Image Transport System (*.fits*) format, first proposed by [160], and then recommended as a standard format for satellite data by the Commission 5 at the 1982 General Assembly of IAU (IAU, Inf. Bull. No.49, 1983),[65].

4.4 GRB960924 - A case study

In this section the analysis of the LAD and SD data for GRB 960924 is presented, as an example. The choice of this burst is motivated by the good quality of the data, due to the extremely high signal-to-noise ratio.

The scientific interpretation of the results of the spectral analysis of GRB960924 will be presented in chapt.7 together with the other bright bursts selected from the BATSE archive.

The basic characteristics of GRB960924 are:

- RA=37°.28, Dec=2°.7, rms=1°.53;
- the peak count rate on different timescales was $C_{max}(64 \text{ ms})=3204 \text{ cts}$, $C_{max}(256 \text{ ms})=11976 \text{ cts}$ and $C_{max}(1024 \text{ ms})=40241 \text{ cts}$;
- the duration was $T_{90\%} = 5.312 \pm 0.091$, calculated from $t=7.74 \text{ s}$ to $t=13.052 \text{ s}$;
- the 4 channel fluences: $F_{ch1} = 1.36 \cdot 10^{-5} \pm 3.8 \cdot 10^{-8} \text{ erg/cm}^2$, $F_{ch2} = 2.16 \cdot 10^{-5} \pm 5.05 \cdot 10^{-8} \text{ erg/cm}^2$, $F_{ch3} = 8.67 \cdot 10^{-5} \pm 1.48 \cdot 10^{-7} \text{ erg/cm}^2$, $F_{ch4} = 1.38 \cdot 10^{-4} \pm 8.72 \cdot 10^{-7} \text{ erg/cm}^2$;
- the photon peak flux on the three timescales: $P(64ms) = 183.3 \pm 1.6 \text{ phot/cm}^2 \text{ sec}$, $P(256ms) = 181.6 \pm 0.8 \text{ phot/cm}^2 \text{ sec}$, $P(1024ms) = 163.3 \pm 0.3 \text{ phot/cm}^2 \text{ sec}$

The light curves, in the 4 broad LAD energy ranges, are reported in fig.4.2. Channel 3 is characterized by the highest count rate if compared with the other 3 energy channels, and this indicates that the burst spectrum likely peaks in the corresponding 110–320 keV energy range.

The duration of the emission is energy dependent (as a GRBs general property, e.g. [34]), being shorter with increasing energy. The light curve obtained summing the count rates from the 4 energy channels is reported in fig.4.3. GRB 960924 has fast rise followed by a slow decay over which possible overlapping substructures could be identified. The LAD and SD spectral data of this burst are considered here to show the main steps of the data reduction and analysis procedure.

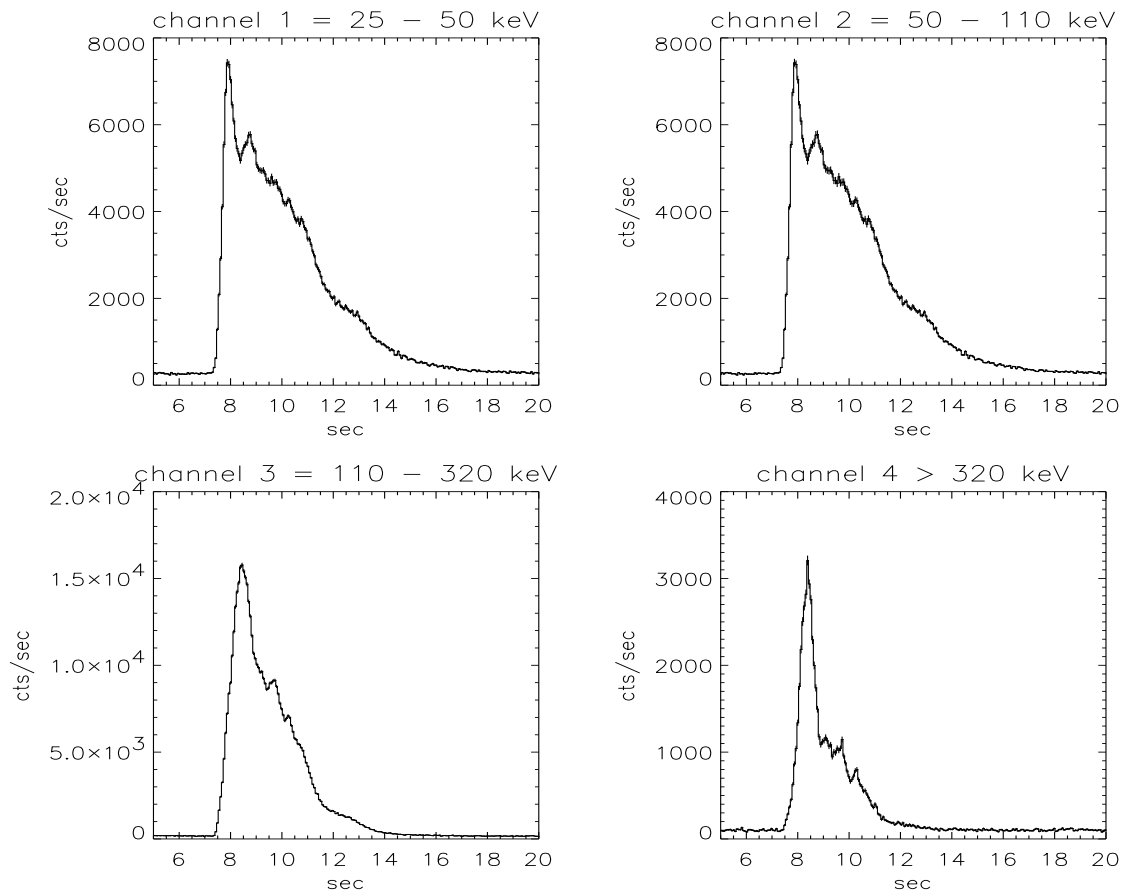


Figure 4.2: Light Curves of GRB960924 accumulated from the 4 LAD modules which were triggered by the burst (n.6,4,7,3) in the 4 energy channels described in the text.

The report file (*report_ibdb_5614.txt*) contains the basic informations about the burst (location and energy thresholds) necessary for the choice of the detector whose data are analyzed

During the trigger, the 4 most illuminated LAD and SD (number 6,4,7 and 3) accumulated the spectral data. The first crucial step in the data reduction procedure is the choice of the detector whose data are used for the study of the burst.

The spectral evolution analysis requires: (1) a good S/N in each spectrum in order to fit a model spectrum and derive, with an acceptable accuracy, the spectral parameters which describe its temporal change; (2) a high temporal resolution in order to follow the spectral variations on timescales of the order of the the variability timescale of the light curve. These two elements are in competition because sometimes consecutive time-resolved spectra need to be summed together to raise the S/N and perform an accurate fit, despite the loss of fine temporal variations. Another element (3) which enters in the data analysis is the detector response matrix: it describes the sensitivity of the detector as a function of the number and of the energy of the incoming photons. For a good

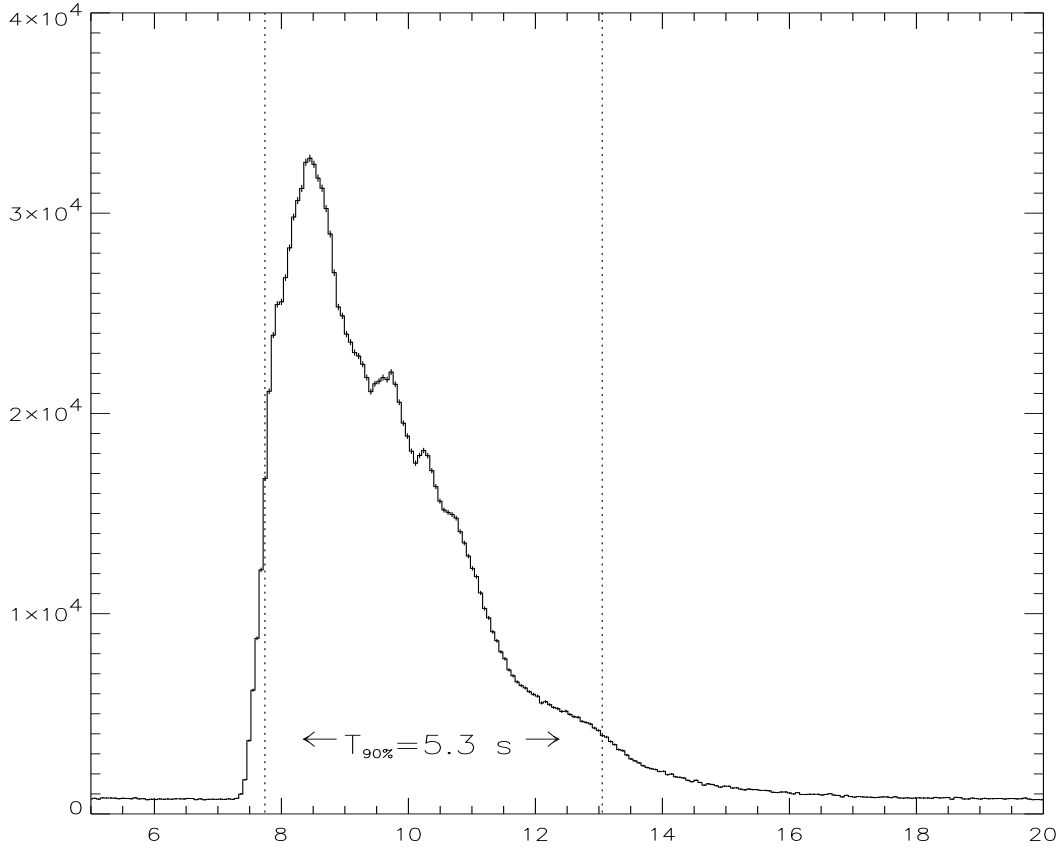


Figure 4.3: Light curve of GRB960924 summed over all the triggered detectors and accumulated from the 4 energy channels.

data analysis it should have a constant profile over the widest spectral range in order to detect the photons homogeneously.

From the operative point of view, there are three technical issues associated with the above requirements: the detector rank of illumination, the calibration line centroid and the source position.

The rank of the illumination represents the degree of photon flux on each detector. This in turn depends, among other operational parameters like energy thresholds and the detector photon conversion gain, on the source position with respect to the satellite coordinate system. The first order detector (i.e. number 6 in the case of GRB 960924) is the most aligned with the source and has the best S/N and the highest temporal resolution (because the integration time algorithm is determined by the statistics). The second and third rank detector have a time resolution which is twice and 4 times the minimum integration time of the first rank detector.

In fig. 4.4 is reported the spectrum, accumulated around the peak of the light curve, for different detectors: LAD 6 and LAD 3 (black and red crosses) and SD 6 and 3 (green

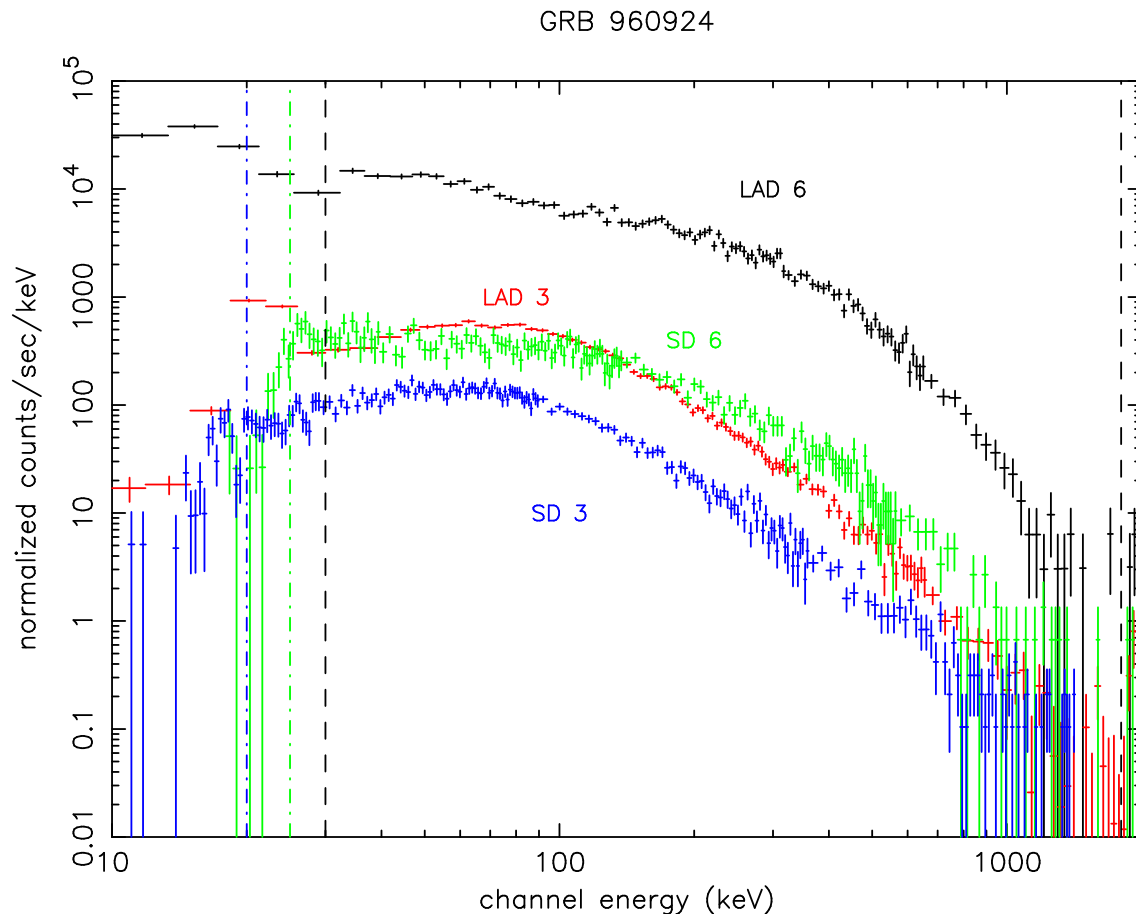


Figure 4.4: Peak spectrum of GRB 960924 accumulated by different detectors. The Large Area Detector 6 (the first rank detector) and the 3 (the fourth rank) are represented by the black and red crosses respectively. The Spectroscopic Detector (6 and 3) spectrum is represented by the green and blue points. The dot-dashed vertical lines represent the low energy boundary of the SD spectral energy range which depends from the gain of the SD.

and blue crosses). These spectra are not background subtracted but it is evident that the spectrum from the most illuminated detector (i.e. number 6) has the highest S/N over almost the entire energy range both for the LAD and SD. It should also be mentioned that SD 3 spectrum extends at very low energies because this detector was operated at the highest gain (see below). The first 10 channels of the SD spectrum are unusable because of nonlinearities in the PHA output [130]. These spectra are cut between 10 keV and 30 keV. The lower level threshold for the LAD data is even higher, limiting the energy coverage to 28 - 1800 keV.

The LAD were gain stabilized during the mission, whereas the gain of the SD was varied. Thus, when analyzing Spectroscopic Data, the gain settings should be considered in the choice of the detector: a higher gain implies a wider spectra coverage, especially at low energies.

Most of the calibrations were performed using the 511 keV line as reference. In fig.4.5 are reported the detection of this line by 3 different LAD and SD detectors (6,7,3) obtained from the calibration file for GRB 960924. From this plot it is evident that the

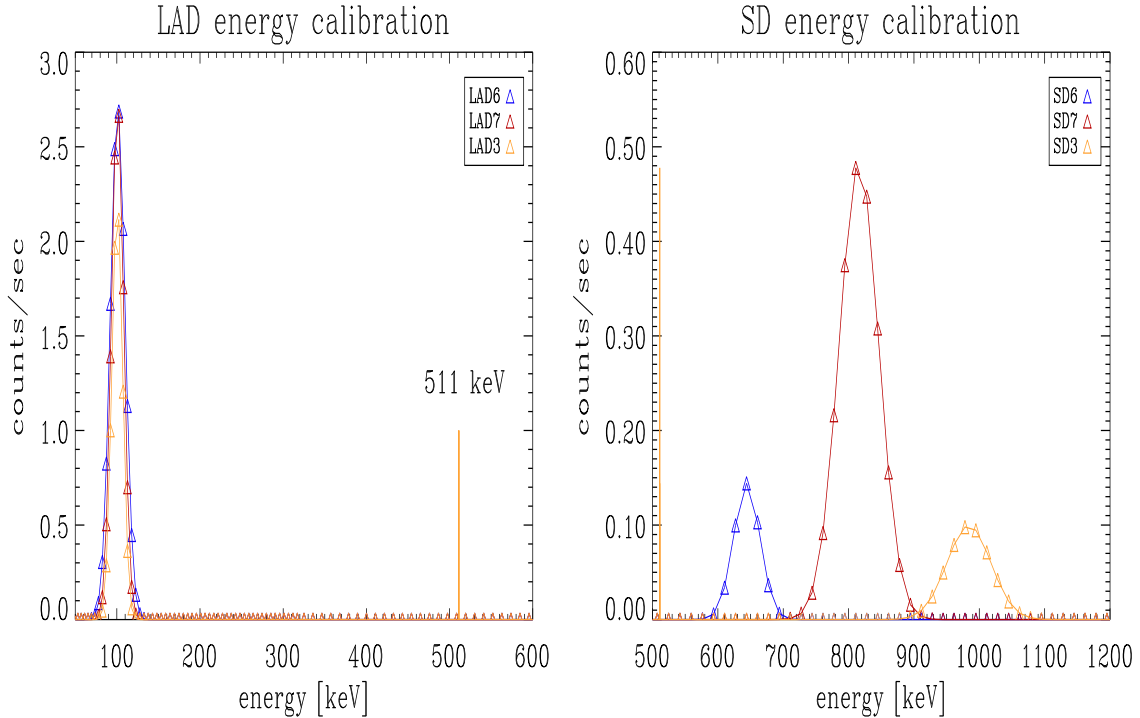


Figure 4.5: LAD and SD energy calibration lines. The set of calibration refers to detector 6 (red), 7 (green) and 3 (blue) which, in terms of illumination, correspond to the 1st, 3rd and 4th rank detectors for GRB 960924.

LAD modules were gain stabilized whereas in the case of the SD the relative centroid of the calibration line is determined by the gain at which the PMT, viewing the detector, is operated. In general, a line centroid at high energies is determined by a high gain of the detector which, in turn, extends the low energy boundary of the spectra below 20 keV for the SD. SD 7 should be chosen for its high gain but this detector, being the 3rd rank, has a low S/N if compared to the first and second rank, so that the analysis of the low energy extension of the spectrum is limited by a low S/N. SD 6 is preferred for the spectral analysis because of its high S/N. As a general rule for the study of the bursts presented in this work, the first and second rank detectors were considered equivalent in the choice of the data provided that their calibration line centroid is above uncompressed channel 800.

The last parameter that determines the choice of the detector is the angle of the source with respect to the detector axis. The detector response matrix (DRM), which is used for deconvolution of the observed spectra, has an efficiency which depends on the angle of incidence of the photons. If the burst position is highly off-axis for the chosen detector the response can be less efficient and a lower rank detector should be considered.

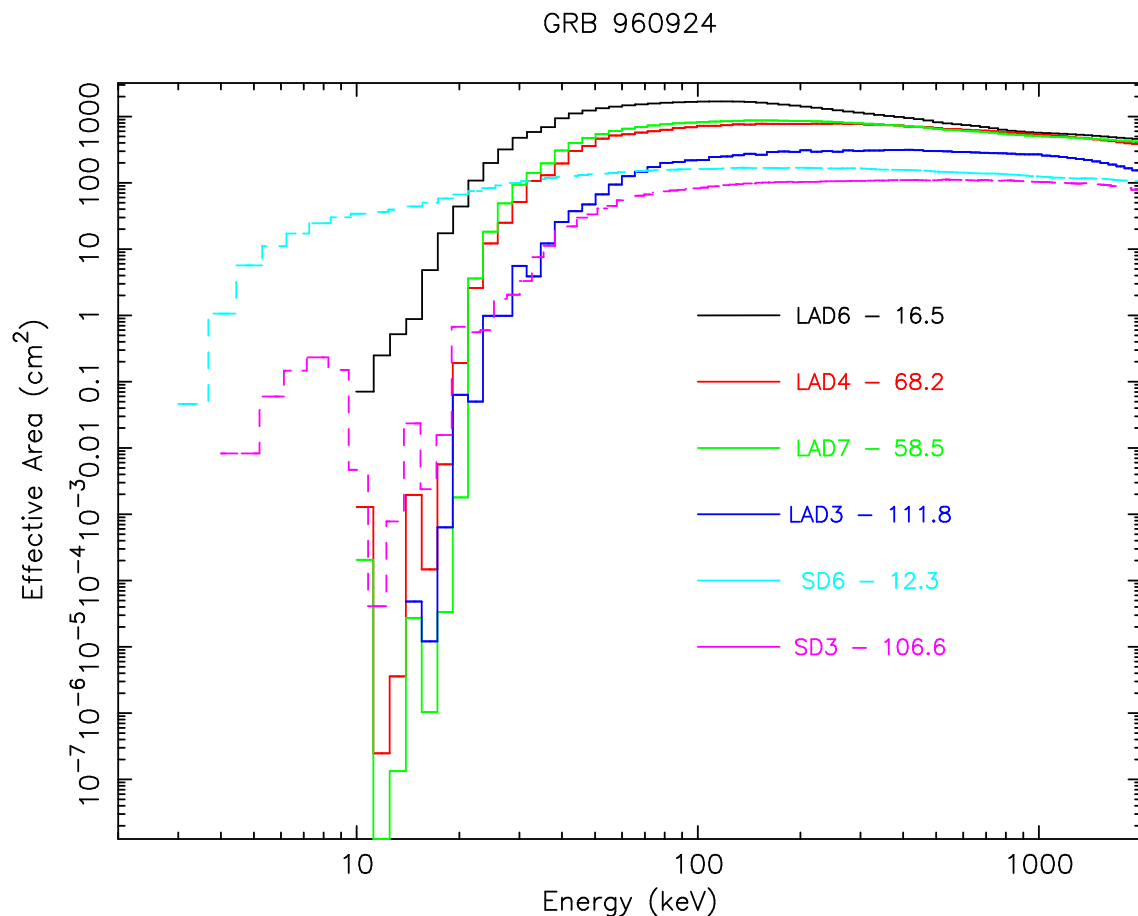


Figure 4.6: Response efficiency expressed as effective area for LADs and SDs. In the legend are also indicated the angles between the source position and the detector normal in degrees.

The detector response efficiency, represented by the effective area, is reported in fig.4.6 for different detectors in the case of GRB 960924. The first rank LAD and SD (black and light blue lines) has the highest efficiency because it almost is constant from low to high energies. In general we assume an upper limit of 85 degrees for the selection of the detector number, for SD data. In conclusion, the best choice would be: detector 6 for the LAD data, and detector 6 or 4 (which is the second rank detector with a zenith angle lower than 85 degrees). It should be noticed that the angular tolerance is anyway high because the scattering off the atmosphere raises the count of the LAD with small angles to the burst, but each SD have a tilt angle of 15 degrees with respect to the LAD axis (Band D., *Private Communication*).

In the following sections the spectral data, as they are accumulated by the detectors, are presented together with the basic operations for the extraction of the spectral information.

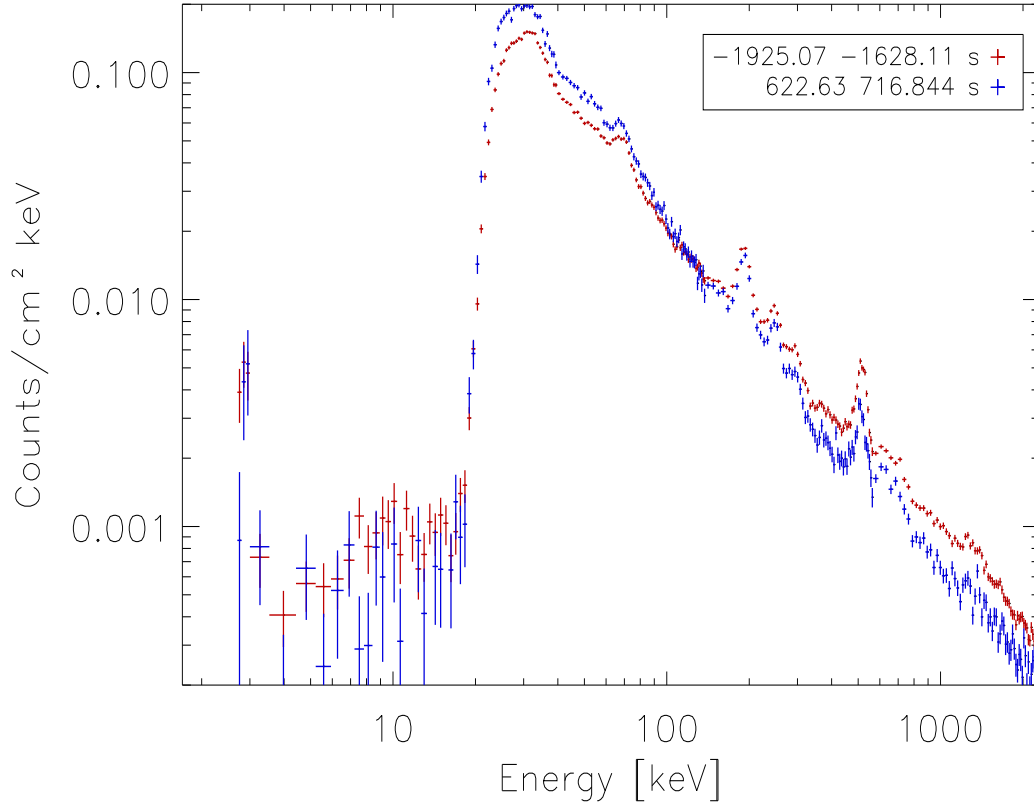


Figure 4.7: Typical SHERB background spectra: two examples of spectra before and after the trigger time. The integration times are referred to the trigger time.

4.4.1 SD and LAD data analysis

The Spectroscopic High Energy Burst file (SHERB) contains a sequence of 109 spectra covering a period of ~ 3400 sec before and after the burst (used for the background calculation) and the time $t = 7 - 13$ sec containing the burst. Fig.4.7 presents two examples of SD spectra as they were accumulated by the detector, for a generic background period before and after the trigger. Notice some features: the NaI K-edge which produces a slope change in the spectrum between 30 and 40 keV, the 511 keV electron positron annihilation line and 4 main activation lines at $\sim 68, 200, 300, 600, 1100$ keV [128]

From fig.4.7 is also evident that some low energy channels shouldn't be included in the spectral analysis because they suffer from instrumental contaminations: the best choice is to start considering the spectrum from ~ 30 keV.

Two example spectra of the LAD are reported in fig.4.8. The comparison with fig.4.7 shows that the LAD have a lower energy resolution but a higher S/N ratio over their energy range, which is typically from 30 keV to 1800 keV.

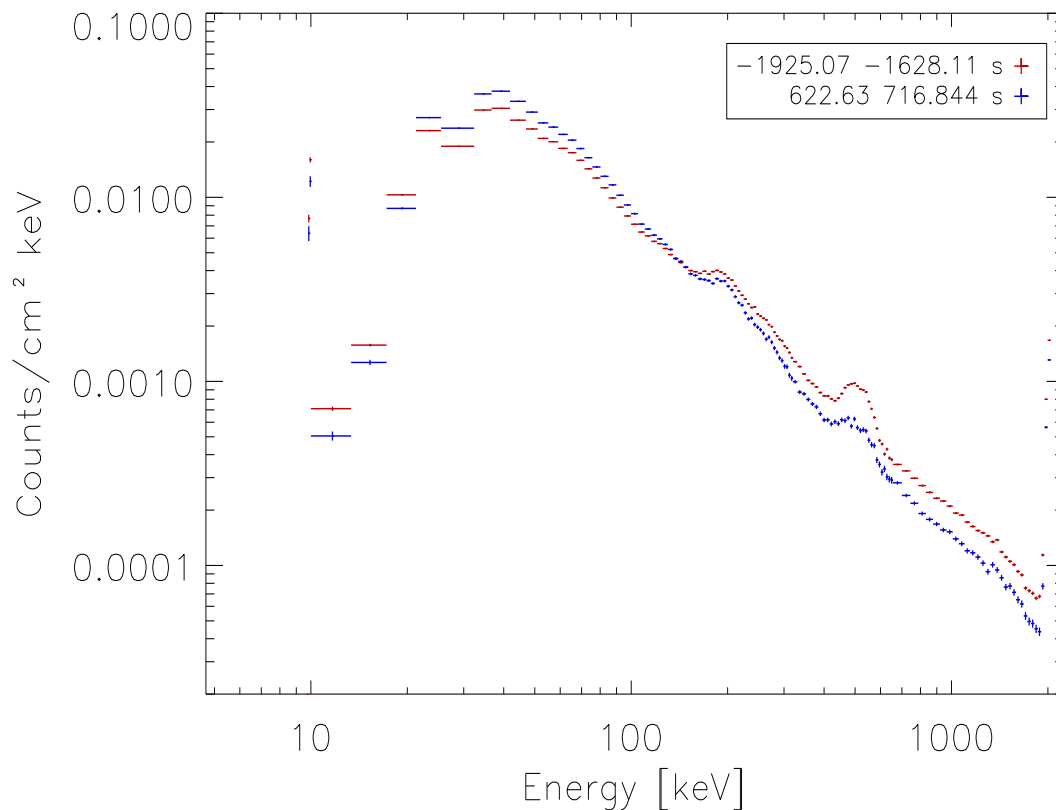
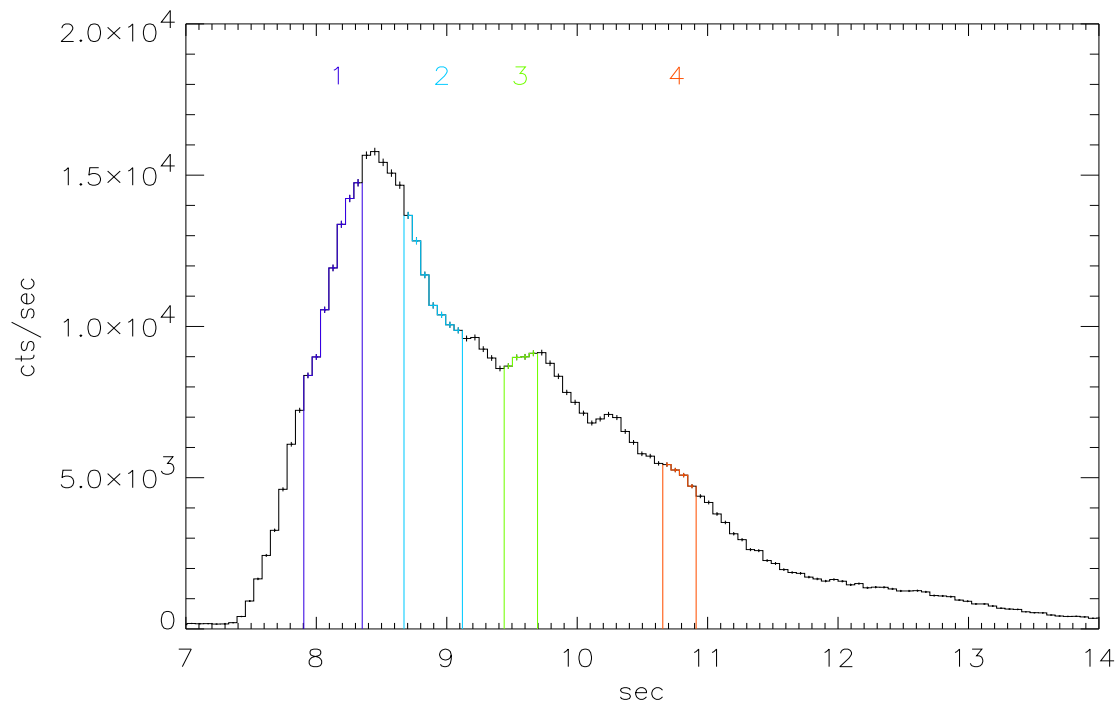


Figure 4.8: Typical HERB background spectra: two examples of spectra before and after the trigger time. The integration times are referred to the trigger time.

Fig.4.9 describes the basic idea of the spectral evolution analysis: the light curve is divided in consecutive temporal slices and the corresponding spectra are added together obtaining a sequence of “time resolved” spectra. This nomenclature is still maintained, although a bit inadequate, to distinguish the spectra accumulated on short period of the light curve (“time resolved”) from the spectrum integrated over the duration of the burst (time integrated). Notice that the single spectra (*bottom panel* of fig.4.9), accumulated at different times on the light curve describe the evolution of the flux: the green spectrum belongs to the decay phase of the burst and has a lower integrated flux than the blue spectrum which is taken during the rise phase of the flux. In this example the time integration intervals were chosen arbitrarily but in the spectral analysis a homogeneous criterion for the temporal accumulation of the spectra was applied (chapt. 5). From this example it becomes evident that the study of the spectral evolution of the burst and the comparison of the evolutionary patterns among different bursts is a fundamental tool for associating the burst temporal and spectral properties.



LAD 6

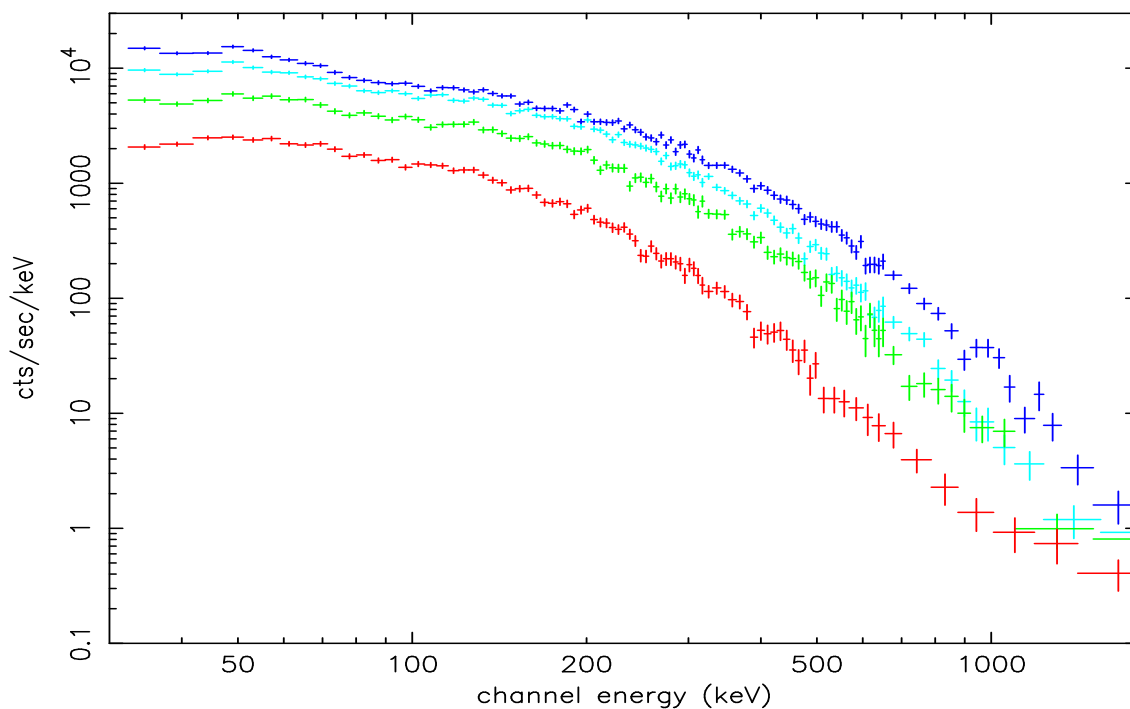


Figure 4.9: GRB960924. *Top panel:* light curve on the 64 ms timescale with the time interval for the accumulations of the 4 example spectra reported in *bottom panel*. The spectral accumulation times are 0.384 s (light and dark blue crosses) and 1.92 s (green and red crosses), respectively.

Background calculation

The spectra accumulated from the instrument are the sum of the source spectrum and of the background. Moreover, some permanent calibration features are present in the instrument spectrum.

For the BATSE bursts the background has been calculated choosing a time interval around the burst which is not contaminated by the burst emission. The background is obtained fitting the spectra, in the specified temporal interval, with a polynomial of 4th order. The fit is performed channel by channel on the sequence of selected spectra and its residuals are inspected for the acceptance of the fit (i.e. non systematic trends in the residuals). A final best fit background spectrum is extrapolated in the time interval of the burst.

In fig.4.10 (from Preece et al. [130]) it is reported a typical HER background spectrum and the different component that can be used to model it: there is a low energy thermal continuum combined with an high energy power law, and the different spectral lines at 68, ~ 200 and 511 keV. In this case-study we choose, for the background calculation, the time

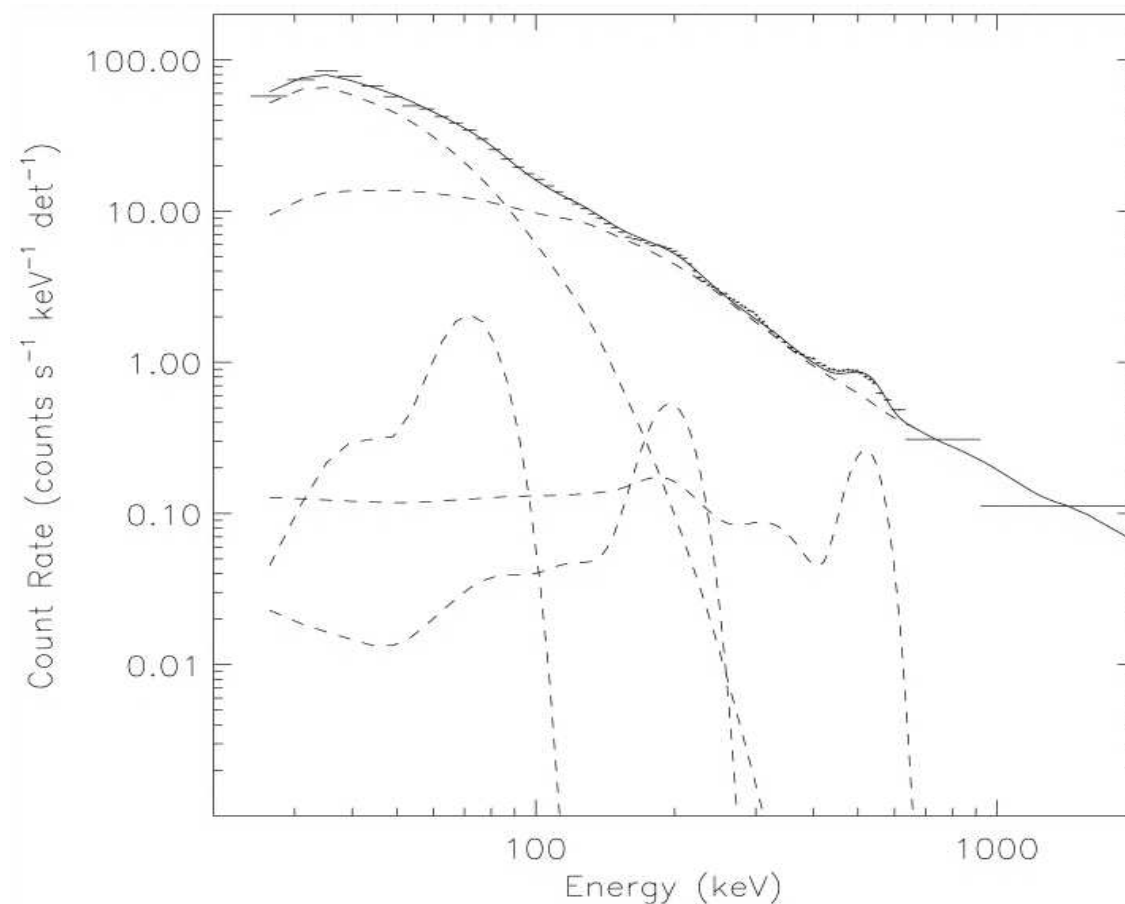


Figure 4.10: Typical HER background spectrum from TJD 10459 with five model component (dashed lines). From Preece et al. [130]

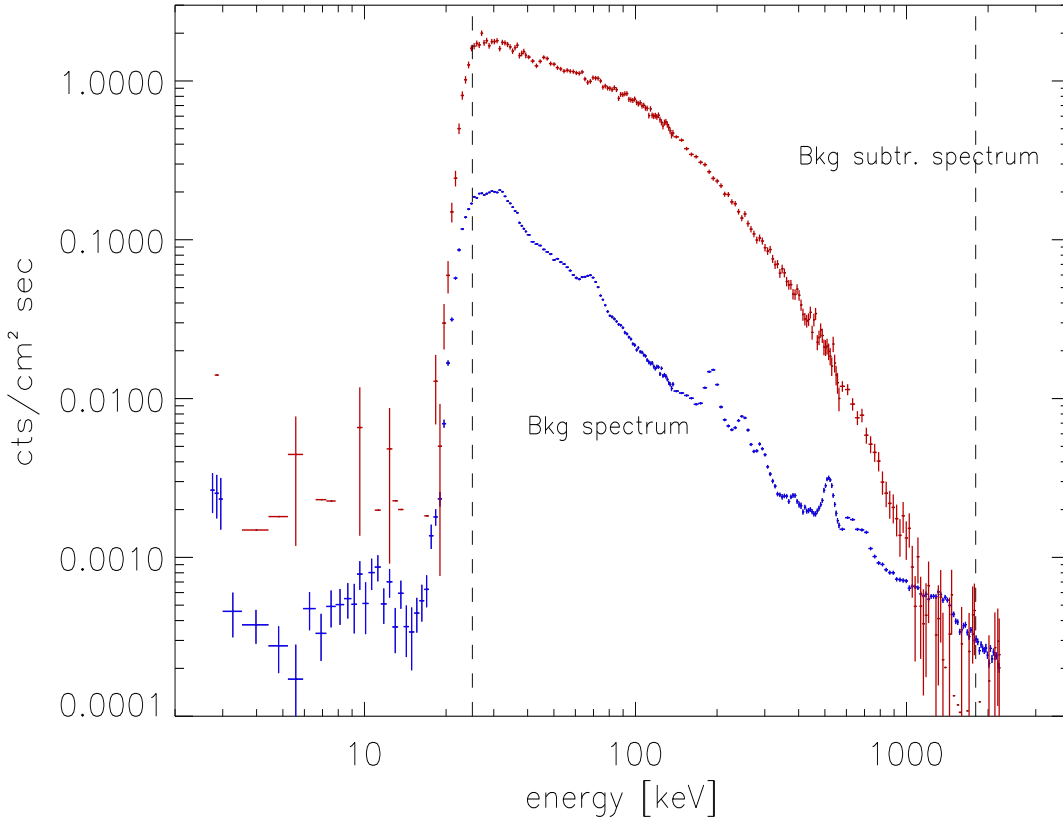


Figure 4.11: Burst time integrated spectrum (from 7.36 to 13.696 sec) background subtracted (red crosses) from SD 6. The background extrapolated spectrum is represented by the blue points.

intervals of about 2000 s centered around the burst (i.e. [-2000,0] and [200,2000]), and the energy range, over which the background is fitted is from 30 to 2000 keV. In this interval there are 32 spectra which are fitted with a 4th order polynomial. In fig.4.11 are reported the spectrum of the burst averaged over its duration and background corrected (red), and the fitted background spectrum (blue) extrapolated to the time interval occupied by the burst.

From fig.4.11 it is evident that the spectrum presents some problems in the high energy channels where the signal of gamma photons is very low, but when fitted with any emission model these channels are important for guiding the fitting routine in determining the high energy spectral tail and so they are not eliminated but weighted for their large statistical errors. The shaded vertical lines indicate the standard energy thresholds within which the spectral analysis is performed.

Fig.4.12 represents the background subtracted average spectrum of the burst together with the corresponding interpolated background from LAD 6. The higher S/N of the LAD (compared to the spectroscopic detectors) is preferred for time resolved spectral

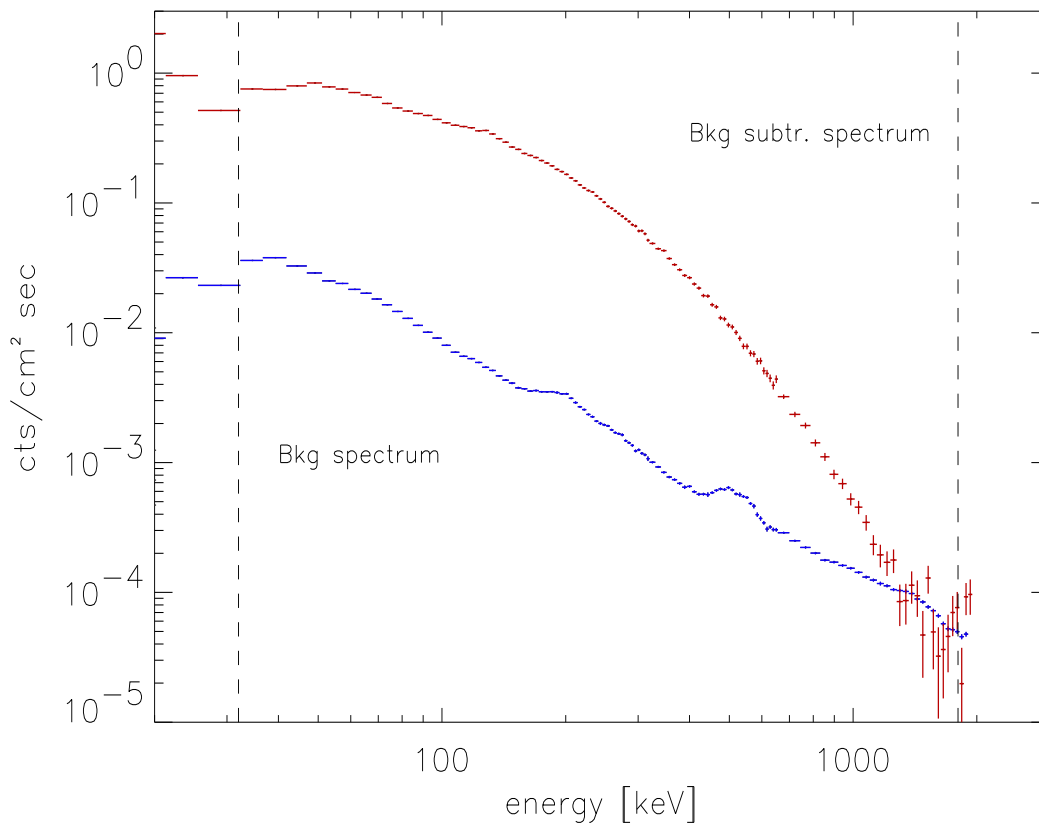


Figure 4.12: Burst time integrated spectrum (from 7.36 to 13.696 sec) background subtracted (red crosses) from LAD 6. The background extrapolated spectrum is represented by the blue points.

analysis because it allows to determine with greater accuracy the spectral parameters, especially in the case of faint bursts.

Detector Response Matrix

The Detector Response Matrix (DRM) is necessary for spectral fitting, because it is convolved with a model function and then fitted to the observed background subtracted spectrum. The detector response matrix is a representation of the BATSE gamma ray detectors' response. The computation of the DRM needs the knowledge of the incident photon energy, the corresponding deposition energy (or the measured energy) and the source position with respect to the detector axis [125] which are combined with a detailed model of the instrument.

In principle when a set of monoenergetic photons (in the ideal case, at least) interacts with the detector crystal the energy deposition of all the electrons, produced by photoelectric effect within the detector, constitutes the energy deposition spectrum. When

this spectrum is processed to incorporate some detector characteristics, and some corrections for spurious events, the detector response profile is produced. Then for every photon input energy there is a count spectrum covering the energy range of sensibility of the detector. The combination of different energy input gives a 3D representation of the response profile. In fig.4.13 is represented the detector response matrix for SD 6 in the case of GRB960927. The DRM is different for different detectors and depends strongly on the source-to-detector angle. The DRMs for the BATSE modules have been calculated by Pendleton ([125]).

A typical feature in the DRM is the diagonal term which derives directly from the photoelectric absorption of photons that interact in the body of the detector. Beside this photo-peak, there is a contribution by the iodine K-shell photon cross section producing a feature at 33 keV. The lower cross section of the iodine K-shell allows some photons to escape the detector. If these photons are the X-ray fluorescence products of the photoelectric absorption of higher energy photons, a lower total energy will be recorded from the original photons. This produces a secondary off-diagonal photo-peak that diverges from the diagonal term at low energies (see fig.4.13)

The most prominent characteristic of the DRM is the NaI K-edge between 100 and 500 keV. This photo-peak doesn't influence a lot the LAD data because their moderate energy resolution smears out the abruptness of this feature, whereas is more effective on SD data (see the spectral slope change around 30 keV in fig.4.7).

The detector response matrix for the LAD (in this example) is reported in fig.4.13. The photon peak at ~ 200 keV corresponding to the peak of the efficiency is evident.

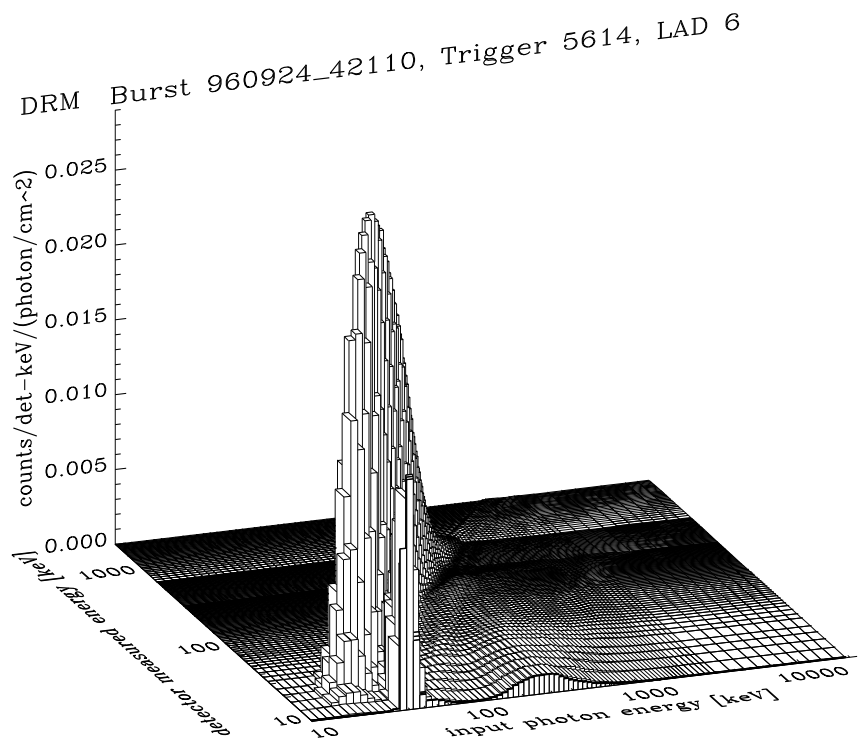
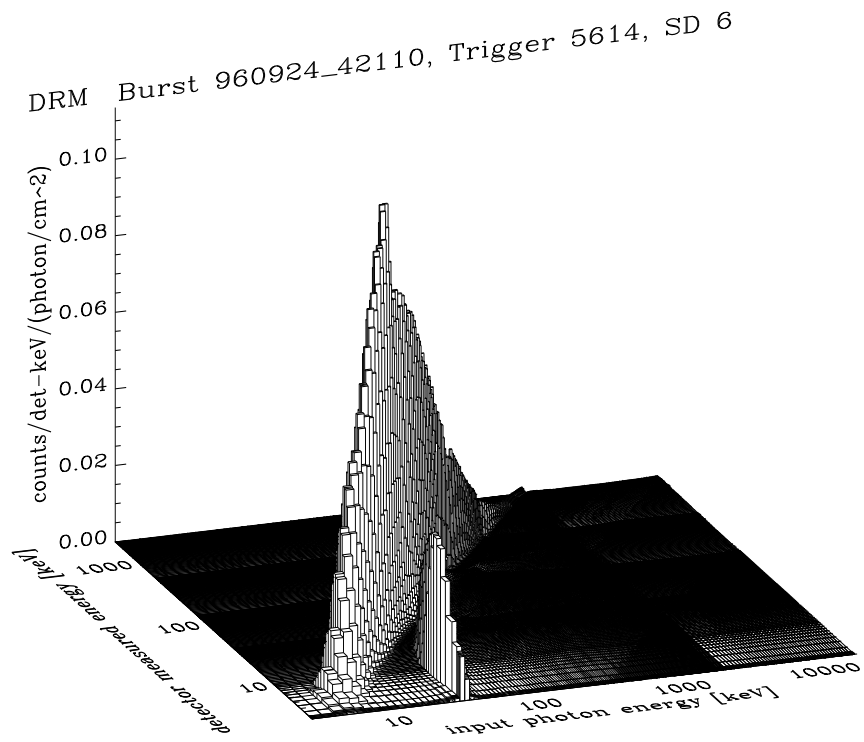


Figure 4.13: Detector Response Matrix of the Spectroscopic Detector 6 for GRB960924 which has an angle of 53.57 degrees with respect to the detector axis.

Chapter 5

Time resolved spectral analysis of bright GRBs

5.1 Introduction

This chapter presents the time integrated and time resolved spectral analysis of a sample of bright bursts selected with $F_{peak} \geq 20 \text{ phot cm}^{-2} \text{ sec}^{-1}$ from the BATSE archive.

From the phenomenological perspective much effort has been made in order to characterize and identify typical spectral properties of bursts, mostly by applying parametric but very general and simple spectral models (sec.5.2.4). Probably the most widely adopted is that suggested by Band et al. ([4]), namely a smoothly connected double power law model. Its attractive feature is that it characterizes, within the observational energy window, the most relevant quantities, namely the peak energy, representing the energy at which most of the emission occurs, and the low and high energy slope. These spectral components are related, according to the most accredited emission theories, to the particle energy distribution and/or to the physical parameters of the emitting region. Indeed GRB spectra are well represented by the Band parameterization ($N(E) \propto E^{\alpha,\beta}$), with typical low energy power law photon spectral indices α between -1.25 and -0.25 , high energy spectral indices β around -2.25 (Preece et al. [129]) and peak energy E_p typically around 100–300 keV.

A fundamental issue in the spectral analysis of GRBs is the integration timescale of the spectra which are observed to vary even on millisecond timescales (Fishman et al. [38]). BATSE spectra, which are integrated for a minimum of 128 ms, therefore represent the best way, presently available, to constrain the burst emission mechanism. Furthermore, in order to compare the average spectral properties of different bursts, also time integrated spectra, covering the duration of the pulse or the entire burst, have been used in the literature.

This analysis aims at comparing the spectra averaged over major pulses in the burst light curve with the time resolved spectra of the very same pulses in order to quantify sys-

tematic differences, considering both empirical (Band model) and physical (synchrotron shock model) spectral models for all spectra and compare the quality of the corresponding fits. In particular each spectrum is fitted with four models (Band's, broken power-law, thermal Comptonization) already used in previous works and , for the first time, with the synchrotron shock model (SSM). The results are compared and the violation of the limiting slope predicted by synchrotron emission is considered, both through the spectral fits parameters values and by the direct fitting of the SSM model.

In sec.5.2.1 and 5.2.2 the data and their selection criteria are presented, while the spectral models adopted for the analysis are detailed in sec. 5.2.3; sec. 5.3 reports the results of the analysis of the time integrated and time resolved spectra. Synchrotron limit violation is discussed in sec.5.3.3. The spectral evolution of the bursts presented in this chapter will be analyzed and discussed in chapt.7. Most of the results presented in this chapter are included in the paper Ghirlanda et al.[51].

5.2 Data selection and analysis

In this section the sample of bright long bursts selected for the spectral analysis, the type of data used to study the burst spectrum and its evolution and the method applied to analyze the spectra are presented.

5.2.1 Data Selection

The BATSE instrument has been already described in chapt.4 together with an overview of the spectral data and the analysis procedure adopted for this work.

The HERB data have been systematically preferred for the analysis because the higher detection area of the LAD ensures higher count rate than the SD detectors. Despite their moderate energy resolution (if compared to the SDs) they are suited for the continuum spectral study (Preece et al. [130]). Nonetheless, there are a few cases (see col. 3 in tab.5.2) for which the SHERB data have been used because of telemetry gaps in the LAD data.

We have analyzed the HERB data from rank 1 detector (see chapt.4 for details). The rank of the detector provides an indication of the relative count rate during the trigger: a 1st rank detector has the highest count rate, the best S/N and the highest spectral time resolution. For the SHERB data, the detector choice is a compromise between the highest degree of illumination (the first rank SD detector) and the highest gain that depends on different ground setting parameters, which were changed during the mission (Band D., private communication). The gain of the photomultiplier, in fact, scales the spectrum up or down in energy: the higher the gain the more the detector is sensitive to low energy photons and the lower is the low energy threshold (Preece et al., [128]; Kitchin [83]). We selected the highest rank SD detector with the 511 keV calibration

line centroid above the uncompressed channel 800 (see chapt.4)

5.2.2 The bursts sample

The bursts were selected from the BATSE 4B catalog which is complete until 29 Aug 1996 (trigger 5586). This catalog was completed with the on line catalog which includes the triggers after 5586 until trigger 8121 (26 May 2000).

Bursts with a peak flux on the 64 ms time scale (calculated according to Fishman et al. [40], Meegan et al. [109], Pacieras et al. [118]) higher than $20 \text{ phot cm}^{-2} \text{ sec}^{-1}$ were selected. This choice is motivated by the fact that bright bursts should provide time resolved spectra with good S/N (also on integration of the order of 128 ms). The general characteristics of the 38 GRBs selected according to this criterion are reported in tab. 5.2: col.1 and 2 give the trigger number and the corresponding burst name, the peak flux is reported in $[\text{phot}/\text{cm}^2 \text{ sec}]$ in col.6. The data type and the corresponding detector number, chosen for the spectral analysis, are represented in col. 3 and 4, respectively.

The sample was reduced during the spectral analysis because of data problems (i.e. data gaps for triggers 1609, 1711, 3480) or because the number of spectra available for the spectral analysis was less than 5 (triggers 1997, 2151, 2431, 2611, 3412, 5711, 5989, 6293, 6904, 7647). This happened particularly in short events with typical duration ≤ 1 sec. The bursts that were not analyzed have dashes entries in tab. 5.2. The final sample of analyzed bursts contains 25 bursts and is obviously not complete with respect to the flux selection criterion. All the analyzed bursts except triggers 5563,7301,7549 are also present in the Preece et al. ([130]) spectral sample.

5.2.3 Spectral analysis

The spectral analysis has been performed with the software *SOAR* v3.0 (Spectroscopic Oriented Analysis Routines) by Ford ([41]). The power of this software is its multi-level routine structure which can be easily modified by the user: we implemented the spectral library with the broken power law and added the possibility of fitting each time-resolved spectrum with a different energy binning scheme. The main capabilities of SOAR are: the possibility of analyzing HERB and SHERB data and rebinning (in time) of spectra in different fashions (according to a fixed number of spectra per group or with a S/N ratio criterion). It is also possible to simulate burst spectra and spectral evolution (Ford [41]).

The package XSPEC, widely used for high energy data, was also employed to test, for two bursts, the spectral analysis procedure. We found, within parameter errors, similar results. Any difference can be ascribed to a different background calculation technique.

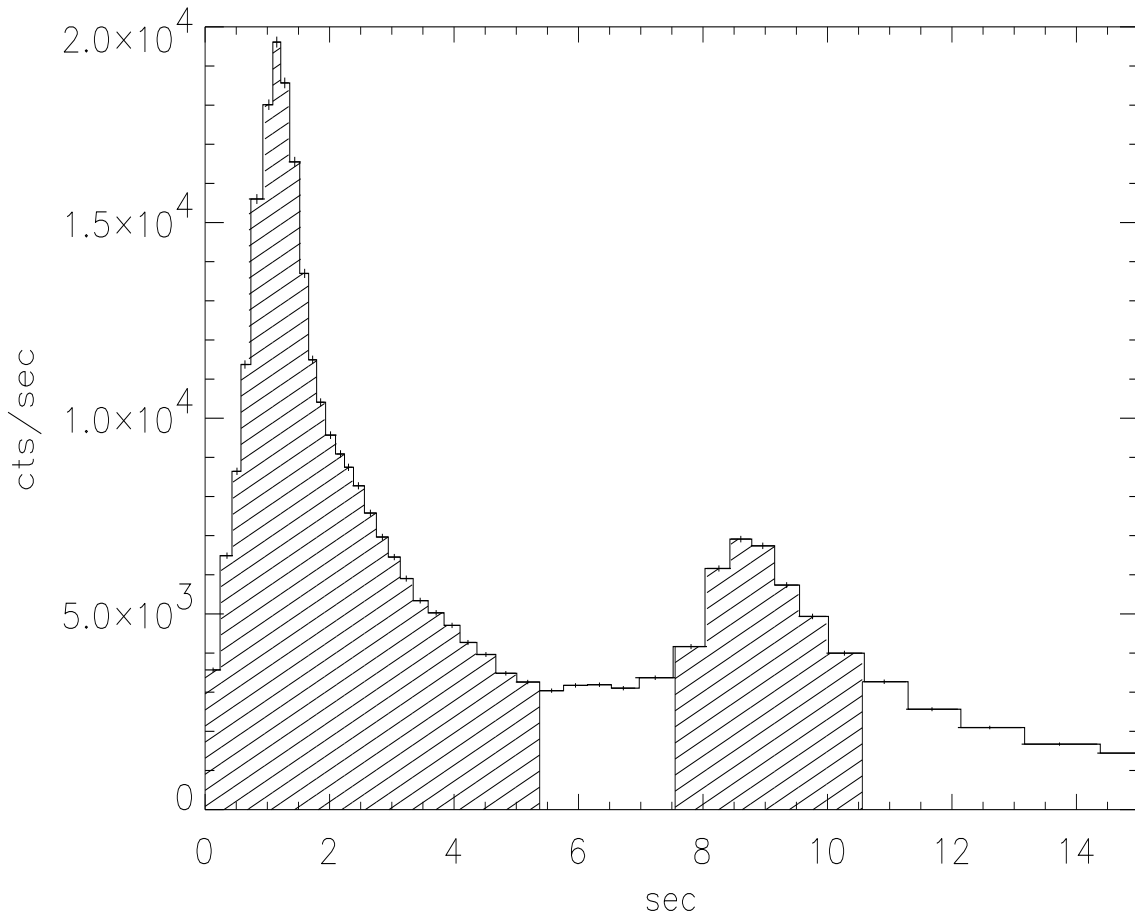


Figure 5.1: Example of light curve (trigger 2083). Each time bin represents the count rate summed over all the detectors that triggered, integrated in energy from 28 to 1800 keV and over the detection area (for details see Preece et al. [130]). The line-filled regions show the time intervals of the average pulse spectrum accumulation. The start and stop times were chosen to have the same flux level. Our analysis is limited to the hatched areas, and therefore excludes the long slowly decaying part of the burst.

The spectral analysis procedure consisted of the inspection of the light curve, i.e. the count rate in cts s^{-1} over the nominal energy band (typically 28–1800 keV) with each time bin corresponding to a time resolved spectrum (with typical integration time of 128 ms). The background was calculated according to the specifications reported in chapt.4. As reported in tab. 5.2, in most cases the degree of the polynomial is 4.

The GRB light curve was used to identify the pulses as those structures in which the flux rises above and decays back to the background level. We accumulated the time resolved spectra within the time interval identified with the pulse: this defines the time average pulse spectrum. In those pulses composed by several substructures we treated them separately only if their flux starts and returns to the background level and if they are separated by at least a 128 ms time bin. While this definition of the pulses is not physical, but only based on a visual method for their identification (as noted by Band

private communication), and the overlapping pulses are then frequently considered as a single structures, we note the difficulty in the definition of a quantitative method for the pulse separation (e.g. Fenimore et al. [35]).

We report in fig. 6.2, as an example, the time intervals for the accumulation of the average pulse spectra, corresponding to the hatched regions in the plot. The time averaged pulse spectrum was then fitted with the 4 spectral models described in the following section. The best fit results were used as initial parameter guesses for fitting the time-resolved spectra.

For the time-resolved spectra we used, as integration times, at first the shortest time available (i.e. 128 ms, at best), again limiting our analysis to the same time-span selected for the time integrated analysis. The best fit parameters were then examined in search for any indetermination: when at least 3 subsequent spectra had one or more unconstrained spectral parameters or the best fit value was equal to one of the limit assumed for the the model, the spectra were grouped according to a S/N criterion. We followed the prescriptions of Preece et al. ([130]) who accumulate subsequent HERB spectra until the S/N (calculated for the 28–1800 keV energy range) is greater than 45; for the SHERB data the S/N threshold was fixed at 15 as already done by Ford et al. ([42]). If after this accumulation the number of time resolved spectra was less than 5 the burst was not included in the final list of analyzed events (see sect.5.2.1).

The spectra were also rebinned in energy in order to be confident that the Poisson statistic is represented by a normal distribution in every channel for the application of the χ^2 minimization technique. The minimum number of counts per energy bin was fixed at 30 and 15 for the HERB and SHERB data, respectively.

5.2.4 Spectral Models

Four spectral models were employed to fit the GRB time averaged and time resolved spectra. These functions were chosen in order to find whether a specific model can be considered as the best representation of the spectral characteristics of pulses in bright GRBs. More complicated spectral models (e.g. the smoothly broken power law (Ryde [136]) or the spectrum Compton absorbed by a cold medium (Brainerd et al. [12]) were not considered at this level of the analysis because they have an higher number of free parameters.

The Band model

This empirical model (BAND hereafter) was first proposed by Band et al. ([4]) and, as already mentioned, well fits the time averaged (Band et al.[4]) and the time resolved spectra (Ford et al [42]; Preece et al. [129]). It contains the two continuum components in the keV–MeV band already discovered before BATSE (chapt.2) : (i) a low energy power law with an exponential cutoff $N(E) \propto E^\alpha \exp(-E/E_0)$ and (ii) a high energy

power law $N(E) \propto E^\beta$ (Matz et al. [102]). In fact the BAND model consists of 2 power laws joined smoothly by an exponential roll-over and has a continuous derivative:

$$N(E) = \begin{cases} A \left(\frac{E}{100 \text{ keV}} \right)^\alpha \exp\left(-\frac{E}{E_0}\right) & \text{for } E \leq (\alpha - \beta) E_0 \\ AE^\beta \left[\frac{(\alpha - \beta) E_0}{100 \text{ keV}} \right]^{\alpha - \beta} \exp(\beta - \alpha) & \text{for } E \geq (\alpha - \beta) E_0 \end{cases} \quad (5.1)$$

where $N(E)$ is in photons $\text{cm}^{-2} \text{s}^{-1} \text{keV}^{-1}$. The free parameters, which are the result of the fits, are:

- A: the normalization constant @ 100 keV;
- α : the low energy power law spectral index;
- β : the high energy power law spectral index;
- E_0 : the break energy, which represents the e-folding parameter.

If $\beta < -2$ the peak energy in the EF_E diagram (F_E is the energy flux in $\text{keV}/\text{cm}^{-2}\text{sec}^{-1}$ keV) is $E_{peak} = (\alpha + 2)E_0$ and represents the energy at which most of the power is emitted.

For the fitting procedure we had to assume an interval for the parameters and we fixed $[-5, 1]$ for α and β and the break energy was allowed to vary in the range $[28-1800]$ keV.

The Broken Power Law model

This model, called BPLW, is the simplest model used for fitting GRB spectra: it consists of two power laws sharply connected, with no curvature. Its analytical form is:

$$N(E) = \begin{cases} AE^\alpha & \text{for } E \leq E_0 \\ AE_0^{\alpha - \beta} E^\beta & \text{for } E \geq E_0 \end{cases} \quad (5.2)$$

The free parameters are as before. In this model the peak energy of the EF_E diagram coincides with the break energy E_0 for $\beta < -2$.

The Comptonization model

This spectral representation (COMP hereafter) is composed of a power law ending in an exponential cutoff, thus fitting well those spectra with a very steep high energy decline:

$$N(E) = AE^\alpha \exp\left(-\frac{E}{E_0}\right). \quad (5.3)$$

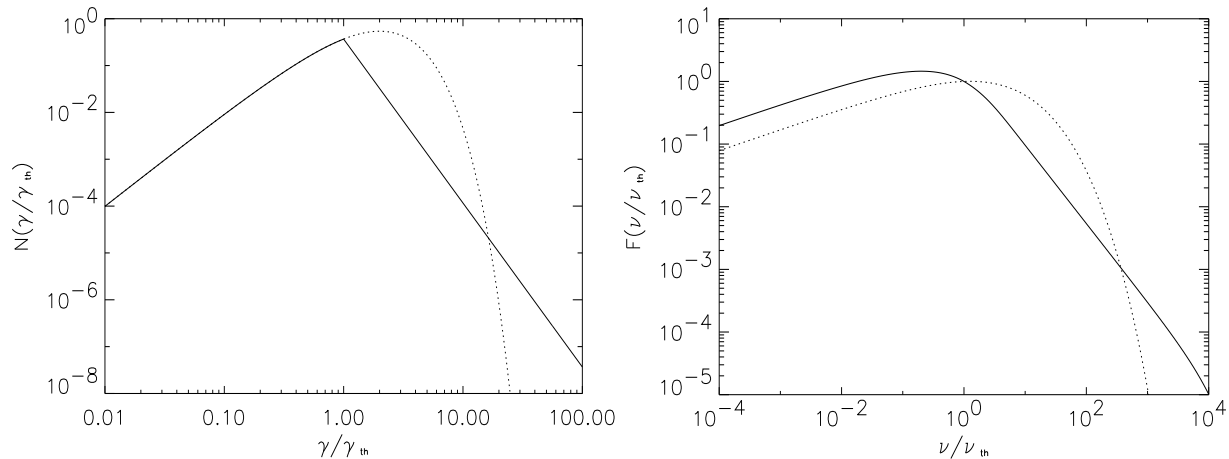


Figure 5.2: *Left*: different electron energy distributions, *solid line*=post shock Maxwellian with a high energy power law tail ($\delta = 3.5$); *dotted line*=pre-shock relativistic Maxwellian. The distributions are functions of γ/γ_* , and $N(\gamma/\gamma_*)$ is in arbitrary units. *Right*: synchrotron spectra corresponding to these two electron energy distributions. *Solid line*=post shock Maxwellian with a high energy power law tail ($\delta = 3.5$); *dotted line*=pre-shock relativistic Maxwellian. The distributions are functions of ν/ν_* . The shown spectra are normalized to their respective peak flux.

The free parameters (A, E_0, α) are as defined for the previous models. In fact the COMP model can be analytically obtained from the BAND assuming $\beta = -\infty$. This model might be considered to mimic the spectrum resulting from multiple Compton emission from a thermal medium.

The Synchrotron Shock Model

This model has been described in chapt.3. It is based on the synchrotron emission of relativistic electrons, whose energy distribution is characterized by a relativistic Maxwellian modified, at high energies, by a power law hard tail. (sec.1.2.3). This model was implemented in a code which gives a spectral form which can be numerically fitted to the observed spectra.

In fig. 5.2 (left panel) are reported two cases of electron energy distribution: the post shock Maxwellian modified at high energies by a power law tail (solid line) and a pre-shock relativistic Maxwellian (dotted line). Notice that in the former case (solid line), the distribution extends on a wider energy range compared with the relativistic Maxwellian. In the figure a typical intermediate value for the power law index $\delta = 3.5$, for the high energy tail, is assumed.

The shape of the synchrotron spectrum emitted by this electron population (Fig. 5.2 *right panel*, solid line) has a continuous curvature and is characterized by a low energy component (namely for $E < E_{peak} \sim 2.5E_*$, where $E_* = m_e c^2 \gamma_*$ is the electron energy before the shock passage) which should be well represented by the single electron

synchrotron spectrum dependence $\sim E^{4/3}$ (in the EF_E diagram, i.e. $\sim E^{-2/3}$ in the count spectrum) and by $E^{-(\delta-3)/2}$ at high energies (i.e. above E_{peak}). This spectral form can account for different high energy slopes but it has a limiting spectral slope at low energies.

The free parameters of the model are the high energy electron spectral index δ and the characteristic energy E_* which describe the electron energy distribution. In the fit of this model to the time resolved spectra we assumed that the maximal interval of variation of these 2 parameters is $\delta \in [1, 10]$ and $E_* \in [10 - 2000]\text{keV}$.

Comparison of the fitting functions

For clarity, in fig. 5.3 are reported the spectral shapes corresponding to the four models considered with their parameters fixed to the average values reported in tab.5.3. The potential of each model to better represent a particular spectral shape is clearly visible: the four models are similar at low energies but they differ in the high energy tail. In general it should be noticed that the average COMP model (*dashed line* in fig.5.3) overestimates the spectral break energy due to the lack of a power law high energy component. Furthermore, the average BAND spectrum (*solid line* in fig.5.3) would tend to be harder at low energies and softer at high energies than the BPLW model (*dotted line*), due to the sharp break of the latter. As will be shown in the presentation of the spectral results, when the statistics is low, particularly for the time resolved spectra, the BPLW model tends to give satisfactory results as much as the BAND model, and it can not be excluded as a bad fitting function. This shows that it is not possible, also with the time resolved spectra, to choose a preferable model although some indications will be outlined in sec.5.3.2. The SSM average spectrum (*long dashed line* in fig.5.3) is harder than the BAND and COMP model as the low energy spectral index of the photon spectrum is fixed in the SSM model to the $-2/3$ value (Katz [77], Tavani [154]), making the average spectral shape harder.

All the 4 spectral models presented above were tested in order to be consistent with the previous works present in the literature (e.g. Preece et al. [130]), and, chiefly, with the aim to compare their results in search of a preferable model.

Finally, it is worth mentioning that the BPLW model is unphysical due to its sharp spectral break, although a sharply broken double power law model has been recently proposed as the natural outcome of the synchrotron emission by electrons in a small scale magnetic field (Jitter radiation - Medvedev [106]). The COMP model can be considered a subset of the more general BAND form when the high energy spectral component has an infinite slope (i.e., $\beta = -\infty$). This model, anyway, has been considered separately because it can accommodate those spectra which have no high energy power law tail, i.e. steeper than E^{-5} . Among the models presented here, the SSM is the most physical spectral model. This is why it has been extensively fitted to the time resolved and time integrated spectra to determine its range of application. As will be shown in the next sections, it can accommodate only those spectra which have a low energy power law

spectral index, as fitted by the other three models, around $-2/3$.

We also want to stress that previous works have tested the SSM model on time resolved spectra using a modified version of the BAND model with the low energy power law spectral index $\alpha = -2/3$, but here its numerical version (Tavani [154]) is fitted to the time resolved spectra and compared to the classical spectral functions.

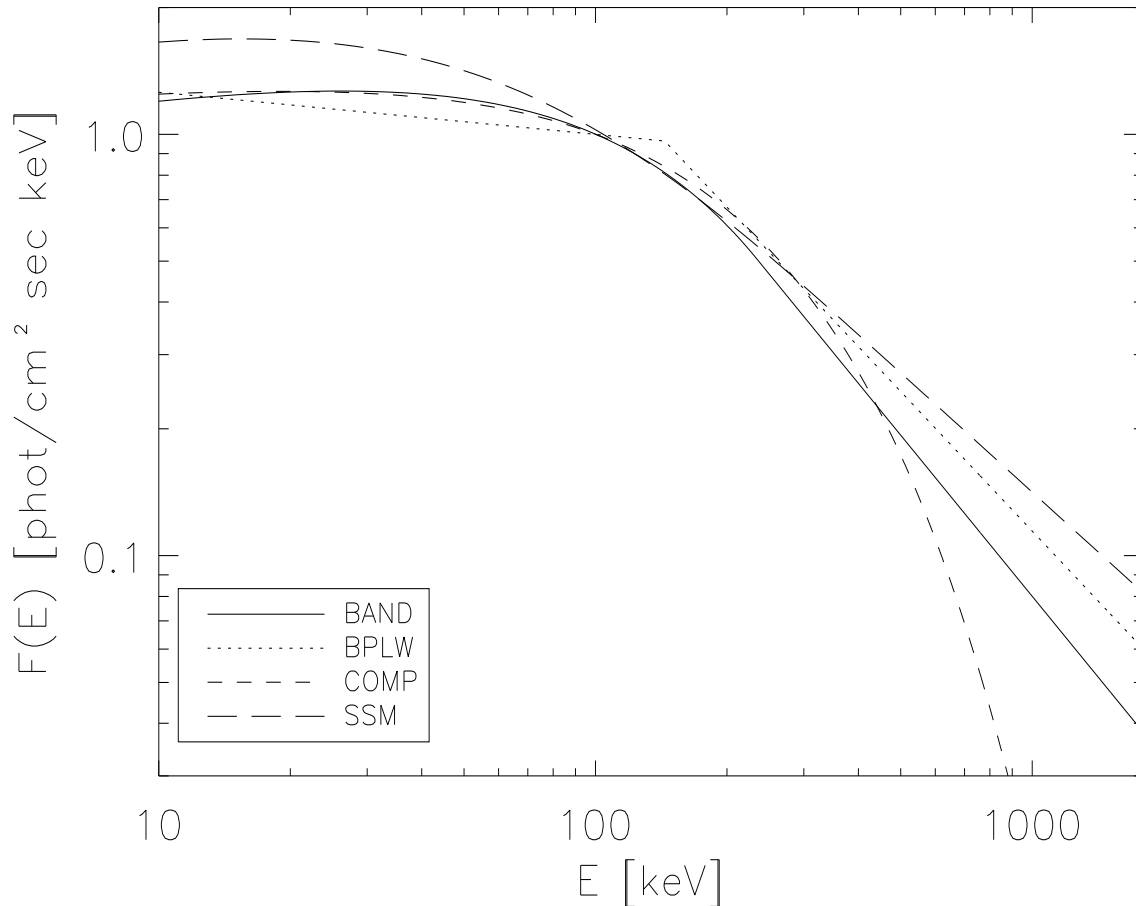


Figure 5.3: The 4 spectral models: the spectral parameters correspond to the average values of the pulse time integrated spectra reported in tab. 5.3. The functions are normalized at 100 keV.

5.3 Results

The 25 GRBs of the sample (tab.5.2) were fitted with the four spectral models presented in sec. 5.2.4. For each peak present in the burst light curve we considered both the time integrated spectrum and the sequence of time resolved spectra. As already mentioned, the goals are the following:

- compare the spectral parameters obtained fitting different models;
- determine the robustness of the spectral quantities with respect to the specific model considered;
- quantify the difference between time integrated and time resolved spectra of the very same peak;
- verify the strongest prediction of the synchrotron theory of a low energy spectral shape not evolving and fixed to $-2/3$ (Katz et al., [77]).

For clarity we first present the results for the time integrated (sec.5.3.1), then for the time resolved (sec.5.3.2) spectra, and finally discuss the violation of the synchrotron 'limit' (sec.5.3.3).

5.3.1 Time integrated pulse spectrum

In tab. 5.3 are reported the best fit parameters of the 4 spectral models obtained by fitting the time averaged spectrum of the different peaks in each GRB. For multi-peaked bursts the number of lines corresponds to the number of peaks analyzed. There are some gaps in each model columns corresponding to those pulses which are not fitted (i.e. the model parameters are undetermined) by that model. Fig. 5.4 shows an example of a fit: the average pulse spectrum of trigger 3492 and the best fit and residuals for each model are displayed.

Comparison of the spectral models

From the time integrated spectral analysis there is not a general and strong indication of a preferred fitting function to represent the spectra. In fact it seems that all the models give acceptable fits, and their χ_{red}^2 (i.e., $\chi^2/\text{degrees of freedom}$) are around one for all the 4 models although their median is definitely greater than one. However there is an indication that the BAND model is the spectral shape which better fits the time integrated spectra. The BAND model has an average $\chi_{red}^2 \sim 1.3$, to be compared with the values 1.67, 1.63, 1.74 of the BPLW, COMP and SSM¹ models, respectively, and the width of the distributions, in terms of standard deviations, is 0.36 for the BAND and ~ 0.68 for the other three models. This indicates that the average pulse spectrum is better represented by the BAND model also considering 100 as a typical number of degrees of freedom. A maximum likelihood test indicates that the improvement of the χ^2 passing from the COMP model with 3 free parameters to the 4 free parameter BAND model corresponds, in most cases, to a better fit, although there exists cases where they are statistically indistinguishable. This result agrees with that found by Band ([4]). Many exceptions exists anyway: as an example let just mention the case of a spectrum

¹The SSM model has to be considered however apart. In fact due to the considerable number of average peak spectra which present an undetermined high energy supra-thermal index ($\delta > 10$), the goodness of the model cannot be easily quantified.

whose high energy part is too steep to be represented by the BAND model power law (i.e. $\beta = -5$, first pulse of triggers 4368, 5567) while the COMP model can accommodate this fast decreasing spectrum with its exponential cutoff. Notice that in these cases also the BPLW model gives acceptable fits for β : this is probably due to the sharp structure of this model which makes the fit overestimate the high energy spectral hardness (i.e. less negative β values).

Note also that a statistically good χ^2_{red} of course cannot be considered a sufficient condition for the quality of the fit and an analysis of the distribution of the residuals is necessary. If the residuals show systematic trends like in the second, third and fourth panels of fig.5.4, the fit is not considered acceptable although its reduced χ^2 might be around 1.

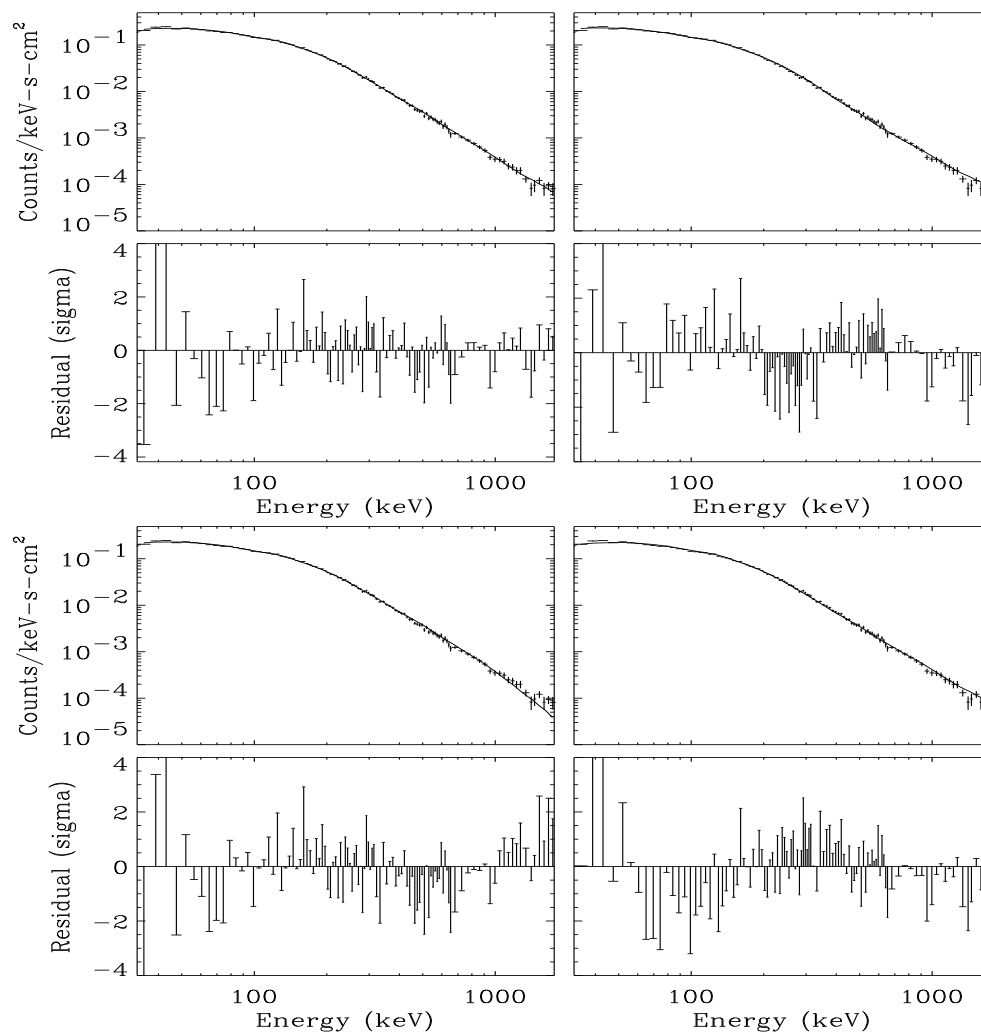


Figure 5.4: Trigger 3492. Spectral fits to the pulse time averaged spectrum. The spectrum is integrated over the time interval [3.008-6.976] sec since the trigger time. The model fits and the residuals are for the BAND, BPLW, SSM and COMP model, displayed clockwise starting from the top left corner

Spectral parameters distributions and average spectral shape

We first computed for each model the distributions of the best fit parameters and found that they agree with the results presented in previous spectral studies (Band et al. [4]). In particular, for the BAND model, we find that there is no correlation between the low and the high energy spectral indices (the Pearson's correlation coefficient is -0.006) but they group in the ranges $-1.8 \leq \alpha \leq -0.6$ and $-3.5 \leq \beta \leq -1.5$ which correspond to the intervals reported by Band et al. ([4]) and include the average values $\langle \alpha \rangle = -1.03$ and $\langle \beta \rangle = -3.31$ found by Fenimore ([36]). The peak energy of the BAND model $E_{peak} \sim 205 \pm 3$ keV is, instead, harder than $\langle E_{peak} \rangle = 150 \pm 50$ keV, reported in Band et al. ([4])². This is probably due to the fact that our burst sample represents the bright end of the BATSE peak flux distribution, and because we integrated the time resolved spectra just around the peak, excluding the major decaying and rising parts of each pulse (see sect. 5.2.3) which are characterized by softer spectra.

Table 5.1 reports the weighted average values of the best fit parameters of tab. 5.3 for the pulse time integrated spectra.

Let us consider the robustness of the parameters found with respect to the choice of the spectral model.

- The α distribution for the BAND model is peaked around -1 and it is similar to the same parameter distribution for the COMP model; the BPLW, due to its sharp spectral break corresponding to the slope change $E^\alpha \rightarrow E^\beta$, gives systematically lower α values and, in fact, its average is $\simeq -1.2$.
- The β distribution clusters around -2.3 in the BAND and BPLW model and for the latter the distribution is shifted towards higher values (i.e. harder spectra). The same happens with the SSM model having an harder average high energy spectral tail ($\beta \sim -2.06$) than the BAND model.
- For the peak energy distribution, the weighted average value for the BAND model is $E_{peak} \sim 205 \pm 3$ keV. The BPLW break energy (\equiv peak energy) is ~ 169 keV, whereas the COMP model, due to the lack of the high energy power law component, overestimates the spectral break, having a broad distribution and a weighted average of 233 keV. The SSM model peak energy is comparable with that of the BPLW model but lower than the BAND and COMP models.

We conclude that the average spectral shape of the GRBs present in our sample does depend on the fitting model and the BAND and COMP model tend to give, although the latter lacks the high energy power law, comparable average spectral shape at low energies. Moreover we have found that the average pulse spectrum, integrated on a time interval around the peak, results somehow harder than the time integrated spectrum

²The error associated with $\langle E_{peak} \rangle$ represents the spread of the values and the uncertainty on E_{peak} is the error on the average.

on the complete duration of the burst (including the slow–long decay part of the light curve). This could be ascribed to the fact that the time resolved spectrum, as will be shown in chap.7, is harder at the peak of the light curve (and in the neighboring time bins) and particularly in those bursts showing a tracking morphology in which the spectral hardness reproduces the time evolution of the flux.

The Synchrotron limit violation

The analysis of the low energy spectral indices shows that there are 4 pulses (those in italics in tab. 5.3) whose average BAND best fit spectrum is harder, at 2σ , than the limit $E^{-2/3}$ predicted by the synchrotron model. Three of these spectra, when fitted with the COMP model, show no α limit violation but their low energy power law spectral index (-0.667 ± 0.01 , -0.64 ± 0.02 and -0.53 ± 0.08) is very close to $-2/3$. The same spectra have a poor fit with the SSM model showing systematic trend in the residuals of the fits on most of the energy range.

The average pulse spectra give only a weak indication of the violation of the synchrotron model low energy spectral index. This is because the low energy spectral index evolves in time and its value averaged on the burst duration cancels out this evidence due to the contribution of spectra with $\alpha > -2/3$ as well as of those with α consistent or lower than this limit. On the other hand, as will be shown in the following, stronger indications of a violation come from the time resolved spectra.

Table 5.1: Weighted averages of the averaged–peak spectral parameters for the four models. The break energy E_{break} and the peak energy E_{peak} are in keV.

	<i>BAND</i>	<i>BPLW</i>	<i>COMP</i>	<i>SSM</i> ^a
$\langle\alpha\rangle$	-0.977 ± 0.003	-1.185 ± 0.002	-1.013 ± 0.002	$-2/3(\textit{fix})$
$\langle\beta\rangle$	-2.27 ± 0.01	-2.09 ± 0.004		-2.06 ± 0.06
$\langle E_{\text{break}}\rangle$	164.4 ± 1.7	161 ± 0.7	210.4 ± 1.3	67.4 ± 0.7
$\langle E_{\text{peak}}\rangle$	205 ± 3	161 ± 0.7	233 ± 2	168 ± 2

^a For this model the spectral parameters are described in the text. Notice that β represents the high energy power law spectral index derived from the slope δ of the particle distribution, as $\beta = -(\delta + 1)/2$ and α is fixed to the limit predicted by the optically thin synchrotron theory.

5.3.2 Time resolved spectra

Let us now consider the results of the fitting of the time resolved spectra with the same four models.

In fig. 5.5 an example of spectral evolution is reported: for each peak we obtain a sequence of best fit parameters relative to the time resolved spectra which characterize the temporal evolution of the spectrum during the burst. While a description and discussion on the parameter evolution will be presented in chapt.7, we note that both the peak energy and the low energy spectral index evolve in phase: the spectrum becomes harder during the flux rise phase and softer during the decay, a behavior already found by Ford et al. ([42]) as a characteristic spectral evolution morphology of several bursts.

In the following we report and comment on the parameter distributions of the 4 models for a comparison (i) among the model themselves and (ii) with the results on the pulse average spectrum. Finally we examine the SSM limit violation in some well defined cases.

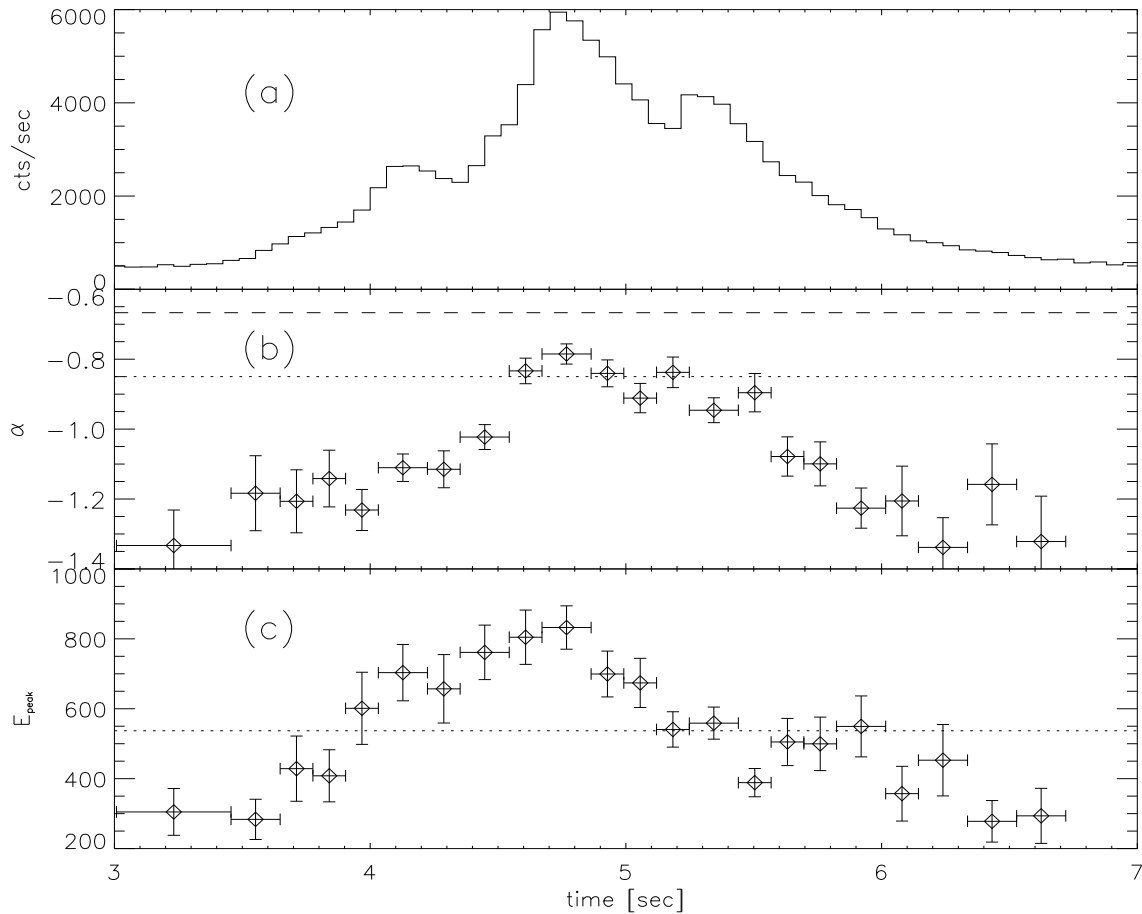


Figure 5.5: Trigger 3492. Spectral evolution of the COMP model parameters fitted to the time resolved spectra. Light curve on the 64ms time-scale (panel a), integrated over the energy range 110–320 keV (corresponding to channel 3 of the detector); low energy spectral index (b), *dotted line*: the average α value, *dashed line*: the synchrotron model limit; peak energy (c), *dotted line*: the average E_{peak} of the COMP model obtained from the time resolved spectra.

Comparison of the spectral models

For a general comparison of the quality of the fits with different models we have plotted in Fig. 5.6 their reduced χ^2 distributions. These are all centered around one and again it is not possible to identify any preferable spectral model even considering their spread. Anyway we can note some important differences: considering that all these distributions are asymmetric towards 2, we fitted a 6 parameter function, namely a gaussian summed to a 2nd order polynomial, (indicating χ_{red}^2 with x):

$$F(x) = A_1 \exp \left[-\frac{1}{2} \left(\frac{(x - A_2)}{A_3} \right)^2 \right] + A_4 + A_5 x + A_6 x^2 \quad (5.4)$$

The parameter A_3 characterizes the width of the χ_{red}^2 distributions around its mean value while the polynomial accounts for the tail. A_3 gives a qualitative indication of the width of the distribution just around the mean, i.e. where the best fit χ_{red}^2 values are clustered and this represents an estimate of the goodness of one model to fit the set of spectra. The indication we obtain is that the BAND and COMP model have the lower dispersed distributions with $A_3^{1/2} \sim 0.14$, to be compared with ~ 0.2 for the BPLW and SSM model. We can say that in terms of reduced χ_{red}^2 the BAND and COMP model could better represent the time resolved spectra of bright bursts. Also in this case some counter examples exist showing that in general, within a single pulse, time resolved spectra can be fitted by different spectral models (see fig. 5.7).

Time resolved vs time integrated spectra

Let us now compare the corresponding results for the time integrated spectra. As an example in fig. 5.7 we report the peak spectrum of the trigger 2083. Comparing with fig 5.4 (showing the spectrum, time integrated over the whole peak, for trigger 4392) it is evident that the time resolved spectra better constraint the best fitting model: in fact (for example in this case) the time averaged pulse spectrum was satisfactorily fitted by all the 4 models whereas the peak time resolved spectrum is not well fitted by the SSM model because the low energy power law spectral index is fixed at $-2/3$ and the spectrum is harder than this slope ($\alpha = -0.03 \pm 0.06$ for the BAND model). In this example the BAND, COMP and BPLW model provide the best fits and among them the BAND model has the best $\chi_{red}^2 = 0.99$.

This represents a clear indication that the time resolved spectra have to be used in determining the spectral properties of GRBs: average spectra can be effective in comparing the global properties of different bursts, but the actual spectral shape requires high temporal resolution data.

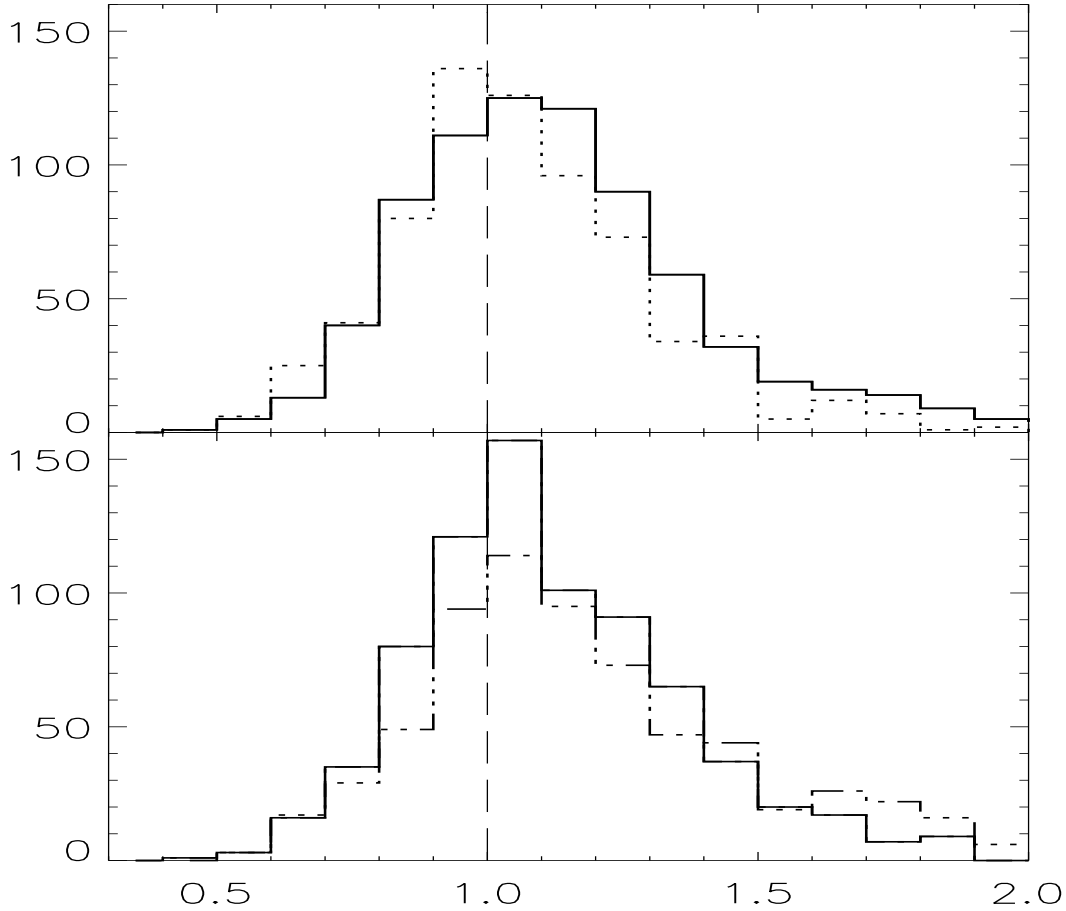


Figure 5.6: Reduced χ^2 distributions for the 4 spectral models: BAND and BPLW (*dotted and solid line top panel*) and COMP and SSM (*solid and dot-dashed line bottom panel*).

Spectral parameters distributions

In this section we consider the distribution of the model parameters as inferred from the time resolved spectral analysis, compare again the different models, and compare these results with the time integrated ones and with previous findings.

- *The low energy spectral component.*

The BAND, COMP and BPLW fits are comparable at low energies as shown by the corresponding α distributions presented in fig. 5.8: the BAND and COMP model distributions are similar, as in the case of the time integrated spectra, and both have a mode of -0.85 ± 0.1 , consistent at 2σ with the BPLW average value -1.15 ± 0.1 . Note that qualitatively the extension of the α distribution of the BPLW model towards lower values could be attributed to the fact that at low energies the sharp break tends to underestimate the hardness of the spectrum compared to a smoothly curved model.

The average low energy spectral slope obtained from the time resolved spectra is

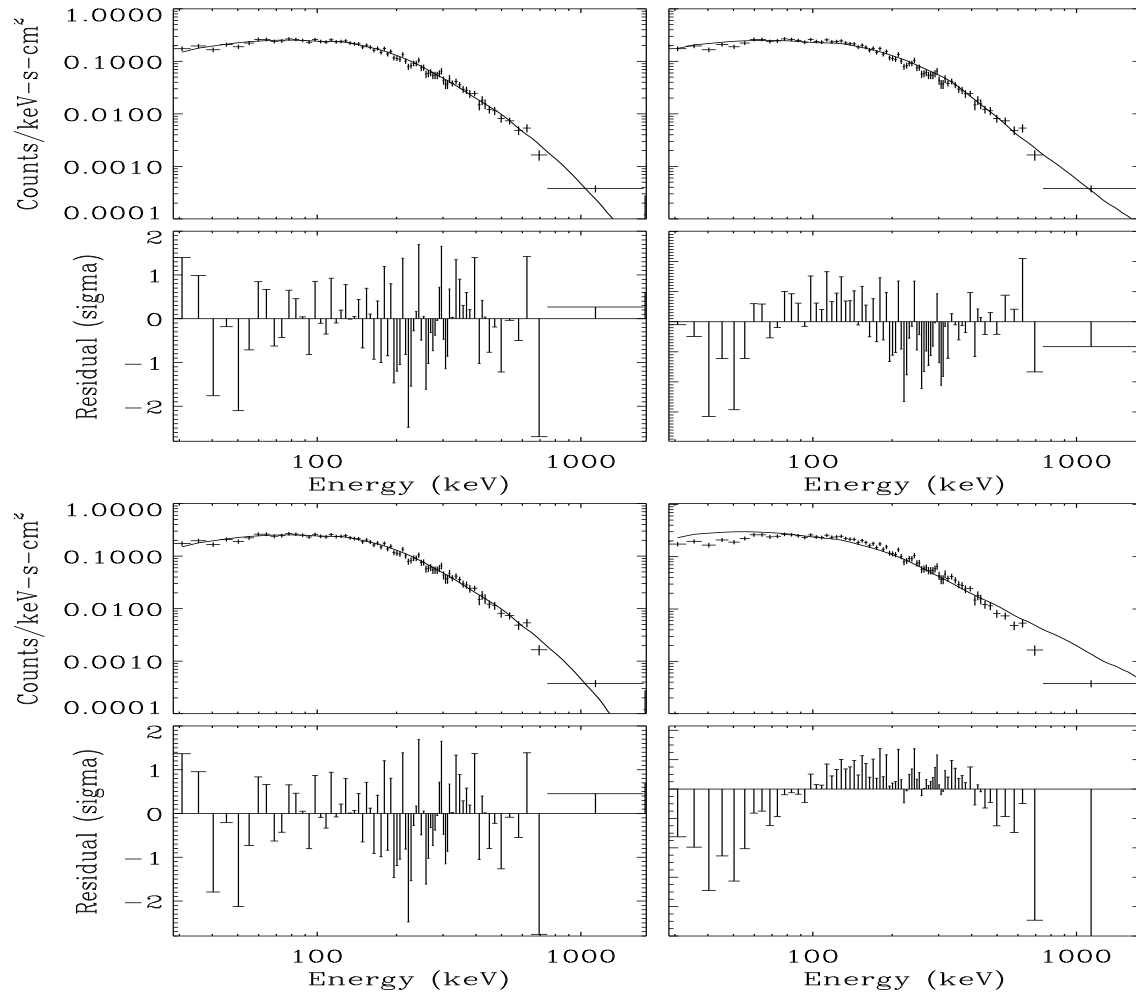


Figure 5.7: Trigger 2083. Spectral fits to the pulse peak spectrum. The spectrum is integrated over the time interval [1.088-1.216] sec since the trigger time. The model fits and the residuals are for the BAND, BPLW, SSM and COMP model displayed clockwise starting from the top left corner.

harder than that obtained with the time integrated pulse spectra for all the three models (BAND, BPLW, COMP). This is a consequence of time integration (i.e. hardness averaging) of the spectral evolution (which can be also very dramatic) over the entire rise and/or decay phase of the pulse.

Even though we present the spectral analysis with 4 models separately we can compare these results with those obtained by Preece et al. ([130]), where they considered the low energy spectral index distribution regardless of the (best) fitted model. We obtain a similar distribution but with a harder average low energy spectrum ($\alpha \sim -0.85 \pm 0.1$ considering the BAND and COMP model, to be compared with $\sim -1.05 \pm 0.1$). This difference might be a consequence of the fact that we are considering a subsample of that of Preece et al. ([130]), including only the bright GRBs which might be intrinsically characterized by a harder spectrum (Borogonovo

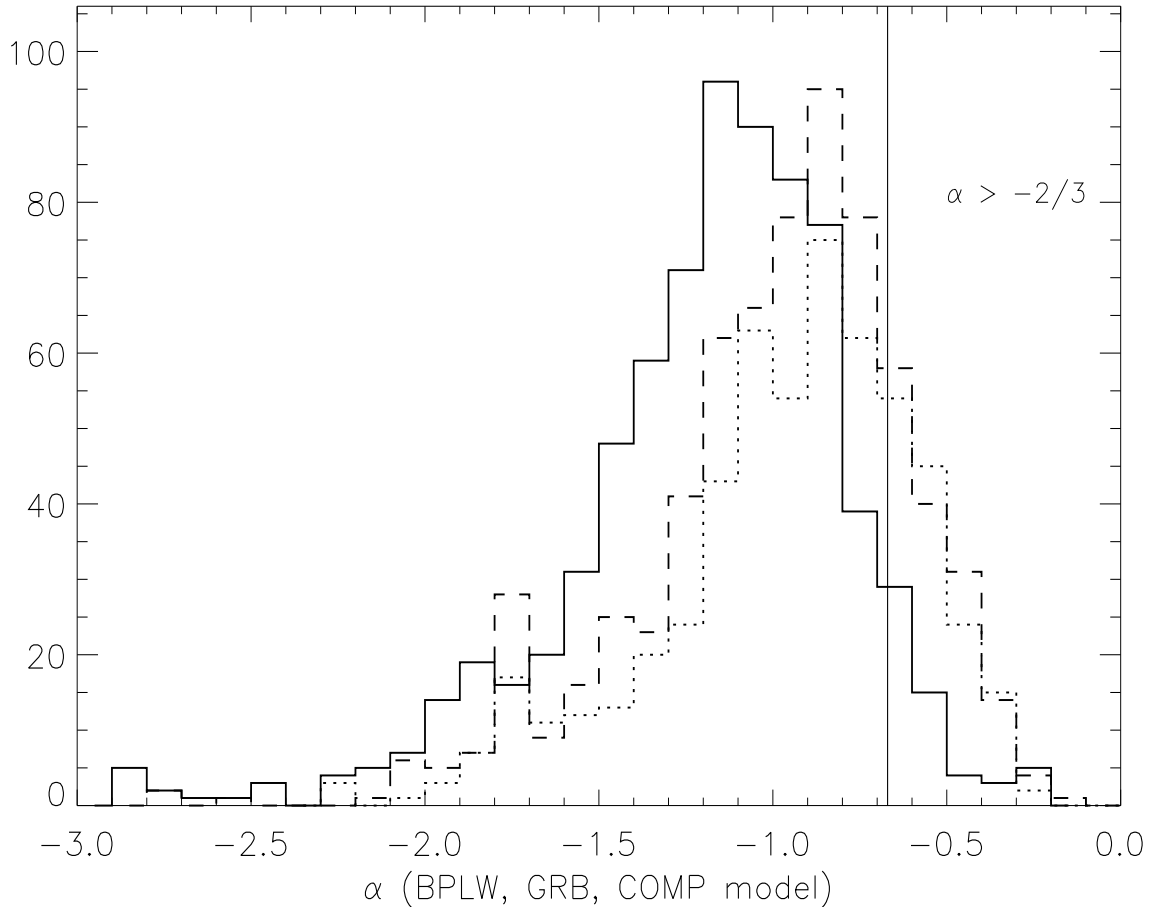


Figure 5.8: Low energy power law spectral index (α) distributions derived from the time resolved spectral analysis. *Solid line*: BPLW model, *dotted line*: BAND model, *dashed line*: COMP model. The vertical line represents the synchrotron limit ($\alpha = -2/3$) for the low energy spectral shape.

& Ryde [11]) and because we restricted our time resolved spectral analysis to the peak interval excluding the inter-pulse phase of multi-peaked events.

- *The high energy spectral component.*

In many spectra the steepness of the count distribution above the break energy E_0 , coupled with the poor S/N ratio, result in a poorly determined value of β . This is true especially in the case of the BAND model: when the break energy E_0 is at high values the exponential roll-over leaves too few high energy spectral channels free for fitting the E^β component properly. In fig. 5.9 we report the BPLW, BAND and SSM β distributions. Also in this case the BPLW model, due to its sharpness, tends to overestimate the hardness of the count spectrum giving systematically higher values of β than the BAND model. The mode of this parameter is -2.45 ± 0.1 and -2.05 ± 0.1 for the BAND and BPLW model, respectively.

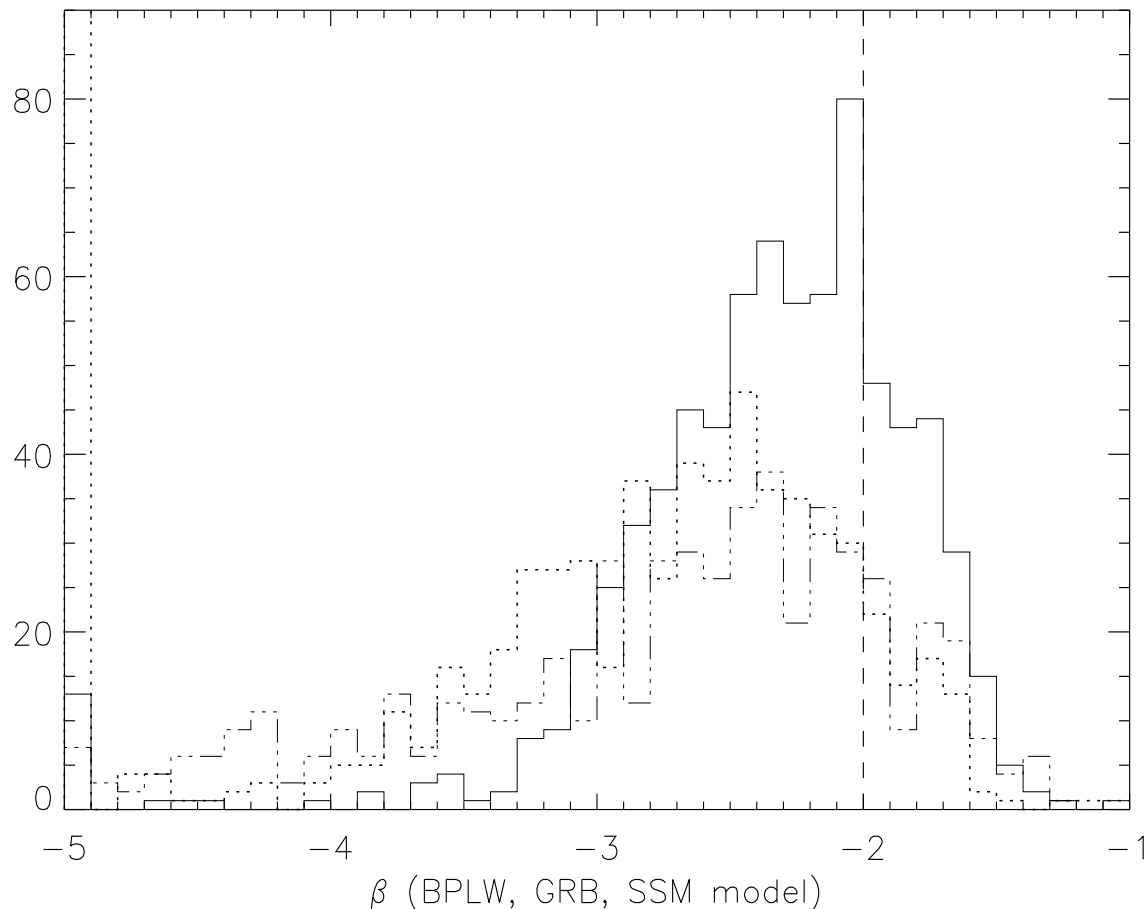


Figure 5.9: High energy power law spectral index (β) distributions for the time resolved spectra. *Solid line*: BPLW model; *dotted line*: BAND model; *dot-dashed line*: SSM model, in this case β is calculated from the δ parameter (see text). Also shown (bin with $\beta=-5$) the time resolved spectra with undetermined high energy spectral index for the BAND model. The dashed vertical line indicates the critical value $\beta = -2$.

The SSM average β is -2.17 which is consistent with what found from the average pulse spectral analysis. The average β value for the BAND model (-2.45 ± 0.1) is softer than the time averaged results, and the BPLW model value (-2.05) is consistent with the results of tab. 5.1.

In fig. 6.6 the critical value -2 is also indicated: spectra with $\beta \geq -2$ are rising in EF_E , and we can set only a lower limit to E_{peak} . These cases correspond to the 18% and 7% of the spectra fitted with the BAND and BPLW model and the 16% for the SSM. Notice that there is also a subclass of soft-spectra with $\beta \leq -3$ which are characterized by a very steep spectral tail: these spectra are clearly better fitted by the COMP model. The spread in these β distributions ($-4 \leq \beta \leq -1.5$) corresponds to what was found by Band et al. ([4]).

- *The spectral break.*

The most important spectral parameter obtained in fitting the spectrum with these models is E_{peak} . As just mentioned this characteristic energy can be obviously calculated only for those spectra (BPLW and BAND model) with $\beta < -2$.

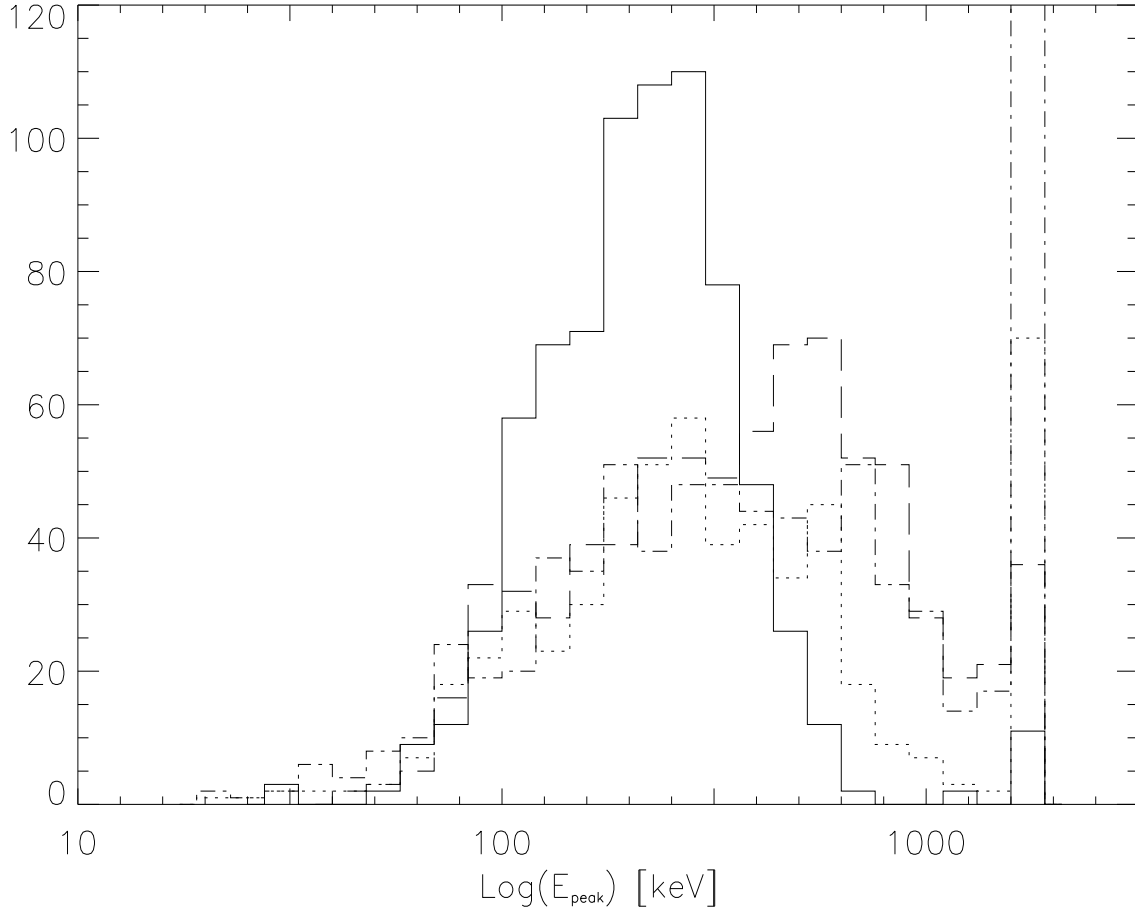


Figure 5.10: Peak energy distribution for the 4 spectral models. *solid line*: BPLW model, *dotted line*: BAND model, *dashed line*: COMP model, *dot-dashed line*: SSM model. Spectra with undetermined peak energy (i.e. the high energy threshold 1800 keV assumed as lower limit) are reported in the last bin.

In fig.5.10 the peak energy distributions for the various models are reported and it is also shown the bin with $E_{peak}=1800$ keV, assumed as lower limit of the peak energy for those spectra in which the BAND, BPLW or SSM model have $\beta \geq -2$.

The mode is $E_{peak} = 280^{+72}_{-57}$ keV for the BAND model, consistent, within its error, with the BPLW most probable value of 211^{+25}_{-22} keV. The COMP model, instead, gives a highly asymmetric peak energy distribution with a mode of 595^{+104}_{-88} keV because the lack of a high energy power law component tends to over-estimate the energy corresponding to the start of the exponential cutoff. The SSM model has an average $E_{peak} \sim 316^{+64}_{-52}$ keV with a wide distribution.

From the analysis of the average spectral shape, obtained from the time integrated and from the time resolved spectral analysis, we would like to stress that if we want

to characterize the spectral hardness it is necessary to extend the single parameter analysis, typically based on the peak energy or the hardness ratio, and consider the low and high energy spectral components (see chapt.7).

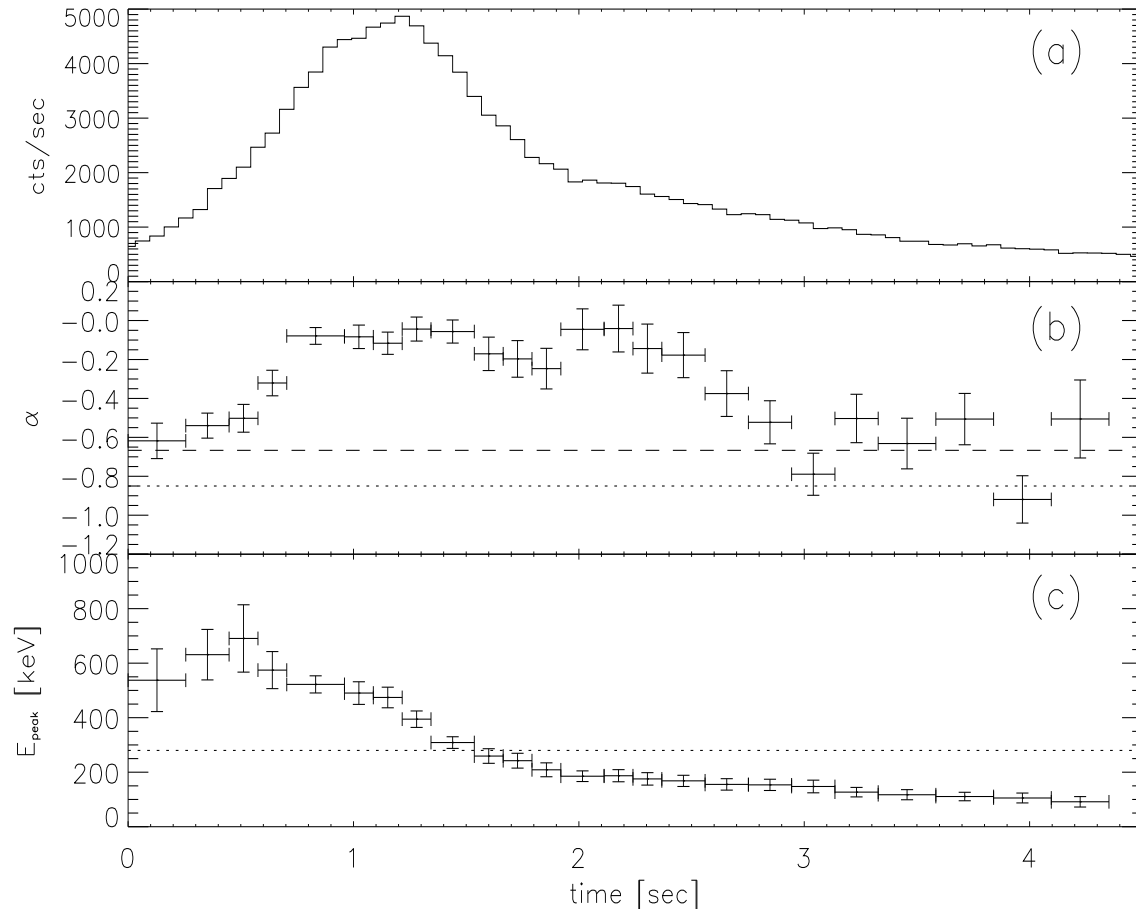


Figure 5.11: Trigger 2083. Spectral evolution of the BAND model parameters fitted to the time resolved spectra. Light curve on the 64ms time-scale (panel a) for the energy range 110–320 keV (corresponding to channel 3 of the detector); low energy spectral index and (*dashed*) synchrotron shock model limit $\alpha = -2/3$ (b); peak energy (c). For reference the average values of α and E_{peak} obtained from the time resolved spectra (*dotted line*) and the synchrotron model limit (*dashed line*) are reported.

5.3.3 The Synchrotron limit violation

A well known prediction of the optically thin synchrotron model is that the asymptotic low energy photon slope α should be lower than or equal to $-2/3$ (Katz et al. [77]). From the analysis of the time resolved spectra we obtain that not only the low energy

power law slope can violate this limit, but it can also evolve dramatically during a single pulse (as already found by Crider et al. [20],[21]).

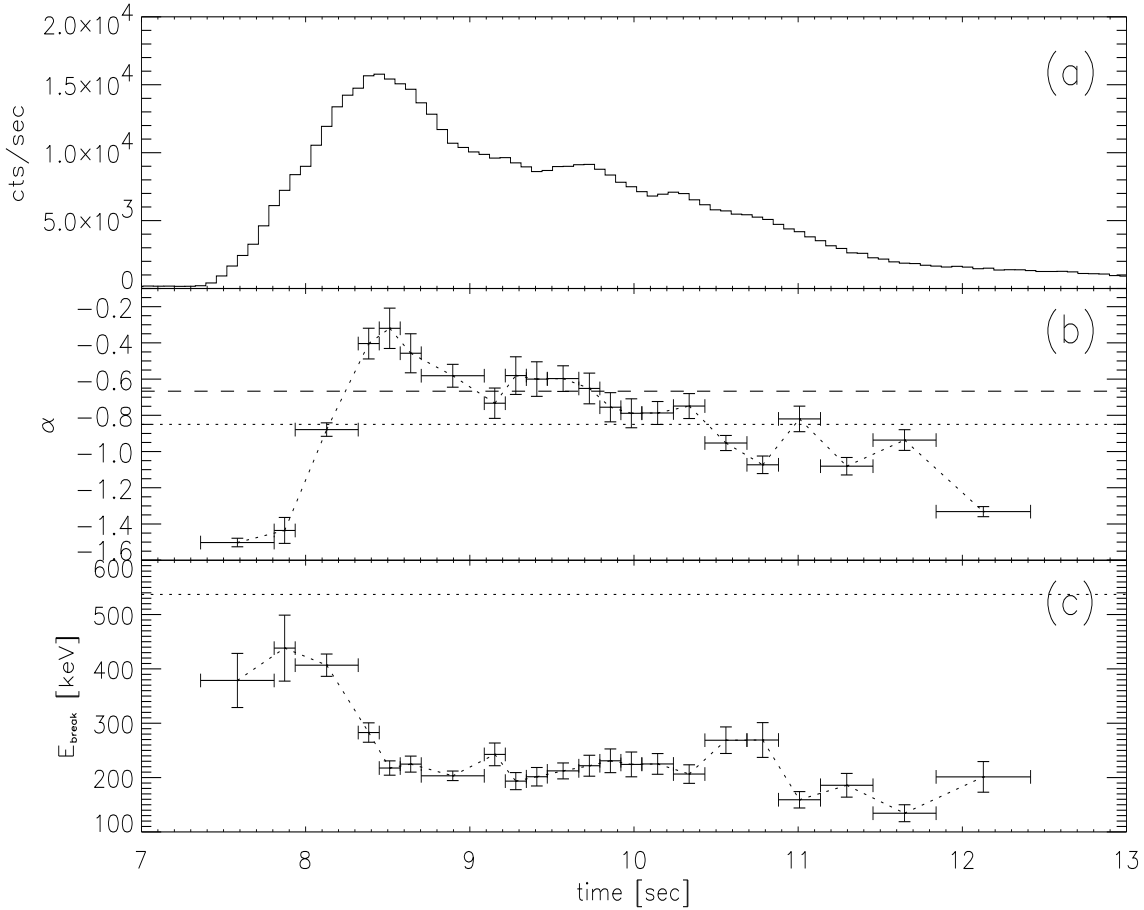


Figure 5.12: Trigger 5614. Spectral evolution of the COMP model fitted to the time resolved spectra. Light curve on the 64ms time-scale panel (a) for the energy range 110–320 keV (corresponding to channel 3 of the detector); low energy spectral index and (*dashed*) synchrotron shock model limit $\alpha = -2/3$ (b); peak energy (c). For reference are reported the average values of α and E_{peak} obtained from the time resolved spectra (*dotted line*) and the synchrotron model limit (*dashed line*).

We can characterize this behaviour, for example, via the BAND and COMP model fits (we exclude the BPLW model which, as showed above, tends to underestimate the hardness of the spectrum at low energies). We obtain that 14% of the time resolved spectra fitted with the BAND model are inconsistent with $\alpha \leq -2/3$ at 2σ . A similar percentage ($\sim 11.7\%$ of course mostly for the same spectra) of spectra violating the α limit is found for the COMP model.

For these extremely hard spectra no correlation between α and any other fit parameter is found, and the violation occurs both in the rise and decay phase of the pulses. The absence of correlation between the low energy spectral index α and the high energy spectral index β or the peak energy E_{peak} is shown in fig.5.13. Notice that the spectra

violating the low energy spectral limit of the optically thin synchrotron model have typical β and E_{peak} spectral parameters.

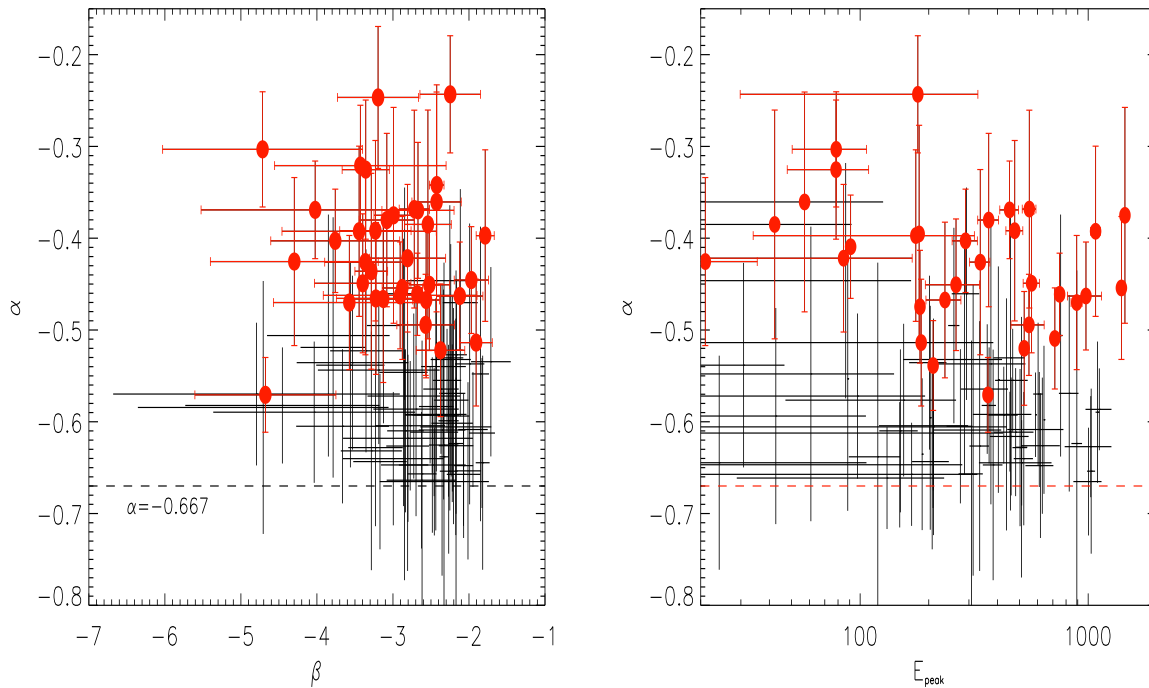


Figure 5.13: *Left*: Low energy spectral index α vs. the high energy spectral index β for the time resolved spectra fitted with the band model. The red points reported the subset of spectra which are harder than the optically thin synchrotron limit at 2σ . *Right*: Low energy spectral index α vs. the peak energy of the νF_ν spectrum in keV.

Moreover $\sim 21\%$ of the time resolved spectra corresponding to the peak time bin violate at 2σ the synchrotron limit, indicating that this violation happens during the peak phase and not preferentially before or after it. As an example in fig. 5.11 we show the spectral evolution of α in the case of trigger GRB921207 (BAND model). During the main peak ($t \in [0.0, 4.5]$ sec) the majority of the time resolved spectra violates the synchrotron model limit (*dashed line* in panel (c)). Notice that during this time interval the low energy spectral index evolves between $-2/3$ and 0.0 and the peak energy (panel (b)) decreases monotonically. Another interesting example is reported in fig. 5.12. GRB960924 shows a low energy spectral shape harder than $-2/3$ only around the peak, and the α evolution during the rise phase covers an interval of $\Delta\alpha \sim 1.4$.

The predictions of the synchrotron model have been recently discussed by Lloyd & Petrosian ([100], L&P2001). They claim that the low energy spectral limit $-2/3$ is not so constraining if (among other assumptions) an anisotropic pitch angle distribution is assumed for the emitting electrons (which should be the case in a low density and intense

magnetic field regime). In the case of small pitch angles ($\Psi \ll 1$) the emitted spectrum should be characterized by three components: a low energy flat count spectrum ν^0 (for $\nu \ll \nu_s \equiv 2/3 \nu_b / (\gamma_m \Psi^2)$) followed by the typical $\nu^{-2/3}$ power law (for $\nu_s \leq \nu \leq \nu_m$) and then by $\nu^{-(p+1)/2}$. p is the electron power law energy index, ν_s the break at the transition from the flat spectrum to the $-2/3$ slope, and ν_m represents the frequency corresponding to γ_m where the electron energy distribution is smoothly cut off (at low energies).

According to L&P2001 $\alpha \geq -2/3$ is allowed and the slope ν^α obtained from fitting a two component model (like the BAND function) to such a three components spectrum is typically an average between ν^0 and $\nu^{-2/3}$. During the emission the electrons cool so that their low energy limit γ_m decreases and as a consequence the peak energy becomes softer $E_{peak} \propto \gamma_m^2$. The electrons average pitch angle decreases (although their distribution can be still anisotropic) and this causes the frequency $\nu_s \propto (\gamma_m \Psi^2)^{-1}$ to increase. The spectral evolution predicted by this model then is of hardening of the low energy power law – because of the progressive disappearance of the $\nu^{-2/3}$ spectral component – while the peak energy naturally evolves from hard to soft. Thus in bursts violating the synchrotron limit, a negative correlation between the peak energy and the low energy spectral index is expected.

We report in fig. 5.14 as an example the evolution during GRB 920525 which shows a low energy spectral component harder than $-2/3$ during the main peak (for ~ 2 sec). We note (panel (b) and (c) in fig. 5.14) that there is no evidence of negative correlation between the peak energy and α : during the rise phase of the flux (panel (a)) the peak energy increases regardless of the rise and partial decay of the spectral index, while for the rest of the pulse the peak energy decreases and α varies above the $-2/3$ limit.

The same happens for GRB 921207 (fig. 5.11) and GRB 960529 (fig. 5.15): in these bursts the peak energy decreases while α goes above and below the synchrotron limit and this is not in agreement with the above prediction of this model.

5.4 Conclusions

We considered a sample of bright bursts detected by BATSE and performed a uniform analysis for the time integrated and the time resolved spectra with four different models proposed in the literature.

We find that even with this time resolution no parametric model can better represent the data and different spectra require different shapes, reconfirming the erratic behaviour of bursts and also possibly indicating that time resolution on timescales comparable with the variability timescale is needed to shed light on such erratic characteristics.

Indeed, an important result we confirm is that the average time integrated spectrum often used in the literature does not well represent the very same event resolved on shorter time-scales. The time integrated spectra might still be used for a comparison of

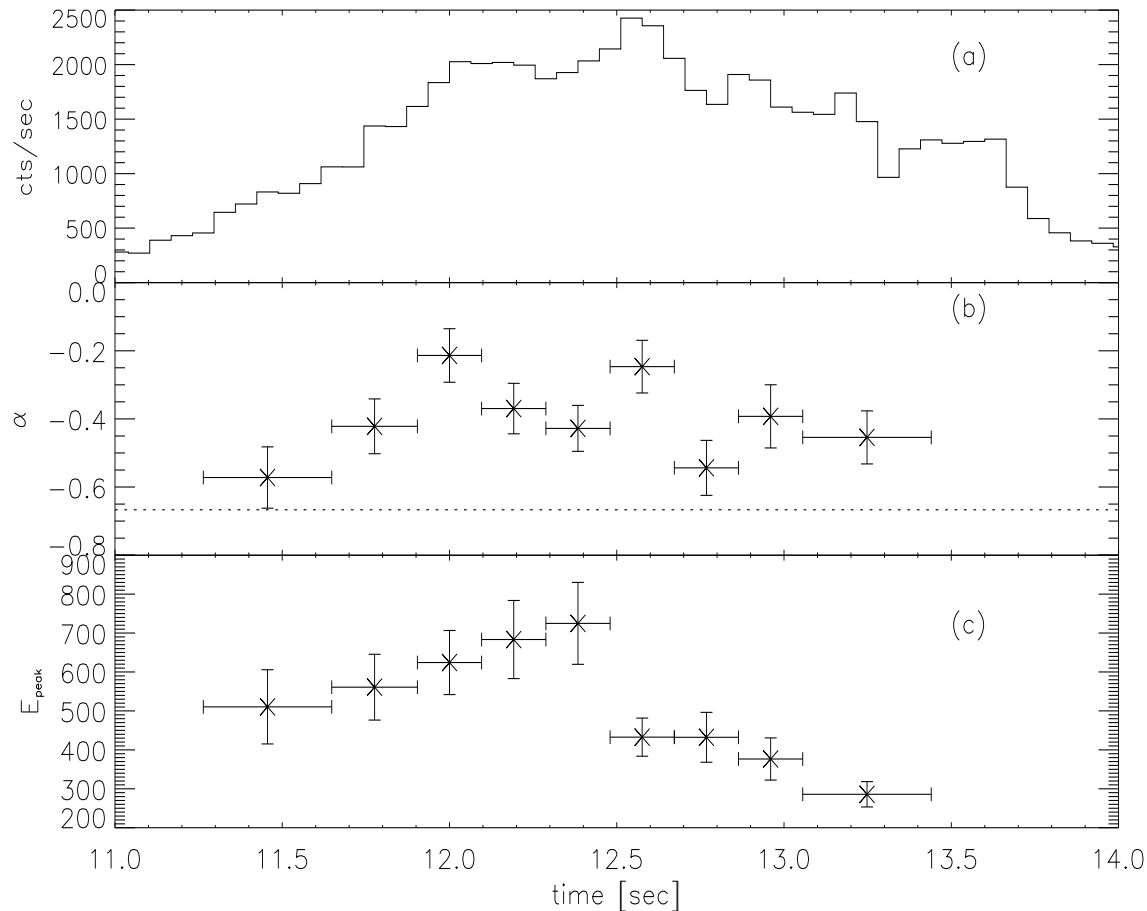


Figure 5.14: Trigger 1625. Spectral evolution of the BAND model parameters fitted to the time resolved spectra. Light curve on the 64ms time-scale (panel a) for the energy range 110–320 keV (corresponding to channel 3 of the detector); low energy spectral index and (*dashed*) synchrotron shock model limit $\alpha = -2/3$ (b); peak energy (c).

the average spectral shape among different pulses and as indicators of the average spectral parameters of the time resolved analysis although only the time resolved spectra should be used in any test of a physical emission model.

Finally, a considerable number of the fitted spectra are characterized by extremely hard low energy components with spectral index α greater than $-2/3$, a value predicted by synchrotron theory (Katz [77]). This violation was found by Crider et al. ([21]) and has been recently reported by Frontera et al. ([47]) in some GRBs observed by BeppoSAX. They report 1 sec time resolved spectra significantly harder than $E^{-2/3}$, mainly during the first phase of the burst emission. We have found that in 11 of the 25 bursts analyzed the α limit violation is evident mainly in the spectra around the peak both during the rise and decay phase, and this could indicate that at least at some stages of the burst evolution – possibly near the peak of emission itself – radiative processes, other than synchrotron, can dominate the emission.

We also reported some examples of bursts which violate the synchrotron limit and

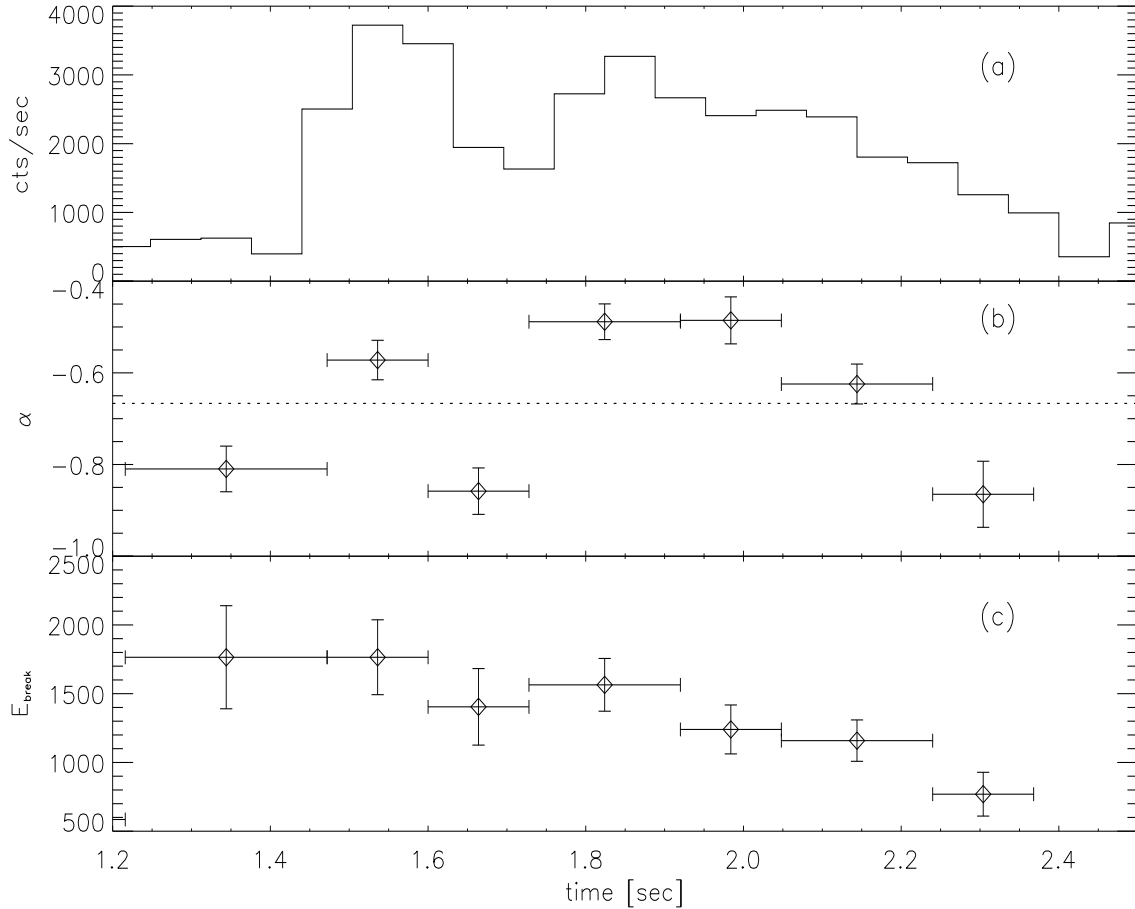


Figure 5.15: Trigger 5477. Spectral evolution of the COMP model parameters fitted to the time resolved spectra. Light curve on the 64ms time-scale (panel a) for the energy range 110–320 keV (corresponding to channel 3 of the detector); low energy spectral index and (*dashed*) synchrotron shock model limit $\alpha = -2/3$ (b); peak energy (c).

are not characterized by the α – E_{peak} anticorrelation predicted by the small pitch angle distribution synchrotron model proposed by Lloyd & Petrosian ([100]).

Alternative models, other than synchrotron, have been proposed also to justify this important observational evidence of low energy spectral components harder than $-2/3$. Among these, the jitter model (Medvedev [106] - see chapt.3, sec. 3.2.5) predicts that the synchrotron emission by relativistic electrons in a non uniform magnetic field, with a small scale structure, can have spectral slopes as hard as $N(E) \propto E^0$, at low energies. Even harder spectra, i.e. E^1 , are predicted by synchrotron self absorption (e.g. Papathanassiou [123]).

Other emission models which can produce low energy spectra harder than the synchrotron limit are thermal or quasi-thermal saturated Comptonization (Liang et al [97], Ghisellini & Celotti [55]), whose spectrum can be as hard as $N(E) \propto E^2$, or Compton attenuation of a seed spectrum by a cold absorber (Brainerd et al. [12]).

Also photospheric emission by the fireball which becomes transparent can be a solution in explaining these hard spectra, also supported by the results presented in chapt.6, since it can produce a low energy spectrum with slope $N(E) \propto E^1$. (Meszaros & Rees [113], Daigne & Mochovitch [25]).

All these alternatives can reproduce the observed low energy hard spectra (15 %) which violate the synchrotron model limit (i.e. with $\alpha > -2/3$).

These results indicate that these models should be compared with other more constraining observational evidences. The search of harder low energy spectra and the analysis of the spectral evolution through the definition of correlations with other burst properties are the contents of the following chapters.

Table 5.2: The GRB sample

<i>Trigger</i> ^a	<i>GRB</i>	<i>Data Type</i> ^b	<i>Detector</i>		<i>PeakFlux</i> ^c [<i>phot/cm²/sec</i>]	<i>Background</i>		<i>Peak</i> ^e	<i>Spectra</i> ^f	<i>S/N</i> ^g ≥
			<i>Number</i>	<i>Rank</i>		<i>#</i> ^d	<i>n</i> ^d			
143	910503	<i>HERB</i>	<i>LAD6</i>	1	52.08 ± 1.43	8	3	4	49	–
1473	920311	<i>HERB</i>	<i>LAD5</i>	1	25.31 ± 0.7	6	2	3	55	–
1541	920406	<i>SHERB</i>	<i>SD2</i>	2	38.32 ± 0.89	5	2	1	9	15
1609	920517	---	---	–	67.59 ± 1.21	–	–	–	–	–
1625	920525	<i>HERB</i>	<i>LAD4</i>	1	28.06 ± 0.74	8	4	3	25	–
1711	920720	---	---	–	21.7 ± 0.7	–	–	–	–	–
1997	921022	---	---	–	40.33 ± 0.85	–	–	–	–	–
2083	921207	<i>HERB</i>	<i>LAD0</i>	1	46.55 ± 0.92	6	2	2	31	–
2151	930131	---	---	–	167.84 ± 2.63	–	–	–	–	–
2329	930506	<i>SHERB</i>	<i>SD2</i>	4	42.57 ± 0.90	11	4	1	42	–
2431	930706	---	---	–	43.83 ± 0.89	–	–	–	–	–
2537	930922	<i>HERB</i>	<i>LAD1</i>	1	27.28 ± 0.7	31	4	3	23	45
2611	931031	---	---	–	35.05 ± 0.89	–	–	–	–	–
2798	940206	<i>HERB</i>	<i>LAD3</i>	1	24.19 ± 0.73	7	3	1	16	–
2831	940217	<i>HERB</i>	<i>LAD0</i>	1	44.34 ± 1.08	10	4	3	28	–
3412	950211	---	---	–	54.82 ± 0.76	–	–	–	–	–
3480	950325	---	---	–	21.61 ± 0.51	–	–	–	–	–
3481	950325	<i>HERB</i>	<i>LAD2</i>	1	25.7 ± 0.6	6	4	3	27	–
3491	950403	<i>HERB</i>	<i>LAD3</i>	1	30.65 ± 0.62	6	3	3	44	45
3492	950403	<i>HERB</i>	<i>LAD5</i>	1	61.44 ± 0.91	6	4	1	22	45
3523	950425	<i>HERB</i>	<i>LAD6</i>	1	21.81 ± 0.53	4	2	2	50	–
4368	960114	<i>SHERB</i>	<i>SD0</i>	1	58.61 ± 0.83	8	4	3	29	45
5477	960529	<i>HERB</i>	<i>LAD1</i>	1	29.35 ± 0.70	7	4	2	12	–
5563	960804	<i>HERB</i>	<i>LAD4</i>	1	22.7 ± 0.59	7	4	1	8	–
5567	960807	<i>HERB</i>	<i>LAD0</i>	1	22.8 ± 0.6	6	4	5	25	45
5614	960924	<i>SHERB</i>	<i>SD6</i>	1	183.37 ± 1.62	12	4	1	22	–
5621	961001	<i>HERB</i>	<i>LAD2</i>	1	25.64 ± 0.61	31	4	2	17	–
5704	961202	<i>HERB</i>	<i>LAD0</i>	1	43.93 ± 0.76	26	4	1	13	–
5711	961212	---	---	–	41.25 ± 0.71	–	–	–	–	–
5989	970201	---	---	–	77.61 ± 0.89	–	–	–	–	–
6198	970420	<i>HERB</i>	<i>LAD4</i>	1	66.5 ± 0.9	12	4	1	38	–
6293	970704	---	---	–	88.53 ± 1.	–	–	–	–	–
6404	970930	<i>HERB</i>	<i>LAD6</i>	1	24.01 ± 0.52	21	4	2	22	–
6581	980125	<i>HERB</i>	<i>LAD0</i>	1	40.91 ± 0.69	15	4	1	17	–
6904	980706	---	---	–	54.62 ± 0.87	–	–	–	–	–
7301	990104	<i>HERB</i>	<i>LAD7</i>	1	86.53 ± 0.93	12	4	5	24	–
7549	990506	<i>HERB</i>	<i>LAD7</i>	1	25.12 ± 0.58	9	4	6	52	–
7647	990712	---	---	–	24.06 ± 0.51	–	–	–	–	–

^a Burst reference number from the Gamma Burst Catalog at
<http://gammaray.msfc.nasa.gov/batse/grb/catalog/current/>

^b (S)HERB: (Spectroscopic) High Energy Resolution Burst data.

^c Peak flux on the 64 ms time-scale, integrated over the 50 - 300 keV energy range.

^d Background is calculated on ” # ” number of spectra and with a polynomial function of degree ”n”.

^e Number of pulses spectroscopically analyzed within each burst.

^f Number of time resolved spectra per burst.

^g S/N method used in grouping the time resolved spectra accumulated by the instrument.

Table 5.3: The pulse average spectral results: for each trigger (col. 1) the best fit parameters, of the four models described in the text, are reported: for multi peaked bursts all the peaks have their set of spectral parameters. The pulses which violate the low energy synchrotron limit are reported in *Italics*. Energy is in keV. α and β represent the photon spectral index as defined for the 4 models presented in the chapter.

Trigger	BAND				BPLW				COMP			SSM		
	α	β	E_0^a	χ_r^2	α	β	E_0^a	χ_r^2	α	E_0^a	χ_r^2	E_0^a	δ	χ_r^2
143	<i>-0.59±0.02</i>	<i>-2.16±0.09</i>	<i>569±33</i>	<i>1.8</i>	-0.79±0.01	-1.88±0.03	335±10	1.4	-0.67±0.01	736±25	2.1	1208±136	7.2±1.8	3.2
					-0.89±0.01	-2.09±0.04	423±14	1.1	-0.72±0.01	755±25	1.5	1184±191	10.	2.22
	-0.79±0.02	-3.21±0.45	568±24	1.6	-1.00±0.01	-2.24±0.04	358±10	1.1	-0.80±0.01	590±17	1.6	728±64	8.8±2.3	2.0
1473	-1.37±0.03	-2.49±0.25	677±79	1.5	-1.52±0.01	-2.27±0.06	281±18	1.4	-1.4±0.02	784±61	1.5	86 ±5	3.0±0.06	2.4
	-0.62±0.04	-2.2 ±0.09	326±27	1.2	-1.15±0.02	-1.89±0.01	137±6	1.1	-1.09±0.01	467±25	1.3	600 ±88	8.2±3.5	1.5
	-0.58±0.04	-2.2 ±0.06	280±22	1.6	-0.94±0.02	-1.96±0.03	210±7	2.2	-0.78±0.02	444±20	1.9	553 ±68	8.6±3.1	1.9
1541	-0.63±0.03	-3.2 ±0.16	183±6	1.7	-1.15±0.01	-2.41±0.03	181±2.8	4.6	-0.68±0.02	198±5.0	1.9			
	-0.9±0.04	-1.98±0.04	248±24	1.0					-0.76±0.03	460±24	1.4	150±10	3.4±0.1	1.0
	-0.88±0.02	-2.07±0.07	608±42	0.9	-1.06±0.01	-1.90±0.03	300±11	1.1	-0.96±0.01	873±35	1.3	422 ±24	3.7±0.2	1.0
1625	<i>-0.58±0.02</i>	<i>-2.79±0.15</i>	<i>343±15</i>	<i>1.4</i>	-0.89±0.01	-2.28±0.04	283±7.	1.7	-0.64±0.02	390±12	1.6	680 ±82	10	3.2
	-0.71±0.02	-3.75±0.6	256±10	1.2	-1.09±0.01	-2.62±0.05	244±5.7	1.7	-0.72±0.02	262±8.8	1.2	392 ±39	10	2.6
	-0.80±0.01	-2.71±0.07	261±7.4	3.1					-0.87±0.01	309±6.3	3.8	343 ±18	10.	3.2
2083	-0.71±0.04	-3.4 ±0.12	78 ±3.	2.2	-1.44±0.02	-2.94±0.04	106±1.8	3.2	-0.81±0.03	87 ±2	2.3	106 ±6.5	10.	4.8
	-1.09±0.01	-1.78±0.03	1136±65	2.6	-1.17±0.01	-1.69±0.01	311±10	2.2				175 ±4	2.3±0.02	6.0
	-1.05±0.05	-2.7 ±0.08	135±11	1.9	-1.55±0.02	-2.57±0.05	130±5	2.3	-1.25±0.03	193±10	2.5	84 ±4	5. ±0.2	1.8
2537	-1.08±0.06	-2.69±0.06	109±9	2.9	-1.62±0.02	-2.58±0.04	108±3.	3.6	-1.33±0.03	169±8.7	3.6	65 ±3	5.0±0.2	2.8
	-1.17±0.05	-2.85±0.06	95 ±7	4.3					-1.4 ±0.03	137±6.	4.7	53 ±2.	5.4±0.2	3.9
	-0.86±0.01	-2.4 ±0.06	507±15	2.0	-1.07±0.01	-2.07±0.01	291±5	2.8	-0.9 ±0.01	607±12	2.5	513 ±20	6.0±0.5	2.3
2831	-0.54±0.04	-5.0	870±112	1.6	-0.70±0.02	-1.88±0.05	451±23	1.7	-0.52±0.03	804±41	1.6	1919±577	7.±5.	2.9
	-0.49±0.03	-3.25±1.60	660±55	1.6	-0.72±0.02	-2.08±0.06	458±19	1.4	-0.50±0.03	676±32	1.6	1786±605	10.	3.2
					-0.93±0.02	-1.96±0.06	412±25	1.18	-0.80±0.02	900±57	1.3	1033±208	6.7±3.1	1.4
3481	<i>-0.59±0.06</i>	<i>-2.54±0.20</i>	<i>209±20</i>	<i>1.3</i>	-1.03±0.02	-2.28±0.08	200±10	1.8	-0.67±0.04	249±17	1.4	391 ±91	10	1.6
	-0.85±0.02	-2.1 ±0.04	337±18	1.6	-1.11±0.01	-1.99±0.02	209±5.6	2.4	-0.97±0.01	511±18	2.4	276 ±12	4.0±0.2	1.5
	-1.09±0.04	-2.55±0.12	194±16	1.9	-1.33±0.03	-2.13±0.03	104±4	2.4	-1.16±0.03	236±14	1.9	101 ±6	4.4±0.2	1.6
3491	-0.92±0.05	-2.11±0.09	298±37	1.1	-1.19±0.02	-1.98±0.04	175±9	1.2	-1.04±0.03	450±37	1.2	201 ±19	3.8±0.3	1.1
	-1.09±0.05	-2.2 ±0.12	394±57	1.1	-1.29±0.02	-2.03±0.05	186±13	1.0	-1.19±0.03	574±54	1.2	147 ±13	3.4±0.2	1.2
	-0.93±0.04	-2.6 ±0.09	197±12	1.3	-1.28±0.02	-2.30±0.03	145±4	1.5	-1.04±0.02	252±11	1.6	165 ±9	6.7±0.4	1.2
3492	-1.05±0.02	-2.38±0.07	546±27	1.3	-1.25±0.01	-2.15±0.02	292±8	1.5	-1.11±0.01	702±21	1.8	243 ±8	3.7±0.1	2.0
					-0.96±0.01	-1.77±0.01	315±6.8	1.5	-0.87±0.01	1003±24	2.6	682 ±31	3.9±0.2	1.7
4368	-1.76±0.02	-5.	813±113	1.1	-1.87±0.01	-2.42±0.04	218±15	1.2	-1.78±0.02	782±60	1.0	31 ±1.4	3.3±0.03	1.7
	-1.73±0.03	-2.9 ±0.16	357±30	1.4	-1.91±0.01	-2.58±0.04	155±7	1.5	-1.76±0.02	410±25	1.3	37. ±1.	3.9±0.05	1.7
5477					-0.79±0.03	-1.38±0.04	288±31	0.9	-0.78±0.03	1765±192	1.0	937 ±208	2.3±0.3	0.9

continued on next page

Table 5.3: *continued*

Trigger	BAND				BPLW				COMP			SSM		
	α	β	E_0^a	χ_r^2	α	β	E_0^a	χ_r^2	α	E_0^a	χ_r^2	E_0^a	δ	χ_r^2
					-0.87±0.01	-1.66±0.07	602±56	1.3	-0.80±0.02	1765±120	1.8	925 ±126	2.3±0.2	1.6
5563	-1.00±0.07	-2.53±0.11	169±20	1.2	-1.42±0.03	-2.36±0.05	140±7	1.2	-1.15±0.04	236±17	1.3	118 ±9.7	4.9±0.4	1.2
5567	-1.93±0.11	-5.0	442±244	1.2	-2.10±0.06	-2.42±0.17	114±34	1.2	-1.93±0.10	436±195	1.1	25±5	3.7±0.2	1.1
	-1.58±0.07	-2.26±0.36	686±282	1.2	-1.69±0.03	-2.28±0.17	219±40	1.1	-1.61±0.04	861±242	1.2	35 ±6	2.9±0.1	1.4
	-1.38±0.05	-3.19±2.8	403±62	1.3	-1.58±0.02	-2.42±0.12	194±17	1.2	-1.39±0.04	413±52	1.3	74 ±7	3.5±0.2	1.6
	-1.32±0.03	-3.3 ±1.2	570±58	1.6	-1.5 ±0.01	-2.45±0.08	271±16	1.4	-1.32±0.02	584±47	1.6	102 ±6.	3.3±0.1	2.8
	-1.13±0.02	-2.8 ±0.2	532±38	1.4	-1.3 ±0.01	-2.18±0.04	242±10	1.3	-1.15±0.02	578±29	1.5	180 ±9	3.7±0.1	2.2
5614				-1.22±0.01	-2.67±0.03	227±3	3.4	-0.9 ±0.01	273±5.	1.4	277 ±10	10.0		
5621	-0.70±0.04	-2.13±0.04	193±14	1.2	-1.08±0.02	-2.00±0.02	144±4.	1.8	-1.02±0.02	400±17	2.4	213 ±11	4.3±0.2	1.5
	-0.99±0.09	-2.2 ±0.06	156±26	1.2	-1.19±0.07	-2.05±0.03	86 ±5.	1.2	-1.30±0.04	323±32	1.5	90. ±8.	3.9±0.2	1.1
5704	-1.21±0.07	-2.7 ±0.28	190±24	0.9	-1.60±0.03	-2.51±0.08	146±9	1.0	-1.26±0.05	215±19	0.9	85 ±9	4.6±0.4	1.0
6198	-1.03±0.01	-2.53±0.06	317±11	1.7	-1.30±0.01	-2.23±0.02	196±3.	2.4	-1.1 ±0.01	387±10.	2.4	184 ±5.	4.5±0.1	2.2
6404	-0.06±0.2	-1.9 ±0.05	68 ±15	1.0	-0.89±0.09	-1.90±0.04	89.±5.	1.1	-0.87±0.07	207±21	1.3	180 ±35	5.5±1.7	1.2
	-0.19±0.14	-2.6 ±0.12	65 ±8	1.1	-1.05±0.06	-2.41±0.06	96 ±4	1.5	-0.53±0.08	92 ±6	1.4	159 ±36	10.	2.3
6581	-1.43±0.08	-2.07±0.29	549±209	0.8	-1.55±0.04	-1.92±0.07	146±23	0.8	-1.50±0.05	730±179	0.8	51.6±8.	2.8±0.1	0.8
7301	-1.14±0.16	-2.3 ±0.1	127±31	0.7	-1.6 ±0.06	-2.3 ±0.06	96 ±8	0.8	-1.4 ±0.06	240±33	0.9	59 ±7	4. ±0.3	0.8
	-1.10±0.03	-3.0 ±0.4	372±28	1.1	-1.37±0.01	-2.45±0.07	250±11	1.5	-1.12±0.02	392±23	1.2	172 ±11	4.2±0.3	1.4
	-0.89±0.02	-2.3 ±0.10	500±33	1.3	-1.11±0.01	-2.06±0.04	290±10	1.8	-0.95±0.02	621±26	1.5	398 ±26	4.6±0.4	1.3
	-1.16±0.04	-2.27±0.18	546±78	0.9	-1.33±0.02	-1.99±0.05	222±16	1.1	-1.2 ±0.03	677±64	0.9	137 ±11	3.0±0.1	0.9
	-1.17±0.04	-1.87±0.1	724±153	0.8	-1.3 ±0.02	-1.8 ±0.05	230±23	0.8	-1.25±0.02	1184±153	0.8	114 ±11	2.5±0.1	0.9
7549					-1.19±0.01	-1.76±0.02	247±11	1.5	-1.13±0.01	1192±59	1.4	182±8	2.6±0.05	1.7
	-0.98±0.03	-2.5 ±0.3	494±46	1.2	-1.19±0.01	-2.17±0.07	282±15	1.4	-1.01±0.02	558±36	1.2	276±22	4.0±0.3	1.3
	-0.68±0.02	-2.64±0.18	397±23	1.1	-0.94±0.01	-2.07±0.04	262±8.3	1.9	-0.72±0.02	446±18	1.2	650 ±82	8.7±3.2	1.7
	-0.97±0.03	-2.2 ±0.07	277±22	1.2	-1.28±0.01	-2.08±0.04	180±7	1.8	-1.09±0.02	396±21	1.6	161 ±9	3.8±0.2	1.1
	-0.84±0.02	-2.67±0.09	201±8	2.0	-1.22±0.01	-2.24±0.03	156±3.1	4.3	-0.91±0.02	232±7	2.3	231 ±15	8.4±1.6	1.7

Chapter 6

Extremely hard GRB spectra prune down the forest of emission models

In this chapter the evidence of very hard low energy spectra during the prompt phase of Gamma Ray Bursts are presented and discussed. In particular we examine the spectral evolution of GRB 980306, 911118, 910807, 910927 and 970111 and check for the significance of their hardness by applying different fitting models. These are among the hardest bursts, sufficiently bright to allow time resolved spectral studies on time intervals of the order of tenths of a second. The hard spectra of these bursts at low energies and their evolution are discussed in the context of several non-thermal emission models, which have been introduced in chapt.3. It will be shown that most of these models appear inadequate to account for these cases.

The extremely hard spectra of these 5 GRBs at the beginning of their prompt emission are also compared with a black body spectral model: the resulting fits are remarkably good, except for an excess at high energies (in several cases) which could be simply accounted for by the presence of a supra-thermal component. These new findings on the possible thermal character of the evolving spectrum and the implications for the GRB physical scenario are considered in the framework of photospheric models, for a fireball which is becoming optically thin, and of Compton drag model, in which the fireball boosts “ambient” seed photons by its own bulk motion. Both these models appear to be qualitatively and quantitatively consistent with the found spectral characteristics.

6.1 Introduction

In chapt.2 the properties of the γ -ray spectrum of GRBs have been reviewed and in chapt.5 we presented and discussed the spectral properties of a sample of bright bursts has been .

From the observational point of view, it is clear that GRB spectra can have quite different shapes among different bursts and can also remarkably evolve with time within

the same GRB. Moreover, different spectral models can adequately fit the time resolved/integrated spectra (chapt.5). Nevertheless, these spectral functions are characterized by a common shape: a low energy power law, typically represented as $N(E) \propto E^\alpha$ (i.e. $EF_E \propto E^{\alpha+2}$), which joins, either sharply or smoothly, to a high energy component which can either be another powerlaw or an exponential cutoff.

From the theoretical point of view, the majority of emission models, which have been proposed to be responsible for the GRB prompt emission phase (chapt.3), make constraining predictions on the low energy spectrum which can be directly compared with observations.

The most popular GRB emission model is synchrotron emission by relativistic electrons in intense magnetic fields (Rees & Meszaros [133]; Katz [77]; Tavani [154]). Optically thin synchrotron emission predicts that the low energy photon spectrum can not be harder than $N(E) \propto E^{-2/3}$. Nonetheless, different authors (Crider et al. [21], Preece et al. [130]) have found violations of this limit in many observed spectra. Following these inconsistencies between the standard synchrotron model and observations, alternative scenarios have been proposed, such as Comptonization of low energy photons by thermal or quasi-thermal particles (Liang et al. [96]; Ghisellini & Celotti [55]). Furthermore, more complex variants of these basic emission processes have also been postulated, such as jitter radiation (Medvedev [107]), synchrotron emission from an anisotropic pitch angle distribution of particles (Lloyd & Petrosian [98],[100]); thin/thick synchrotron emission from a stratified region (Granot, Piran & Sari [63]); synchrotron self-Compton or inverse Compton off photospheric photons (Meszaros & Rees [113]); Compton drag (Lazzati et al. [91]; Ghisellini et al. [56]).

The physical parameters of these models can be tuned and combined to justify the principal observed temporal and spectral characteristics of GRBs, producing a considerable number of plausible spectral shapes, but the most extreme (in this case hardest low energy) observed spectra and their evolution can be used to rule out or constrain some possibilities.

Another relevant aspect of GRB spectra is their possible thermal character. In fact, the fireball model (Goodman [61], Paczynski [119]) naturally predicts thermal radiation when the fireball becomes transparent. The lack of **observational** evidence of thermal spectra motivated the proposal of the internal shock model (Rees & Mészáros [133]) in which the fireball energy could be efficiently extracted and transformed into radiation with a non-thermal spectrum as observed in most bursts. Nonetheless, evidence for possible thermal spectra in some GRBs has been reported by Preece ([131]) for GRB 970111 and Schaefer et al. (poster P-56 presented at the Rome 1998 Whorkshop on GRBs, private communication). Furthermore Blinnikov et al. ([1999]) propose that also the spectra observed in most GRBs could be interpreted as superposition of black body spectra with different temperatures. From a theoretical point of view thermal emission from the fireball is expected if the dominant acceleration agent is internal pressure (Daigne & Mochovitch [25] 2002). Alternatively, magnetic acceleration (e.g. by Poynting flux) would determine a non-thermal spectrum (Drenkhahn & Spruit [32]). The analysis

of spectra with a possible thermal character can therefore have important implications for the understanding of the nature of the fireball acceleration mechanism.

To the aim of testing the validity/generalizability of the proposed models we have then searched in the published spectral catalogue of Preece et al. ([130]) the bursts with a low energy time resolved spectrum harder than E^0 which represents a limit for most of the above models (see sec.6.1.1). We found two extremely hard bursts: GRB 911118 (whose peak energy spectral evolution has been reported in Ford et al. [42] spectral catalogue) and a new case, GRB 980306. These two GRBs are carefully studied here in terms of their low energy spectral hardness and especially their spectral evolution on timescales of few tenths of a second, together with other hard bursts reported by Crider et al. ([24]): GRB 910807, GRB 910927 and GRB 970111 (sec.6.4). These bursts have been re-analyzed in order to test the reliability of their low energy spectral hardness. In fact, we present the tests that we performed in order to determine the statistical robustness of the spectral hardness, and in particular a model independent approach consisting in the comparison of each spectrum with a template one of given hardness (sec.6.3.3). The evidence that at least at the beginning of the bursts the spectra could have a black body character is discussed in sec.6.5. The comparison with the low energy spectral limits predicted by different models (briefly recalled in sec. 1.2 together with the previous evidence of hard spectra) is the content of the discussion (sec.6.6) where also some possible interpretations of the initial quasi-thermal spectral evolution, in the context of the hot fireball model and in the Compton drag model, are presented. We draw our conclusions in sec.6.8.

6.1.1 Spectral slopes and emission models

The majority of GRB spectra (Preece et al. [130], and chapt.5) have a low energy power law spectral index $-3/2 < \alpha < -2/3$, i.e. within the limits predicted by the optically thin synchrotron model (Fig. 6.2, *dashed lines*; see also Katz [77]), but there is a non negligible fraction of bursts ($\sim 15\%$, see also Preece et al. [130]) showing a slope harder than $\alpha = -2/3$. The spectral analysis of a GRB sample by Crider et al. ([21]) revealed that the spectrum, integrated over the pulse rise phase, is harder than $E^{-2/3}$ for the 40% of their bursts and can be as hard as $N(E) \propto E^1$ (i.e. $EF_E \propto E^3$).

For comparison in fig.6.1 are reported the distributions of the low energy spectral index α of the sample of bright long bursts already presented in chapt.5 (solid line), and for the time resolved spectra of the bursts discussed in this chapter (gray histogram). It shows that the latter distribution extends the possible slope of the low energy spectrum up to $E^{1.5}$.

Let us here just recall that this evidence is hardly reconcilable with the simplest formulation of the synchrotron model (predicting a limiting value $\alpha = -2/3$) and some alternatives have been proposed to account for these observations within the frame of this emission process (Papathanassiou [123], Granot, Piran & Sari [63] - see chapt.3 for more details). Lloyd & Petrosian ([98]) propose a scenario in which electrons have a

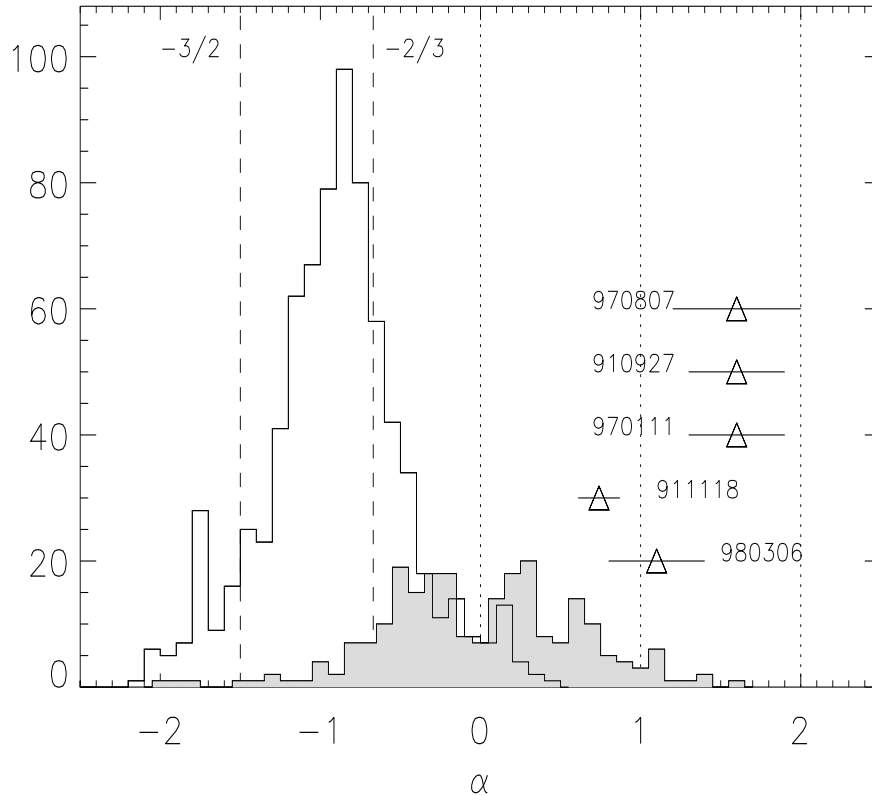


Figure 6.1: Low energy spectral index distribution from Ghirlanda et al. ([51]). The vertical lines represent the limits of the emission models reported in tab. 6.1 and plotted in fig. 6.2. *Triangles* represent the maximum values found from the spectral analysis of the bursts presented in this work along with their 90% confidence interval (horizontal bars). The gray histogram shows the distribution of the low energy spectral index for the same bursts.

small pitch angle distribution (SPD in fig. 6.2), extending the range of possible low energy spectral indices produced via synchrotron to the limit $\alpha \sim 0$. The same limiting slope can be obtained in the “jitter” radiation theory, which results from synchrotron emission in a non uniform magnetic field with inhomogeneities on length scales smaller than the electron gyro-radius (Medvedev [107]). Slopes even harder (i.e. $\alpha \sim 1$) may instead correspond to thermal radiation, such as a portion of a black body spectrum or saturated Comptonization spectra with Wien peaks which can be as hard as $\alpha \sim 2$ (Liang et al. [96], Ghisellini & Celotti [55], Ghisellini et al. [56]).

As reference for the following sections tab. 6.1 summarizes the model predictions for the low energy spectral index. In fig.6.2 the corresponding spectral slopes are represented and, for comparison, the typical BAND and COMP spectral functions are displayed.

Table 6.1: Low energy limiting photon spectral index α [i.e. $N(E) \propto E^\alpha$] for various emission models. For clarity the indices in flux $F(E)$ and $EF(E)$ representations are also reported.

$N(E) \propto E^\alpha$ phot/cm ² s keV	$F(E) \propto E^{\alpha+1}$ keV/cm ² skeV	$EF_E \propto E^{\alpha+2}$ keV(keV/cm ² skeV)	Model
-3/2	-1/2	1/2	Synch. + cooling
-1	0	1	Quasi-saturated Comptonization
-2/3	1/3	4/3	Synch. instantaneous
0	1	2	Small pitch angle/jitter/IC single e^-
1	2	3	Black Body
2	3	4	Wien

6.2 Data Analysis

The spectral analysis of the 5 bursts presented in this chapter was performed with the BATSE-HERB data. The details of the data reductions have already been discussed in chapt.4 and 5.

The fit of the spectra was carried out with the most commonly adopted spectral functions: the BAND model (Band et al. [4]) and the COMP model (described in sec. 5.2.4). The choice of these models is motivated by the fact that they characterize the low energy part of the spectrum with a spectral parameter (i.e. the spectral index α) which can be compared with the predictions of different theoretical models (tab.6.1).

Because of the extreme spectral hardness found in these bursts, we decided also to verify if thermal, black body like, emission was consistent with the low energy data. This was done on the hardest spectra, selected for having a spectral index greater than $\alpha > 0.5$ from the BAND/COMP models. This indicative value which is softer than $\alpha = 1$ (i.e., the Rayleigh-Jeans limit of a black body spectrum) has been chosen to: a) account for typical errors in the determination of α with the BAND or COMP models; b) include the possibility that the spectrum could be softer than $\alpha = 1$, if its peak is at low energies (due to the spectral curvature).

The result of each fit was then considered acceptable if the reduced χ^2 was lower than 1.5 for typically 110 degees of freedom (d.o.f.). In fact, the statistical probability of having a better fit is around 0.5 if the reduced χ^2 is around 1, but a limiting value of $\chi_{\text{red}}^2 \sim 1.5$ is suggested if one considers that χ_{red}^2 depends on the quality of the data (Bevington & Robinson [8]). In addition we visually inspected the data-to-model ratio to look for possible systematics (i.e., sequence of points significantly above or below unity). We discarded the black body as a good fit when an excess of flux occurred at low energies (i.e. in the E^2 part of the spectrum), while we allowed for (a moderate) deviation from unity at high energies (i.e. in the exponential part). This latter choice reflects the possible (or even likely) situation of having a ‘‘supra-thermal’’ tail to a Maxwellian distribution in quasi-thermal plasmas or multi-temperature black body emission as proposed by

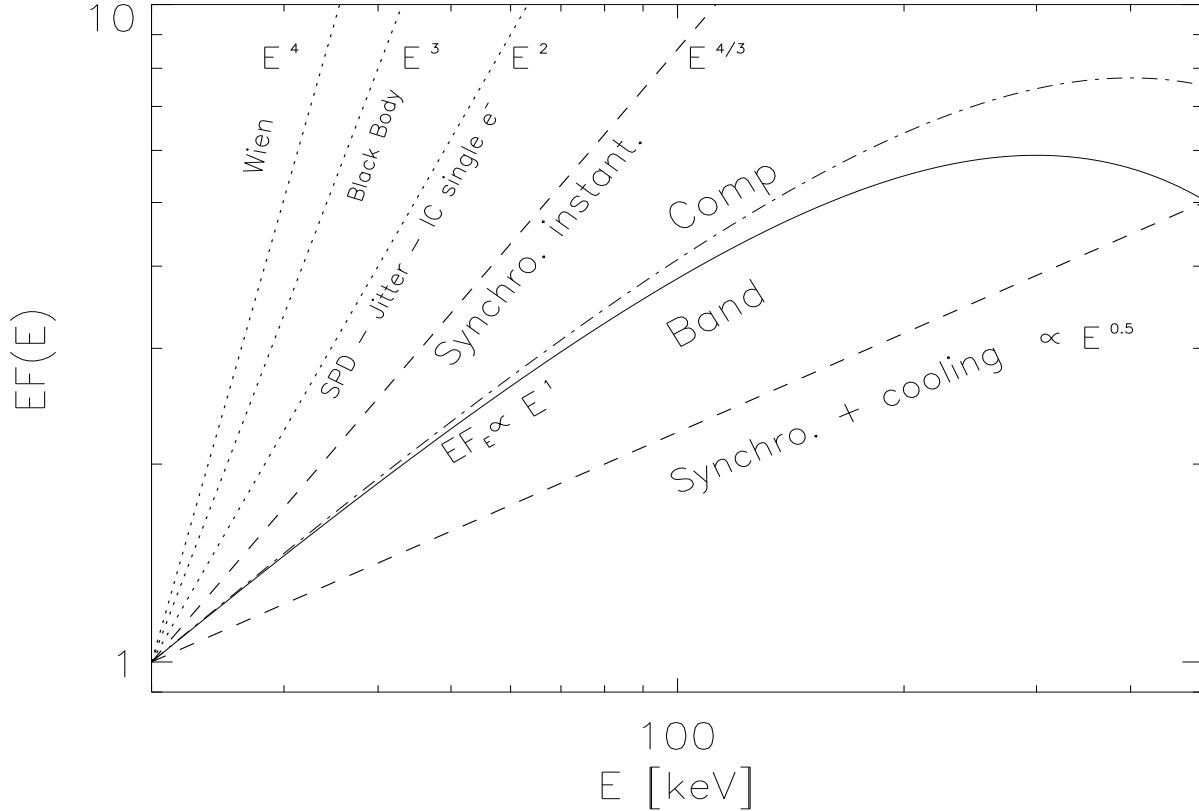


Figure 6.2: Low energy spectral component. Example of the BAND (*solid line*) and COMP model (*dot-dashed line*) with the low energy spectral index fixed at -1 [i.e. $EF(E) \propto E^{-1}$]. For comparison we report the spectral slopes predicted by the emission processes reported in tab. 6.1.

Blinnikov et al. [1999].

6.3 Results

In sec.6.3.1 is presented a new case of hard low energy burst: GRB 980306. In particular, its early phase spectrum, which is extremely hard, is analyzed. The detailed spectral analysis of GRB 911118 (also reported by Ford et al. [42], only in terms of the time evolution of its peak energy) is reported in sec.6.3.2 with emphasis (again) on the low energy spectral index evolution.

In sec.6.4 are discussed other 3 bursts, i.e. GRB 910807, GRB 910927 and GRB 970111, which have been found through a search in the literature. In particular for GRB 910807 we have extended the time analysis beyond the first 5 seconds that were previously studied by Ryde & Svensson [136].

The significance of the hardness of all these bursts is verified with different spectral

tests applied to the raw data in sec.6.3.3.

Sec.6.9 presents the results of systematic fit of the hardest spectra of *all* these 5 bursts with a black body spectral model.

6.3.1 GRB 980306

GRB 980306 (BATSE trigger 6630) represents a newly discovered case of hard burst. It is a single peak FRED-like burst (fig. 6.3, *top panel*) with duration of ~ 6 s, peak flux of (17.2 ± 0.4) phot cm $^{-2}$ s $^{-1}$ at $t_{peak} \sim 2.2$ s and a total (100–300) keV fluence of $\sim 10^{-5}$ erg cm $^{-2}$. This burst was already present in Preece et al. ([130]) spectral catalogue but, as it had been fitted with a BPLW model only, it did not reveal its hard low energy component. In fact, as already noticed in chapt.5, a fit of a sharply connected model, like the BPLW, to a smoothly curved spectrum, although can still give acceptable fits, tends to underestimate the low energy spectral hardness.

Its hardness evolution, during the first 6 s, divided in 14 time resolved spectra, is reported in fig.6.3. The spectral fits with the different models show that the spectra are better represented by the COMP model, since the high energy parts are very steep (i.e., steeper than a powerlaw with $\beta \sim -10$ the limit of the fitting function). The time evolution of the low energy spectral index α and of the peak energy E_{peak} are plotted in fig. 6.3 (mid and bottom panels).

The hardness evolution of the burst is typically described, at low energies, by how the spectral index α and $E_{peak} = (\alpha + 2)E_0$ change in time (here E_{peak} is the peak energy and E_0 the characteristic energy of the exponential cutoff). For this specific burst the evolution is hard-to-soft, as shown by the peak energy (bottom panel of fig. 6.3) decreasing in time from ~ 150 keV to ~ 50 keV at the end of the peak. The evolution of α (mid panel of Fig. 6.3) indicates that, in the rising phase of the burst, the maximum hardness ($\alpha = 1.1 \pm 0.2$) is reached for $t_{max} < 1.5$ s. The first 4 spectra are indeed consistent with a non evolving spectrum (the low energy spectral index can be considered equal to its average value $\langle \alpha \rangle \sim 0.73 \pm 0.03$ at 92% confidence level for the first 1.5 sec). After t_{max} the spectrum softens, but it remains harder than $\alpha = 0$. We stress that the low energy spectrum is significantly (more than 3σ) harder than $\alpha = 0$ for each of the first 7 time resolved spectra (between $t = 0$ and $t = 2.24$ s).

In view of the discussion on the spectral models (sec.6.6) we also checked the inadequacy of the optically thin synchrotron model by fitting the BAND spectrum with the low energy power law slope fixed at $-2/3$, which is a good representation of the spectrum predicted by this model. As expected, the reduced χ^2 is larger (blue diamonds in fig.6.5) than the value obtained with the COMP model (light blue diamonds in fig.6.5) and this is evident particularly in the first spectra; moreover the inspection of the residuals shows at low energies a systematic excess indicating that the model is not a good representation of the data.

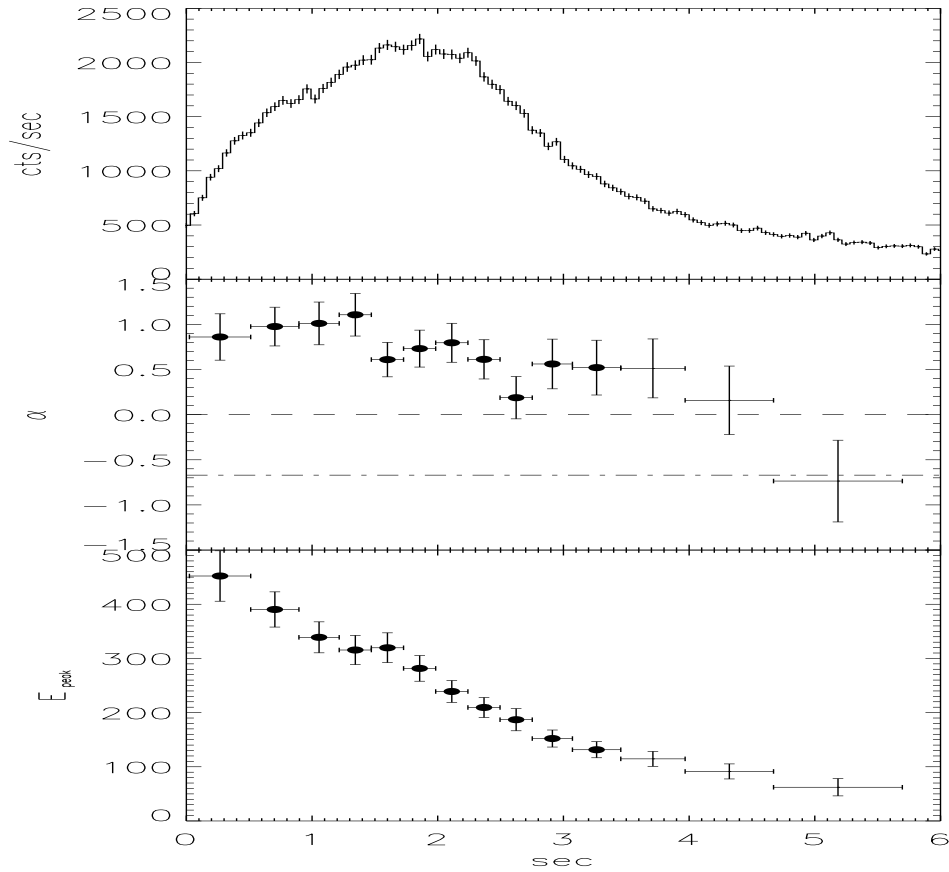


Figure 6.3: Light curve and best fit parameters for GRB 980306, according to the best fit COMP model. Top panel: light curve on the 64 ms timescale. Mid panel: low energy power law spectral index (α). Horizontal lines mark the limits $\alpha = -2/3$ and $\alpha = 0$. Bottom panel: peak energy E_{peak} [in a $EF(E)$ diagram]. Error bars represent the 90% confidence interval on the best fit parameters. The filled circles indicate the spectra which have been fitted also with a blackbody model (see tab. 6.2 and sec.6.5).

6.3.2 GRB 911118

The light curve of GRB 911118 (BATSE trigger 1085), reported in fig. 6.4 (*top panel*), has two main peaks which partially overlap. It is a typical long burst with total duration $T_{90} = 19.2 \pm 0.1$ s and a background subtracted peak flux of (30.6 ± 0.8) phot $\text{cm}^{-2} \text{s}^{-1}$ at $t_{\text{peak}} = 6.08$ s. Its fluence, in the 100–300 keV energy range, is $(27.8 \pm 0.1) \times 10^{-6}$ erg cm^{-2} .¹

The spectral analysis that we present is limited to the first 13 s after the trigger time (for a total of ~ 50 spectra), in which the time resolved spectrum evolves dramatically with an excursion of $\Delta\alpha \sim 1$ and $\Delta E_{\text{peak}} \sim 400$ keV. The best fit is obtained with the BAND model. The low energy spectral index is $\alpha > 0$ for the first ~ 6 s (32 spectra,

¹<http://coss.c.gsfc.nasa.gov/batse/4Bcatalog/index.html>

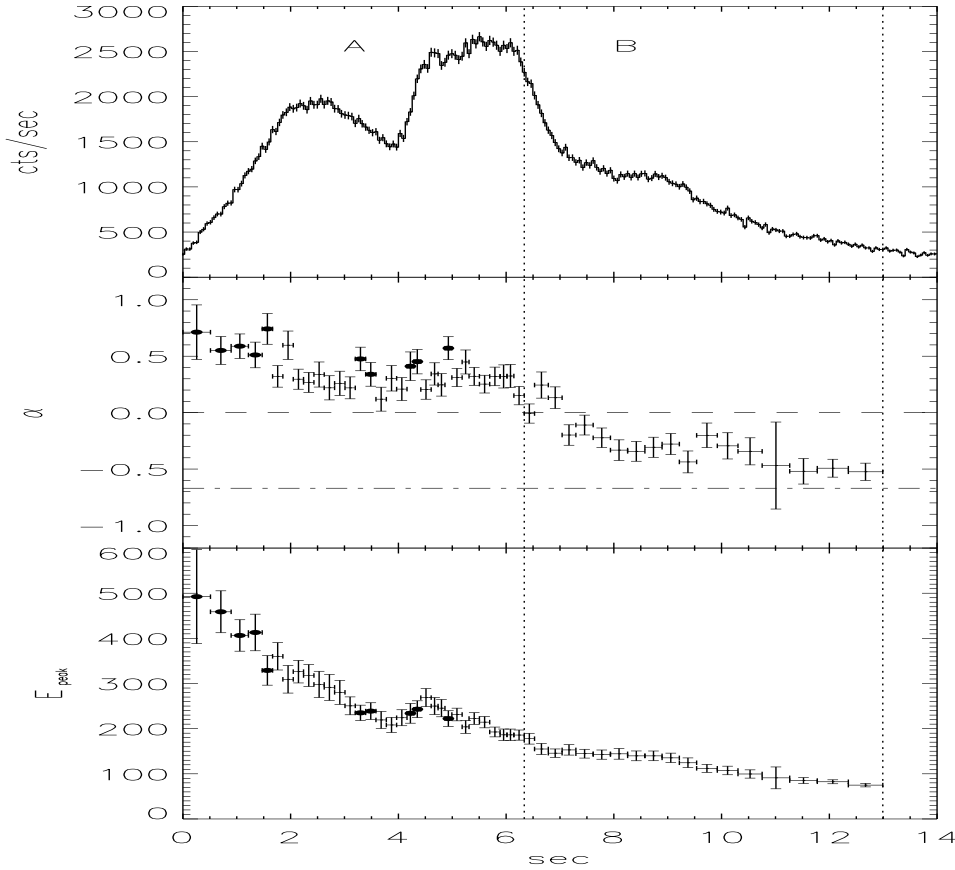


Figure 6.4: The light curve and time evolution of the BAND best fit parameters for GRB 911118. Top panel: light curve on the 64 ms timescale in the energy range 100–320 keV, summed over all the triggered detectors. The vertical *dotted* lines represent the boundaries of the phases in which the spectrum is harder than E^0 (phase A) and $E^{-2/3}$ (phase B). Mid panel: low energy power law spectral index α , with the limits $\alpha = -2/3$ (*dot-dashed*) and $\alpha = 0$ (*dashed*). Bottom panel: Peak energy in the EF_E spectrum. The filled circles represent the spectra which have been fitted also with a blackbody model (see tab 6.2 and sec. 6.5).

phase A of Fig. 6.4, mid panel) and decreases with time (the spectrum softens), but remains harder than $-2/3$ for the time interval up to the end of phase B. After $t \sim 13$ s, the spectrum has a typical $\alpha < -2/3$ slope. The hardest spectrum (at $t \sim 1.5$ s after the trigger) has $\alpha = 0.74 \pm 0.13$ corresponding to $EF_E \propto E^{2.74 \pm 0.3}$. The statistical significance of a positive value of α for the spectra of phase A is high, being $> 3\sigma$ for most of the individual spectra (23/32). The peak energy evolution reported in fig. 6.4 (bottom panel) is consistent with what reported by Ford et al. ([42]) and Crider & Liang ([21]). According to these fits, the 18 spectra belonging to phase B have $-2/3 < \alpha < 0$ and their evolution is of the “hard-to-soft” kind, i.e. the peak energy decreases in time (becoming smaller than 200 keV in phase B). From fig. 6.4 it can be seen that there is

a correlation between the peak energy E_{peak} and α .

It has been pointed out (Lloyd & Petrosian [98]) that such correlations could result from the effect of the curvature of the fitted model when the peak energy is particularly low (e.g., below ~ 100 keV and close to the low energy spectral threshold). However, in the case of GRB 911118 we can exclude this effect because the peak energy evolves between 500 keV and 200 keV during phase A.

Again we also tried to fit the simplest optically thin synchrotron model (by fixing the low energy spectral index of the BAND model to $-2/3$). In fig. 6.5 we report, for comparison, the values of the reduced χ_r^2 for all spectra. The best fit is given by the BAND model (red circles) while the ‘‘synchrotron’’ (the green circles) is inadequate to fit these spectra because the χ_r^2 is typically >2 (for ~ 110 d.o.f.) during phase A. The value of χ_r^2 for the synchrotron model becomes marginally acceptable (< 1.5) for some spectra in phase B. We conclude that the time resolved spectra of this burst are best represented by the BAND model with the 4 fit parameters free to vary and that most of the spectra of phase A have $\alpha > 0$ at a $> 3\sigma$ level.

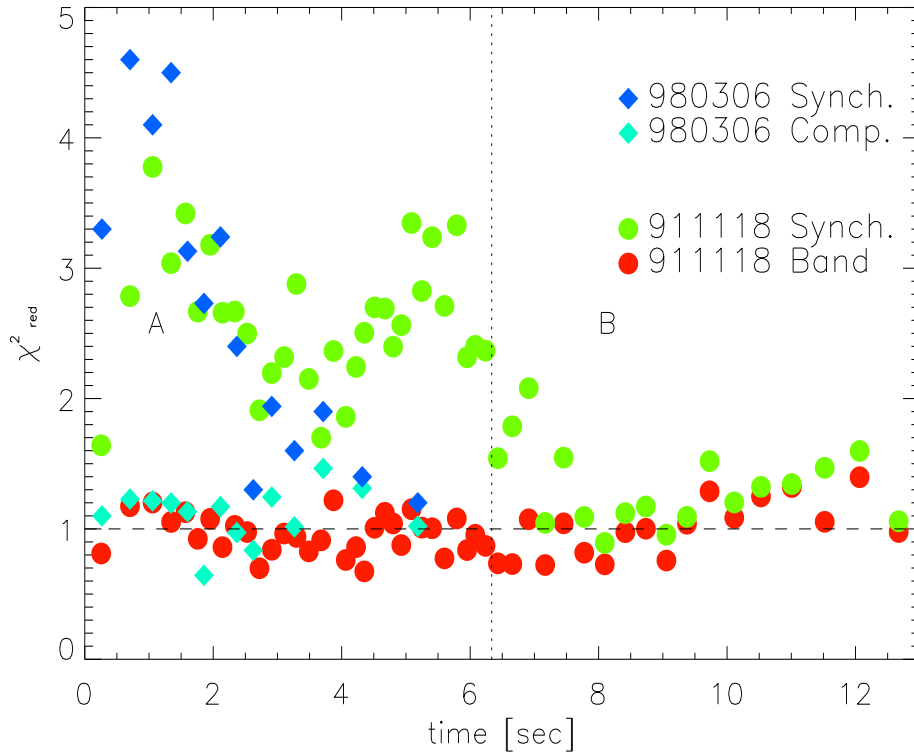


Figure 6.5: Reduced χ^2 of the fits with different models to the spectra of GRB 911118: BAND model (red circles), BAND model with the low energy spectral index fixed at $-2/3$ (green circles). The same for GRB 980306: COMP model (light blue diamonds) and BAND model with $\alpha = -2/3$ (blue diamonds).

6.3.3 Tests of the significance of the spectral results

Considering the relevance of the extreme hardness of these bursts for the comparison with the models, we performed different checks to verify if and at what confidence level they can be considered harder than the predictions of the proposed spectral models reported in tab. 6.1. In the following paragraphs the results of these checks are reported and in particular we stress the relevance of a direct comparison of the observed spectra with a simulated flat spectrum, with fixed low energy spectral slope $\alpha = 0$.

Reduced fitting energy range

We eliminated from the fitting energy range the high energy channels to test if they substantially influence the low energy fitted spectral slope. The energy window of the spectral analysis was restricted to the range 28–600 keV. The upper limit represents the maximum peak energy which resulted from the spectral analysis of the time resolved spectra of these two bursts ($E_{peak,max} \sim 500 \pm 100$ keV, for the first spectrum of GRB 911118 - fig.6.4). The results of the fit on the entire energy range (28-1800 keV) and on the reduced window were compared. We found that the best fit spectral parameters are consistent within their errors. The slope of the low energy spectral index obtained from the fit on the reduced energy range is still inconsistent with $\alpha = 0$. Moreover, Preece et al. ([128]) found a soft low energy component in some bursts through the analysis of other data type extending below the standard LAD threshold of 28 keV. This component could make the fitted low energy spectral slope softer than it really is and the fit results for the α parameter presented here should be considered as lower limits thus reinforcing the evidence of extremely hard spectra. We tested this possibility by fitting the spectra with a low energy threshold at 50 and 100 keV. The comparison with the fits on the entire energy range (28 - 1800 keV) showed consistent spectral parameters within their 90% confidence intervals. Thus we conclude that the high energy low statistics does not influence (i.e. determines an overestimate of) the low energy best fit α value;

Background Spectrum

If the background spectrum were characterized by any feature or absorption edge at low energies (e.g. dependent on some electronic failure or anomalous observational conditions) this might determine particularly hard low energy power laws in the background subtracted spectra. As described in the data analysis section (chapt.4, sec. 2.4.1), we calculated the background spectrum as the average over several time resolved spectra before and after the GRB, selecting a time interval far enough from the burst not to include the GRB emission itself. For these extremely hard bursts we computed several background spectra, selecting different time intervals for each burst, and compared them with those obtained from other bursts with normal low energy spectral slopes, observed at other locations in the sky and/or with other BATSE LAD detectors. We have found that the background spectra, for the 5 bursts under discussion, are represented by a

power law, in agreement with Preece et al. ([130]), with calibration features at different energies, differing only for their normalization. We can be confident that α is not affected by anomalous features or bad determination of the background spectrum;

Detector response

The detector response matrix, if incorrectly calculated, could determine a wrong set of best fit parameters. We believe this is unlikely as, by fitting the spectra with the detector response matrix (DRM) associated with another burst but for the same LAD, the resulting spectral parameters are still consistent within their 90% confidence level. Moreover, although we used the data of the mostly illuminated detector, we also tried to fit the data from the other three detectors that were triggered by these bursts. Although the lower signal to noise ratio in these “secondary” detectors resulted in a lower statistical significance of the best fit parameters, these fits confirmed the extremely hard low energy spectral slope of these bursts at least in the second best illuminated detector. For the remaining two detectors the results are consistent, although the low statistics does not allow to confirm the hardness. Note also that Crider et al. [21] showed that combining different detectors can make the low energy spectral component softer than it really is.

Comparison with a simulated spectrum

A direct and robust way to verify if the deconvolved spectra are really as hard as we found is to compare them with a reference spectrum whose shape is well defined.

For every time resolved spectrum that we analyzed, we thus simulated a reference (template) spectrum with a low energy power law slope $\alpha \sim 0$ and a break energy fixed at the value obtained from the fit of the observed spectrum. We divided channel by channel the observed spectrum by the template and then analyzed their ratio. As expected if the observed spectrum is harder than the template their ratio, at low energies, increases with energy. In order to quantify this behaviour the observed-to-template-spectrum ratio has been fitted with a power law $AE^\delta + B$. If the fitted index δ is greater than 0 this indicates that the observed spectrum is harder than the template, and for the choice of the spectral parameters, harder than E^0 .

In fig.6.6 is reported the fitted index δ to this ratio, for GRB 911118 and GRB 980306 (left and right panel, respectively). We note that during phase A (the first 6 s after trigger) of GRB 911118 (left panel of fig.6.6) each of the time resolved spectra is at least 3σ harder than a flat spectrum (i.e. with the same level of confidence that was found with the direct fitting method). In the case of GRB 980306 this test gives a fitted ratio with a poor level of confidence ($< 2\sigma$) for each spectrum (with only two spectra at $> 2\sigma$) because of the low S/N due to low statistics and to the propagation of errors in dividing the observed spectrum by the template one. This significance, can be anyway increased if, say, the first 8 spectra are rebinned in time (although of course we loose the fine time resolved spectral information) obtaining a value of $\delta > 0$ at 3.7σ .

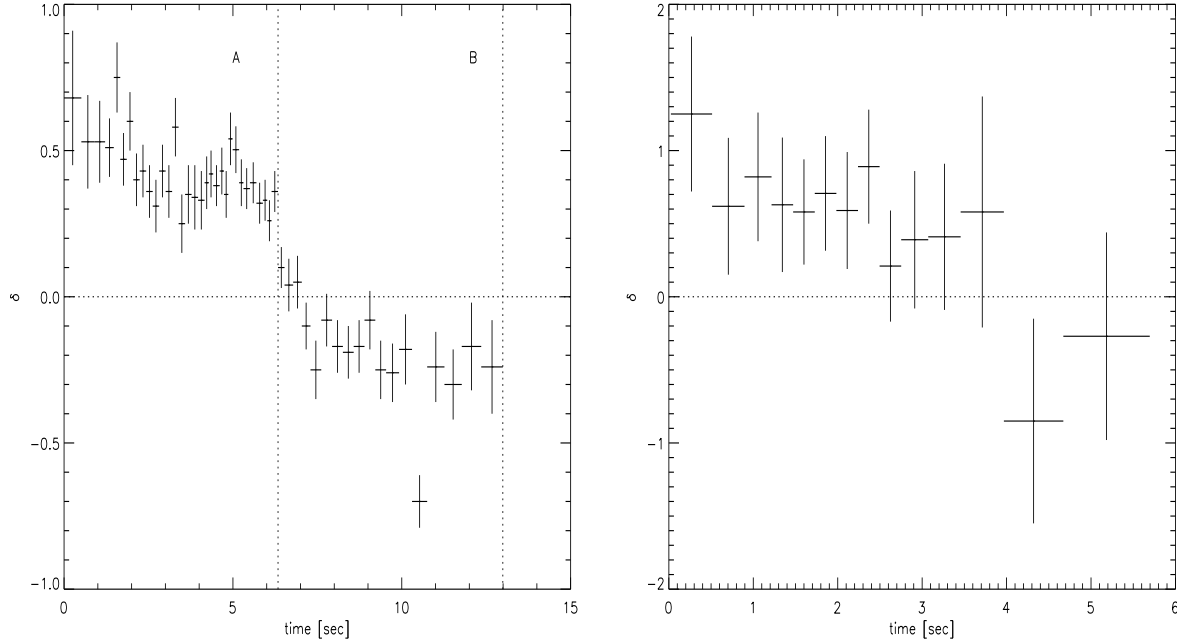


Figure 6.6: Slope of the power law E^δ fitted to the ratio between the observed time resolved spectra and the template spectra (simulated with $\alpha = 0$ and $E_{break} = E_0(fit)$). Left: GRB 911118, labels A and B refer to the two phases of GRB 911118. Right: GRB 980306. The dotted line $\delta = 0$ represents the case of an observed spectrum with flat slope, like the simulated spectrum i.e. a constant observed-to-model ratio.

Furthermore, also in the case of GRB 980306 the significance of $\delta > 0$ (fig. 6.6) is higher when considering the sequence of δ values as a group (since δ remains systematically positive).

As a final consideration let us stress that in the case of GRB 911118 (fig. 6.4) and GRB 980306 (fig. 6.3) there is a minority of hard spectra (9 and 4, respectively) which have $\alpha > 0$ at a level of significance lower than 3σ . Nonetheless the fact that a considerable number of subsequent spectra (32 for GRB 911118 and 12 for GRB 980306) in the first few seconds have a spectrum harder (at more than 3σ) than E^0 increases the level of significance of this result, if they are considered as a whole.

6.4 Other hard bursts

There are other bursts with low energy hard spectra for a major part of their evolution, which have already been reported in the literature. In particular, we found three bursts with very hard spectra if fitted by the BAND function. In order to have homogeneous results we have then re-analyzed their spectra and also applied the tests described in the previous subsection. In addition for these bursts we have fitted the black body spectrum and found that their early phase spectra are consistent with a thermal shape: these

results are presented and discussed, together with those for GRB 980306 and 911118, in the next section. In the following we briefly summarize the spectral characteristics of these other three extremely hard bursts.

GRB 910807

This is a weak burst with a peak flux of (7.2 ± 0.5) phot cm $^{-2}$ s $^{-1}$. The spectrum is harder than $\alpha = 0$ for the first ~ 5 s, and remains quite constant (~ 0) during the overall burst, which lasts about 28 s, as already pointed out by Ryde et al. ([136]). The peak energy instead shows a tracking pattern correlated with the flux and hardens in correspondence of the second peak (at $t = 12$ s).

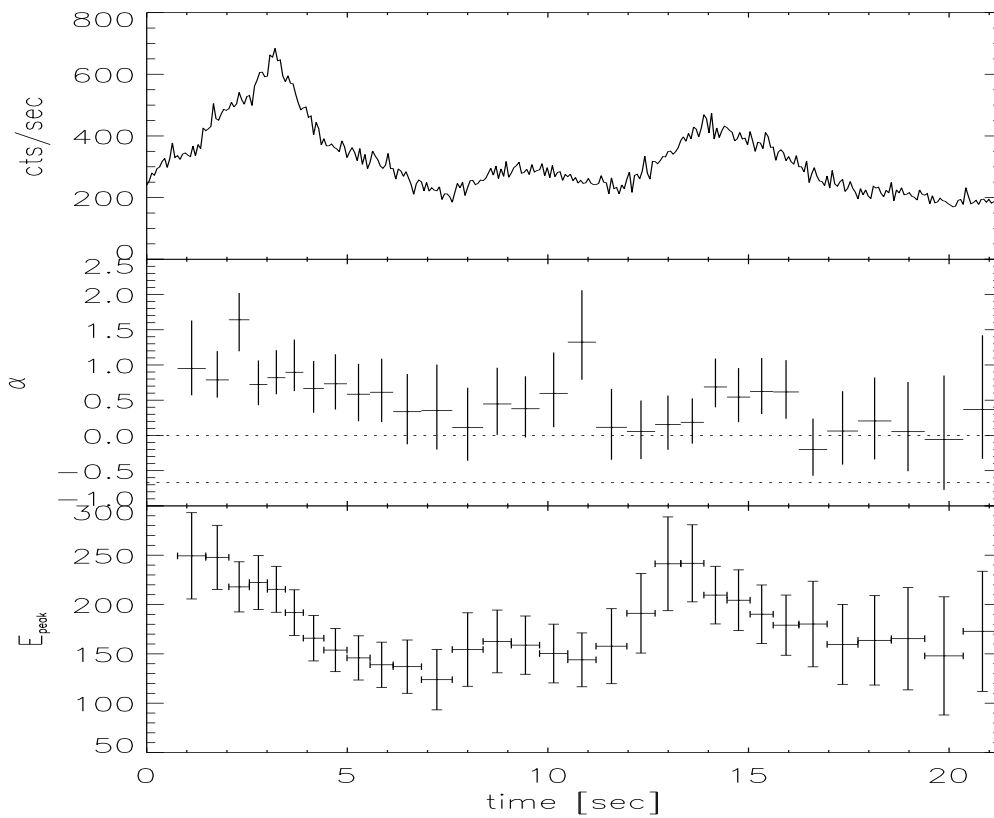


Figure 6.7: GRB 910807 spectral evolution. Same as fig. 6.3

The complete spectral evolution is reported in fig. 6.7. The hardest spectrum has $\alpha = 1.6 \pm 0.5$ at 90% confidence level. This value is somewhat harder, but consistent with what quoted by Crider et al. ([24]). A (successful) check for the hardness of the first few spectra of this burst has been performed using the last method (comparison with a simulated spectrum) described in the previous section.

GRB 910927 & GRB 970111

These two bursts have been reported by Crider et al. ([24], [21]) and GRB 970111 also by Crider et al. ([22]) and Frontera et al. ([47]). They are two other cases with extremely hard low energy spectral component ($\alpha = 1.6 \pm 0.3$ in the case of GRB 910927).

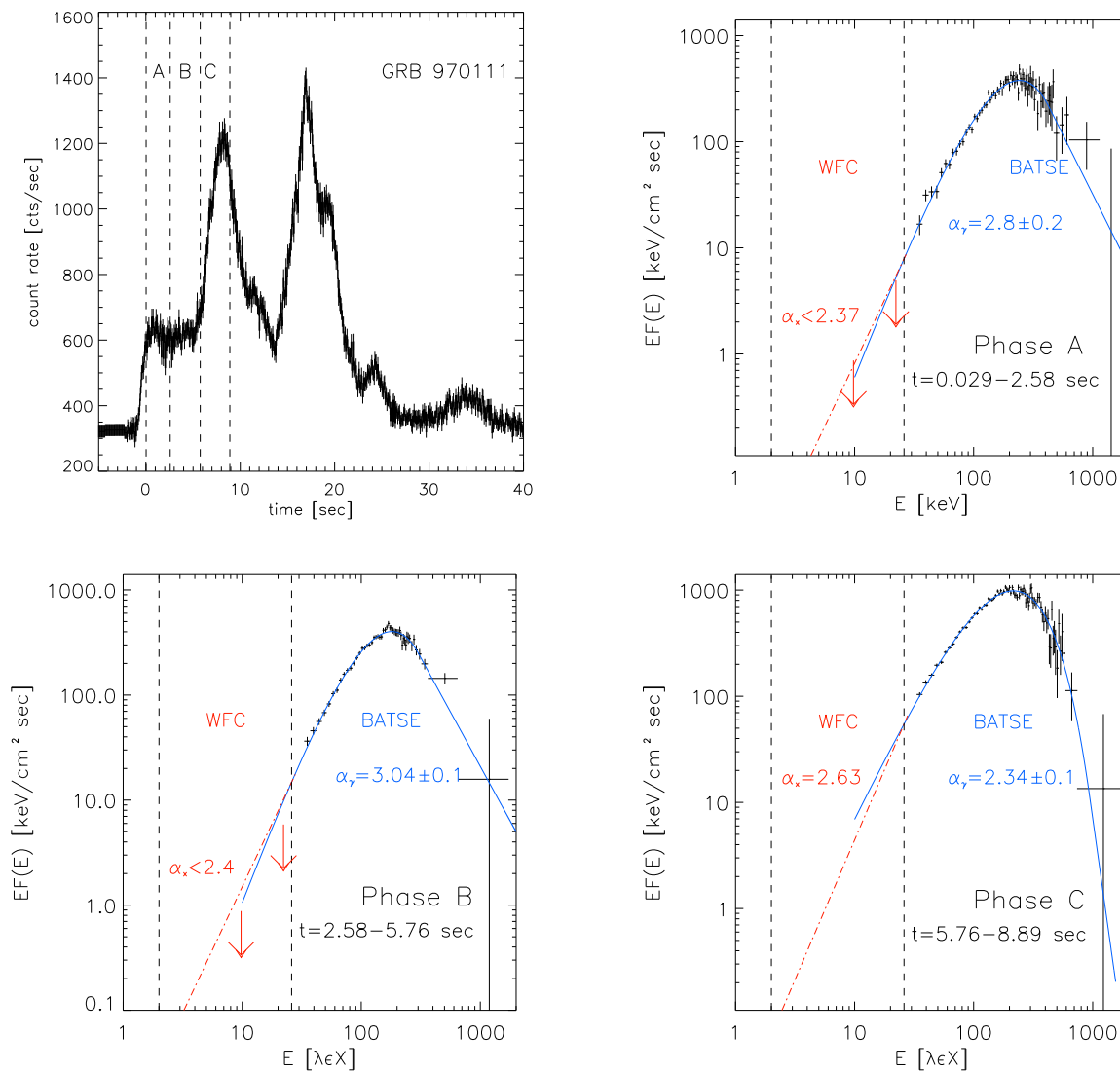


Figure 6.8: BATSE spectra and WFC spectral limits for GRB 970111. Top left: light curve (64ms time resolution on $E > 100$ keV) and the three phases corresponding to the time bins reported by Frontera et al. [47]. The corresponding BATSE spectra and the best fit model (blue line) together with the WFC (red line) limiting slopes are reported in the three panels. The WFC spectral components have been arbitrarily normalized to match the best fit model fitted to the BATSE data at 25 keV. The errors indicate that the X ray spectral slope (dot-dashed line) is a lower limit.

GRB 970111 was also studied by Frontera et al. ([47]) joining the data of the X ray instrument (WFC) of *BeppoSAX* with those of the gamma ray instrument (GRBM) on board the same satellite. Its extremely hard low energy spectrum was confirmed to extend down to 5 keV. Unfortunately, the lack of spectral resolution of the GRBM instrument above 40 keV does not allow to study the complete spectrum, especially at its peak. For this reason we considered the BATSE data which have about 15 energy channels corresponding to the lower energy GRBM channel between ~ 40 and 100 keV. This allows to compare the slope determined by the WFC spectrum with an energy resolved (15 channels) spectrum in the soft ($E \leq 100$ keV) γ -ray band.

As shown in fig.6.8 the first phases of the burst (phases A and B, corresponding to ~ 2.5 sec of integration - top right and bottom left panels in fig.6.8) are characterized by a spectrum whose slope is consistent with the upper limit found from the fits of the WFC X-ray data. The spectrum corresponding to phase B (bottom right panel of fig.6.8) instead is composed by a steeper slope below 26 keV than the γ ray band spectrum: this could be determined by absorption by cold material in the vicinity of the burst as proposed by Brainerd et al ([12]). These results are an additional evidence of the hardness of this burst because also the low energy X-ray spectrum is characterized by $\alpha > 0.3$.

In addition we found in the spectral catalogue of Preece et al. ([130]) other 3 bursts (BATSE triggers 1974, 2855 and 6350) with $\alpha > 0$, but with a low significance level ($< 1\sigma$) and for a short interval of the light curve. Note that also these cases contribute to the $\alpha > 0$ tail of the spectral index distribution reported in fig. 6.1.

6.5 Black body spectra

As anticipated we performed fits on the hardest spectra also with a black body model to test if the emission is consistent with having a thermal character. In fact, the first spectra of all the bursts discussed in this work are typically harder than $E^{0.5}$ and thus could be consistent with the Rayleigh–Jeans part of the black body. Note that the fit could, however, be unacceptable in terms of χ^2 if the curvature around the peak (i.e. typically in the range 100–300 keV) were broader than a black body one.

Table 6.2: Black body fits.

GRB	t_{start} sec	t_{stop} sec	kT keV	N erg/cm ² sec	χ_r^2 (dof)	F phot/cm ² sec	α	$\chi_{r,\alpha}^2$ (dof)
980306	0.024	0.512	$104^{+4.8}_{-4.8}$	$46^{+2.7}_{-2.8}$	1.15(107)	8.4	0.86 ± 0.15	1.09(109)
	0.512	0.896	$93^{+4.6}_{-3.4}$	$63^{+3.2}_{-2.8}$	1.27(107)	12.9	0.98 ± 0.13	1.21(104)
	0.896	1.216	$81^{+2.9}_{-2.8}$	$63^{+2.8}_{-2.8}$	1.27(107)	14.7	1.01 ± 0.13	1.2(106)
	1.216	1.472	$78^{+2.7}_{-2.6}$	$68^{+3.1}_{-3.0}$	1.19(103)	16.6	1.11 ± 0.14	1.19(102)
	1.472	1.728	$72^{+2.5}_{-2.1}$	$70^{+3.1}_{-2.7}$	1.44(105)	18.4	0.61 ± 0.12	1.12(104)
	1.728	1.984	$65^{+2.1}_{-1.6}$	$66^{+2.7}_{-2.6}$	0.86(107)	19.10	0.73 ± 0.12	0.7(106)
	1.984	2.24	$57^{+1.6}_{-1.8}$	$59^{+1.7}_{-2.6}$	1.33(104)	19.09	0.8 ± 0.13	1.16(103)
	2.24	2.496	$49^{+1.5}_{-1.4}$	$52^{+1.8}_{-1.8}$	1.26(104)	19.3	0.61 ± 0.13	0.96(103)
	2.496	2.752	$42^{+1.3}_{-1.4}$	$39^{+1.3}_{-1.4}$	1.39(101)	16.6	0.19 ± 0.14	0.8(100)

	2.752	3.072	$37^{+1.1}_{-1.1}$	$30^{+0.9}_{-0.9}$	1.45(104)	14.1	0.56 ± 0.17	1.2(103)
	3.072	3.456	$33^{+1.0}_{-1.0}$	$23^{+0.7}_{-0.8}$	1.23(107)	12.14	0.52 ± 0.19	1.0(106)
911118	0.000	0.512	$114^{+8.0}_{-8.0}$	$23^{+2.0}_{-3.0}$	0.95(111)	3.92	0.71 ± 0.24	0.8(109)
	0.512	0.896	$98^{+4.0}_{-5.0}$	$39^{+2.0}_{-3.0}$	1.39(109)	7.61	0.55 ± 0.12	1.1(107)
	0.896	1.216	$87^{+3.0}_{-5.0}$	$52^{+3.0}_{-3.0}$	1.51(105)	11.28	0.59 ± 0.11	1.2(103)
	1.216	1.472	$89^{+3.0}_{-4.0}$	$69^{+4.0}_{-4.0}$	1.45(107)	14.78	0.51 ± 0.11	1.0(105)
	1.472	1.664	$76^{+3.0}_{-3.0}$	$68^{+4.0}_{-3.0}$	1.35(105)	16.93	0.74 ± 0.13	1.1(103)
	3.2	3.392	$52^{+1.0}_{-2.0}$	$65^{+2.0}_{-2.0}$	1.52(104)	22.76	0.5 ± 0.1	0.9(102)
	3.392	3.584	$52^{+1.3}_{-2.0}$	$59^{+2.0}_{-2.0}$	1.51(107)	20.61	0.57 ± 0.1	0.87(105)
910807	0.768	1.472	$71^{+4.6}_{-4.6}$	$9.4^{+0.8}_{-0.8}$	1.10(113)	2.51	0.95 ± 0.29	1.2(111)
	1.472	2.048	$61^{+3.3}_{-3.5}$	$11^{+0.4}_{-0.9}$	1.29(113)	3.3	0.78 ± 0.21	1.0(111)
	2.048	2.56	$59^{+2.8}_{-2.6}$	$17^{+0.8}_{-0.8}$	1.05(112)	5.32	1.64 ± 0.25	0.8(110)
	2.56	3.008	$57^{+2.2}_{-2.3}$	$19^{+1.2}_{-2.3}$	0.78(111)	6.12	0.72 ± 0.19	0.84(109)
	3.008	3.456	$53^{+2.2}_{-2.1}$	$21^{+0.9}_{-0.9}$	0.94(109)	7.36	0.82 ± 0.18	0.95(107)
	3.456	3.904	$53^{+1.8}_{-1.9}$	$24^{+1.0}_{-1.0}$	1.00(112)	8.43	0.89 ± 0.21	1.06(110)
	3.904	4.416	$47^{+1.8}_{-1.6}$	$19^{+0.9}_{-0.8}$	1.09(111)	7.42	0.67 ± 0.23	0.97(109)
	4.416	4.992	$41^{+1.7}_{-1.5}$	$14^{+0.6}_{-0.6}$	1.06(113)	6.05	0.58 ± 0.25	1.0(111)
	4.992	5.568	$38^{+1.5}_{-1.6}$	$11^{+0.5}_{-0.5}$	0.84(112)	5.39	0.61 ± 0.28	1.1(110)
	5.568	6.144	$36^{+1.5}_{-1.5}$	$11^{+0.5}_{-0.5}$	1.11(112)	5.23	0.6 ± 0.33	1.17(110)
	9.792	10.496	$39^{+2.0}_{-1.9}$	$7.7^{+0.4}_{-0.4}$	1.24(113)	3.56	1.32 ± 0.40	1.63(111)
	10.496	11.2	$37^{+2.0}_{-2.0}$	$6.8^{+0.4}_{-0.4}$	1.21(114)	3.2	0.54 ± 0.23	1.03(112)
	14.464	15.04	$50^{+2.3}_{-2.2}$	$14^{+0.7}_{-0.8}$	0.83(112)	5.16	0.62 ± 0.24	0.83(110)
	15.04	15.616	$49^{+2.2}_{-2.2}$	$13^{+0.8}_{-0.7}$	1.11(115)	4.851	0.62 ± 0.27	1.4/109
	15.616	16.256	$46^{+2.2}_{-2.2}$	$12^{+0.6}_{-0.7}$	0.9(112)	4.6	0.61 ± 0.27	1.4(109)
910927	0.000	0.704	$63^{+3.8}_{-3.8}$	$7^{+0.6}_{-0.5}$	0.82(107)	2.26	0.62 ± 0.26	0.96(105)
	0.704	1.28	$53^{+2.0}_{-2.4}$	$12^{+0.6}_{-0.6}$	0.91(109)	4.05	1.02 ± 0.28	0.93(107)
	1.28	1.792	$46^{+1.7}_{-1.7}$	$12^{+0.6}_{-0.6}$	1.3(107)	4.9	1.04 ± 0.25	1.13(105)
	1.792	2.304	$42^{+1.4}_{-1.3}$	$12^{+0.5}_{-0.6}$	1.23(105)	5.35	1.24 ± 0.24	0.9(103)
	2.304	2.752	$41^{+1.3}_{-1.4}$	$14^{+0.5}_{-0.6}$	0.99(104)	5.9	1.1 ± 0.24	0.8(102)
	2.752	3.2	$37^{+1.1}_{-1.2}$	$15^{+0.6}_{-0.5}$	0.98(105)	6.9	1.05 ± 0.24	1.0(103)
	3.2	3.584	$37^{+1.0}_{-1.2}$	$17^{+0.6}_{-0.7}$	0.98(101)	7.85	1.12 ± 0.25	1.0(99)
	3.584	3.968	$36^{+1.0}_{-1.0}$	$17^{+0.6}_{-0.6}$	0.99(101)	8.03	0.98 ± 0.19	1.1(99)
	3.968	4.416	$32^{+1.0}_{-1.0}$	$13^{+0.5}_{-0.5}$	0.8(105)	6.9	0.83 ± 0.2	0.8(103)
970111	0.576	1.088	$61^{+2.0}_{-2.0}$	$11^{+0.8}_{-0.8}$	0.97(108)	3.2	1.51 ± 0.4	0.96(106)
	1.088	1.6	$56^{+2.3}_{-2.3}$	$10^{+0.6}_{-0.6}$	1.15(105)	3.23	1.31 ± 0.34	1.07(103)
	1.6	2.112	$51^{+2.3}_{-2.3}$	$9.3^{+0.6}_{-0.6}$	1.00(108)	3.3	1.11 ± 0.28	0.9(106)
	2.112	2.58	$49^{+2.4}_{-2.4}$	$9^{+0.6}_{-0.6}$	1.43(105)	3.32	1.02 ± 0.31	1.2(103)
	2.58	3.008	$48^{+2.4}_{-2.4}$	$9^{+0.6}_{-0.6}$	0.98(104)	3.3	1.6 ± 0.4	0.9(102)
	3.008	3.456	$49^{+2.4}_{-2.4}$	$10^{+0.6}_{-0.6}$	0.93(104)	3.6	1.02 ± 0.32	0.8(102)
	3.456	3.904	$46^{+2.1}_{-2.1}$	$10^{+0.5}_{-0.5}$	0.97(102)	4.0	1.85 ± 0.38	0.7(100)
	3.904	4.288	$46^{+2.0}_{-2.0}$	$10^{+0.6}_{-0.6}$	0.95(104)	4.06	1.83 ± 0.4	0.9(102)
	4.288	4.672	$40^{+1.9}_{-1.4}$	$9.7^{+0.6}_{-0.6}$	1.16(100)	4.27	1.25 ± 0.31	1.2(98)
	4.672	5.056	$42^{+2.0}_{-2.0}$	$10^{+0.6}_{-0.6}$	1.13(98)	4.3	1.34 ± 0.41	0.92(96)
	5.056	5.44	$43^{+2.0}_{-2.0}$	$11^{+0.7}_{-0.7}$	0.96(104)	4.7	0.79 ± 0.31	1.07(102)
	5.44	5.76	$44^{+2.0}_{-2.0}$	$12^{+0.7}_{-0.7}$	0.85(101)	5.0	0.84 ± 0.28	0.82(99)

As already mentioned (sec.6.2) the fits have been performed only on spectra with $\alpha \geq 0.5$. In order to determine the value of this threshold in α we simulated spectra with a black body model assuming the detector response of these bursts and a typical exposure time ~ 0.2 sec (i.e. the average integration time of the spectra presented before). We then fitted these simulated thermal spectra with a non-thermal model

$N(E) \propto E^\alpha \exp(-E/E_0)$ where the power law spectral index α was fixed at different values between 0 (a flat photon spectrum) and +1 (which best approximates a thermal spectrum). The residuals of these fits indicated that for $\alpha < 0.5$ the model spectrum (at low energies) deviates systematically from the data (i.e. residuals different from 0) at more than 2σ . For this reason we selected $\alpha = 0.5$ as the threshold for fitting the spectra with a black body model. The criteria applied for the goodness of the fit were:

- the reduced χ_r^2 should be smaller than a fixed reference value of 1.5. We performed the fits also on spectra with a low energy component softer than our threshold value $\alpha = 0.5$ and found that these fits are unacceptable and typically have $\chi_r^2 > 1.5$.
- the data-to-model ratio in each energy bin can be systematically and significantly greater than 1 only at energies above the peak. This is because in this case a deviation of the observed spectrum from a pure black body at high energies can be still consistent with the hypothesis that the spectrum is indeed a black body if for example there is a supra-thermal component or a multi-temperature black body. The deviation of the observed data points from the black body shape at low energies instead were considered an indication of an inconsistency of the spectrum with the thermal model.

The results of the fits with a black body to the time resolved spectra of all the five bursts discussed before are reported in table 6.2: the start and stop time of each spectrum, with respect to the trigger time, are given in col. 2 and 3. The model temperature kT (keV) and its normalization ($\text{erg cm}^{-2} \text{s}^{-1}$) are reported in col. 4 and 5. The value of the reduced χ_r^2 and the photon flux, computed from the fitted black body model in the 28–1800 keV energy range, are given in col. 6 and 7, respectively. Column 8, reports the values of the low energy spectral index obtained fitting the BAND or the COMP model and the relative reduced χ^2 is represented in col.9.

For illustration, we report in fig. 6.9 some examples of fitted spectra and the corresponding data-to-model ratio in the case of GRB 980306. The first two spectra are considered well fitted by the model because $\chi_r^2 = 1.19$ and 0.9 (for 111 d.o.f), respectively, and the ratio is systematically greater than 1 only at high energies. In the other two cases the black body fits give less acceptable results because the data-to-model ratio shows systematic deviations from 1 at low energies.

All the fitted spectra listed in tab.6.2 are reported at the end of this chapter. Considering the χ^2 obtained from the fit with the black body and the residual of each spectrum, we can say that in most of the bursts the best fit, with the black body, is obtained at the beginning: in the late phases (e.g. after 2.5 sec in the case of GRB 980306, bottom right and left panels of fig.6.9) the low energy component softens and becomes incompatible with a black body model as the reduced χ^2 and the model-to-data ratio indicate.

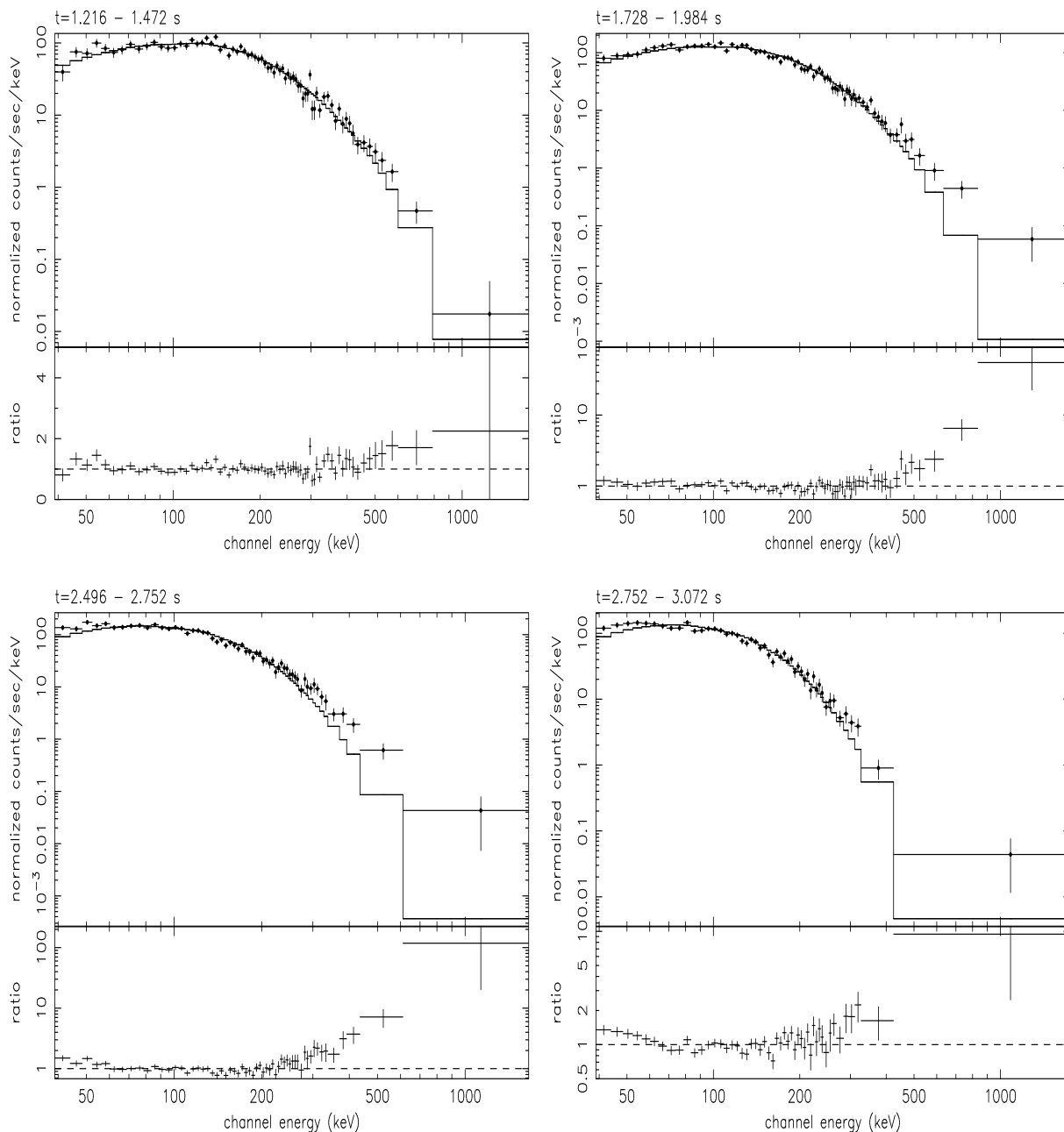


Figure 6.9: Examples of black body fits for GRB 980306 (see tab.6.2. The integration times are indicated for each plot. The data-to-model ratio are reported in the bottom panels.

It should be noted that the black body fits which result in a characteristic temperature $kT \leq 30$ keV have a limited portion of their Rayleigh–jeans part in the BATSE energy band and the associated black body fits are not well determined. These spectra have not been considered.

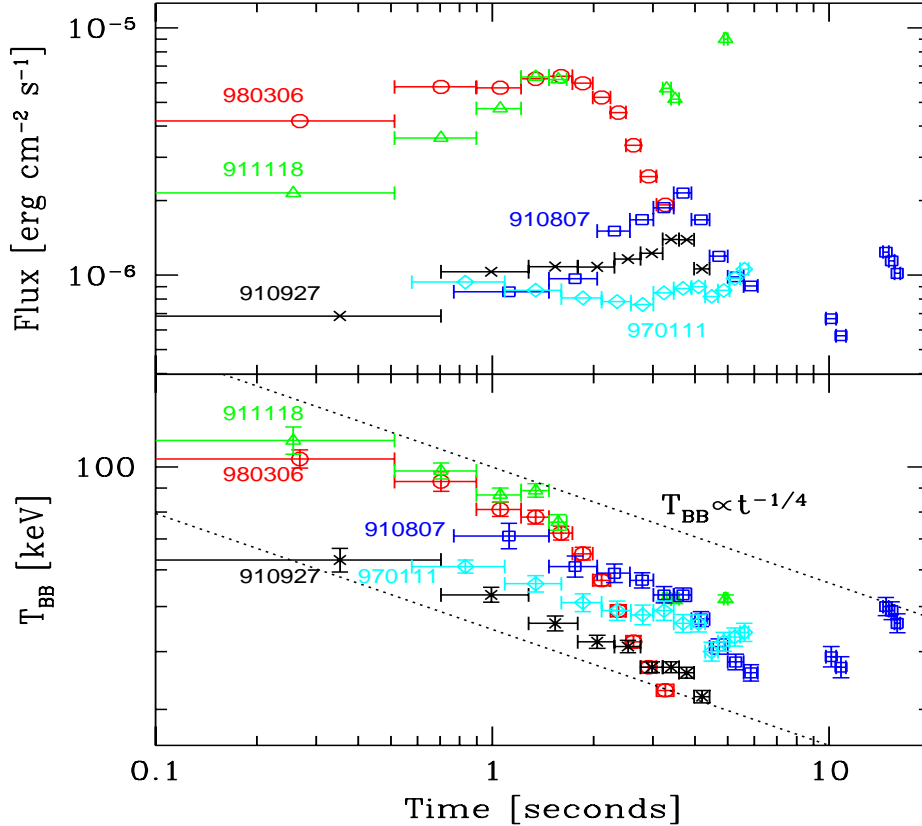


Figure 6.10: Total flux (top panel) and black body temperature (bottom panel) as a function of time for the spectra reported in Tab. 6.2 and considered acceptable in terms of residuals. The dashed lines in the bottom panel correspond to $T_{BB} \propto t^{-1/4}$.

It is still useful to consider from tab.6.2 the relation between the total flux (derived integrating the best fit black body model) and the black body temperature with time (reported in fig.6.10 in the top and bottom panels, respectively). The decrease of the temperature T_{BB} with time for almost all the 5 bursts is consistent with a power law decay with index $-1/4$, i.e. $T_{BB} \propto t^{-1/4}$. It should also be noted that while the temperature decreases the flux slightly increases (e.g. GRB 911118) or remains quite constant (e.g. GRB 970111) in the first phase and rapidly decreases thereafter.

6.6 Discussion

GRB 980306, together with GRB 911118, 910807, 910927 and 970111, brings new evidence of extremely hard low energy spectra (especially in the initial phase) that any emission process, responsible for the prompt phase, must be able to justify.

These bursts represent the cases with the hardest low energy powerlaw spectral index and significantly contribute in extending the α distribution reported by Preece et al. [130]

and Ghirlanda et al. [51]) to values greater than $\alpha = 0$, up to $\alpha \sim 1.5$.

For the bursts analyzed in this chapter, we have shown that α , the spectral index of the low energy power law component which can be used to fit the spectra, remains positive for a major part of the pulse/s, like in the case of GRB 911118 (fig.6.4) or GRB 970111, or for its first rising part (GRB 980306 and GRB 910807 - fig.6.3 and 6.7, respectively).

The results presented in the previous sections allow to consider several emission models present in the literature (and reviewed in chapt.3) to see if they can account for these hard spectra. A separate consideration is reserved to the possible origin of the quasi-thermal shape of the initial phases of these bursts within the framework of the photospheric and Compton drag model (sec. 6.7)

6.6.1 Synchrotron emission

Standard thin synchrotron emission

The optically thin synchrotron model (sec.3.2.1), in its simplest formulation, can produce at most a spectrum as hard as $\alpha = -2/3$ (Katz [77]) below the peak energy E_{peak} . This is not consistent with the 15% of spectra with $\alpha > -2/3$ which have been found by the time resolved analysis of the burst sample presented in chapt.5 and also with the same percentage found by Crider et al. [21] and Preece et al. [130]. Moreover, the time resolved spectra of the 5 hardest bursts discussed in this chapter indicate that, at low energies they are harder than $\alpha = 0$ at several σ s. This evidence is even more in contradiction with the model predictions if the very short cooling timescales (much shorter than any conceivable current exposure time) are considered: in this case, in fact, the predicted ‘cooled’ spectrum (sec.3.2.2) has $\alpha = -3/2$ (Ghisellini et al. [56]).

Synchrotron self-absorption

This alternative, investigated among others by Papathanassiou ([123]), is based on the absorption of the low energy spectrum by the same medium responsible for the synchrotron emission (sec. 3.2.1). In this case it is possible to produce low energy spectral slopes as hard as $\alpha = 1$, if the emitting electrons have a thermal or a power law energy distribution with a low energy cut-off, or $\alpha = 1.5$, for a power law electron energy distribution extending to low energies.

However, for synchrotron self-absorption to be effective in the typical BATSE energy range, a very high density of relativistic electrons is necessary. Assuming that the electron distribution extends to low energies (this minimizes the required particle number) with a power law distribution of index p (i.e. $N_e(\gamma) \propto \gamma^{-p}$, where γ is the Lorentz factor of the electrons), the synchrotron self-absorption frequency ν_t in the comoving frame, is

(eq.3.10 - chapt.3)

$$\nu_t \simeq C(p)^{2/(p+4)} \nu_B (\tau_T/B)^{2/(p+4)} Hz \quad (6.1)$$

where τ_T is the Thomson optical depth, $\nu_B = eB/(2\pi m_e c)$ is the Larmor frequency, and $C(p)$ a combination of constants and Gamma functions². For $p = 2$ the numerical value results $C(p) \simeq 1.7 \times 10^5$, and the above equation becomes

$$\nu_t \simeq (2 \times 10^5) \nu_B (\tau_T/B)^{1/3} Hz \quad (6.2)$$

In order to have $\nu_t \sim 10^{16}$ Hz, corresponding to an observed absorption energy $\sim \Gamma \nu_t$ falling in the BATSE range³, we need

$$\tau_T B^2 \sim 5.7 \cdot 10^{12} \nu_{t,16}^3 \quad (6.3)$$

where $\nu_{t,16}$ is the frequency expressed in units of 10^{16} Hz.

The Comptonization parameter $y \sim \tau_T \langle \gamma^2 \rangle$ corresponding to the required particle density, would largely exceed unity (making inverse Compton process more efficient than synchrotron) unless the magnetic field is extremely high ($B \sim 10^7$ G). This would in turn imply a (magnetically dominated) fireball with isotropic (equivalent) energy in excess of 10^{54} erg, using $E \sim 4\pi R^2 (B^2/8\pi) \Gamma^2 ct_{burst}$ and assuming $\Gamma \sim 10^2$ and $R \sim 10^{13}$ cm. A magnetic field of $\sim 10^7$ G has been derived also by Crider & Liang ([?]) from the fit of a simplified self absorbed synchrotron model to the spectrum of GRB 970111.

Synchrotron from a stratified region

Granot, Piran & Sari ([63]) have pointed out that if the electrons producing synchrotron emission are accelerated in a shock, than the emission region is plausibly stratified, with the most energetic electrons present only in the vicinity of the shock front, while colder electrons propagate further away from it (sec. 3.2.4). This inhomogeneity introduces some modification in the predicted self-absorbed synchrotron spectrum which may be relevant for the interpretation of the afterglow emission, but does not change the above conclusion on the role of synchrotron self-absorption as responsible for the hard γ -ray spectra. In fact the resulting spectrum is characterized below the peak energy by a $F(E) \propto E^{11/8}$ slope, produced by this complication, between the self absorption power law component (i.e. $F(E) \propto E^2$) and the typical synchrotron power law $E^{1/3}$ (see eqn. 3.21). This can accommodate spectral slopes steeper than the typical synchrotron limit (i.e. $1/3$, or $-2/3$), particularly if the $\propto E^{11/8}$ and $\propto E^2$ power laws are fitted by a single spectral component (like for the majority of the spectral functions employed in the data analysis) but still suffers the same problems discussed for the synchrotron self absorption case.

² $C(P) = \left[\frac{3^{p/2} A(p) \pi \sqrt{3\pi}}{4} \frac{e}{\sigma_T} \right]$

³for $\Gamma \sim 10^3 - 10^4$ the observed energy results of some keV.

Small pitch angles

This model (sec. 3.2.6) has already been discussed for its predictions about the correlations between the spectral parameters in bursts with a low energy spectral index $\alpha \geq 1/3$. The basic features of this model, proposed by Lloyd & Petrosian ([98]) are based on the idea that in the rarefied, highly magnetized plasmas characteristics of GRBs, turbulence can give origin to an anisotropic pitch angle distribution of emitting particles. In this case the thin synchrotron emission is modified at low energies (compared to the standard $F(E) \propto E^{1/3}$), with a limiting slope $F(E) \propto E^1$ (eq. 3.34). This can accommodate some, but not all, of the hard spectra presented before. Note also that according to this scenario to prevent strong cooling the particles have to be re-accelerated, contrary to one of the basic assumptions of the internal shock scenario, and in order not to be re-isotropized by scattering, the inverse Compton process must be much less efficient than the synchrotron one. Moreover the requirement of small pitch angles implies that the ratio between the electron velocity components (perpendicular and parallel to the field lines, v_{\perp} and v_{\parallel}) is $v_{\perp}/v_{\parallel} \ll \gamma_e^{-1}$. This as a consequence produces a low efficiency of radiated energy $\epsilon \sim v_{\perp}^2/v_{\parallel}^2 \ll 1$.

Jitter radiation

A variant of the standard synchrotron theory, the jitter radiation (Medvedev [107]), can justify flat to mildly inverted low energy spectral slopes (sec. 3.2.5). It is the emission of relativistic electrons in a non uniform magnetic field: if the inhomogeneity length scale is smaller than the Larmor gyro-radius, the electron jitters around its average direction of motion. Medvedev ([107]) proposed a composite model for GRB spectra (Jitter + Synchrotron) by assuming the presence of a small scale magnetic field, which causes the jitter radiation component and its spectral slope at low energies $F(E) \propto E^1$, while a softer component, produced by the large scale magnetic field, is the typical synchrotron spectrum. The composition of these two spectra, at low energies, can produce also a concave spectrum (see fig. 3.2). In general, the composite spectrum has a broad bump in correspondence of the jitter radiation characteristic energy, which depends only on the magnetic field properties and not on the electron energy (Medvedev [107]): if the small scale magnetic field prevails, the spectrum has a limiting low energy spectral index $\alpha = 0$. This implies that only a minority of the hard spectra reported here could be consistent with such a model because most of the initial phases of GRB 980306 and 911118 are harder than E^0 at more than 3σ . On the other hand, one appealing feature which has not been investigated in this model, is the spectral evolution (in particular of the low energy component) from hard to soft: it could likely be (as also shown by 2D numerical simulations) that the small scale magnetic field evolves in time becoming progressively dominated by a large scale structure. This implies that at the beginning the jitter component might prevail over synchrotron, and the spectrum has a steep $\alpha = 0$ slope, whereas at late times the large scale magnetic field determines the synchrotron component to be the observed one. This is in agreement with the low energy hard to

soft spectral evolution and could be quantitatively investigated for the verification of the typical timescales. From actual simulations the timescale of the small-to-large scale shift is $t \sim 10^{-8} n_e^{-1/2}$ sec, and this requires an extremely low density to make this time of the order of some seconds (but see cautions in Kazimura et al. [79])

6.6.2 Compton attenuation

Although not a radiation mechanism, Compton attenuation (Brainerd et al. [12]) can produce a low energy (20–100 keV) hard component because of the propagation and scattering of the intrinsic spectrum by material (not participating to the bulk flow) located between the fireball and the observer (sec. 3.3.4). The Compton attenuation cross section is energy dependent so that the original spectrum, emitted by the source, can be unaltered at high energies because of the decline of the Klein–Nishina cross section with energy, while, at lower energies, where the scattering process is more efficient, the spectrum is hardened. The most appealing features of this model are that it could explain the clustering of the peak energy of bursts around some hundred keV (sec. 2.3) and produce an arbitrarily steep slope at low energies. But in order for this to work, the Thomson optical depth of the scattering material must be quite large (of the order of $\tau_T \sim 10$) and this would smooth out the observed burst light curve by smearing the variability on the smallest time scales. Furthermore, by decreasing the transmitted (spectrally unaltered) flux, this mechanism requires intrinsic powers greater than what we observe, exacerbating the energy budget problem.

6.6.3 Quasi-thermal Comptonization

The above models are based on the assumption that the emitting particles are highly relativistic, as a result of “instantaneous” acceleration at a shock front. However, if the heating mechanism operates on timescales of the order of the dynamical time (or the light crossing time of a shell in the internal shock scenario), then the heating and cooling processes could balance, leading to typical energies of the electrons that are sub or only mildly relativistic (Ghisellini & Celotti [55], see also sec. 3.3.6). In this case the dominant radiation process is Comptonization of seed soft photons by a quasi-thermal particle distribution. Different models assume different sources for the seed photons and different parameters (i.e. typical size for the emitting region, magnetic field, role of the photospheric radiation, and so on) within the internal shock scenario.

Liang et al. ([96]), among the first to propose such process for the prompt emission, considered a relatively large emitting region embedded in a relatively weak magnetic field, so that the resulting observed spectrum in the GRB prompt phase is due to multiple Compton scattering of self emitted soft (synchrotron and bremsstrahlung) photons. This model was applied to GRB 990123 by Liang et al. ([97]), who found quite extreme best fit values for the required total power and total number of emitting particles: in particular the baryon number was found to be $N_b = 2.7 \times 10^{60} R_9^2 \Omega_{4\pi}$, and for a typical shell

emission distance R_9 and in the isotropic case (as upper limit), the required shell mass would be of $\sim 1M_\odot$ (or even more dramatically $\sim 1000M_\odot$, considering only protons).

Ghisellini & Celotti ([55]) proposed the Comptonization model based on the self-absorbed cyclo-synchrotron radiation produced by the same quasi-thermal particles responsible for the multiple scattering process, and pointed out the role that electron-positron pairs can have in keeping the temperature (or the mean energy) of the particles within a narrow range. On the same line Meszaros & Rees ([113]) stressed the importance of the residual photospheric emission as source of soft photons.

The basic features of the Comptonization model is that, in the quasi-saturated regime a Wien peak with its characteristic $F(E) \propto E^3$ shape (tab. 6.1) can form at high energies (i.e. for $h\nu \sim kT$). In principle this can thus explain very hard spectra like those reported above. One possible difficulty of this model lies in the low energy spectral component which, in saturated regime (e.g. $\tau_T \gg 1$) should have a slope $F(E) \propto E^0$.

A further possible problem for quasi-thermal Comptonization is that the temperature of the emitting particles (in the comoving frame) is expected to be of order of ~ 50 keV, which would lead to an observed E_{peak} of few MeV (Ghisellini & Celotti [55]). This is a somewhat high value, also in the light of the results presented in this work, which show that even spectra time resolved on scales ≤ 1 sec present a peak energy of $E_{peak} \leq 500$ keV.

6.6.4 Photospheric emission

When the fireball is becoming optically thin, its internal radiation, during the acceleration or coasting phase, is emitted with a black body spectrum whose observed temperature kT is blue-shifted by a factor Γ with respect to the comoving one kT' . Recently, Daigne & Mochkovitch ([25]) have explored this possibility, finding quite tight limits on the model of hot fireballs accelerated through internal radiation pressure, based on the absence of an initial emission phase (or precursor) with a black body shape. Since we do find, especially in GRB 980306, that the emission can be modelled by a black body during the first phase of these extremely hard bursts (sec. 6.5), this possible model and its implications for the determination of the fireball parameters will be discussed in more details in sec. 6.7.1.

6.6.5 Compton drag

If the circum-burst environment is characterized by quite a large photon density, as is the case of bursts following a supernova explosion, or for fireballs produced in the matter-evacuated funnel of an hypernova, then there can be a strong interaction between these seed photons and the fireball itself, as postulated in the so-called Compton drag model. The ambient photon energy is boosted by the factor Γ^2 at the expense of the fireball kinetic energy (Lazzati et al. [91]). If the funnel or the young supernova remnant are

characterized by a single temperature T_{SN} , and if the fireball does not decelerates, then the emitted spectrum is black body at a temperature $T \sim \Gamma^2 T_{\text{SN}}$. If instead the seed photons have a range of temperatures (as likely to be in the case of a funnel, hotter in the central parts - see also sec. 6.7.2), and/or the process is so efficient to decelerate the fireball, then the final spectrum will be a superposition of the locally produced black body spectra, as calculated by Ghisellini et al. ([56]), and summarized in sec. 3.3.8. The resulting spectrum can be as hard as $F(E) \propto E^2$, i.e. the Rayleigh–Jeans part of the seed thermal spectrum. Moreover, according to this mechanism the observed hard spectra should characterize the initial phase of the emission since, once the first shells have swept up the seed photons, the efficiency of Compton drag is greatly reduced, due to the long time (longer than the burst duration) required to replenish the circum–burst environment with seed photons. On the other hand the Compton drag model favors the formation of internal shocks, since after the first shells deceleration, the subsequent ejecta can more easily collide with them and produce shocks and share the energy among baryons and the magnetic field. Then another radiation source (e.g synchrotron) can become efficient after the first phase (lasting ~ 1 to a few seconds). Another appealing feature of the Compton drag model is the natural justification of the hard to soft spectral evolution (chap.2 and 7): at first the spectrum, due to Compton drag, is very hard at low energies ($F(E) \propto E^2$), whereas at later times the spectrum produced in internal shocks through other processes becomes responsible for the softer ($F(E) \propto E^{1/3}$ or $\propto E^0$) component.

6.7 The possible thermal character of the initial phase

It has been shown in sec 6.5 through direct spectral fitting that the first 1–5 s of the emission of the bursts presented in this chapter are consistent with a black body spectrum. The typical temperatures are, initially, around 100 keV and then decrease to 30–40 keV, possibly with a common decay law $\propto t^{-1/4}$. After this initial phase the spectrum becomes softer and shows a non–thermal or possibly multi–temperature softer character. The black body initial spectrum and its spectral evolution to a softer non-thermal spectrum represent powerful diagnostics for the prompt phase emission mechanism.

In particular, in the following sections, the photospheric (6.7.1) and the Compton drag emission (6.7.2), which are able to produce such thermal spectra and their observed evolution, are discussed in the light of the new evidences presented in sec.6.5. These models allow to determine some physical parameters of the fireball model and also some simple scaling relations which could be verified by future spectral analysis and refined by a more detailed formulation.

6.7.1 Photospheric emission

As already outlined in sec. 6.6.4, this model predicts the emission of a back body spectrum when the photosphere becomes optically thin.

In the simplest scenario one could associate the observed thermal spectra of the initial phases of the GRB to a single fireball becoming transparent. In this case, it will be shown that the energy content derived using the spectral analysis results presented before, is unreasonably large.

Another possibility, which has been recently investigated also by Daigne & Mochkovitch ([25]), considers an ensemble of \mathcal{N} shells which become independently transparent and contributing, individually, a thermal spectrum.

In both cases the emission is related to the thick/thin transition, corresponding to:

$$\tau_{\text{T}} \sim 1 \quad (6.4)$$

Considering a shell (but the case of \mathcal{N} shells is equivalent) of width ΔR which becomes transparent at a distance R_t (the transparency radius, hereafter), moving with a bulk Lorentz factor Γ and particle density n , its optical depth is defined as:

$$\tau_{\text{T}} = n\sigma_{\text{T}}\Delta R = \frac{M/m_p}{4\pi R_t^2 \Delta R} \sigma_{\text{T}} \Delta R \quad (6.5)$$

substituting the definition of the shell mass $M = E_f/c^2\Gamma$ (where E_f is the fireball energy a fraction ϵ_γ of which is radiated into photons), and including the possible collimation of the fireball in two cones of semi-aperture angle θ , we obtain (generalizing to the case of multiple shells \mathcal{N}):

$$\tau_{\text{T}} = \frac{E_f\sigma_{\text{T}}}{2\pi\theta^2 R_t^2 m_p c^2 \Gamma \mathcal{N}} \sim 1 \quad (6.6)$$

If the shell emits at the transparency radius R_t a black body spectrum with comoving temperature T' , the observed temperature will be $T_{\text{obs}} = \Gamma T'$ and the luminosity of the black body radiation can be expressed as:

$$\langle L_{\text{BB}} \rangle = \frac{\epsilon_\gamma E_f}{t_{\text{BB}}} \quad (6.7)$$

where t_{BB} is the time during which the black body luminosity has been observed (not to be confused with the time corresponding to the transparency transition) and $\langle L_{\text{BB}} \rangle$ represents the *average* black body luminosity observed for the time t_{BB} . σ is the Stefan-Boltzmann radiation constant. This last equation can also be expressed as:

$$\langle L_{\text{BB}} \rangle = \frac{\epsilon_\gamma E_f}{t_{\text{BB}}} = 2\pi\theta^2 R_t^2 \sigma \left(\frac{T_{\text{obs}}}{\Gamma} \right)^4 \Gamma^2 \quad (6.8)$$

We can immediately derive an interesting result: both eq. (6.6) and (6.8) are characterized by the same dependence of $E_f \propto \theta^2 R_t^2$ which allows to solve for the Lorentz factor:

$$\Gamma = \left(\frac{\sigma_{\text{T}} \sigma}{m_p c^2} \frac{T_{\text{obs}}^4 t_{\text{BB}}}{\epsilon_\gamma \mathcal{N}} \right)^{1/3} \sim 3 \times 10^3 T_{\text{obs},9}^{4/3} t_{\text{BB}}^{1/3} \epsilon_\gamma^{-1/3} \mathcal{N}^{-1/3} \quad (6.9)$$

with $T_{\text{obs}} = 10^9 T_{\text{obs},9} \text{ K}^4$ (corresponding to the observed black body peak of $\sim 100 \text{ keV}$). This estimate of the bulk Lorentz factor is consistent with the typical values of the fireball model and it is appealing that it results independent from the beaming of the fireball θ .

The transparency condition (eq.6.6) and the average black body luminosity (eq.6.9) emitted by a single shell or by a number \mathcal{N} of shells lead to the determination of some fundamental parameter of the fireball, like the energy content and the radius of emission of bulk of the thermal photons. In the following we explore these two scenarios separately.

Single shell

t_{BB} is, in this case, the time necessary for the single shell to become transparent and is related to the transparency radius:

$$R_t = ct_{BB}\Gamma^2 \sim 3 \times 10^{17} T_{\text{obs},9}^{8/3} t_{BB}^{5/3} \epsilon_\gamma^{-2/3} \text{ cm.} \quad (6.10)$$

where the expression of the bulk Lorentz factor (6.9) has been used.

For typical fireball parameters ($\epsilon_\gamma \sim 0.1$) the transparency radius results very large $\sim 10^{18} \text{ cm}$ (at least comparable with the radius where the external shock develops - see chapt.1). Moreover, the fireball energy (computed substituting the the expressions of Γ and R_t obtained from eq.(6.9) and (6.6), respectively) results:

$$E_f \sim 3 \times 10^{58} \theta_{0.1}^2 T_{\text{obs},9}^{20/3} t_{BB}^{11/3} \epsilon_\gamma^{-5/3} \text{ erg.} \quad (6.11)$$

which is unreasonably high and would produce a too large black body luminosity.

Multiple shells

If the observed emission is associated with a series of \mathcal{N} shells, each becoming transparent at a given radius R_t , then the expression (6.10) cannot be used because each shell becomes transparent at an unknown time t_i . The Lorentz factor (eq. 6.9) can be substituted in eq. 6.6 deriving an expression for the transparency radius:

$$R_t \sim 5 \times 10^{13} \frac{E_{f,51}^{1/2}}{\theta_{0.1} \mathcal{N}^{1/3}} \left(\frac{\epsilon_\gamma}{t_{BB} T_{\text{obs},9}^4} \right)^{1/6} \text{ cm.} \quad (6.12)$$

where a typical fireball energy $E_f = 10^{51} E_{f,51} \text{ erg}$ has been assumed. In this case the transparency radius of the single shells is smaller than the estimate in the single shell scenario. We conclude that a series of shells (of total energy E_f) each becoming transparent at R_t can account for the observed black body emission. Note also that the case of \mathcal{N} shells, for large \mathcal{N} , is equivalent to a continuous or quasi-continuous flow. In this case, in fact, the flow would become transparent at a fixed distance. As Daigne & Mochkovitch ([25]) pointed out, the photospheric radiation is likely to be visible only during the first phases of the burst light curve, until the optical depth of the material ahead of the shell is negligible and before internal shocks take over.

⁴Here we use the standard notation $Q_x = Q/10^x$

Scaling relations

In the above scenario we can also derive the scaling relations for the shell parameters L and Γ with the radius and the temperature. These relations can be further combined with the observed temporal trend of T and L to derive approximately the shell evolution in terms of its physical parameters. In fact, until now, we only used the experimental evidence, presented in sec. 6.5, that the thermal character of the spectrum is evident in the initial phase of the burst emission, but we can also consider the results of fig.6.10 where the luminosity and temperature time dependencies are reported.

As reported in Fig. 6.10 in all the 5 bursts, the black body temperature decreases with time (bottom panel) and its evolution is intriguingly close to $T_{\text{obs}} \propto t^{-1/4}$ for the first few seconds, and then drops. In the same time interval the luminosity (L_{BB}) remains constant or mildly increases (top panel of Fig. 6.10). We therefore observe, at least in the first phase, a decrease in the observed temperature without a corresponding decrease in the observed black body flux.

The luminosity of the i th shell, becoming transparent at the distance $R_{t,i}$ is,

$$L_i \propto R_{t,i}^2 \left(\frac{T_{\text{obs},i}}{\Gamma_i} \right)^4 \Gamma_i^2 \quad (6.13)$$

where, for the moment we do not consider the possible variation of beaming with time.

The transparency condition for the i th shell, similarly to eq. 6.6, gives a relation for its energy,

$$E_{f,i} \propto R_i^2 \Gamma_i \quad (6.14)$$

By definition the shell luminosity can also be expressed as the energy radiated by the shell (a fraction ϵ_γ of the shell energy $E_{f,i}$) and the characteristic time t_i at which the shell becomes transparent $L_i = (\epsilon_\gamma \cdot E_{f,i}) / t_i$. The time t_i represents the interval between the i th shell production and its thick/thin transition, and is $t_i = R_i / \Gamma_i^2 c$, which substituted, gives:

$$L_i \propto \frac{\epsilon_\gamma E_{f,i} \Gamma_i^2 c}{R_i} \quad (6.15)$$

Combining eq. (6.14) and (6.15) we get,

$$L_i \propto \frac{\epsilon_\gamma R_i^2 \Gamma_i \Gamma_i^2 c}{R_i} \propto \epsilon_\gamma \Gamma_i^3 R_i \quad (6.16)$$

Assuming $\epsilon_\gamma = \text{const}$, from the last and the first expression of the black body luminosity,

$$\Gamma_i^3 R_i \propto \frac{R_i^2 T_{\text{obs},i}^4}{\Gamma_i^2} \quad (6.17)$$

Thus, considering the shell black body luminosity and the transparency condition the Lorentz factor of the shell can be derived as a function of the radius at which bulk of the thermal photons are emitted and of their temperature:

$$\Gamma_i \propto R_i^{1/5} T_{\text{obs},i}^{4/5} \quad (6.18)$$

Similarly the shell luminosity is:

$$L_i \propto \frac{R_i^2 T_{\text{obs},i}^4}{R_i^{2/5} T_{\text{obs},i}^{8/5}} = R_i^{8/5} T_{\text{obs},i}^{12/5} \quad (6.19)$$

Let us now consider the possibility of combining these relations to describe the temporal evolution of the complete set of physical parameters of the shell: the Lorentz factor Γ , the luminosity L and the radius of photon escape R , the energy content E and the associated mass M .

As shown by the black body spectra discussed in this chapter (fig.6.10) the best fit temperature decreases with time while the photon flux increases or remains constant so that we can assume a relation $T_{\text{obs}} \propto t^{-\alpha}$. Γ and L then scale as:

$$\begin{cases} \Gamma_i \propto R_i^{1/5} t^{-4\alpha/5} \\ L_i \propto R_i^{8/5} t^{-12\alpha/5} \end{cases} \quad (6.20)$$

Let's consider first a special situation in which the transparency radius is constant and discuss these time dependencies. In this case the luminosity scales as $t^{-12\alpha/5}$, i.e. faster than the Lorentz factor which is proportional to $t^{-4\alpha/5}$. The faster decrease of the black body luminosity could explain the appearance of the thermal spectrum only at the beginning of the bursts and for a limited time interval (few seconds). Nonetheless, the slower decrease of Γ could determine still an Compton drag boosting of the thermal photons when their luminosity is already low. After the shell has decelerated considerably then only a non-thermal component, e.g. the shock synchrotron emission, could start to dominate. In this sketched scenario, there could be a "continuous" radiative transition between the initial thermal character of the extremely hard bursts observed and their final non-thermal emission.

On the other hand if also the luminosity of the fireball is parametrized as $L \propto t^\beta$ (see fig.6.10 top panel), then the radius and the Lorentz factor become (from eq.6.21):

$$\begin{cases} R_i \propto t^{(\frac{5}{8}\beta + \frac{3}{2}\alpha)} \\ \Gamma_i \propto t^{(\frac{\beta}{8} - \frac{1}{2}\alpha)} \end{cases} \quad (6.21)$$

Approximating the relations reported in fig.6.10 with $\alpha = 1/4$ and $\beta = 1/3$ (which seems to be a reasonable slope at least for some of the bursts represented in the figure) one can

uniquely derive the temporal evolution of the physical parameters of the shell:

$$\left\{ \begin{array}{l} \Gamma_i \propto t^{-1/12} \\ L_i \propto t^{+1/3} \\ R_i \propto t^{+5/6} \\ E_i \propto t^{+3/2} \\ M_i \propto t^{+19/12} \end{array} \right. \quad (6.22)$$

These relations are represented in fig.6.11 (solid lines) assuming the observed temperature evolution $T_{\text{obs}} \propto t^{-1/4}$.

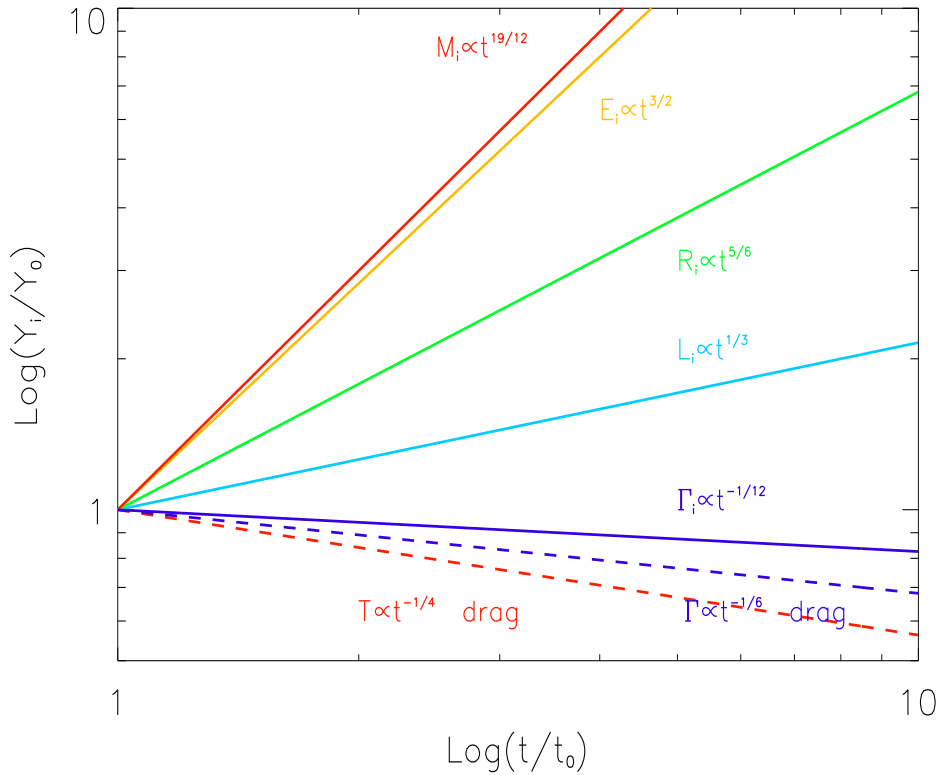


Figure 6.11: Scaling relations for the photo sphere model (solid lines) and the limiting relations for the Compton drag model (dotted lines). These relations are determined (see text) assuming the approximate scaling relations found for the temperature and the luminosity of the initial phase of the 5 bursts presented in this chapter: $T_{\text{obs}} \propto t^{-1/4}$ and $L \propto t^{-1/3}$.

This result, although obtained from simplified and approximate relations between the parameters, indicates that the photospheric model can directly link the spectral ob-

servables to the dynamics: in particular if the spectrum is observed to have a black body shape evolving for some initial part of its emission, it is possible to describe the temporal evolution of the fireball.

In the context of the photospheric model discussed in Sec. 5.7.1, the black body evolution could be explained by successive shells having an increasing baryon loading and smaller Lorentz factor, thus becoming transparent at increasing distances R_t . This can cause the observed temperature to decrease (because the Lorentz factor is smaller) without a decrease in flux (because the radius is larger).

6.7.2 Compton drag

As mentioned in sec.6.6.5, if the circum-burst environment is characterized by quite a large photon density, as is the case of bursts following a supernova explosion, or for fireballs produced in the matter–evacuated funnel of an hypernova, there can be a strong interaction between these seed photons and the fireball itself, as postulated in the so-called Compton drag model. The ambient photon energy is boosted by the factor Γ^2 at the expense of the fireball kinetic energy (Lazzati et al. [91]). If the funnel or the young supernova remnant are characterized by a single temperature T_{SN} , and if the fireball does not decelerate, the emitted spectrum is a black body at a temperature $\sim 2\Gamma^2 T_{\text{SN}}$. If instead the seed photons have a range of temperatures (as likely to be in the case of a funnel, hotter in the central parts), and/or the process is so efficient to decelerate the fireball, than the final spectrum will be a superposition of the locally produced black body spectra, as calculated by Ghisellini et al. ([56]).

We assume that the time interval for which the black body lasts (that was indicated as t_{BB} in the previous section) corresponds to the emission from a single shell, since one problem of this model is the replenishment of the circum-burst environment with seed photons for the subsequent shells. We also assume that the emission peaks when when the shell becomes transparent (e.g. the 4th spectrum in the case of GRB 980306, see tab.6.2), implying that the relation $R_t \sim ct_t \Gamma^2$ is valid.

The observed temperature T_{obs} is a factor $\sim 2\Gamma^2$ larger than the temperature of the seed photons T_{SN} (chapt.3), and the total energy E_{CD} due to the Compton drag process, produced in the observed time t_t is of the order

$$E_{\text{CD}} = 2\pi\theta^2 R_t^3 (2\Gamma^2) a \left(\frac{T_{\text{obs}}}{2\Gamma^2} \right)^4 = \frac{\pi}{4} \theta^2 c^3 t_t^3 a T_{\text{obs}}^4 \quad (6.23)$$

where $a = 7.56 \times 10^{-15} \text{ erg cm}^{-3} \text{ K}^{-4}$ is the radiation constant. Expressed in typical units this results:

$$E_{\text{CD}} = 3 \times 10^{51} \theta_{0.1}^2 t_t^3 T_{\text{obs},9}^4 \text{ erg.} \quad (6.24)$$

We stress that in this form E_{CD} does not depend on Γ (although T_{SN} does), and is in agreement with the basic energetic requirements of the standard model.

Also in this case the optical depth and the transparency condition give eq.(6.6) which, combined with $R_t = ct_t\Gamma^2$, allow us to derive an expression for the transparency radius:

$$R_t = \left(\frac{\sigma_T c^{3/2} t_t^{7/2} a T_{\text{obs}}^4}{8\epsilon_\gamma m_p} \right)^{2/5} \sim 3 \times 10^{14} T_{\text{obs},9}^{8/5} t_t^{7/5} \epsilon_\gamma^{-2/5} \text{ cm} \quad (6.25)$$

and for the bulk Lorentz factor,

$$\Gamma = \left(\frac{R_t}{ct_t} \right)^{1/2} \sim 100 T_{\text{obs},9}^{4/5} t_t^{1/5} \epsilon_\gamma^{-1/5} \quad (6.26)$$

assuming a temperature of the seed photons corresponding to $T_{\text{SN}} \sim 5 \times 10^4 \text{K}$.

Although these are still rough estimates they indicate that the Compton drag model is a viable mechanism for the production of extremely hard spectra at the beginning of the burst.

Scaling relations

Also within the framework of the Compton drag model we can derive some interesting scaling relations from the approximations of the temporal behaviour of the temperature and the luminosity reported in fig.6.10

The luminosity of the Compton drag, in the lab frame, can be approximated as:

$$L_{\text{CD}} \propto \frac{E_{\text{CD}}}{t} \propto \frac{R^2 \Delta R}{t} \left(\frac{T_{\text{obs}}}{\Gamma^2} \right)^4 \Gamma^2 \quad (6.27)$$

and using the relation $R \propto ct\Gamma^2$, becomes

$$L_{\text{CD}} \propto t^2 T_{\text{obs}}^4 \quad (6.28)$$

The observed black body temperature is $T_{\text{obs}} \sim \Gamma^2 T_{\text{seed}}$ and assuming that the temperature and the Lorentz factor are functions of the radius, the scaling relations are

$$\begin{cases} T_{\text{seed}} \propto R^{-a} \rightarrow T_{\text{obs}} \propto \Gamma^2 \Gamma^{-2a} t^{-a} \\ \Gamma \propto R^{-b} \rightarrow \Gamma \propto t^{-b/(1+2b)} \end{cases} \quad (6.29)$$

Combining these two relations, we find that the temperature scales as

$$T \propto t^{-(a+2b)/(1+2b)} \quad (6.30)$$

If we take the approximate relation of fig.6.10 for the temperature, with $T \propto t^{-1/4}$ we can derive a relation between the indices a and b

$$\frac{3}{2}b + a = \frac{1}{4} \quad (6.31)$$

The values of the indices a and b are likely constrained to be ≥ 0 because otherwise we could have an increase of the Lorentz factor or of the temperature with the radius which is hardly reproducible. Thus $a = 0$ and $b = 0$ correspond to the limiting cases for the scaling relations assumed for the temperature and the Lorentz factor, respectively, which lead to $T_{\text{SN}} = T_{\text{obs}} \propto t^{-1/4}$ in the case $\Gamma = \text{const}$ (i.e. $b = 0$) and $\Gamma \propto t^{-1/6}$ if $T_{\text{SN}} = \text{const}$ (i.e. $a = 0$). These two scaling relations are reported in fig.6.11.

In the context of the Compton drag model, a decrease in the observed temperature can be due to the deceleration of the fireball and/or a decreasing temperature of the seed photons with distance. If we consider the luminosity due to the Compton drag process (Eq. (8)), we have $L_{\text{CD}} \propto E_{\text{CD}}/t \propto t^2 T_{\text{obs}}^4$, which predicts $L_{\text{CD}} \propto t$ if the time behavior of the observed temperature is indeed $T_{\text{obs}} \propto t^{-1/4}$. A weaker dependence of the observed flux on time can occur if the fireball is becoming transparent (i.e. only a fraction τ_{T} of the seed photons can be scattered) with τ_{T} decreasing with distance and/or if the fireball distance becomes larger than the typical dimension occupied by the seed photons.

6.8 Conclusions

In this work we have presented the spectral evolution of GRB 911118 and of a new case of hard burst, GRB 980306, together with some other hard bursts already reported in the literature. Their low energy spectral component is harder than $N(E) \propto E^0$ for a considerable period of their main peak emission and even after this initial phase their spectrum remains harder than the synchrotron limit $E^{-2/3}$. We have applied different tests to verify the significance of the low energy hardness, concluding that these results are indeed robust.

These GRB prompt spectra represent a challenge for the emission scenarios as shown through a comparison with the limiting spectral shapes predicted by such models. We pointed out the difficulties that synchrotron emission, even including the effects of self-absorption, small pitch angles particle distributions and jittering, has in explaining spectra harder than $N(E) \propto E^0$. Comptonization models also have difficulties, even if they are consistent with very hard spectra in a limited range of energies.

The main new result of this study is the possible thermal character of the first emission phase of all the bursts we considered and the evolution of such a thermal phase. The conventional scenario, of a fireball accelerated by its own internal pressure, indeed *predicts* such an initial thermal character when the fireball becomes transparent and it was its absence in previously considered bursts that led Daigne & Mochovitch ([25]) to favor a rather cold fireball scenario, where at least part of the acceleration was due to magnetic forces. In our bursts, on the contrary, the luminosity in the thermal phase is a significant fraction of the total, therefore consistent with the hot fireball scenario. Note also that, although the fireball could start rather cold and be heated through internal shocks occurring well before it becomes transparent, this would require rather small values of the bulk Lorentz factors, smaller than what we have derived in the previous

section. Alternatively, a cold fireball could work if the thermal spectrum we see is produced by Compton drag, in which circumburst radiation is boosted to high energies by the fireball bulk motion.

Indeed it seems that both these models are indeed viable, especially if other emission processes, possibly linked to internal shocks start dominating at later phases. A possible way of discriminating between these two possibilities is by the duration of the black body phase. In fact, in the Compton drag model, the initial shells will scatter most of the available seed photons and the timescale required to refill the circumburst medium is longer than the burst duration. Therefore, observing black body emission for a long time or during the rising phase of two time resolved peaks would be difficult to explain in terms of the Compton drag process.

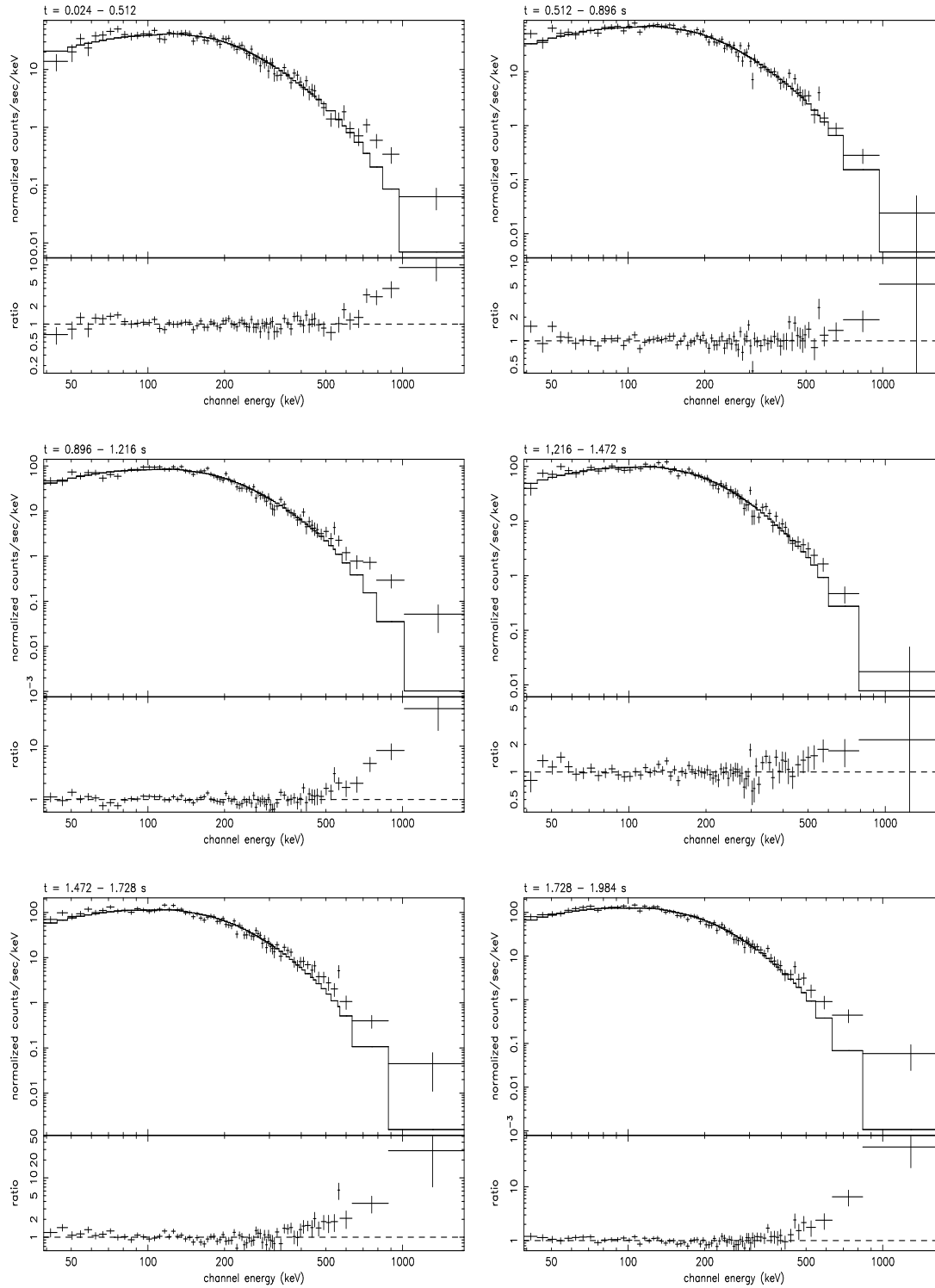
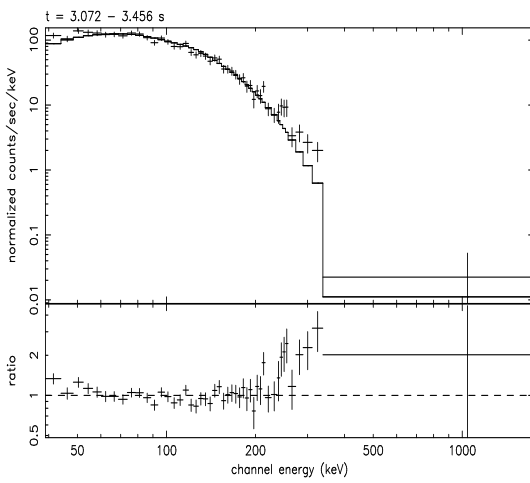
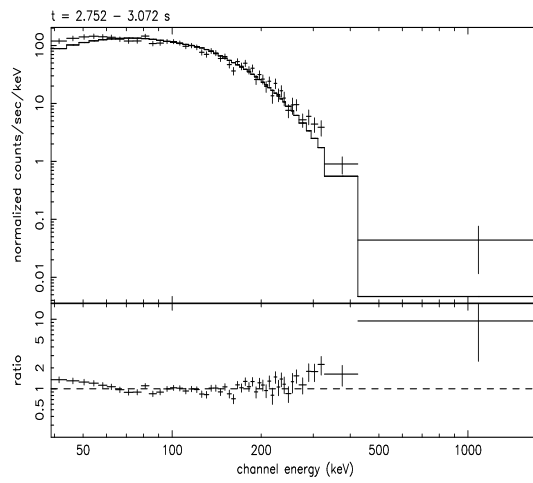
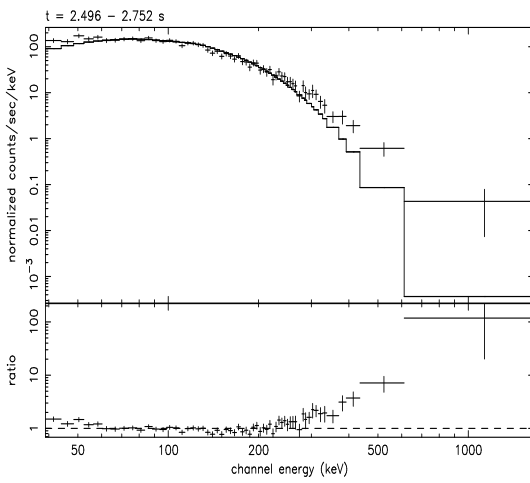
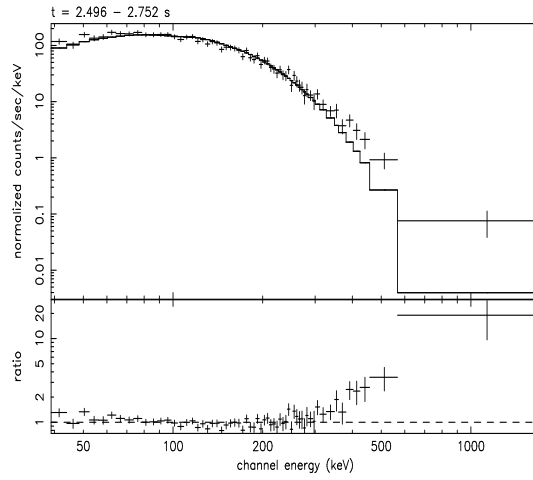
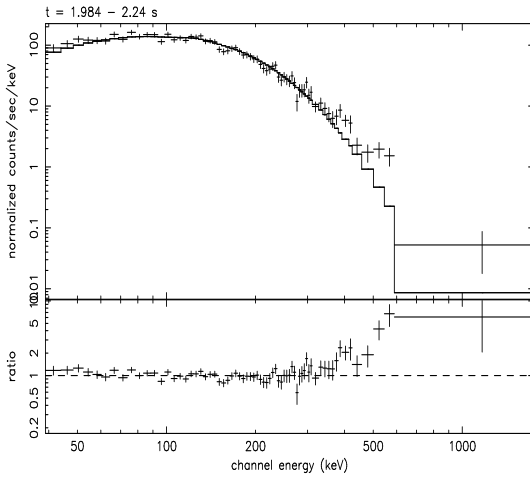


Figure 6.12: Black body fits for GRB 980306 (see Tab.6.2).



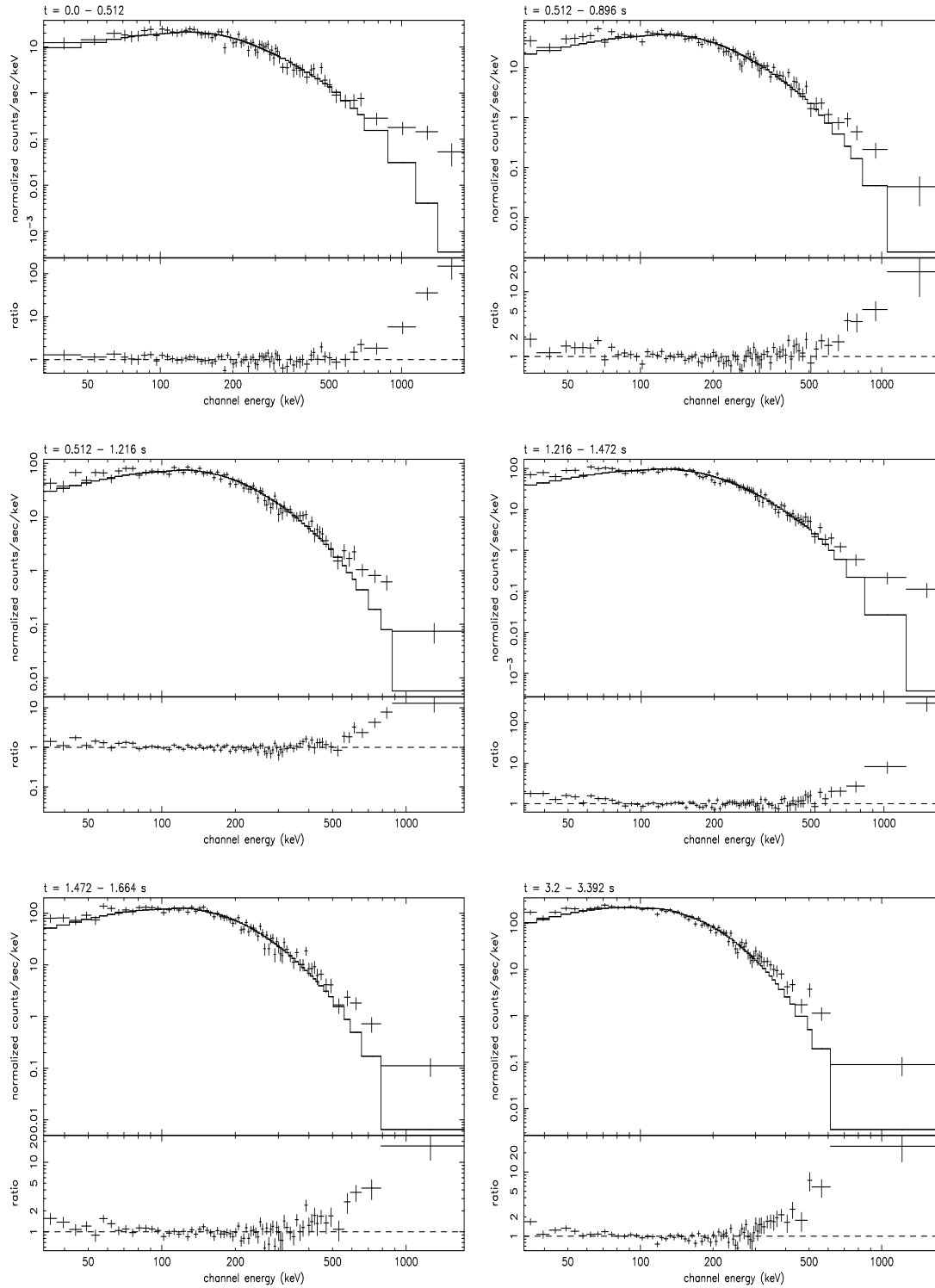
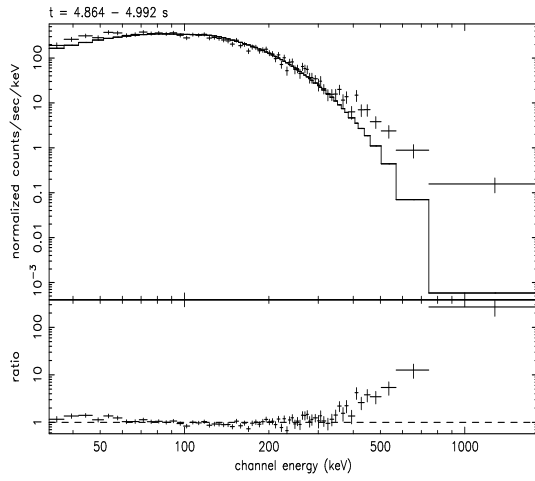
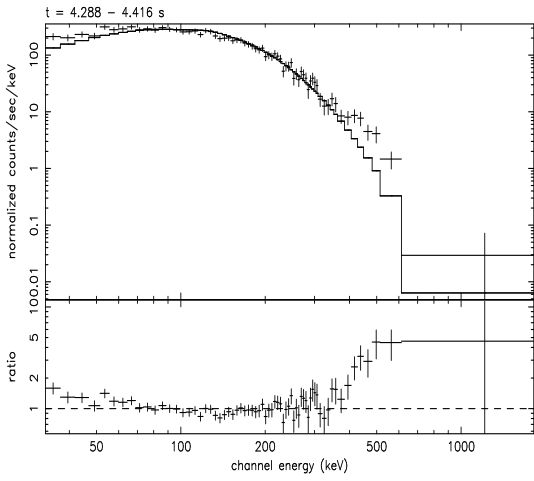
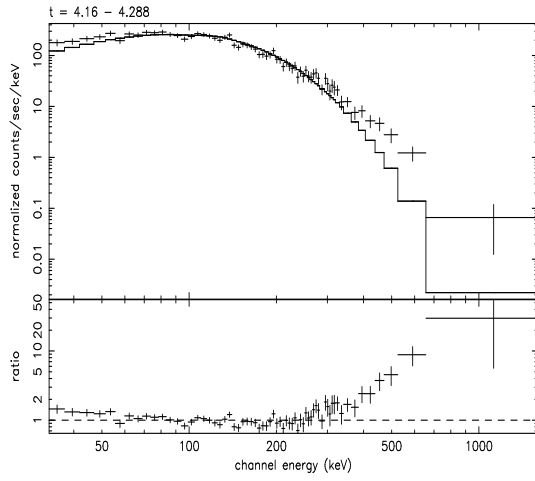
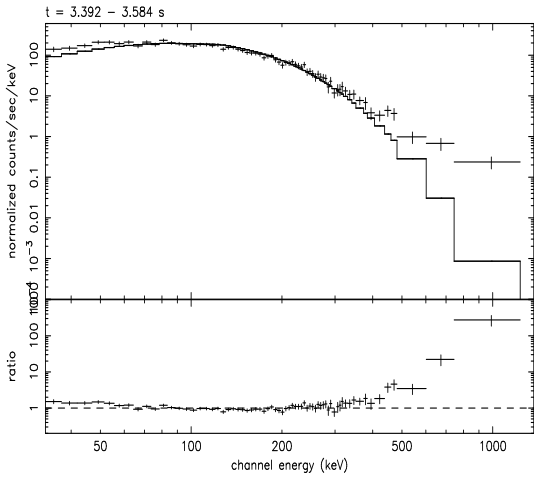


Figure 6.13: Black body fits for GRB 911118 (see Tab.6.2).



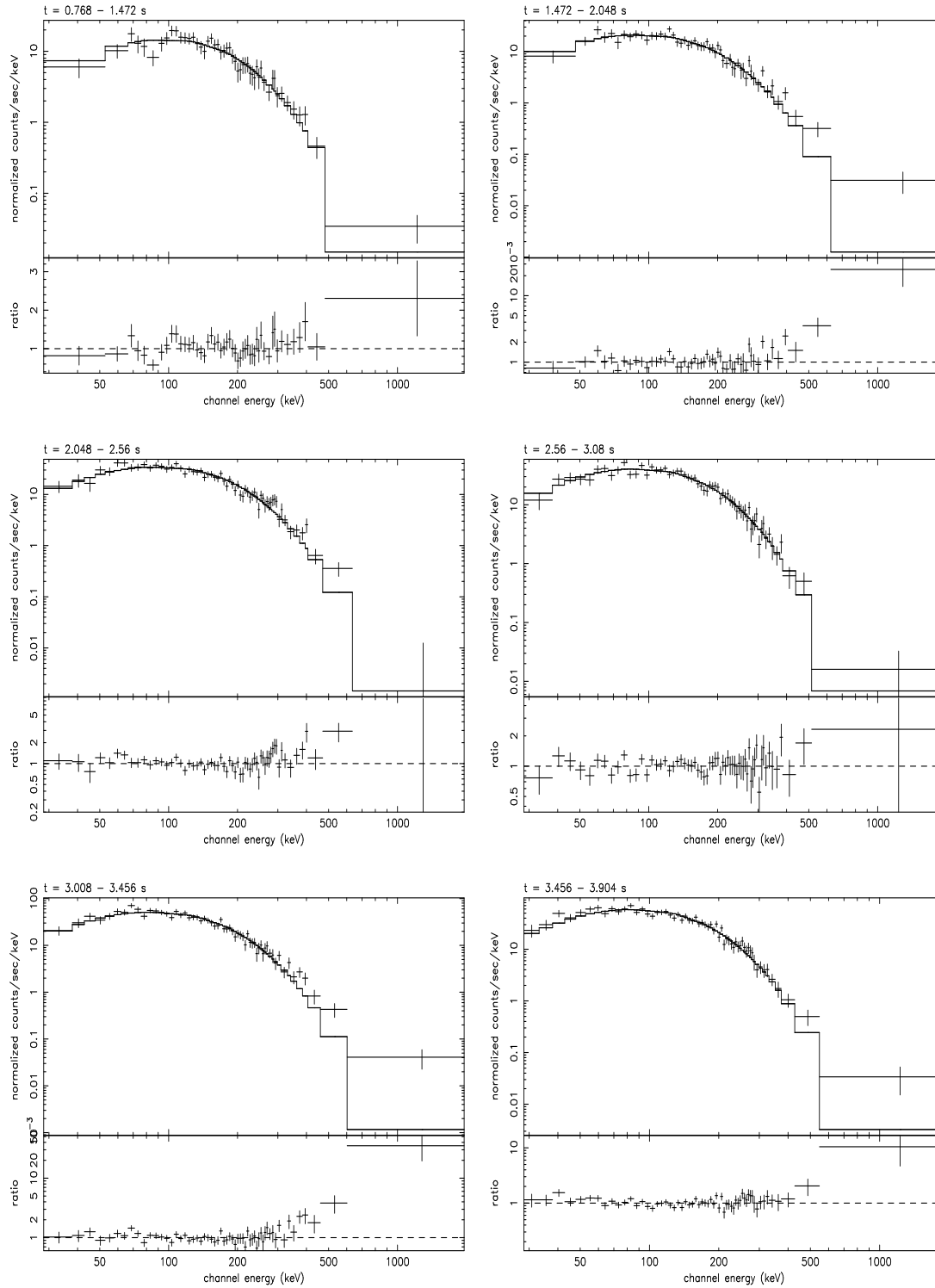
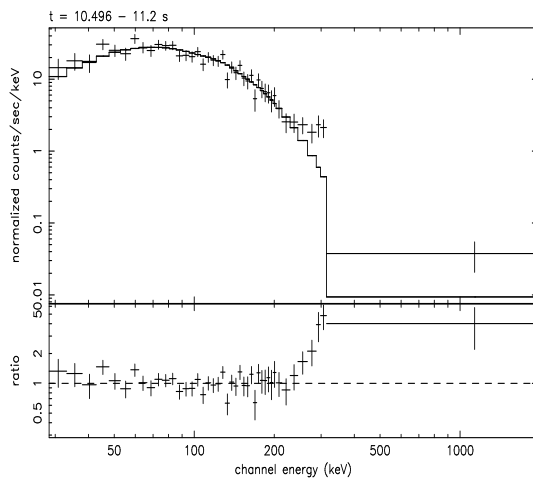
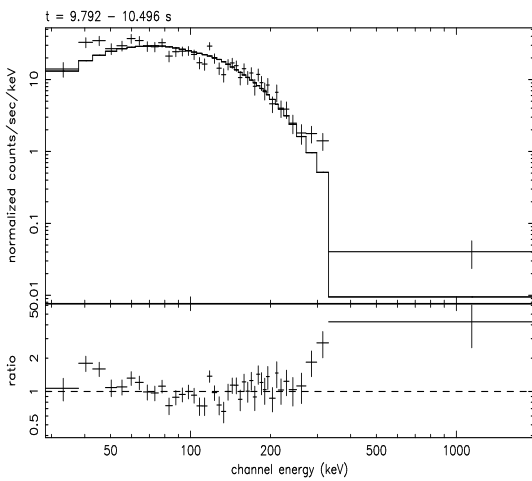
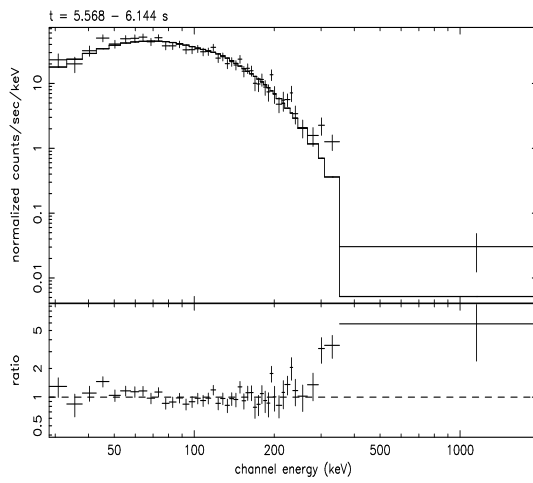
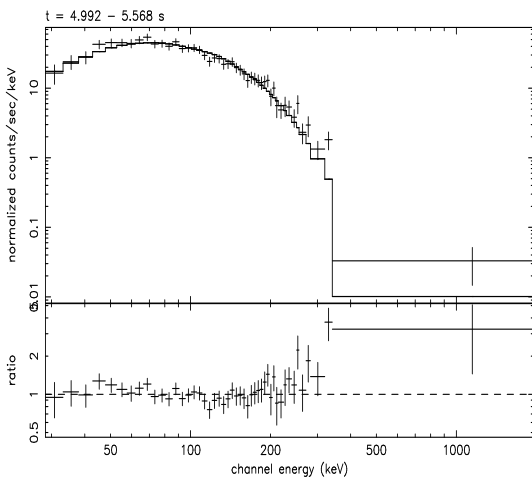
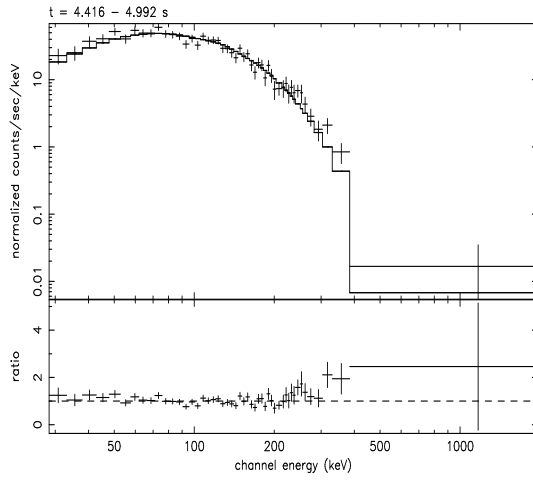
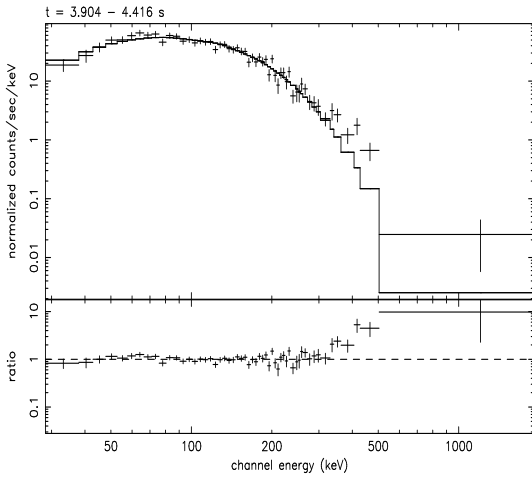
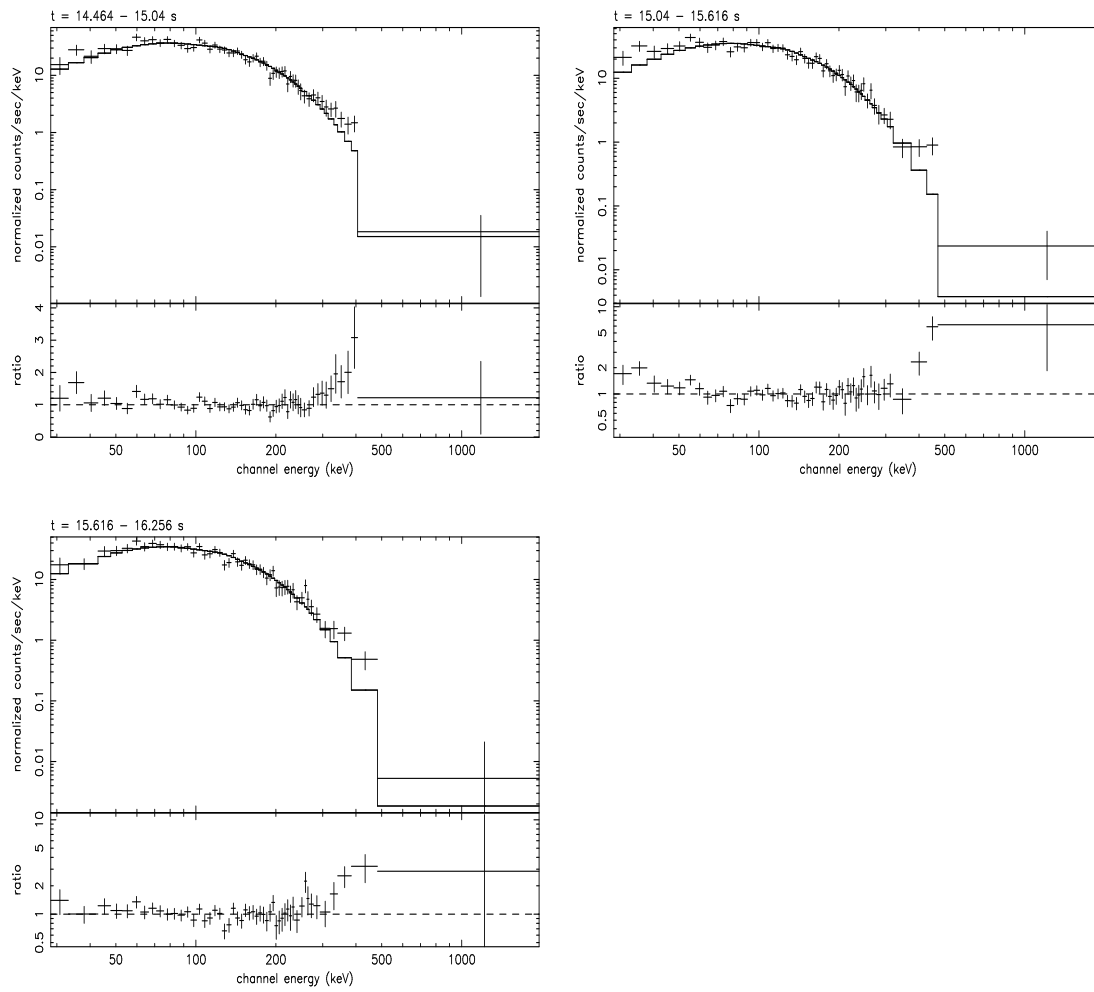


Figure 6.14: Black body fits for GRB 910807 (see Tab.6.2).





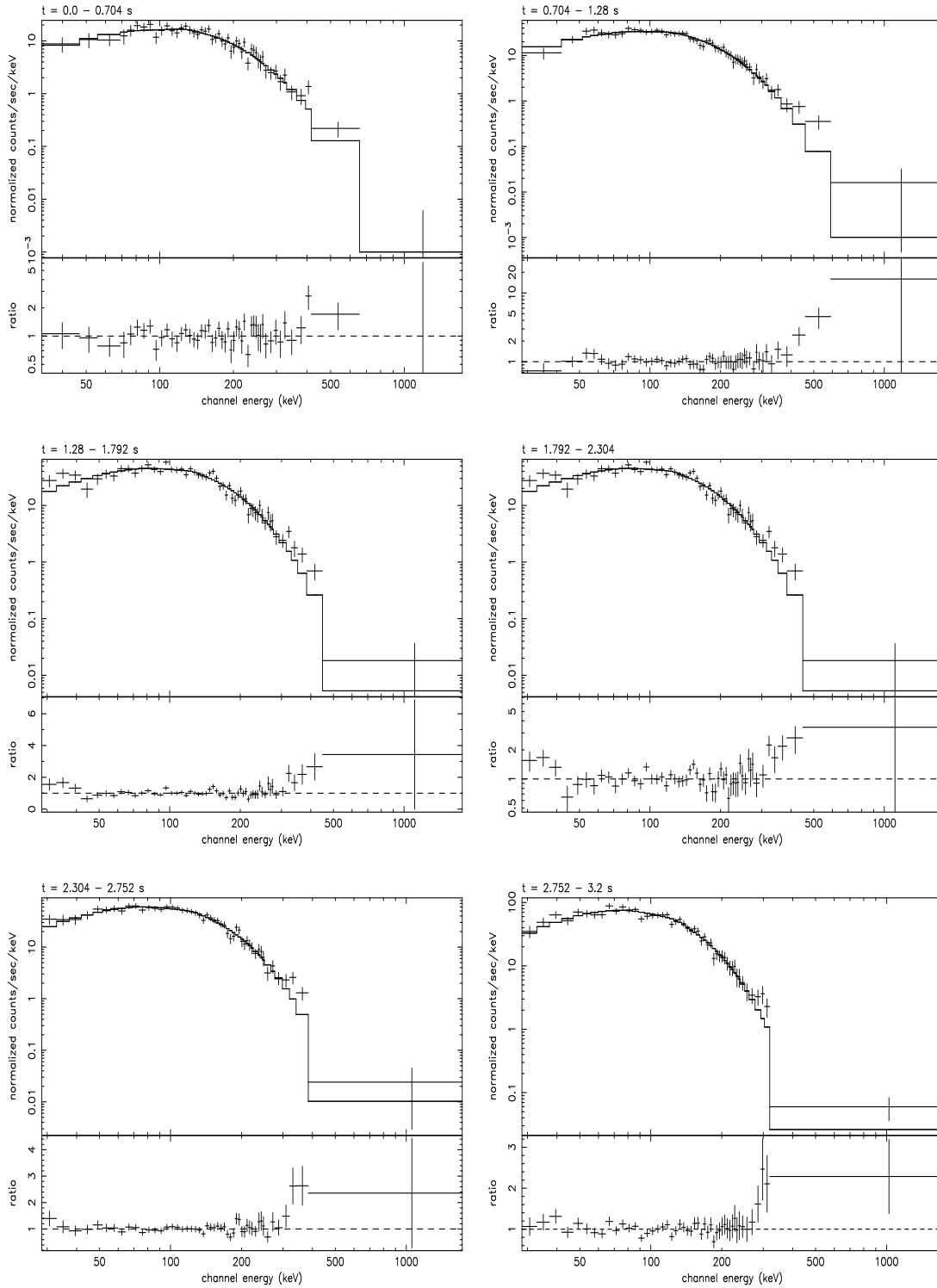
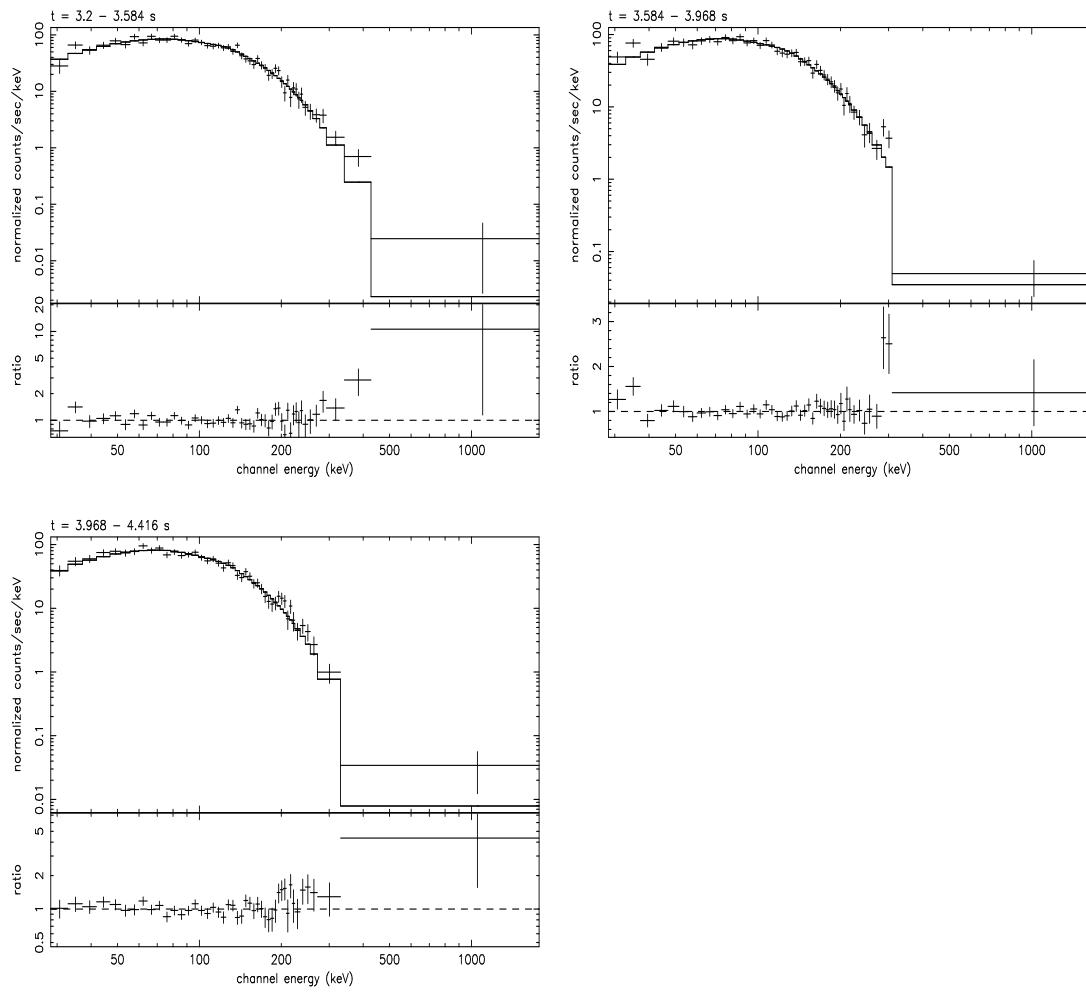


Figure 6.15: Black body fits for GRB 910927 (see Tab.6.2).



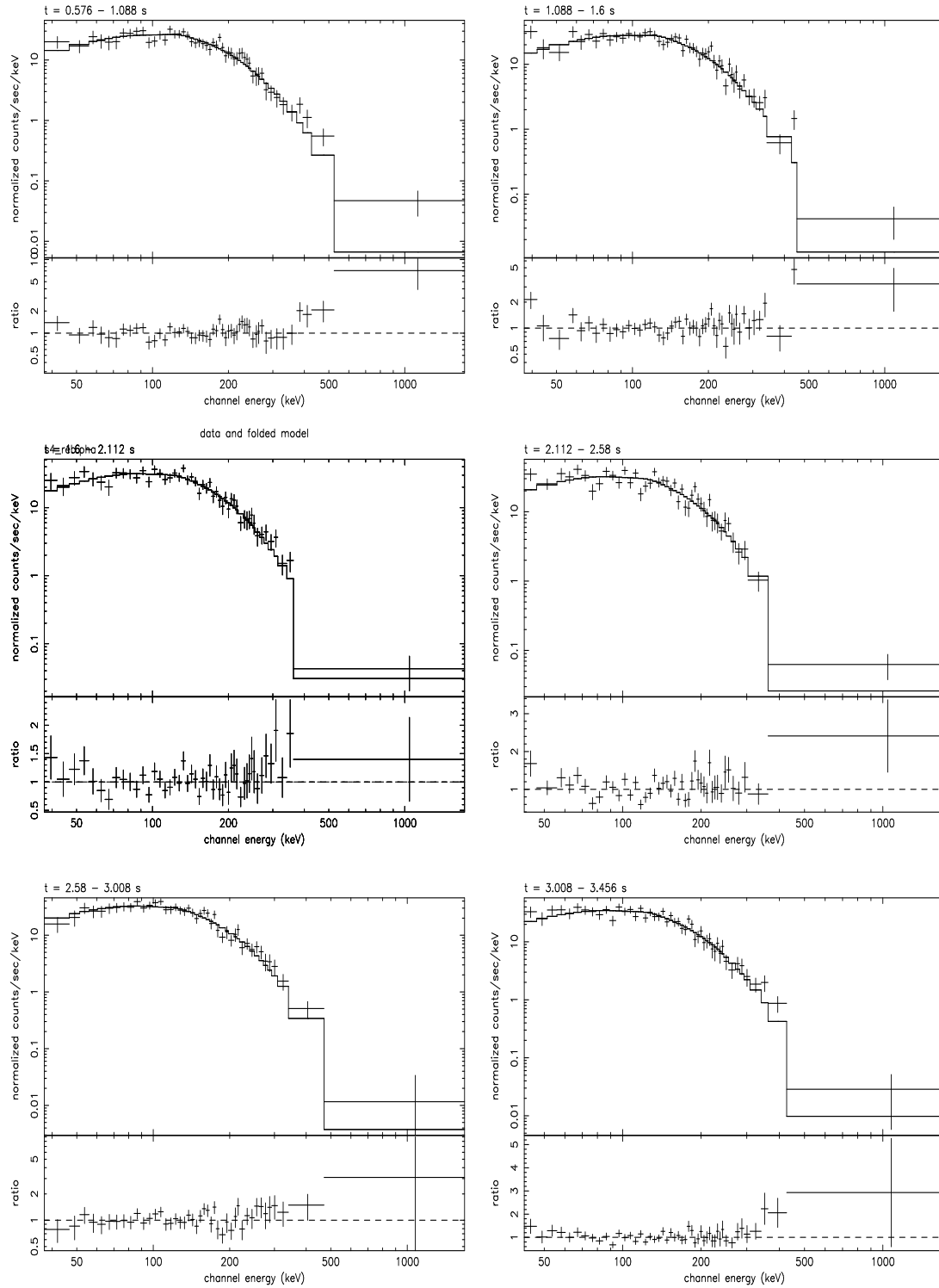
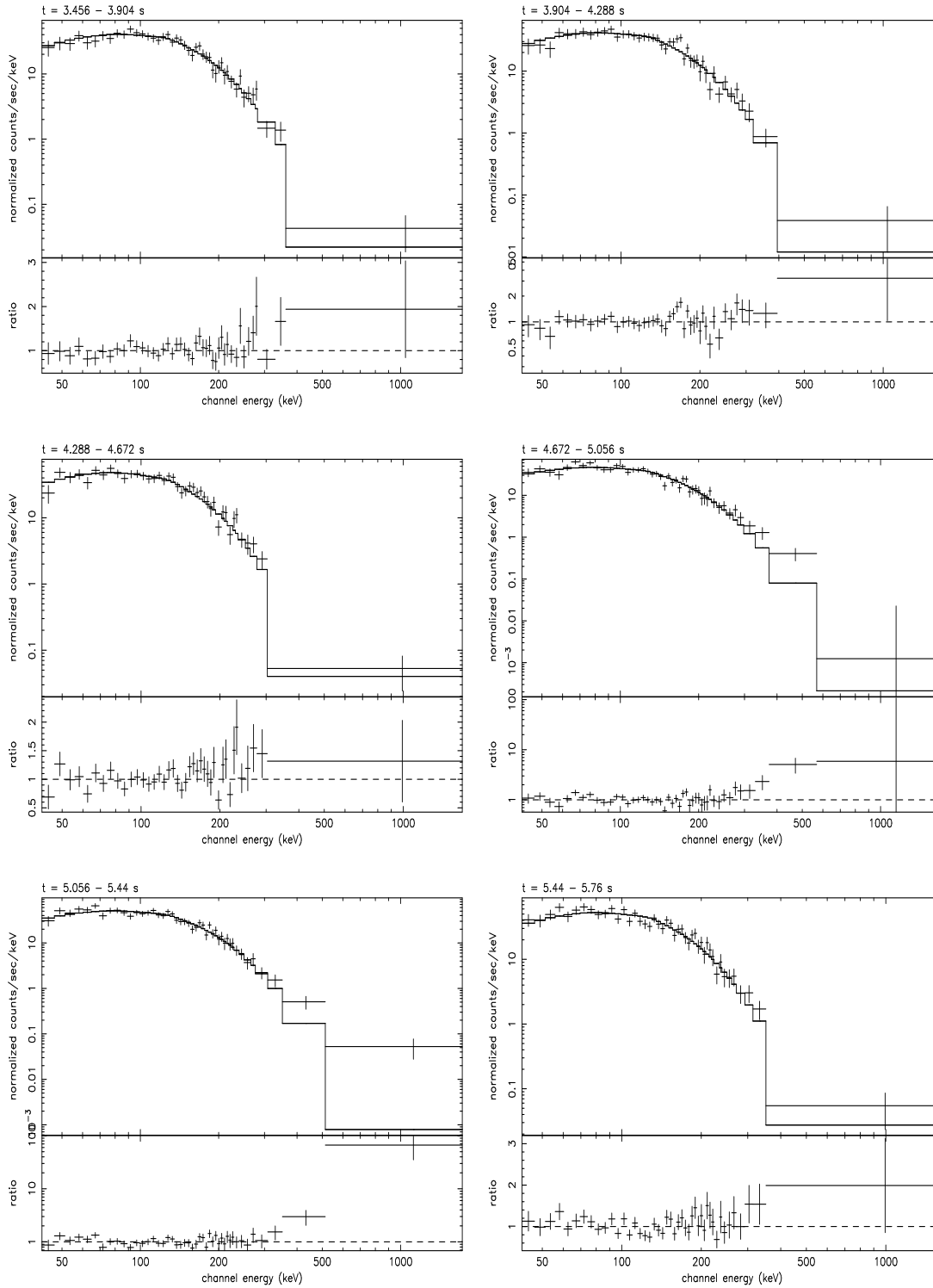


Figure 6.16: Black body fits for GRB 970111 (see Tab.6.2).



Chapter 7

Spectral evolution morphologies

7.1 Introduction

As outlined in chapt.2, the classical approach to the spectral evolution analysis of GRBs has been based on the use of a *single parameter* (typically the peak energy) to represent the hardness of the time resolved spectra. A classification on the basis of this parameter led to the definition of two distinctive and recurrent morphological classes, “tracking” and “hard-to-soft” (Ford et al. [42]), while a quantitative description of the spectral evolution has focused on the decay phase of selected pulses (Ryde & Svensson [137]) in search for a relation between the hardness parameter and the burst intensity.

The existence of such trends in GRBs spectral evolution represents an important clue for the study of the burst emission process and progenitor nature: in the standard internal shock scenario, for instance, the observed trends could be the superposition of the single shells spectral evolution or of the environment variations induced by the emission, or, more directly, the result of the evolution of the inner engine. Nonetheless, no clear and unique relation between the observed trends and any other spectral or temporal burst property seems to emerge from the spectral evolution analysis.

Chapt.5 showed that the characterization of the time resolved spectra is not unique because different spectral model can result in acceptable fits and the time resolved spectra show a large variety of spectral shapes also within the same burst evolving in time in different ways. In chapt. 6 we showed that the spectrum can have a thermal character at the beginning of the burst which then evolves assuming a prevalent “non-thermal” shape.

For these reasons in this chapter, beside the standard approach to the analysis of the spectral evolution (sec.7.1), essentially based on the time evolution of the peak energy, we explore the possibility of studying the complete spectrum, as it is described by its low and high energy components (sec.7.2), evolving in time.

This method, though complicated by the number of spectral parameters involved, reveals the possible existence of other trends (sec.7.3) which can be present only in the

low or high energy part of the time resolved spectrum and which are not immediately evident from the standard analysis. Moreover, as a first step in the analysis of these new trends, we describe the correlation analysis of the spectral parameters and quantify these spectral trends (sec.7.4). Some of the morphologies found by this analysis are briefly described separately in sec.7.4.1, 7.4.2 and 7.4.3.; while a sketch of some ideas for a future development in the investigation of these findings is drawn in sec.7.4.4.

We propose, as a future extension and development of this analysis the comparison of these trends and peculiar evolutions with the proposed emission models.

7.2 The standard spectral evolution analysis

In the standard spectral analysis the hardness of the burst was defined (following e.g. Band et al. [4], Ford et al. [42], Liang & Kargatis [94]) through the peak energy of the νF_ν spectrum, which represents the energy where most of the power is emitted (see also chapt.2 for alternative hardness indicators). This parameter can be calculated directly from the best fit parameters of the model spectrum. In the case of the BAND model (defined in sec.5.2.4), it results in

$$E_{peak} = (\alpha + 2)E_0$$

where α is the low energy power law spectral index and E_0 is the break energy, as defined in sec. 5.2.4. In the case of the BPLW model (sec.5.2.4) the peak of the νF_ν spectrum corresponds, instead, to the beak energy $E_{peak} = E_0$. The definition of E_{peak} is subject to the value of the high energy power law spectral index: in fact, if $\beta > -2$, the spectrum increases with energy in a νF_ν representation, being $\propto E^{\beta+2}$, and does not peak within the spectral energy range [28,1800] keV of the instrument.

We have applied this spectral evolution analysis, based on the study of the temporal evolution of the peak energy, to the sample of bright bursts presented in chapt.5. We considered the bursts reported in tab.5.2 which were selected from the BATSE catalog as those with the highest photon peak flux, and, as described in sec.5.2.3, we analyzed their time resolved spectra. The spectral results that we obtained fitting the spectral models described in sec.5.2.4 and discussed from the statistical point of view in sec.5.3, are here considered in terms of their relation with time as indicators of the spectral evolution of single bursts.

The temporal resolution of our spectra, accordingly to the limitations described in sec.5.2.3, was in a few cases 128 ms and typically 256 ms for the spectra corresponding to the time bins around the peaks, where the S/N is higher.

In the standard analysis the peak energy is defined from the model used in fitting the time resolved spectra. In most cases we adopted the BPLW model which, due to its sharp break can accommodate most of the time resolved spectra although also other models (see chapt.5) can adequately accommodate the spectral shape. In fact, different models

can result in different absolute values of their best fit parameters, and still be acceptable in terms of χ^2 and residuals, but the particular choice of the model to represent the spectral evolution does not influence much the analysis because it is its relative, rather than absolute, values which determine the scope of describing its spectral evolution.

Also in the BPLW model the value of the high energy spectral index β is determinant for the definition of the peak energy: if $\beta > -2$ (i.e. the spectrum does not peak within the BATSE energy range) we decided to set the value of E_{peak} to the upper limit of the energy band over which the spectrum is observed. This value, i.e., $E_{peak} = 1800$ keV, represents a lower limit for the peak energy.

The application of the standard spectral analysis based on the peak energy to the bursts of chapt.5 with the above conventions and definitions, revealed that also in our sample of bright bursts there are the typical evolutionary morphologies found in other burst samples and described by Ford et al. ([42]) or Golenetskii et al. ([60]). In the following we report the main results of the classification of these morphologies:

- E_{peak} follows the flux reproducing its rise and decay pattern (*tracking*). This morphology seems to be dominant within the bursts analyzed. It is evident, as an example, in GRB 940217 (fig.7.1, left panel) which presents a multi-peaked structure in the light curve which is, indeed, reproduced by its peak energy. Another example is GRB 990104 (fig.7.1, right panel). Additionally, there are some bursts showing a temporal lag between the peak of the light curve and that of the peak-energy light curve, as already reported by Ford et al. ([42]).
- the peak energy can evolve decaying with respect to the flux rise and decay in the light curve (*hard to soft*). In our sample we have found representative cases of this kind of evolution like GRB 921207 reported in fig.5.11 (chapt.5), or GRB 910503 reported in fig.7.2 (left panel) on its first peak. The number of bursts characterized by this evolutionary morphology are, anyway, a minority (6/17) (see tab.7.1) in the sample of bright bursts analyzed, and in most cases the value of the peak energy starts from the upper threshold (1800 keV) due to an extremely hard high energy spectrum (i.e. $\beta > -2$). We briefly note, as it will be more detailed in sec.7.4.3, that in these cases the evolution of the spectrum above the upper limit of the BATSE band is not determined: it could equally be tracking or hard to soft.
- the burst evolution, either tracking or hard to soft, seems to be dominated by a general softening of the peak energy which becomes more evident considering the hardness of the late pulses compared to that of the early ones. This is the envelope. This is not a distinctive morphology as it seems to be independent from the spectral evolution of the pulses: some examples of the presence of this envelope have been found in the bursts, already cited above, such as GRB 910503 (fig.7.2, left panel) or GRB 920311 (fig.7.2, right panel). This envelope is found to be of the hard to soft type in all the cases: the late pulses are, as described by the peak energy, softer than at the beginning.

These results are in agreement with those found from the previous spectral evolution analysis of larger samples of bursts, and, in this context, we would like to stress that:

- i in a small sample of bursts, selected for their peak flux and characterized mostly by a complex, i.e. multi-peaked light curve, we have found the same spectral trends of Ford et al. ([42]) or Kargatis et al. ([76]).
- ii these trends and morphologies could be very likely a consequence (i.e. the observable) of the spectral evolution of the shells (assuming for instance the standard scenario) or the result of the time evolution of the inner engine and/or of its environment. Thus the interpretation of such evolutions could give important hints for the characterization of the emission process, of the inner engine and or, in general, on the physics of the prompt event.

Nonetheless, as already pointed out by previous works, we can not find any clear association between these evolutionary morphologies, on one hand, and the general temporal (e.g duration, number of peaks, variability) and spectral properties (e.g. average spectrum) of the bursts.

Starting from this consideration we tried to relax a basic assumption of the spectral analysis methodology i.e., the characterization of the burst hardness with only the peak energy and considered a more general approach in which the *total spectrum*, composed by its low and high energy components, is analyzed to evolve with time.

7.3 A different approach

If the spectral evolution is described through the complete spectrum (*multi-parameter* approach), the complete set of spectral parameters obtained from the fits and their time dependence should be considered: i.e. $\alpha(t)$, $\beta(t)$, $E_{peak}(t)$.

We are aware that this approach, which considers more than one spectral parameter and its temporal evolution, can be model dependent. Nonetheless, we think that, as a first level analysis aimed at testing a possible different approach to the spectral evolution study and interpretation, the choice of a simple spectral model, such as the BPLW, can be an acceptable solution.

On one hand, this method, with respect to the assumption of the peak energy as hardness indicator, has the difficulty of handling, simultaneously, more than one spectral parameter. Nonetheless, the main advantage is the characterization of the time dependence of the complete spectral form, which, as also shown by the findings of chapt.6, can be also extremely hard at the beginning of the burst and then becomes softer.

The consideration of the temporal evolution of each spectral parameter independently revealed some new trend and possibly a new leading spectral class which was not evident in the single parameter standard analysis.

7.3.1 Evolutionary Morphologies

Multi-parameter spectral evolution analysis revealed that the bursts (reported in tab.7.1) are characterized by the classical hard to soft and tracking morphologies but there are some new cases and possibly a different classification emerges:

- i the *tracking morphology* is present in about half of the bursts. But, differing from the standard classification, there are cases in which only the low energy spectral index α or the peak energy E_{peak} tracks the flux, like for GRB 930506 or GRB 950403 and 930922, respectively. In most cases of tracking morphology we have found that both α and E_{peak} track the flux, as shown in fig.7.1 by GRB 940217 and 990104: the low energy spectral index (panels (d)) has the same peaks of the peak energy (panel (c)) and both reproduce the evolution of the photon flux (panel (b));
- ii the *hard to soft evolution*, of the complete burst, i.e. of all its peaks, has not been found in any burst. This could be a consequence of having considered the three parameters separated: in fact, the peak energy is computed from α and E_0 , and their combination could generate a softening of E_{peak} even though one parameter does not effectively evolve from hard to soft. The only marginal case of possible hard to soft evolution on both α and E_{peak} is GRB 950325;
- iii a considerable number of bursts have a *mixed evolution* combining the hard to soft and the tracking pattern in different pulses. An example is reported in fig.7.2 which shows a hard to soft spectral evolution on the first peak which then changes into tracking.

This morphology is represented mainly by α and E_{peak} , although we have found some cases (GRB 970420 and 970930) in which a mixed evolution is evident also from the parameter β . Typically the evolution is hard to soft on the first peak and then tracking on the others. Only in two cases the opposite evolution has been found. These are GRB 960807 and GRB 970930 which have a tracking evolution on the first peak which then becomes hard to soft. It should be noticed anyway that in these two particular cases the hard to soft evolution is not well constrained by the parameter's uncertainties;

- iv the *envelope* is also present in bursts belonging to the above different classes. It results by the comparison of the spectral hardness of the early pulses (harder) with respect to the late ones (softer). In some cases it is present in the peak energy and in the low energy spectral index, for example in GRB 940217 (fig.7.1): in this case a further complication is evident because it limits in hard to soft the evolution of α (solid lines in fig.7.1, panel (d)) and soft to hard as far as the peak energy is concerned (panel (c));
- v there is a case of linear decay of the both α and β (GRB 960807, fig.7.2) in the second peak. On the other hand we have found that in some bursts, the high

energy power law spectral index β can be consistent with being constant (like in the first peak of GRB 920525, left panel of fig.7.2)

- vi In GRB 930506, in the initial phase the hardness of the high energy spectrum (i.e. $\beta > -2$) makes the classical approach useless. This burst, in fact, has a tracking spectral evolution only if described by its low and high energy spectral components.
- vii Finally we have found two intriguing morphologies which are described in more details in sec.7.4.2. These two bursts show a strong anticorrelation of the low and high energy spectrum while the peak energy correlates with the flux. We are trying to see if this morphology might be a standard class and in this case if it can be associated with some other characteristic of the burst light curve.

The result of this analysis, which embraces all the spectral parameters describing the spectrum and their temporal evolution, has pointed some peculiarities: the spectral evolution is complex and, within the same burst can change from the initial phase to the late phase, it can be “limited” by a sort of envelope for the complete duration of the burst, there can be peculiar evolutions possibly strongly related to the pulse shape and temporal properties.

An important consideration can be derived from these results which could be further investigated: the hard to soft or tracking evolutions seem to be two basic distinctive evolutionary morphologies of the bursts (as also found in the application of the standard analysis with the peak energy). Additionally, we do not find in those bursts showing a mixed spectral evolution, any case of a transition from one morphology to the other within a single pulse: the possible change, which occurs in those bursts with a mixed evolution, happens between different pulses. This, if proved through extensive data analysis, could be related, for instance, with the pulse shape or with any other spectral or temporal property of the pulse, and consequently unveil some properties of the emission mechanism.

This wide range of spectral evolutions requires a deeper analysis to characterize these trends and possibly to derive any information for their interpretation.

7.4 Correlations and trends

The spectral evolution and the possible peculiar morphologies, which have been revealed considering the evolution of the complete spectrum of the bursts presented in the previous sections, require a more detailed, and possibly quantitative, definitions of such trends. We therefore decided to explore the correlations between the spectral parameters and the possible trends that they can reveal.

The search for correlations among the spectral parameters was performed computing the Spearman’s rank-order correlation coefficient (and relative probability) between α ,

β , E_{peak} and the photon flux (obtained integrating the model spectrum over the observational energy band). This coefficient in fact describes the degree and sign of the correlation among the spectral parameters: $r_s = -1$ indicates anticorrelation, whereas a value $+1$ is for positively correlated parameters.

The significance of this parameter, in revealing possible correlations is represented by the probability that any random sample of two uncorrelated variables gives a rank correlation coefficient greater than the one calculated from the data: a low probability indicates a statistically significant correlation.

The tracking evolution, as defined in standard spectral analysis, would be characterized by the correlation of the peak energy with the flux. In the case all the spectral parameters are considered, the same definition applies but the low energy spectral index can be highly correlated with the flux in tracking pulses. The definition of the hard to soft evolution in terms of correlations, instead, is more difficult: in fact, the standard approach defines this evolution on the entire burst, and if considered for the low energy spectral index this should decrease while the flux rises and decays in the single pulses composing the burst. We expect that the rank correlation would be near 0 (poor) because all the burst is considered.

In particular, for the hard to soft spectral evolution we expect that the consideration of the complete spectrum, instead, and the separation of the pulses should reveal this morphology also through the correlation analysis of the spectral parameters. In fact we suggest, though it has not been tested on these results, that if the correlation between each spectral parameter and the flux is computed during the rise and decay phase of the pulse separately, an anticorrelation should be expected in the former and a correlation in the latter.

The search for correlation was performed on single pulses, within each burst, identified from the photon light curve (e.g., panels (b) in fig.7.2). They were selected by eye considering approximately where the pulse, in the photon light curve starts and falls to a background level which is defined considering the time interval before and after the burst. If the pulses are clustered and close one another, then they were separated in correspondence of the minimum photon flux time bin between the pulses. These pulses can be composed by sub-structures, as shown with better time resolution by the 64 ms light curve of panels (a) (e.g., fig.7.1), but as we are exploring the correlations of the best fit parameters with a measure of the burst intensity, as represented by the integration of the best fit model over the spectral analysis energy band, we used the photon light curve to select the pulses over which the correlations are computed.

The correlations were computed among the parameters of the best fit spectra composing a pulse and the flux obtained from the integration of the best fit model, on a time interval corresponding to the single pulses selected according to the previous criterion. In multi-peaked bursts (which are the majority in the sample of bright bursts that we have analyzed) each pulse is described by three correlation coefficients obtained computing the Spearman rank order correlation between the low energy spectral in-

dex α , the high energy spectral index β , and the peak energy E_{peak} with the photon flux $F(N) = \int_{28}^{1800} B(E, \delta t) dE$, where $B(E, \delta t)$ is the best fit photon spectrum corresponding to the time interval δt .

The search for correlations on the spectral parameters of the sample of bursts presented in chapt.5 and described for their spectral evolutions with their complete spectrum, has revealed some interesting properties which we introduce in the following sections.

The rank correlation coefficients are reported in tab.7.1: a high positive correlation is found in those bursts with a clear tracking trend on α and E_{peak} . For example trigger 143, which according to the standard approach would be classified as tracking, instead shows that its first peak is characterized by a low r_s on α , β and E_{peak} which, compared with the plot of the spectral evolution reported in fig.7.2 (left panel), reveals that the first peak evolves, indeed, hard to soft. The second and third peak instead are characterized by a higher correlation between α and the flux ($R_s=0.95$) and they are tracking. This burst, in fact, has a mixed evolution.

Trigger 2083, instead, shows an high degree of correlation both in the first and in the second peak on α and, with a lower rank, on E_{peak} . Nonetheless, this burst would have been classified as hard to soft if only considering its E_{peak} , due to the uncertainty on its value.

Again another example is represented by trigger 2329: it cannot be classified, according to the standard method, because most of its spectra have $\beta > -2$, and, consequently, its peak energy is undetermined within the BATSE range. The search for correlations instead reveals that the low energy spectral evolution is tracking (and also with an high rank of correlation).

From the analysis of the rank correlations coefficients reported in tab.7.1 it is evident that the relevant parameters which can be used in the spectral analysis are the low energy spectral index and the peak energy. In most cases, in fact, the high energy spectral index β is poorly correlated with the fluxes.

Presently we have explored the correlations on the single pulses within the bursts computing the correlations over the time interval corresponding to the pulse duration. Considering that, applying a multi-parameter approach, we have found different morphologies in the spectral analysis of a sample of bright bursts, we intend to select other possible time interval within the pulses to determine the correlations between the spectrum and the flux associated with particular phases of the burst. In particular a first step could be considering the rise and decay phase of the pulse in those cases showing a hard to soft spectral evolution: in the rise phase the hardness of the spectrum should be anticorrelated with the flux, whereas in the decay phase they should correlate. It would be interesting to study this correlation, and the time where it changes sign and its position with respect to the peak flux. In fact, as many bursts with a tracking morphology show a possible time lag between the peak energy maximum and the flux maximum, it could be that a similar trend is present in the hard to soft morphology but can be

revealed only considering the correlation coefficient in the rise/decay phase.

7.4.1 The envelope

As briefly outlined in sec.7.3 in many bursts ($\sim 50\%$) we have found the presence of an envelope which constrains the temporal evolution of the spectral parameters and typically determines a global softening of the burst in the late pulses. This morphology, which had been found also by Ford et al. ([42]), could be the signature of a decrease of the efficiency of the central engine or of a change in the environment where radiation is released, and then should be better quantified.

As a first level analysis we tried to characterize this evolution through the comparison of the spectral peaks within the same burst: the envelope in fact determines the late peaks to be softer than the early ones. For this reason we described each pulse with the spectrum corresponding to its peak and with two spectra corresponding to the minima which separate it from the subsequent pulses or from the background. This is, for the moment a non-quantitative pulse selection method, which can be further refined considering a parameter which for instance describes the relative flux at the bottom and at the top of the pulse and then select the boundaries and the peak of the flux. The spectra (typically three in each pulse) selected in this way, for the pulses within the same GRB were fitted (for the peaks and for the minima separately) with a linear function. The results, i.e. the coefficients and the relative significance (in terms of probability) of the fit, are reported in tab.7.1 for α and E_{peak} corresponding to the minima and to the peaks of the pulses within each burst.

Although the sample of burst is not complete, we computed the distributions of the spectral parameters for the peak and minima spectra isolating the pulses for those burst showing an envelope. In fig.7.4 are reported the distribution of the low energy spectral index α for the spectra corresponding to the peaks (*solid line*) of the light curve for the bursts showing the envelope, and for the spectra separating the same peaks (*dotted line*). The same distributions for the high energy spectral index β and for the peak energy E_{peak} are reported in fig.7.4 and fig.7.5, respectively. These distributions could indicate the existence of preferable values of the spectral parameters, corresponding to the peak and the minima, which limit the spectral evolution of the pulses within a burst but a larger sample of bursts is needed to explore this possibility.

A more reliable evidence is instead the presence of the envelope as an independent spectral evolution in bursts showing the hard to soft and/or the tracking morphology. This indicates that the global hard to soft evolution of the pulses within the burst, which is evident from the envelope, is independent of the single pulse spectral evolution and could be associated with the temporal evolution of the energy input of the inner engine and/or with the change of the radiative parameters, e.g. a global progressive thinning - in the framework of the Compton attenuation model - or a less efficient acceleration of the particles at the shock front - in the framework of the standard internal synchrotron shock model. Moreover it could be possible that the envelope present in hard to soft

multipeaked bursts or in tracking GRBs presents some differences and possibly has a different nature.

These possibilities are worth to be further considered with the selection of other burst sample, possibly with multipeaked structures, to be analyzed with the procedure described in this chapter.

7.4.2 Peculiar evolutions

Among the spectral evolution morphologies presented before, we also found some interesting and peculiar cases in which the spectrum evolves as if it shrinks (i.e. in a νF_ν representation the low and high energy spectral slope becomes steeper) during the rise phase of the light curve and widens during the decay phase. This evolution is present in few (4) pulses in different burst of the sample analyzed. The search for it can be complicated by the erratic behaviour of one of the three parameters during the pulse or by the superposition of other morphological trends: in fact we suggest, based, for the moment only on the most reliable cases that we have found in our bursts, that this peculiar evolution could be associated with intense bright pulses, maybe under particular emission conditions. Here we just report the preliminary results of this peculiar evolution.

In fig.7.7 are reported the most representative cases of this kind of evolution: it can be identified in general by the anticorrelation between the peak energy and the high energy spectral index β and by the correlation between the peak energy and the low energy spectral index α . In GRB 960924 (left column of fig.7.7) the main peak at $t \sim 5$ sec is characterized by a strong anticorrelation between the peak energy (panel (c)) and the high energy spectral index β (panel (e)) with a correlation coefficient of -0.97 (and associated probability of $3e-5$). This indicates that while the peak energy increases during the rise phase of the pulse, the high energy spectral component in a νF_ν representation (i.e. $\beta + 2$) becomes steeper; during the decay portion of the light curve the peak energy decreases and the high energy power law becomes flatter. The low energy spectral index α , instead, is anticorrelated with β and correlates with the peak energy (with a coefficient of 0.95) and this means that during the rise phase it steepens and softens during the decay. This evolution is peculiar because it indicates that as the count rate rises the corresponding spectrum becomes narrower as if there is a concentration of most of the photons around a characteristic energy of ~ 800 keV (in this case).

The right column of fig.7.7 represents the spectral evolution of GRB 970420. The general evolution of this burst is tracking, and in particular the low energy spectral index tracks the photon flux. The peculiar evolution is present on the main peak which starts at $t \sim 45$ sec, after the trigger, and lasts until $t=48.5$ sec. In this case again there is a strong anticorrelation between E_{peak} and β also indicated by the corresponding Spearman's correlation coefficient which is 0.78. The low energy spectral index α is correlated with the peak energy (with a coefficient of 0.8). In order to clarify this peculiar evolutionary morphology we report in fig.7.6 the spectral evolution of the main peak of GRB 970420 as represented by the best fit model to the single time resolved spectra.

These evolution, if proved by further analysis of GRBs, could be, as possibly indicated by the analysis of the few cases found in our sample, associated with the temporal properties of the pulse. In fact, it seems that this morphology is evident on well shaped, symmetric pulses with duration lower than 5 seconds which are separated from the rest of the light curve. It could be speculated that they represent the phases in which there is less superposition of different emission episodes and evolutionary morphologies, or it could be associated with a particularly efficient radiation emission due to a strong shell crossing episode, which determines the appearance of the outstanding pulse in the light curve and produces this peculiar evolution. In this view, this evolution could be further investigated as a possible fundamental trend present associated with the radiation mechanism.

7.4.3 The hard to soft evolution in mixed morphologies

The spectral evolution described with the low energy α , high energy β and peak E_{peak} parameters has revealed in 50% of the burst analyzed a mixed morphology. Some of the peaks, in these bursts, evolves hard to soft and some others have a tracking morphology. Still among these cases there are some differences, in fact in 5 bursts the hard to soft evolution is present in their first peak. The following peaks have a tracking evolution. Moreover in these cases the first peak (which evolves hard to soft) has time resolved spectra, corresponding to the rise phase, with $\beta > -2$. This means that the peak energy is not within the observational band and that the spectrum peaks above ~ 1800 keV.

The possible implication of this trend (if confirmed through the analysis of more cases) could be associated with the properties of the emission process at the beginning of the burst: in fact, this should produce an extremely hard high energy spectrum (i.e. with $\beta > -2$) and then determine its evolution, in a time interval of few (~ 5) sec, so that in the decay phase of the burst its spectral shape at high energies is softer and the spectrum peaks within the energy band.

The relevant points that emerged from the analysis presented in this chapter, about the evolution of the spectrum in bright GRBs, and that can be considered in drawing a possible schematic picture of an evolutionary model are:

1. the tracking morphology, present in many bursts, which is characterized by an association between the spectral hardness (either indicated by the peak energy alone or by the low and high energy spectral components);
2. the presence, in other bursts, of a hard to soft evolution typically on the first pulse, which then becomes tracking in the following pulses;
3. the fact that in hard to soft pulses the peak of the spectrum is often above the upper limit of the observational energy range because the spectrum has a high energy spectral slope harder than E^{-2} ;

4. the presence of an envelope which constrains the evolution of the spectral parameters, at low and high energies as well as at the peak of spectrum, and, in most cases, seems to determine a global softening of the spectrum
5. some peculiar evolutions characterized by a shrink and relaxation of the spectrum possibly in association with bright symmetric pulses.

7.5 Conclusions

In this chapter we have presented the spectral evolution of the bright bursts whose general properties have been discussed in chapt.5. In particular the standard spectral evolution analysis based on the study of the temporal variation of the peak energy E_{peak} has been applied to this sample of bursts.

Similarly to previous authors (Ford et al. [42]) we could find, within the spectral evolutions of these bursts, the typical hard-to-soft and tracking morphologies, with the latter being the most frequently encountered. Nonetheless, no clear and unique relation between the observed trends and other spectral or temporal burst properties emerged from the application of this standard analysis. Moreover, the findings of chapt.5 showed that the spectrum can have a large variety of spectral shapes at low and high energies and the new results of chapt.6 have pointed out that the spectral character of the bursts can evolve from thermal to non-thermal from the first phases to the later time emission.

These facts indicate that the spectral evolution of the burst should be described by the complete spectral form rather than by a single parameters like the peak energy. For this reason we reconsidered all the spectral evolutions of the same bursts studying the temporal dependence of the complete time resolved spectrum, i.e. considering its low and high energy components in addition to its peak energy, on the single pulses. This analysis was quantified, in order to study the different spectral morphologies, in terms of correlations among the spectral parameters and the burst flux.

This multi-parameter analysis revealed that in the burst sample are present the standard evolutionary morphologies (tracking and hard-to-soft) which are associated also with the low and high energy spectral components. The interesting findings and possible new trends revealed through this approach are:

- the tracking morphology is present in 9 (over 18) bursts. In these cases the spectral parameters (mostly the low energy spectral index and/or the peak energy) evolve in phase with the flux;
- 8 bursts present a mixed evolution with peaks evolving hard-to-soft and tracking; in 5 cases this evolution is hard-to-soft on the first peak and the spectrum in the rise phase of this peak does not peak within the observational band ($\beta > 2$).
- the presence of an envelope which determines a general softening of the pulses during the complete burst; this envelope is evident in the low and high energy

spectral slopes and it seems to be present in bursts with the hard-to-soft or the tracking morphology. This might indicate that it is related possibly to the inner engine temporal evolution;

- 2 peculiar cases in which, during an intense pulse of the light curve there is a clear correlation between the peak energy, the low energy spectral slope and the flux, on one side, and an evident anticorrelation of the high energy spectral slope with the flux on the other. This indicates that the spectrum (as represented in νF_ν) shrinks during the pulse rise phase and relaxes during the decay.

The interpretation of these findings might reveal new aspects of the burst evolution or of the emission process producing the prompt phase γ photons.

This work is still in progress and the principal directions of research which are planned in the near future are: the analysis of the spectral evolution of these bursts with a well defined quantitative method based on the possible correlations among the spectral parameters and the burst flux in order to compare GRBs with similar evolutions; the search for other morphologies and the confirmation of the new trends through the analysis of other bursts; the characterization of the envelope with other multi-peaked bursts and its interpretation in relation to the physics of the fireball; the definition of a strategy for the association of the spectral evolution within a burst with its temporal properties like the rise and decay phase and the time delay between the pulse peak and the hardest spectrum.

Trigger	Flux correlation			Peak spectra						Minima spectra					
	α	β	E_{peak}	m	α q	P	m	E_{peak} q	P	m	α q	P	m	E_{peak} q	P
143 - T	0.14	-0.41	-0.13	-0.01	-0.72	0.15	-62.8	640.3	0.93	-0.13	-0.78	0.8	-39	327	0.9
	0.95	-0.3	0.9												
	0.95	-0.14	0.26												
1473 - T	0.7	0.7	0.8	-0.04	-0.39	0.4				-0.02	-0.78	0.15			
	0.55	0.02	0.52												
	0.08	0.-0.1	0.12												
1625 - T	0.59	0.18	0.53	0.002	-0.51	0.38	-46.	1225	0.74	0.02	-1.12	-0.18	10.7	98.7	0.9
	0.72	-0.06	0.49												
	0.6	0.2	0.5												
2083 - HtS	0.85	0.01	0.64	-0.07	-0.076	0.67	-54.	575	0.49						
	0.88	0.7	0.82												
2329 - ??	0.99	-0.5	-0.46	0.04	-1.02	0.005	-326	4406	0.005	-0.015	-1.06	0.5	-628	8024	0.3
	0.98	-0.8	-0.35												
	0.94	-0.9	-0.6												
2537 - T	-0.4	-0.41	0.8	-0.04	-1.44	0.83	-2.9	146	0.8						
	0.1	-0.3	0.94												
	0.65	0.14	0.36												
2831 - T	0.9		0.88	-0.03	0.55	0.92	14.7	953	0.54	0.007	-1.12	0.01	-23.	1146	0.98
	0.9		0.8												
	0.8		0.8												
3491 - HtS/T	0.35	-0.56	-0.46	-0.13	0.44	0.79				-0.09	-0.41	0.05	-22.	335	0.99
	0.91	-0.49	0.97												
	0.9	-0.9	0.8												
3492 - HtS	0.95	0.61	0.83												
3523 - T	0.46	-0.71													
5567 - ??	0.75	-0.5	0.14							0.007	-0.65	0.72	1.13	186	0.85
	0.25	-0.46	0.53												

5614 - T	0.83	-0.81	0.76												
5621 - HtS	0.4	-0.15	0.49							-0.06	-0.69	0.64	-11.25	166	0.75
6198 - HtS/T	0.78	0.71	0.85	-0.014	-1.45	0.43	-0.005	-0.75	0.08						
	0.9	0.6	0.1												
	0.98	-0.11	0.93												
6404 - HtS	-0.14	0.33	0.9												
	0.73	0.61	0.45												
6581 - T	0.57	-0.61	0.95												
7301 - T	0.3	-0.9	-0.7				-49	1213	0.057				128	-1750	0.1
	0.5	-0.5	0.6												
	0.77	0.37	0.94												

Table 7.1: Classification of the spectral evolutions in the sample of bursts analyzed. The trigger is reported in the first column along with the morphological classification following the standard method: T = tracking, HtS = hard to soft both defined only on the basis of the E_{peak} evolution. The correlations between the spectral parameters α , β and E_{peak} with the flux within each pulse are reported in the next column. The average values of the best fit parameters for each pulse within the burst are also reported. Trend in the low energy spectral index α and in the peak energy E_{peak} are separated for the spectra corresponding to the peaks and to the minima. The parameters (m,q) refers to the linear fit of these parameters as a function of time since trigger and P is the associated probability.

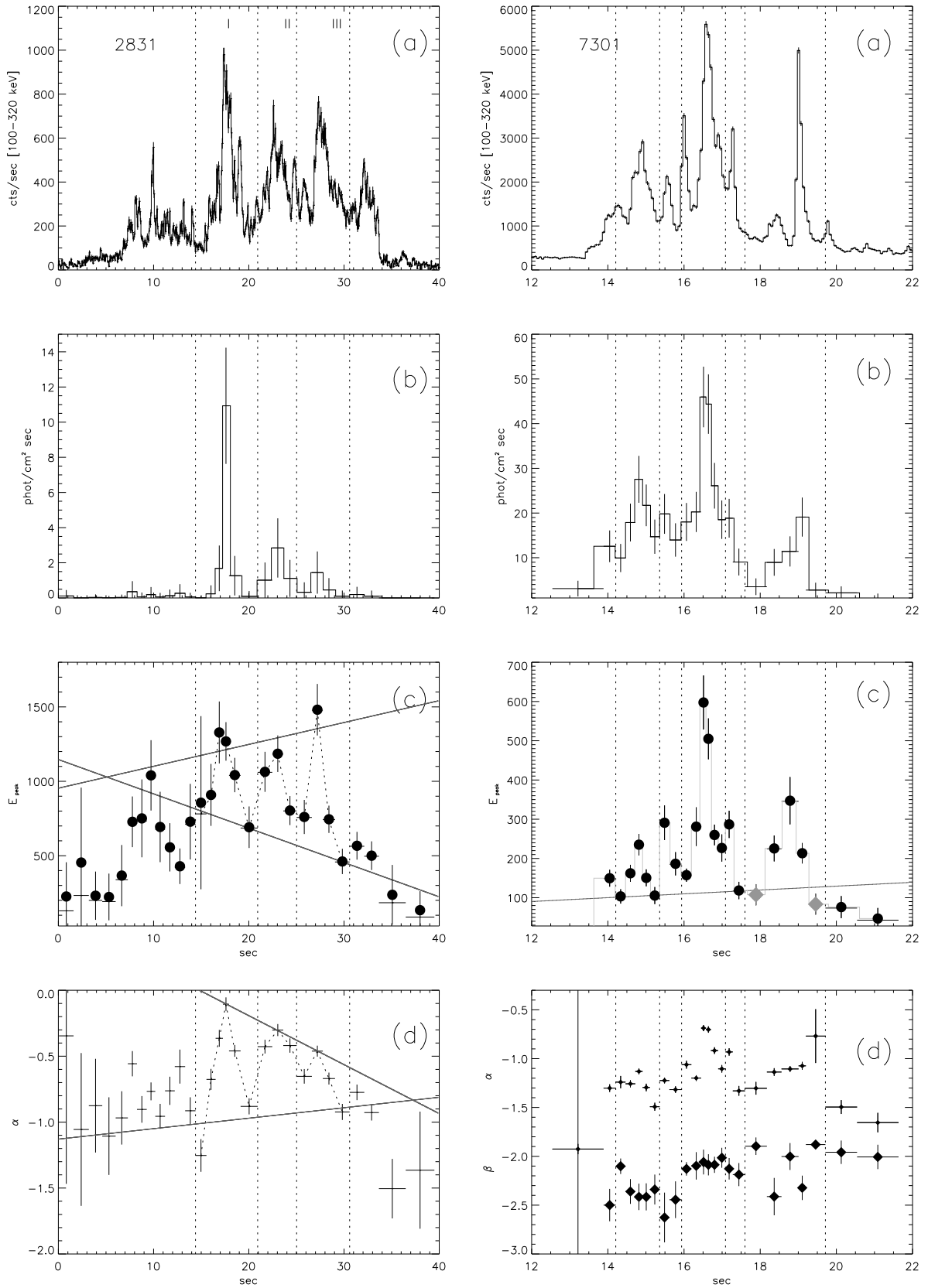


Figure 7.1: Examples of tracking evolution. Left: GRB 940217. Right: GRB 990104

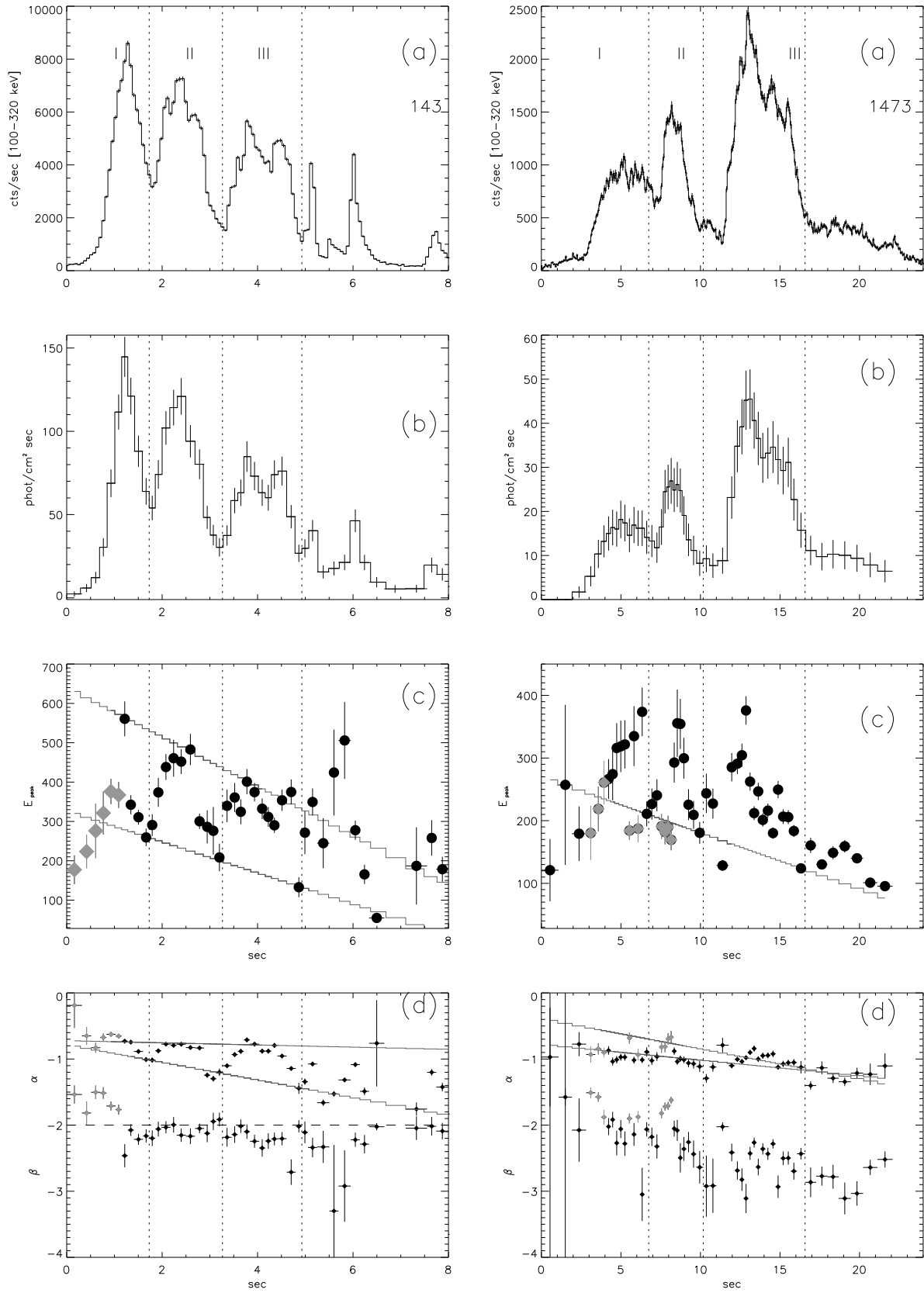


Figure 7.2: Examples of mixed evolution. Left: GRB 910503. Right: GRB 920311

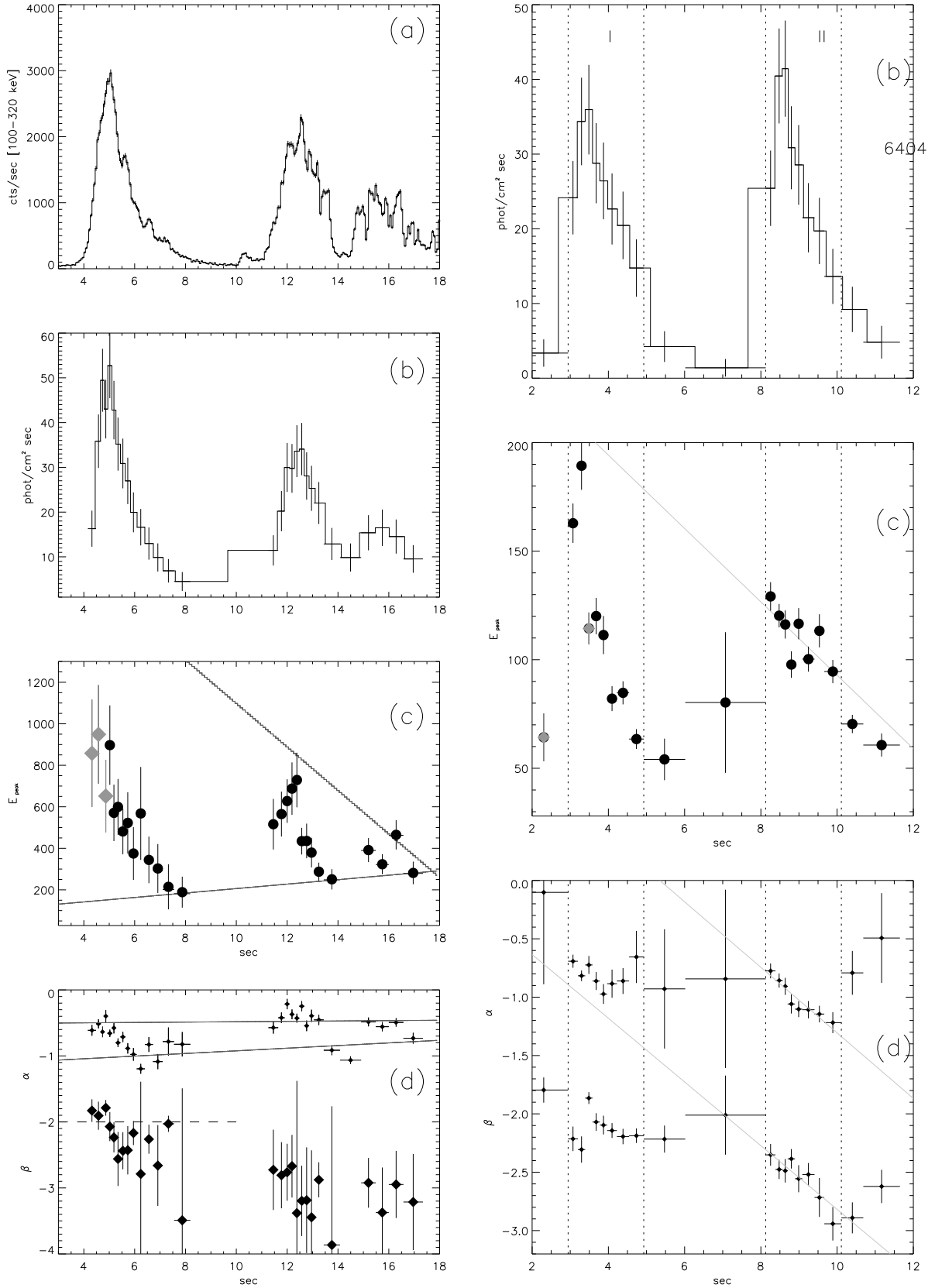


Figure 7.3: Examples of mixed evolution. Left: GRB 920525, same as fig.7.2. The lines represent the limiting evolutionary trends represented by the peak spectra and by the spectra represented by the minima. Right: GRB 960807

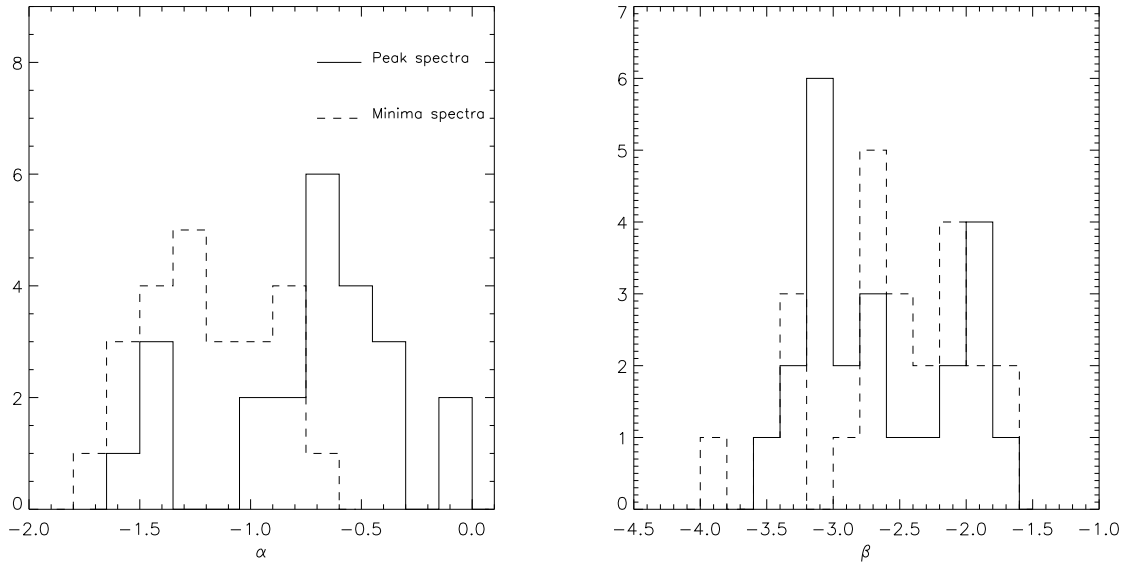


Figure 7.4: Left: Low energy spectral index distribution for the spectra corresponding to the peaks (*solid line*) and to the minima separating the pulses (*dotted line*) for those bursts showing an envelope in their evolution. Right: high energy spectral index for the same spectra

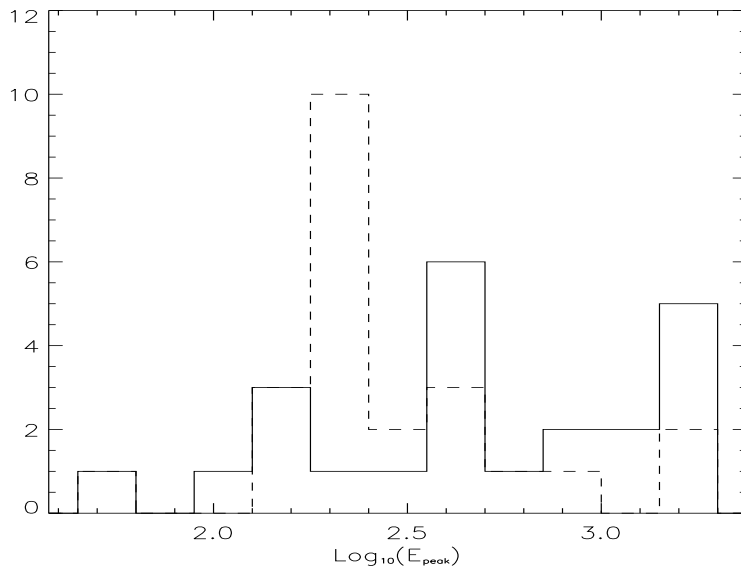


Figure 7.5: Peak energy distribution for the spectra corresponding to the peaks (*solid line*) and to the minima separating the pulses (*dotted line*) for those bursts showing an envelope in their evolution.

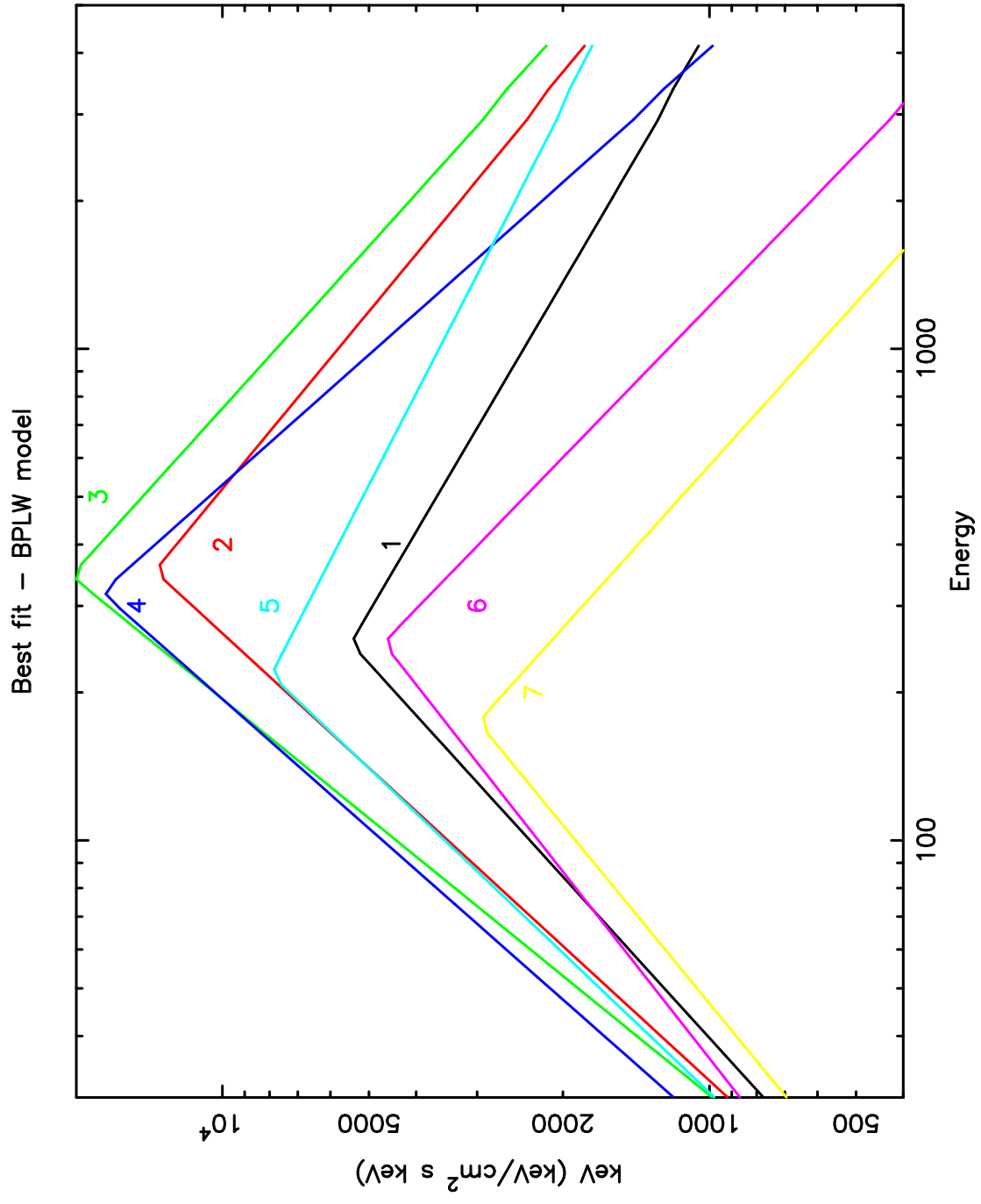


Figure 7.6: Best fit model evolution for GRB 970420. The numbers indicate the sequence of the spectra which have a peculiar evolution.

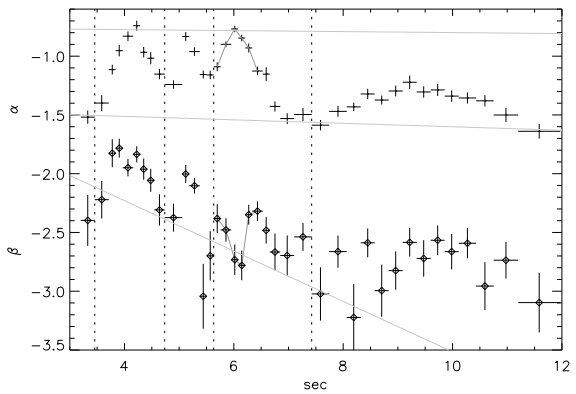
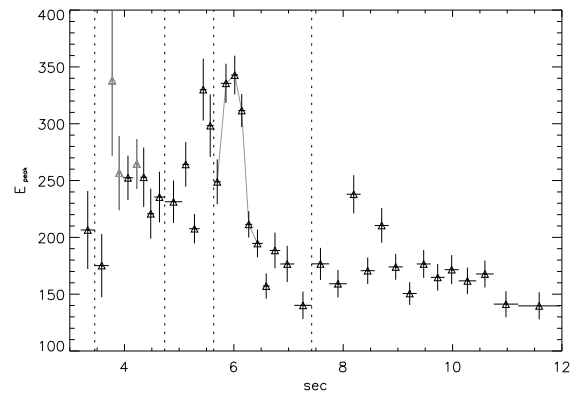
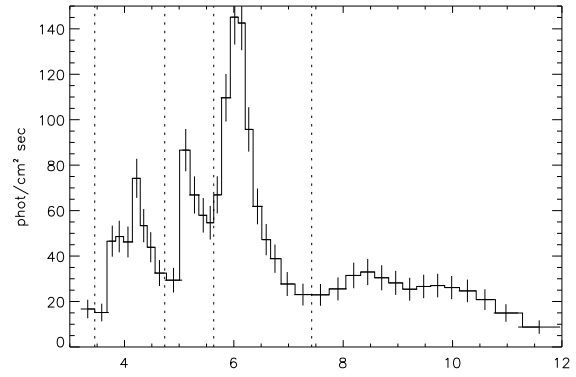
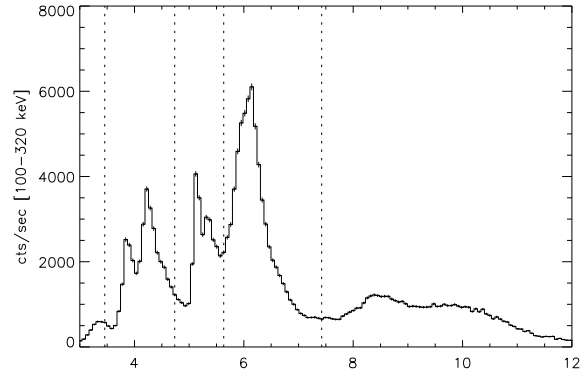
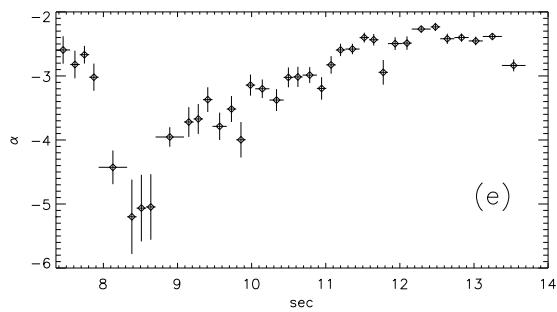
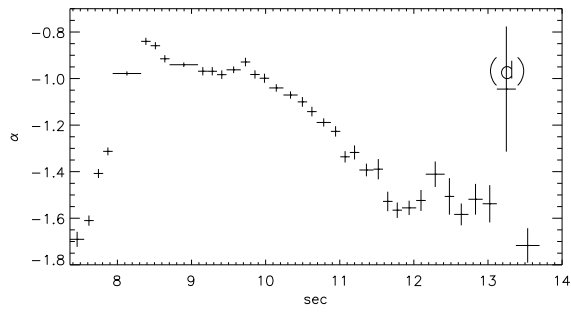
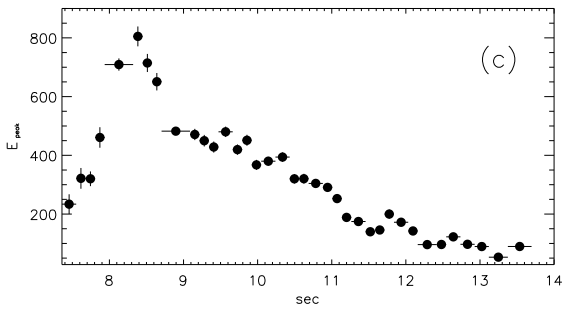
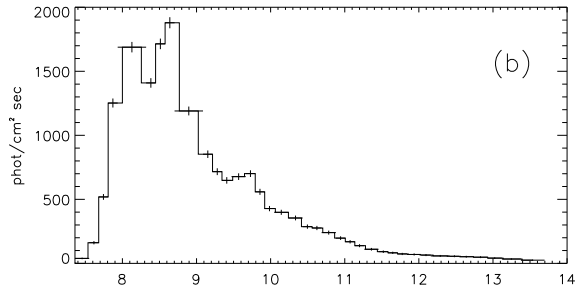
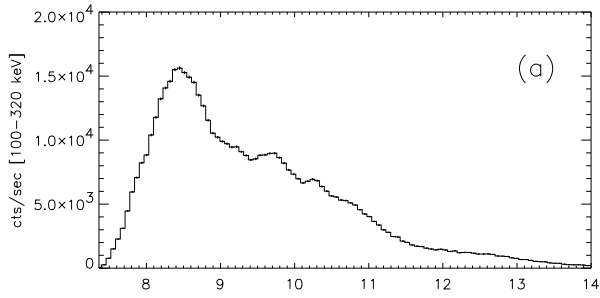


Figure 7.7: Examples peculiar evolution morphologies. Left: GRB 960924. Right: GRB 970420

Conclusions

The analysis of the time resolved and time integrated spectra of a sample of bright bursts, with the most commonly adopted spectral models, has pointed out that different spectral shapes can reasonably represent the observed spectra. If any of these spectral functions is adequate to represent the basic spectral shape of GRBs, this can be revealed by the analysis of the spectrum integrated on the smallest (available) timescale. In fact, the main results of this thesis (i.e the violation of the synchrotron limit, the constraints for the alternative models, the thermal emission of the first phases in extremely hard bursts) have been obtained by means of the high time resolution of the data selected for this analysis.

The low energy spectral slopes of $\sim 14\%$ of time resolved spectra are harder than the optically thin synchrotron limit ($F(E) \propto E^{1/3}$) and indicate that this violation is present both in the rise and decay phase of the pulses and that the optically thin synchrotron model faces serious difficulties in reproducing the observed low energy hard spectra. A conclusive test of this model, that was performed for the first time, was the fit of its spectral shape to the time resolved spectra of these bright bursts, which, when harder than the above limit, resulted in unacceptable fits.

Modifications of the standard theory, accounting for more realistic conditions such as self-absorption, electron small pitch angle distribution, magnetic field small scale structure, stratified emission, have been proposed to overcome these difficulties, within the framework of synchrotron theory. Also alternative models, based on Comptonization due to thermal or quasi-thermal electrons in saturated regime, photospheric emission and Compton drag, have been suggested in order to justify these hard spectral slopes. However, these models, predict limiting slopes which could/should be compared with other, harder spectral constraints.

The analysis of 5 bursts, among the hardest observed by BATSE, revealed that the low energy spectrum is harder than $F(E) \propto E^1$ for a considerable period of their main peak emission. This evidence further indicates that synchrotron emission, even including the above effects, cannot reproduce all the observed ranges of slopes. Comptonization models, instead, represent possible alternatives although some of them require implausible physical conditions (e.g. optical depth, particle densities or soft seed photon source) to account for the observed hardest spectra.

One of the most interesting experimental evidence resulting from the analysis of these

hard bursts is their consistency, at least in the initial phases of their main peaks, with thermal black body emission. The luminosity of this thermal phase is a considerable fraction, or even the bulk, of the total burst luminosity. This emission can be identified as the possible thermal radiation predicted by a fireball, composed either by a single or many shells, becoming transparent, or in the context of the Compton drag model.

The indications that have been derived seem to exclude the single fireball scenario, which would require an extremely high internal energy ($\sim 10^{58}$ erg) to produce the observed luminosities, and favor the multiple-shell model which predicts a transparency radius of $\sim 10^{13}$ cm (for typical assumed values of the fireball parameters) similar to the prediction of the “standard” model.

Identically acceptable to justify this thermal initial phase is the Compton drag scenario which, with the results obtained from the black body fits, implies a Lorentz factor $\Gamma \sim 100$. It should also be noted that in this model, after the thermal phase, the shocks can form, due to the deceleration of the fireball. This can explain the observed transition to a non-thermal phase after the first 5-10 seconds.

We plan to further investigate these results, also by comparison with the predictions of a time dependent Compton drag model. In particular the search and analysis of other hard bursts (also among the non triggered BATSE events) could reveal if the thermal emission is systematically present in the initial phases of the hardest bursts. The possible evidence of a black body emission on a second peak within the same burst, would not be easily explained by the Compton drag model. In this case, in fact, it is not clear how to replenish the emission region with seed photons which are required to produce the second peak thermal emission.

The analysis of the spectral evolution of the bright bursts presented in this thesis indicates that new morphologies can be revealed if the complete burst spectrum, as described by its low and high energy components, is considered in addition to the classical analysis based only on the temporal evolution of the spectrum peak energy. These morphologies have also been quantified with the analysis of the correlations between the spectral parameters and the flux.

In particular this has revealed the presence of an “envelope” which regulates the global softening of the late pulses with respect to the early one. Moreover its presence in multi-peaked bursts resulted to be independent of the particular evolution morphology of the burst itself (tracking, hard to soft or mixed).

Clearly, the existence of an overall regulated behaviour of the sequence of peaks might reveal the direct signature of the engine temporal activity. Because of its potential importance I intend to further explore the character of this behaviour and in particular seek for its relations with the peak durations and intensity and with the spectral hardness. The already found trends, as well as any future one, will be considered - as a first step - within the frame of the emission scenarios proposed so far.

The spectral evolution analysis has also shown that in some bursts there is a transition from an hard to soft morphology, in the first pulse, to a tracking one in the rest of

the burst. The immediate development of this analysis will verify if this behaviour is associated with the duration of GRBs and/or with their fluence.

A further aspect which has been raised by the above analysis is the possibility that the behaviour typical of a mixed morphology shown in the first peak of some bursts can be actually an “artifact” due the fact that the spectral peak is in fact initially located above the BATSE threshold (1800 keV). The clarification of this issue clearly requires the analysis of the burst spectral evolution over a wider energy range, such as that which will be possible thanks to the observations by AGILE, SWIFT and especially GLAST.

Indeed impressive progress in the understanding of the temporal and spectral properties of GRB is expected in the forthcoming future because of the launch of these satellites. Although it is not easy to anticipate the actual physical insight which will be gained from that, from a phenomenological point of view the increased energy range (they will expand the BATSE range, covering the interval from ~ 5 keV to 30-300 GeV), temporal resolution (GLAST is expected to achieve a time resolution of few μs), and sensitivity will provide the opportunity of studying the burst spectral evolution over its minimum variability timescale - plausibly associated with the central engine activity - detected so far. Indeed a seriously exciting prospect!

Bibliography

- [1] Akerlof C., W. Nature **398** 400 (1999)
- [2] Andersen et al. A&A **364**, L54 (2000)
- [3] Band D. L. et al. Experimental Astronomy **2** 307 (1992)
- [4] Band D. L. et al. ApJ **413**, 281 (1993)
- [5] Band D. L. et al. ApJ **447**, 2891 (1995)
- [6] Band D. L. et al. ApJ **458**, 746 (1996)
- [7] Berger & Kulkarni ApJ **560** 652 (2001)
- [8] Bevington & Robinson *Data reduction and error analysis for the physical science*
McGraw-Hill, 1992
- [9] Balndford & Znajek MNRAS **179** 433 (1977)
- [1999] Blinnikov Astron. Rep.,**43** , 739 (1999)
- [10] Bloom J. et al. ApJ **123** 1111 (2002)
- [11] Borgonovo & Ryde ApJ, **548**, 770 (2001)
- [12] Brainerd ApJ **428** 21 (1994)
- [13] Cavallo G. & Rees M. J. MNRAS **183** 359 (1978)
- [14] Cen et al. ApJ **507**, L131
- [15] Cline T. L. & Desai U. D. ApJ **185**, L1 (1973)
- [16] Cline T. L. & Desai U. D. ApJ **196**, L43 (1975)
- [17] Costa E., et al. Nature **387**, 783 (1997)
- [18] Costa E. A&AS **138** 425 (1999)
- [19] Covino S. et al. A&A **348** L1 (1999)
- [20] Crider A. , 1997, AIP Conference series 428, Gamma Ray Bursts: 4th Huntsville Symposium, ed. Meegan C. A., pp.359-363

- [21] Crider A., Liang E.P., Smith I.A. ApJ **479** L39 (1997)
- [22] Crider A., Liang E.P. & Preece R.D. astro-ph/9711100 (1997)
- [23] Crider et al. ApJ **519**, 206 (1999)
- [24] Crider A. & Liang E.P. ApJ **127** 283 (2000)
- [25] Daigne & Mhovich astro-ph/0207456 (2002)
- [26] Dermer & Boettcher ApJ **534**, L155 (2000)
- [27] Dermer et al. astro-ph 0107217 (2001)
- [28] Djorgovski et al. GCN **289** (1999)
- [29] Dar A. et al. Astro-ph/0112227 (2000)
- [30] Djorgovsky et al. Astro-ph/0107535 (2001)
- [31] Djorgovski et al. astro-ph/0106574 (2001)
- [32] Drenkhahn G.& Spruit H. C. A&A **391** 1141 (2002)
- [33] Epstein R. I., ApJ **183** 593 (1973)
- [34] Fenimore E.E. et al. ApJ **448** L101 (1995)
- [35] Fenimore et al. ApJ **473** 998 (1996)
- [36] Fenimore E. E. ApJ **518** 375 (1999)
- [37] Fenimore & Ramirez-Ruiz astro-ph/0004176 (2000)
- [38] Fishman & Meegan ARA&A **33** 415 (1995)
- [39] Fishman G. J. Proc. *Gamma Ray Observatory Science Workshop* (Washington:NASA),3-47. (1989)
- [40] Fishman G. J. et al. ApJS **92** 229 (1994)
- [41] Ford L. *A Guide to the Spectroscopic Oriented Analysis Routines* version 2.1 (1993)
- [42] Ford L.A. et al. ApJ **439** 307 (1995)
- [43] Frail D. et al. Nature **389**, 261 (1997)
- [44] Frail et al. Astro-ph/0102282 (2001)
- [45] Fryer C. ApJ **526** 152 (1999)
- [46] Frontera et al. A&A **334** L69
- [47] Frontera F. et al. ApJS **127** 59 (2000)

- [48] Galama T. et al. Nat. **395** 670 (1998)
- [49] Galama T. et al. ApJ **536** 185 (2000)
- [50] Gallant et al ApJ **391** 73 (1992)
- [51] Ghirlanda G. et al. A&A **393** 409 (2002)
- [52] Ghirlanda G. et al. A&A **406** 879 (2003)
- [53] Ghisellini G. & Lazzati D. MNRAS **309** L7 (1999)
- [54] Ghisellini G. astro-ph/9905181 (1999)
- [55] Ghisellini G. & Celotti A. ApJ **511** L93 (1999)
- [56] Ghisellini G. et al. MNRAS **316** L45 (2000)
- [57] Ghisellini G. et al. MNRAS **313** L1 (2000)
- [58] Ghisellini G. et al. ApJ **389** L33 (2002)
- [59] Ghisellini G. et al. astro-ph/0205227 (2002)
- [60] Golenetskii S. V. et al. Nature **306**, 451 (1983)
- [61] Goodman J. ApJ **308** L47 (1986)
- [62] Goodman J. New Astronomy **2** 449 (1997)
- [63] Granot J., Piran T. & Sari R. ApJ **534** L163 (2000)
- [64] Groot et al. IAU Circ.**6588** (1997)
- [65] Grosbol P. Bull. Inform. CDS **35** 1988
- [66] Gruzinov & Waxman ApJ **511** 852 (1999)
- [67] Haeger & Woosley astro-ph/0206005 (1999)
- [68] Harrsion et al. ApJ **559** 123 (2001)
- [69] Heise J. et al. astro-ph/0111246 (2001)
- [70] Hjonth et al. Sci **283** 2073 (1999)
- [71] Horack, J.M. *NASA Reference Publication 1268* (1991)
- [72] Hoshino et al ApJ **390**, 454 (1992)
- [73] Israel G. et al. A&A **348** L5 (1999)
- [74] Jackson J.D. *Classical Elettrodynamics* New York: Wiley
- [75] Kargatis V. et al. ApJ **422**, 260 (1994)

- [76] Kargatis et al. *Ap&SS* **231**, 177 (1995)
- [77] Katz *ApJ* **432**, L107 (1994)
- [78] Katz J. *ApJ* **490** 633 (1997)
- [79] Kazimura et al. *ApJ* **498** L183 (1998)
- [80] Kennel C. F. et al. *ApJ* **283** 694 (1984)
- [81] Kippen M. et al. *astro-ph/0102277* (2001)
- [82] Kippen M. R. et al. *astro-ph/0203114* (2002)
- [83] Kitchin C. R., *Astrophysical Techniques* 2nd ed., Adam Hilger (1991)
- [84] Klebesadel R. et al. *ApJ* **182** L85 (1973)
- [85] Kommers M. J. et al. *ApJSS* **134** 385 (2001)
- [86] Kouveliotou C. et al. *ApJ* **413**, L101 (1993)
- [87] Kulkarni S. R. *Nature* **398** 389 (1999)
- [88] Lamb D. Q. *astro-ph/0210434* (2002)
- [89] Lamb D. Q. & Reichart D. E. *astro-ph/0109037* (2001)
- [90] Lazzati D. et al. *ApJ* **529** L17 (1999)
- [91] Lazzati D. et al. *ApJ* **529** L17 (2000)
- [92] Lee et al. *ApJ* **561** 183 (2001)
- [93] Li & Fenimore *ApJ* **469** L115 (1996)
- [94] Liang & Kargatis *Nature* **381**, 495 (1996)
- [95] Liang *ApJ* **491** L15 (1997)
- [96] Liang E. et al. *ApJ* **479** L35 (1997)
- [97] Liang et al. *A&A* **138**, 529 (1999)
- [98] Lloyd N.M. & Petrosian V. *ApJ* **543** 722 (2000)
- [99] Lloyd & Ramirez-Ruiz *Astro-ph/0205127* (2002)
- [100] Lloyd N. M & Petrosian V., *ApJ* **565** 182 (2002)
- [101] MacFadyen & Woosley *ApJ* **524** 262 (1999)
- [102] Matz S. M. et al. *ApJ* **288**, L37 (1985)
- [103] Mazets E. P. et al. *JETP lett.* **19**, 77 (1974)

- [104] McLaughlin et al. *ApJ* **567** 454 (2002)
- [105] Medvedev M.V. astro-ph/9904363 (1999)
- [106] Medvedev *ApJ* **540**, 704 (2000)
- [107] Medvedev M.V. astro-ph/0001314 (2001)
- [108] Meegan C. A. et al. *Nature* **355**, 143 (1992)
- [109] Meegan & Pendleton *ApJS* **106** 65 (1996)
- [110] Meszaros P. & Rees M. J. *ApJ* **405** 278 (1993)
- [111] Meszaros P. & Rees M. *ApJ* **482** L29 (1997)
- [112] Meszaros & Rees *ApJ* **476** 232 (1997)
- [113] Meszaros P. & Rees M. *ApJ* **530** 292 (2000)
- [114] Meszaros P. ARAA to be printed astro-ph/0111170 (2002)
- [115] Mitrofanov et al. *ApJ* **504** 925 (1998)
- [116] Norris J. P. et al. *ApJ* **301**, 213 (1986)
- [117] Norris et al. *ApJ* **459** 393 (1996)
- [118] Paciasas W. S. et al. *ApJ SS* **122** 465 (1999)
- [119] Paczynsky B. *ApJ* **308** L43 (1986)
- [120] Paczynsky B. et al. *PASP* **107**, 1167 (1995)
- [121] Paczynsky B. *ApJ* **494** L45 (1998)
- [122] Panaitescu & Kumar *ApJ* **560** L49 (2001)
- [123] Papathanassiou H. *A&AS* **138** 525 (1999)
- [124] van Paradijs J. et al. *Nature* **386**, 686 (1997)
- [125] Pendleton G. N. et al. *Nuc. Inst. and Methods in Phy. Res.* **A 364** 567 (1995).
- [126] Piran T. *Physics Report* **575** 667 (1999)
- [127] Piro et al. *ApJ* **514** L73 (1999)
- [128] Preece R. et al. *ApJ* **473**, 310 (1996)
- [129] Preece et al. *ApJ* **548496**, 849 (1998)
- [130] Preece R. et al. *ApJS* **126**, 19 (2000)
- [131] Preece R.D., 2001, submitted to World Scientific

- [132] Ramirez-Ruiz & Fenimore A&A SS **138** 521 (1999)
- [133] Rees M. J. & Meszaros P. ApJ **430** L93 (1994)
- [134] Rohads J. E. ApJ **525** 737 (1999)
- [135] Ruderman M. Ann. N. Y. Acad Sci. **262** 164 (1975)
- [136] Ryde F. Astro Lett. & Communications **39** 281 (1999)
- [137] Ryde & Svensson ApJ **529**, L13 (2000)
- [138] Ryde & Petrosian Astro-ph/0206204 (2002)
- [139] Rybicki G. B. & Lightman A. P., *Radiative Processes in Astrophysics*, New York: Wiley 1979
- [140] Salmonson & Wilson astro-ph/0208303 (2002)
- [141] Sari R. et al. ApJ **473** 204 (1996)
- [142] Sari et al. ApJ **497** L17 (1999)
- [143] Sari R. & Piran T. ApJ **520** 641 (1999)
- [144] Sari R. et al. ApJ **519** L17 (1999)
- [145] Sari R. & Esin A. A. ApJ **548** 787 (2001)
- [146] Scalo & Weeler ApJ **562** 664 (2001)
- [147] Schaefer et al. ApJ **492**, 696 (1998)
- [148] Schaefer & Walker ApJ **511**, L89 (1999)
- [149] Shemi & Piran ApJ **365** L55 (1990)
- [150] Smail et al. ApJ **449** L105 (1995)
- [151] Spruit A&A **381** 923 (2002)
- [152] Svensson ApJ **258** 335 (1982)
- [153] Svensson MNRAS **209** 175 (1984)
- [154] Tavani M. ApJ **466** 768 (1996)
- [155] Totani T. et al. ApJ **486** L71 (1997)
- [156] Vietri M. ApJ **507** L45 (1998)
- [157] Vietri M. et al. ApJ **308** L29 (2000)
- [158] Zhang & Meszaros Astro-ph/0206158 (2002)

[159] Walker ApJ **537** 264 (2000)

[160] Wells and Greisen, Image Processing in Astronomy (1979)

[161] Winkler C. et al. A&A **302** 765 (1995)

[162] Woosley S. ApJ **405** 273 (1993)